Electron Microscopy Characterization of Pentacene and Perfluoropentacene Grown on Different Substrates

Dissertation

zur
Erlangung des Doktorgrades
der Naturwissenschaften
(Dr. rer. nat.)

dem

Fachbereich Physik
der Philipps-Universität Marburg

vorgelegt von

Rocío Félix Ángel

aus
La Palma del Condado, Huelva, Spanien

Marburg/Lahn, 2017

Vom Fachbereich Physik der Philipps-Universität Marburg
als Dissertation angenommen am:
Erstgutachter: Prof. Dr. Kerstin Volz
Zweitgutachter: Prof. Dr. Sangam Chatterjee
Tag der mündlichen Prüfung:
Hochschulkennziffer 1180

Contents

Abstract

‘The secret of getting ahead is getting started. The secret of getting started is breaking your complex overwhelming tasks into small manageable tasks, and then starting on the first one’ — Mark Twain

This thesis deals with the study of the morphology, arrangement and orientation of organic semiconductor films by (scanning) transmission electron microscopy ((S)TEM) techniques. The organic semiconductor perfluoropentacene (PFP) as well as the organic heterostructures of pentacene (PEN) and PFP have been investigated. PFP has been grown on graphene substrate, while the organic mixtures formed by PEN and PFP have been deposited with different mixing ratios on two different substrates, i.e. SiO_2 and KCl.

PFP deposited on graphene exhibits an epitaxial growth in island shapes where the molecules lie flat and parallel to the substrate adopting the so called 'π-stacked polymorph'. Within this work, the lateral alignment of the PFP molecules with respect to the graphene substrate has been determined. It was found that the long molecular axis of PFP is aligned along the zig-zag direction of the graphene. However, this alignment is not exactly parallel, but exhibits a small offset.

Furthermore, the morphology of the PFP islands has been investigated. A characteristic angle around 68° was found between confining edges of PFP islands. The combination of TEM micrographs and electron diffraction patterns has enabled the determination of the planes that run parallel to the confining edges of the islands 'as seen' by the electron beam in the two-dimensional projection. From that the possible side facets associated with each confining edge have been suggested. Finally, electron tomography experiments were used to gain insight into the shape of the PFP islands, allowing the 3D reconstruction of them.

PEN:PFP blends have been prepared with mixing ratios of [2:1], [1:1] and [1:2] on an inert substrate such as SiO_2. Although different phases and morphologies have been observed for each mixture, a *mixed phase* made out of PEN and PFP which exhibits similar lattice parameters in all cases has been found independently of the mixing ratio. The monocrystalline SAED pattern of the mixed phase has been shown for the first time on this substrate. The diffraction pattern is rather similar to the one of the pure PEN in [0 0 1] direction, suggesting that the crystal structure of the mixed phase is similar to the one of pure PEN. For non-equimolecular blends, the respective pure phase in excess is present apart from the mixed phase.

A different morphology was observed for the different PEN:PFP mixing ratios. The equimolecular mixture of PEN and PFP exhibits fiber-like structures consisting of the mixed phase. For the mixture with PFP in excess, some fibers are formed on a background layer. The PFP is contained in the fibers, while the background layer is made out of the mixed phase. For the mixture with PEN in excess, a grainy structure (grain size of 10 nm-60 nm) with contributions of pure PEN and of the mixed phase is detected.

PEN:PFP blends with mixing ratios of [2:1] and [1:2] grown on KCl substrates have been investigated too. The mixed phase formed by PEN and PFP is also present and both blends reveal a quite different morphology. The composition, orientation and crystalline details of each phase have been inspected.

In the blend with PEN in excess, the mixed phase together with the pure PEN phase are found in a uniform layer formed with domains that are rotated in-plane by 90° towards each other. In contrast, the blend with excess of PFP presents two different arrangements. The majority of the sample exhibits some spicular fibers made out of PFP on a background layer composed by the mixed phase. The other arrangement present to a lesser extent consists of a film of pure PFP lying in direct contact with the KCl substrate.

The importance of PFP grown on graphene lies in the relevance of the graphene substrate together with the π-stacked arrangement exhibited by PFP on this substrate. This motif enhances charge carrier mobility along the stacking direction. The knowledge of the relative alignment as well as the faceting are a key information since the physical properties depend on these parameters. Furthermore, considering the role of the organic heterostructures in the development of organic electronic devices, a detailed understanding of the basic arrangement of the organic molecules in the organic blend is a requirement for the development of new organic devices.

Zusammenfassung
(Abstract in German)

‘Wenn du es dir vorstellen kannst, kannst du es auch machen’

— Walt Disney

Die vorliegende Arbeit befasst sich mit der Analyse der Morphologie, des Arrangements und der Orientierung organischer Halbleiterschichten mittels (raster-) transmissionselektronischer Methoden (im englischen: (scanning) transmission electron microscopy (S)TEM). Der organische Halbleiter Perfluoropentacen (PFP) sowie organische Heterostrukturen bestehend aus Pentacen (PEN) und PFP wurden untersucht. PFP wurde auf Graphen Substrate ausgewachsen, während die organischen Halbleiter PEN und PFP mit unterschiedlichen Mischungsverhältnissen auf zwei verschiedenen Substraten (SiO_2 bzw. KCl) abgeschieden wurden.

PFP bildet auf Graphen inselförmige Strukturen, die mit dem Substrat in einer epitaktischen Beziehung stehen. Die PFP Moleküle liegen flach und parallel zum Substrat und bilden das so genannten „π-stacked Polymorph“. Im Rahmen dieser Arbeit wurde die laterale Ausrichtung der PFP Moleküle bezüglich des Substrates bestimmt. Es zeigte sich, dass die lange Molekülachse des PFPs abgesehen von einem geringen Offset parallel zu der zig-zag Richtung des Graphens liegt.

Des Weiteren wurde die Morphologie der PFP Inseln untersucht. Zwischen den Inselkanten wurde ein charakteristischer Winkel von etwa 68° gemessen. Die Ebenen, die sowohl zur Richtung des Elektronenstrahls als auch zu den Inselkanten parallel verlaufen, konnten über eine Kombination der Informationen aus den TEM Aufnahmen und den Beugungsbildern indiziert werden. Aus diesen Ergebnissen konnten wiederum die möglichen Seitenfacetten der Inseln ermittelt werden. Um zusätzliche Informationen über die dreidimensionale Form der Inseln zu erhalten, wurden elektronentomographische Untersuchungen durchgeführt.

PEN:PFP Proben, die mit verschiedenen Mischungsverhältnissen von [2:1], [1:1] und [1:2] auf das inerte Substrate SiO_2 aufgewachsen wurden, wurden mittels SEM und TEM untersucht. Obwohl sich für jedes Mischungsverhältnis unterschiedliche Phasen und Morphologien bildeten, entstand in allen Fällen eine Mischphase aus PEN und PFP, die für alle Proben ähnliche Gitterparameter aufwies. Das einkristalline Beugungsbild dieser Mischphase auf SiO_2 wurde in dieser Arbeit zum ersten Mal aufgenommen und analysiert. Dieses Beugungsbild ist dem des PENs sehr ähnlich und suggeriert, dass PEN und die Mischphase eine ähnliche Kristallsymmetrie besitzen. Für Mischungsverhältnisse mit einem Überschuss an

PEN bzw. PFP zeigte sich, dass sich die jeweilige überschüssige Phase zusätzlich zur Mischphase ausbildet.

Die verschiedenen PEN:PFP Mischungsverhältnisse resultierten in unterschiedlichen Morphologien. Die Mischung gleicher Anteile von PEN und PFP führte zu der Bildung faserartiger Strukturen bestehend aus der Mischphase. Bei einem PFP Überschuss entstanden PFP Fasern, die sich auf einer Schicht aus der Mischphase befinden. Bei einem Überschuss an PEN hingegen ließ sich eine körnige Struktur (Korngröße 10 nm-60 nm) mit Beiträgen puren PENs und der Mischphase beobachten.

Zusätzlich zu dem inerten Substrat wurde das kristalline Substrat KCl verwendet, um das Wachstum von PEN:PFP Gemischen mit den Mischungsverhältnissen [2:1] und [1:2] zu untersuchen. Die zuvor nachgewiesene Mischphase bildete sich auch bei diesen Proben aus.

Bei der Probe mit PEN Überschuss liegen sowohl PEN als auch die Mischphase in einer einheitlichen Schicht vor, die in der Ebene um 90° zueinander rotierte Domänen enthält. In der Probe mit PFP Überschuss konnten zwei verschiedene Arrangements bestimmt werden. Der Großteil der Probe setzt sich aus nadelförmigen PFP Fasern zusammen, die sich auf einer Schicht der Mischphase befinden. Ein geringerer Anteil der Probe besteht aus einem Film reinen PFPs, das direkt auf das KCl Substrat aufwuchs.

Die Bedeutung von PFP, das auf Graphen aufgewachsen ist, liegt in der Relevanz des Substrates selbst, zusammen mit der Anordnung entlang des π-Orbitals, die das PFP auf ihm ausbildet. Dieses Arrangement verbessert die Ladungsträgermobilität entlang der Stapelrichtung. Die Kenntnis über die relative Ausrichtung zwischen PFP und Graphen sowie über die Facettierung der PFP Inseln ist von hoher Bedeutung, da die physikalischen Eigenschaften von diesen Parametern abhängen.

Bezüglich der Rolle organischer Heterostrukturen in der Entwicklung organischer elektronischer Bauteile ist ein tiefgehendes Verständnis der Anordnung der organischen Moleküle in den Gemischen erforderlich, um neue organische Bauteile zu konzipieren.

Acknowledgements

‘Let your dreams be bigger than your fears, your actions louder than your words, and your faith stronger than your feelings’ — unknown

It is hard to believe that almost four years have passed since I first arrived in Marburg to begin my graduate studies. The road to my PhD would have not been successful without the help and support of others.

First and foremost I would like to express my deepest gratitude to Prof. Dr. Kerstin Volz to give me the opportunity to belong to this great group, the STRL Group, and to give me all the support during the course of this thesis.

Second, I would like to express my sincere appreciation to my research advisor Katharina Gries for her guidance, infinite patience, time investment, commitment and understanding throughout the journey of this dissertation.

I would also like to thank Dr. habil. Wolfgang Stolz for his kindness and his interest in the progress of my work.

Furthermore, I want to express my gratitude to Prof. Dr. Sangam Chatterjee for his role as a second examiner, as well as, the rest of my dissertation committee, Prof. Dr. Kerstin Volz, Prof. Dr. Florian Gebhard and Assistant Prof. Dr. Ana M. Beltrán, for their availability and commitment to take part of it.

I am thankful to my office colleagues Katharina Gries and Andrea Ott for making the day-to-day of my PhD enjoyable. Furthermore, sincere thanks are given to my colleagues who have read some parts of the thesis and have given me very nice advices and suggestions to improve it: Katharina Gries, Andrea Ott and Jürgen Belz, I will keep this gesture in my heart. Moreover, my thanks go to all the other previous and current STRL and NAsP members that have not been mentioned so far for their friendly atmosphere and funny activities: Michael Hellwig, Isabelle Kimmel, Maximilian Widemann, Shamail Ahmed, Elke Vaupel, Marina Koch, Andreas Beyer, Kakhaber Jandieri, Han Han, Laura König, Lennart Duschek, Christian Fuchs, Rainer Straubinger, Thomas Ochs, Stefan Reinhard, Pirmin Kükelhan, Shalini Gupta, Saleh Firoozabadi, Dominic Duffy, Jan Oliver Oelerich, Celina Becker, Lukas Nattermann, Eduard Sterzer, Oliver Maßmeyer, Thilo Hepp, Uwe Fickenscher, David P. Krug, Peter Ludewig, Antje Ruiz Perez, Christoph Möller, Johannes Zimmet, Ulrike Häuplik, Andreas Oppermann, Tatjana Wegele, Katharina Werner and Nikolai Knaub.

In addition, I would like to thank Prof. Dr. Gregor Witte and Dr. Tobias Breuer for providing all the samples investigated during the experimental stage of this dissertation, doing some measurements and the fruitful discussions concerning our cooperation. Furthermore, I want to express my gratitude to the rest of all collaboration partners.

I am also thankful to the German Science Foundation (DFG) in the framework of the SFB 1083 for the financial support.

Since research can (sometimes) become frustrating and exasperating, people that have reminded me that life goes on outside the laboratory are also taken into account, hence I am grateful for the Marburger‘s friendship of Bea, Pablo, Dani, Alberto, Alejandro, Carla and Carolina.

I would also like to mention my old TEM group in Cadiz, the old TEP-120 group, where I started my career in this field. In particular, I am thankful to Prof. Dr. Rafael García, Prof. Dr. Francisco Miguel Morales and Dr. José Manuel Mánuel for introducing me in the TEM and semiconductor world and for their continuing support.

Special thanks go to Anita for becoming as a ‘shoulder’ for me and giving me all her friendship and unconditional support by enlightening conversations, turning into an essential pillar in these almost four years.

Much gratitude also goes to my ex-colleagues of my BSc in Chemistry (Ángela, Nina, Sole, Fátima, Eu, Luisa, Jose and Mercedes) to preserve our friendship and to all those who helped me in my different professional experiences (CENTA, Microal, SISE, CLC and SNC-Lavalin). I still keep a good relationship with some of my ex-coworkers.

Also, I wish to take this opportunity to extend my sincere thanks to all of my teachers from kindergarten to graduate school, ‘Colegio Nuestra Señora del Carmen’ and ‘Instituto de Educación Secundaria La Palma’, both from La Palma del Condado. They have instilled me the values of effort and spirit of sacrifice and the passion for the science’s world.

I am also greatly thankful to my lifelong friends in La Palma del Condado ,'Peña Tanoye', for their companionship, continuous support and encouraging words even thousands of miles away. They have made the effort to be with me every time that I have visited Spain. Special appreciations go to Manué to make time for me.

I also express my gratitude to some other friends in Sanlúcar La Mayor and in some other places who have supported me. In particular, I would like to give my appreciation to my in-laws, Antonio, Pepi and Isabel, for never-fading and their love, support and encouragement.

My sincere gratitude goes to my partner, Antonio, for waiting me these years and giving me an unwavering love and support. I can never thank him enough for his unconditional support and sacrifice.

Finally, my thanks go to my relatives (uncles and cousins) and my special gratitude goes to my family, my parents and my brother, without their love and support this thesis would have not been possible. I thank my parents for teaching me good values such as effort, humility, patience, appreciation, courage, kindness and loyalty, without their advices and effort to guide me I would not be the person that I am today. I also want to thank my brother Manolo to be my great mentor and my other self. I am greatly thankful to his unconditional and endless love and support every day. I cannot imagine being the person I am today without such a great brother through the years.

This thesis is also dedicated to people who loved me but they have already passed away, especially mi grandmother Rocío. I think they would be proud of me.

'Gracias mamá, gracias papá, porque esta tesis es también fruto de vuestro trabajo, esfuerzo y sacrificio durante todos estos años de formación. Sin vuestra constancia y apoyo no habría podido lograr este objetivo ni sería la persona que soy hoy en día. Gracias por todo, gracias a todos'.

1.Introduction

‘Many small people, in small places, doing small things can change the world’

— Eduardo Galeano

1.1. Synopsis

The field of organic semiconductors (OSCs) has experienced a fast growth in the last years, covering a broad range from nanoelectronic devices to macroelectronic systems. OSCs attract a lot of attention due to their properties of flexibility, low cost, lightweight and ease of fabrication [1–5], which differ from those of conventional inorganic crystalline semiconductors. Technological and scientific advances have been made in this field leading to practical applications such as organic light-emitting diodes (OLEDs) [6,7], organic field-effect transistors (OFETs) [8,9] and organic photovoltaic cells (OPVs) [10,11]. A deeper knowledge of OSC physics is imperative to advance further with the associated applications.

Organic films can be characterized by X-ray techniques, spectroscopic and electron microscopic methods. Although X-ray and optical spectroscopic analyses are considered as good and suitable tools to study OSC materials, they are commonly used to examine rather large areas of typically several hundred microns squared. In contrast, (scanning) transmission electron microscopy ((S)TEM) possesses the advantage to carry out chemical and microstructure inspections of films with high lateral resolution at small length scales. Thus, in the present thesis imaging, diffraction and compositional analyses are conducted in (S)TEM, and they are combined in order to give detailed insights into the properties and behavior of crystalline materials at nanoscale dimension.

Efficient charge transport in OSCs is the key for their application in organic electronics [12,13]. Poor charge mobility and thus poor device performance can occur if the organic molecules of crystalline structures are not properly oriented with respect to each other. In small molecules of OSCs, charge is transported preferentially along the direction of intermolecular π-stacking of the aromatic rings [13,14]. Hence, arrangements that favor this transport are highly desirable [15–21]. In this regard, perfluoropentacene (PFP) deposited on graphene substrate is an interesting model system, in which PFP exhibits the so called π-stacked polymorph (*PS-polymorph*) [22].

The growth of PFP films on graphene substrate occurs in island shapes. The PFP molecules are epitaxially aligned with the substrate due to the good match between the phenyl units of PFP and the graphene lattice [22,23]. Graphene presents two high-symmetry directions, i.e. the zig-zag and armchair directions, which are crystallographically and energetically different. Previous works reported that the long molecular axis of PFP might align either along these two directions of graphene, or solely along one of both [22]. Given the interest in the model system PFP/graphene and its important implications in charge transport, the determination of the lateral alignment between PFP and graphene is an information rather relevant, and therefore, it is one of the aims of this dissertation.

The current work deals with the revelation of the lateral positioning of the organic PFP molecules on the graphene substrate together with the detailed analysis of the facets of the PFP islands. Since potential electronic coupling mechanisms are also expected to depend on the relative alignments and shapes of organic films [12,24], these results can serve as a starting point for the improvement of the physical properties of the PFP/graphene system and they might have an impact on future electronic and optoelectronic devices.

In addition, the use of heterostructures combining different OSCs is interesting for novel materials with new electronic functionalities [25]. In order to push the development and the success of OSCs forward, it is essential to understand the arrangement and distribution of different compounds which form the organic heterostructures. The efficiency of such devices depends on the intermixture, ordering and the relative conformation of the components [25,26].

Among others, organic heterostructures formed by the p-type OSC pentacene (PEN) and its perfluorinated version PFP (n-type) are of particular interest in the field of OSCs for applications where p-n junctions are required. For this reason, the analysis of such blends is a main target of the present thesis. Since the supporting substrate can decisively influence on the molecular arrangement and orientation of the deposited organic layers, two different substrates are chosen for the investigation: SiO_2 and KCl.

SiO_2 is an amorphous substrate which minimizes the substrate-film interactions, leading to polycrystalline phases [27]. In contrast, KCl has been found to lead to an epitaxial growth and crystalline films on both compounds PEN and PFP [28–31].

Looking at technological importance of organic heterostructures, the findings of this thesis help to resolve the impact of molecular arrangement and composition of organic heterostructures. This knowledge becomes particularly important for the creation of efficient organic donor-acceptor interfaces used in organic photovoltaic devices and may serve as an important landmark for the development of novel organic material systems, where molecular p-n junctions are involved.

1.2. Objective of the work and organization of the thesis

The goals of the current thesis are based on the characterization of the morphology, orientation, arrangement and crystalline properties of the following systems:

- The OSC PFP grown on graphene substrate.
- The organic heterostructures formed by PEN and PFP deposited with different mixing ratios on an amorphous substrate as SiO_2 and the crystalline substrate KCl.

The first study presented in this dissertation deals with the determination of the lateral alignment of the PFP molecules with respect to the graphene substrate. (S)TEM techniques together with some other analyses, performed by other research groups, are utilized to investigate the materials.

Furthermore, PFP on graphene exhibits a characteristic growth in islands shapes. The morphology of the PFP structures is also investigated to obtain information on the facets that form the PFP islands. Electron tomography (ET) measurements are additionally applied to achieve a three-dimensional (3D) reconstruction of the PFP islands.

The second part of the thesis focuses on the investigation of PEN:PFP mixtures via (S)TEM techniques. It is known that the molecular orientation and ordering of OSCs depend on substrate interactions. In this way, this chapter delves into the analysis of the different arrangements formed by the PEN:PFP mixtures depending on: (i) the substrate utilized for the growth, SiO_2 or KCl; and (ii) the mixing ratio used during the codeposition of the PEN:PFP blends.

The thesis is organized as follows:

In this first chapter, a brief introduction about the background of the research, importance and history of OSCs as well as the aims of the work are shown.

The second chapter presents the fundamental and basic properties of OSCs. The most common arrangements adopted by OSCs together with the materials used for the investigations are also introduced.

In chapter number 3, the physical background together with the different (S)TEM techniques utilized are explained in detail. Additionally, the method to fabricate the organic thin films is described briefly.

Chapter 4, 'Microstructural characterization of PFP grown on graphene', presents the first part of results. In this chapter, a thorough investigation of the morphology and orientation of the OSC PFP deposited on graphene substrate is addressed. TEM techniques, in particular electron diffraction experiments, together with ET analyses help to resolve the main issues of the work. Additionally, scanning electron microscopy (SEM) and STEM provide overviews of the sample, and some other techniques, i.e. X-ray diffraction (XRD), scanning tunneling microscopy (STM) and molecular mechanics (MM) calculations, are applied to obtain complementary information.

Chapter 5 deals with the second part of the results and includes the study of the heterostructures formed by PEN and PFP grown on different substrates. This chapter is in turn divided in two subchapters:

- *PEN:PFP blends grown on SiO_2* (subchapter 5.3)
- *PEN:PFP blends grown on KCl* (subchapter 5.4)

In this chapter, SAED patterns combined with dark field-TEM (DF-TEM) and bright field-TEM (BF-TEM) methods are mainly used to analyze the morphology, and resolve the distribution and orientations of the phases found in the PEN:PFP mixtures.

The thesis is summarized in *chapter 6*. Although the present work addresses the questions concerning the orientation, arrangements and distribution of organic molecules in the organic films, there are still open questions that will be the aim of further work.

Finally, most of the research presented in this dissertation has resulted in publications in both the journal *Crystal Growth and Design* (x1) and the *Journal of Crystal Growth* (x2). The publications are as follows:

1) R. Félix, T. Breuer, P. Rotter, F. Widdascheck, B. Eckhardt, G. Witte, K. Volz, K. I. Gries, *microstructural analysis of perfluoropentacene films on graphene and graphite: interface-mediated alignment and island formation*, Cryst. Growth Des. 16 (2016) 6941–6950, doi:10.1021/acs.cgd.6b01117 [32].

2) R. Félix, K. Volz, K. I. Gries, *codeposited pentacene:perfluoropentacene grown on SiO_2: a microstructural study by transmission electron microscopy*, J. Cryst. Growth 458 (2017) 87–95, doi: http://dx.doi.org/10.1016 j.jcrysgro.2016.09.77 [33].

3) R. Félix, T. Breuer, G. Witte, K. Volz, K. I. Gries, *microstructural study of codeposited pentacene:perfluoropentacene grown on KCl by TEM techniques*, J. Cryst. Growth 471 (2017) 29–36, doi: http://dx.doi.org/10.1016/j.jcrysgro.2017.05.009 [34].

1.3. Importance of semiconductor materials for the 21st Century

The 21st Century is already been considered as the ‘Information Age’ thanks to the development of revolutionary new products for communication, information storage and computing. This revolution goes hand in hand with the development of semiconductors, which are considered as the ‘philosopher's stone’ of this new time frame. Semiconductor materials are present in every sphere of human activity, i.e. communication, banking, trading, learning and teaching, entertainment, socializing, government or management, being an essential part in most of the modern electronic devices that are currently used. The main driving force behind this growth has been the unprecedented progress in digital integrated circuits technology as described by Moore’s law in 1965 [35] which states that device complexity doubles about every year. A rate that he later revised to every two years [36] and others have set at 18 months [37].

Nowadays, life cannot be imaged without internet, advanced smartphones and powerful laptops. The invention and progress of the laser have been of key importance for the development of fiber-optic communication devices. Transistors and many other electronic devices, which are components of bars code, computers, microprocessors, displays, etc. are made of semiconductors.

Thus, semiconductor materials and the electrical engineering theories associated to them have allowed this era of information revolution and the enhancement of our current modern life.

1.4. History of organic semiconductors

OSCs are a kind of materials that combine the electronic advantages of semiconducting materials with the chemical and mechanical benefits of organic compounds.

The first electronic revolution began in 1947 with the invention of the first transistor made of germanium by Bardeen, Brattain and Shockley [38]. Later, silicon would be the most widely used material in the production of transistors. However, nowadays, in the midst of the 21st Century, a new electronic revolution has become possible due to the development and understanding of OSCs [39]. They are an interesting alternative to silicon-based materials since their properties can be tuned to make processed them easily, allowing them to coat a variety of surfaces, including soft substrates at relatively low temperatures [40–43].

The earliest known organic conductive material was discovered by Henry Letheby in 1862. Using anodic oxidation of aniline in sulfuric acid, he produced a partly conductive material that was later identified as polyaniline [44]. Furthermore, anthracene was the first organic compound in which photoconductivity was observed by Pochettino in 1906 [45] and Volmer in 1913 [46]. In the 1950s, it was discovered that polycyclic aromatic compounds form semiconducting charge transfer complex salts with halogens. This fact showed that some organic compounds could be conductive as well [47]. Further works expanded the range of known organic conductive materials. A high conductivity of 1 S/cm was reported in 1963 for a derivative of tetraiodopyrrole [48–50]. In 1972, researchers found metallic conductivity (conductivity comparable to a metal) in the charge transfer complex tetrathiafulvene-tetracyanoquinodimethane (TTF-TCNQ). In 1977, Shirakawa and co-workers reported high conductivity in oxidized and iodine-doped polyacetylene [51]. Related to this finding, MacDiarmid, Heeger, and Shirakawa were awarded the Nobel Prize in Chemistry in 2000 for ‘the discovery and development of conductive polymers’ [52]. Similarly, highly-conductive polypyrrole was rediscovered in 1979 [53–55], and superconductivity in charge transfer complexes was first reported in the Bechgaard salt, $(TMTSF)_2PF_6$ in 1980 [56].

In the 80's and 90's, several studies were devoted to realize successful demonstrations in the field of organic electronics [57–66]. In this sense, Ching W. Tang is considered as the father of organic electronics for his works in this field [57,58,67].

Currently, the main areas of application of organic electronics are: OLEDs, OPVs, and OFETs.

OLED technology can be found in display and lighting applications, or photocopying machines. This technology generates light within the device itself, in contrast to the liquid crystal display (LCD) technology where a backlight source is required. This leads to better color reproduction, high contrast and faster refresh rate compared to LCD or Plasma displays. Moreover, their flexibility and softness enable the development of thin and lightweight large area displays which can be even curved and transparent. Figure 1.4-1(a) is an example of an OLED TV with a thickness of 2.57 mm shown by LG in the 2017 annual Consumer Electronics Show (CES).

OPVs are considered as a competitive alternative to the standard silicon cells in photovoltaics, although their conversion efficiencies still need to be improved (near 11 % for OPVs vs (20–25) % for silicon cells [68]). Currently, there are some companies working in the development of this technology. For example, the Belectric OPV Company showed solar tree-OPV polymers at the German pavilion in the Milan EXPO 2015 [69] (cf. Figure 1.4-1(b)).

Field-effect transistors are considered as the most essential component in modern electronic circuitry. The improvements in materials performance have facilitated the inclusion of organic materials in this technology. OFET technology can be applied in e-paper displays [70], simple circuits [71] and chemical and biological sensors [72]. Companies such as Plastic Logic (cf. Figure 1.4-1(c)) have fully industrialized OFET technology and have demonstrated that their manufacturing yields and reliability can be as high as in conventional silicon-based manufacturing.

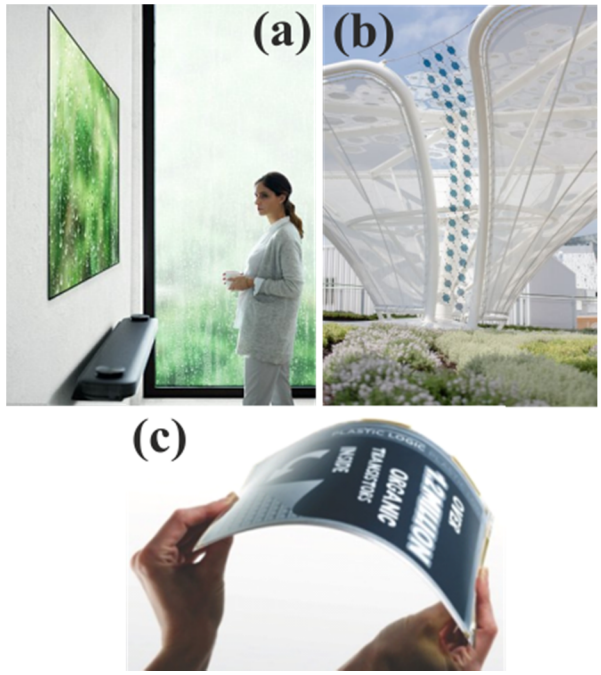

Figure 1.4-1. (a) LG Signature OLED W7 exhibited in the CES 2017. (b) Energy-generating solar trees at the German pavilion at world expo in Milan 2015. (c) Flexible electrophoretic ink display driven by an active-matrix of 1.2 million OFETs (source: Plastic Logic).

2.Basic principles

‘Success is doing ordinary things extraordinarily well’

— Jim Rohn

2.1. Fundamental of organic semiconductors

OSCs consist of organic materials, which are mostly made out of carbon. They can be broadly classified into two groups according to their molecular weight: small-molecules (given by the repetition of few monomer units with lengths of few nanometers) and polymers (given by the repetition of many monomer units with lengths of hundred nanometers) [73]. Both are based on the sp^2 hybridization of carbon atom: the three atomic orbitals of carbon 2s, $2p_x$ and $2p_y$ undergo hybridization and transform into three equivalent sp^2 orbitals in a trigonal planar conjugated system. In such sp^2 hybridization, the remaining p_z orbital exists normal to the plane of these hybridized sp^2 orbitals. A carbon sp^2 orbital can overlap with the sp^2 orbital of another carbon atom in a very strong σ-bond [74], while the non-hybrid orbital $2p_z$ overlaps laterally with the $2p_z$ orbital of adjacent carbon atom to form a π-bond as shown in Figure 2.1-1.

The larger overlap of σ-bonds makes them strong bonds as compared to less overlapping π-bonds. The overlapping of p_z orbitals results in two orbitals with different energy levels, a bonding (π) orbital at low energy level and an antibonding (π*) orbital at high energy level. Similarly, the overlap of sp^2 orbitals results in two orbitals, a bonding (σ) orbital at low energy level and an antibonding (σ*) orbital at high energy level [74–76]. From the macroscopic point of view, the orbital structure of OSCs can be treated similarly as inorganic semiconductors. In this way, highest occupied molecular orbital (HOMO) and the lowest unoccupied molecular orbital (LUMO) of OSCs are analogous to the valence band (normally filled with electrons) and the conduction band (normally free of electrons) of inorganic semiconductors, respectively. Since π-bonds are weaker than σ-bonds, the HOMO and LUMO represent the energy difference between bonding and antibonding molecular π-orbitals (cf. Figure 2.1-1). The smaller energetic difference between the HOMO and LUMO (typically between 1 eV and 4 eV [74,75,77]), leads to strong absorption or emission in or near the visible spectral range, and gives the semiconducting properties.

Carbon atoms can form larger molecules, commonly with benzene rings as the basic unit, in which single and double covalent bonds are alternated between the carbon atoms. In these larger molecules, the electrons of the π-bonds are delocalized via conjugation with their neighboring π-bonds, thus giving a π-system over the domain of the whole structure (delocalization). The gap between occupied and empty states in these π-systems (π-π* transitions) becomes smaller when the delocalization - and therefore the size of the π-system - increases [39,74,75,77] (cf. Figure 2.1-2).

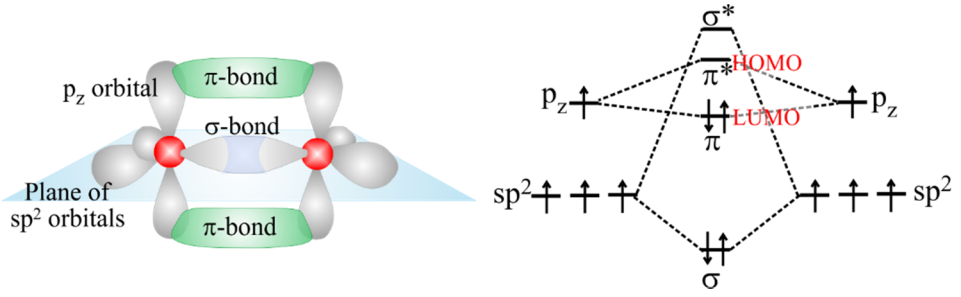

Figure 2.1-1. Orbital scheme (left) and molecular orbital diagram (right) of two sp^2 hybridized carbon atoms. Figure adapted from [78].

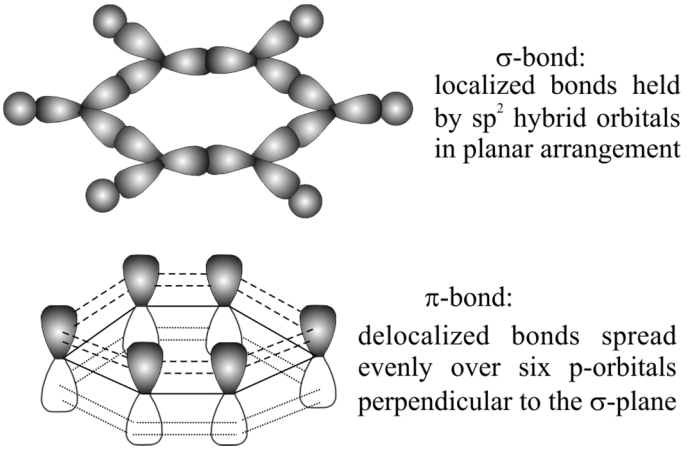

Figure 2.1-2. Localized σ-bond (top) and delocalized π-bond (bottom) of a benzene ring. Figure adapted from [78].

2.2. Basic properties of organic semiconductors

The basic properties of OSC molecular solids are determined by the nature of bonding, which is very different from conventional inorganic semiconductors. OSC crystals, like any other crystal, are characterized by a perfectly ordered point lattice and a basis. In inorganic crystals, such as germanium or silicon, this basis consists of individual atoms strongly tied by covalent bonds; whereas in OSC molecular solids, this basis is formed by molecules bonded by weak Van der Waals forces. This fact has consequences on mechanical and thermodynamic properties as well as on optical properties and charge carrier transport mechanisms. A comparison of Van der Waals bonded molecular crystals in OSCs and covalent atomic crystals in inorganic materials is shown in Table 2.2-1 [79].

	Inorganic semiconductor solid	**Organic semiconductor solid**
Bonding	covalent	Van der Waals
Charge carrier	Electron, holes, ions	Polarons, exciton (though neutral)
Effective mass	m_e or less	$(10^2\text{-}10^3)\ m_e$
Transport	Band	Hopping
Mobility	$10^2\text{-}10^4\ cm^2 \cdot V^{-1} \cdot s^{-1}$	$10^{-6}\text{-}10^0\ cm^2 \cdot V^{-1} \cdot s^{-1}$
Exciton	Wannier-Mott	Frenkel, charge transfer
Luminescence	Band to band recombination	Exciton recombination

Table 2.2-1. Comparison of properties of inorganic semiconductor solids vs organic semiconductor solids. Table adapted from [79].

In inorganic semiconductor crystals, the strong coupling between the constituting atoms and the long-range order leads to the delocalization of the electronic states and the formation of allowed valence and conduction bands separated by a forbidden gap. By thermal activation or photo-excitation, free carriers are generated in the conduction band, leaving behind positively charged holes in the valence band. This transport

mechanism is known as ‘band transport’. The strong overlap of the respective atomic orbitals usually leads to broad bands, where the movement of charge carriers within these bands can be described by Bloch wave. In contrast, the molecular orbitals overlap only weakly in OSCs due to the sufficiently large separations between molecules in these crystals. In consequence, charge carriers are more localized and interact strongly only with the present electronic and nuclear subsystems. The motion of carriers takes place in the form of ‘hopping transport’. In this case, a charge carrier, i.e. hole or electron can reside in the HOMO or LUMO (respectively) of an OSC. Strong electron-phonon coupling in OSCs leads to the formation of polarons which become localized on individual molecules or chain segments. Charge transport within this energetic landscape proceeds via consecutive hopping from one localized state to the next one. Excitons in OSCs are mostly Frenkel type (large binding energies) while those in inorganic semiconductors are typically Wannier-Mott type (small binding energies). In inorganic semiconductors carrier mobilities are higher than OSCs (10^{2}-10^{4} $cm^{2}\cdot V^{-1}\cdot s^{-1}$ vs 10^{-6}-10^{0} $cm^{2}\cdot V^{-1}\cdot s^{-1}$, respectively). Therefore in inorganic semiconductors, increasing temperature reduces the carrier mobilities as a result of carrier scattering. Moreover, OSCs usually have larger band gap and smaller band widths [80,81].

2.3. Classification of organic semiconductors

OSCs can be broadly divided into two groups according to their molecular weight: conjugated polycyclic compounds if their molecular weight is less than 1000 $g\cdot mol^{-1}$, and heterocyclic polymers if their molecular weight is greater than 1000 $g\cdot mol^{-1}$ [82]. OSCs with low molecular weight can be thermally evaporated and have better crystallinity than polymers. This fact together with polymers present low solubility in organic solvents and loss of mobility upon functionalization, lead to consider the use of small molecules better than polymers as semiconductors [83–88]. Small molecules can also be subclassified in polycyclic aromatic hydrocarbons, (PAHs) which consist of laterally fused benzene rings, and heterocyclic oligomers. **This thesis** only **focuses** on **PAHs**, hence within this work the term OSC is used to **refer to acene molecules** exclusively.

2.4. Common acene packing motifs

The intermolecular order adopted by the individual molecules in the solid state plays a decisive role in the electronic performance of organic devices. Both exciton migration and carrier mobility (electronic transport) are strongly modulated by the solid state packing of the conjugated chains. In general, good electronic performances require strong electronic coupling between adjacent molecules. For most conjugated aromatic molecules, this strong overlap is achieved via two common crystal packing structures: *herringbone* (HB) and *π-stacked* arrangement. These structures result as a competition between the intermolecular interactions and molecule-substrate interactions. In case of HB motif, the intermolecular interactions dominate tending to form standing-up orientations with respect to the substrate surface (cf. example in Figure 2.4-1(a)). When the molecule-substrate interactions impose, the π-stacked arrangement occurs. This yields a lying-down geometry of the molecules, in which, the organic molecules are parallel to the substrate surface (cf. example in Figure 2.4-1(b)). These two solid state packing motifs are also known as edge-to-face and face-to-face for the HB and π-stacked arrangements, respectively [12,89–91].

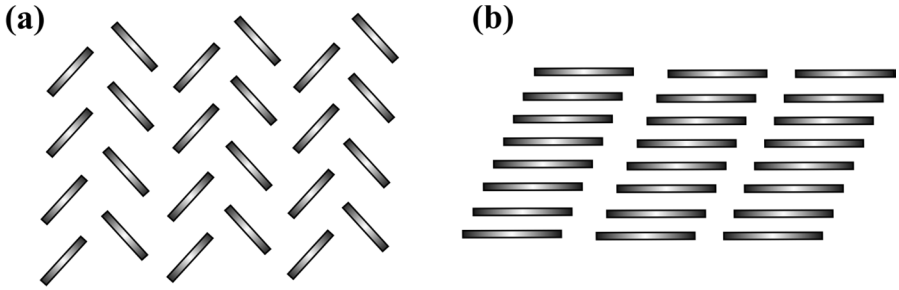

Figure 2.4-1. Molecular packing motifs in acene crystals. Examples of (a) herringbone and (b) π-stacked arrangements.

The majority of the conjugated aromatic molecules adopt the HB structure, whereas the ones with π-stacked structure are scant. However, π-stacked is considered to be the superior motif because it has a significant physical overlap of the π-orbitals between the faces of adjacent molecules, leading smaller intermolecular distances. This causes the enhancement of electronic charge carrier mobility as compared to the edge-to-face structure.

For this reason, considerable research efforts have been concentrated on modifying the molecular packing of OSCs from HB to π-stacked in order to improve the mobility and stability of conjugated OSCs [16,92–97].

2.5. Materials

There are two different materials which are of particular importance in this dissertation: PEN and its perfluorinated version, PFP. This work pays all the attention to these compounds in their pure forms, as well as, their mixtures, i.e. PEN and PFP heterostructures.

2.5.1. Pentacene: PEN, $C_{22}H_{14}$

Pentacene is one of the most widely studied OSCs [98] and consists of five linearly fused benzene rings, as shown in Figure 2.5-2(a), top panel. This material has a chemical formula of $C_{22}H_{14}$ with a molecular weight of 278 $g \cdot mol^{-1}$ and a density of 1.33 $g \cdot cm^{-3}$. Pentacene is a benchmark OSC in thin film organic electronic devices because of its π-conjugated electronic structure, its relatively low HOMO-LUMO gap and the relatively high charge carrier mobility of its solid state films. In particular, the interest in PEN as an OSC is mainly due to two reasons: its crystal order and its high hole mobility leading to a p-type organic semiconduction. Mobilities up to 2.2 $cm^2 \cdot V^{-1} \cdot s^{-1}$ for purified pentacene [99] and even to 40 $cm^2 \cdot V^{-1} \cdot s^{-1}$ have been found when pentacene is peroxidized forming pentacene-quinone [100]. These mobility values are among the highest for OSCs reported up to date [101].

So far PEN is known to crystalize at least in six different crystallographic morphologies (polymorphs) that are sensitive to substrate temperature and nature, film thickness, surface energy, and some other parameters [102–106]. Three bulk forms of crystalline pentacene have been experimentally identified: the high temperature (HT) structure [105], the Campbell phase [102] and the low temperature (LT) structure [103]. Furthermore, a thin film (TF) polymorph [107] has also been identified. The other two polymorphs are detected only for a few layer films and are strongly affected by the surface and preparation method [107–109], hence not many authors consider them.

The HT, Campbell, LT and TF polymorphs belong to the triclinic space group P $\bar{1}$ and present the HB arrangement, in which there are two inequivalent molecules per unit cell (Z = 2), twisted with respect to each other and sitting on layers parallel to the (0 0 1) plane. An example using the PEN TF polymorph is illustrated in Figure 2.5-2(a), lower panel. The lattice parameters of these four polymorphs are provided in Table 2.5-1.

PEN polymorph	a (Å)	b (Å)	c (Å)	α (°)	β (°)	γ (°)	Space group
HT [105]	6.140	7.930	14.90	96.80	100.5	94.10	P $\bar{1}$
Campbell [102]	7.900	6.060	16.01	101.9	112.6	85.80	P $\bar{1}$
LT [103]	6.265	7.777	14.53	76.48	87.67	84.71	P $\bar{1}$
Thin film [107]	5.958	7.596	15.61	81.25	86.56	89.80	P $\bar{1}$

Table 2.5-1. Unit cell parameters of different PEN polymorphs.

The thin film phase has been reported to grow up to film thickness of 50 nm at substrate temperatures close to room temperature [30,108] onto weakly interacting substrates, like: SiO_2 [110], glass [111] or alkali halides [30]. Further film thickness (>50 nm) might crystalize in the PEN Campbell structure (bulk polymorph).

The PEN structure detected in the results part of this thesis is compared to the PEN TF and Campbell phases. Their SAED patterns in the [0 0 1] orientation normal to the substrate surface are illustrated in Figure 2.5-1.

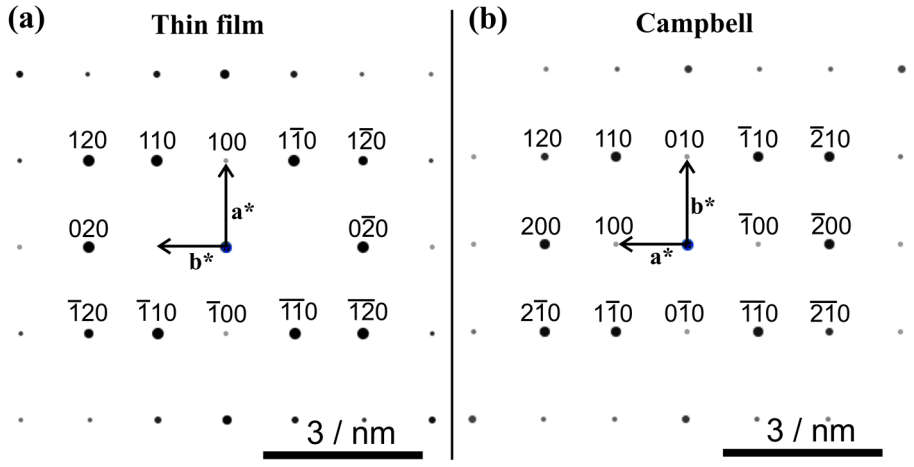

Figure 2.5-1. SAED patterns of the (a) PEN TF [107] and (b) Campbell [102] polymorphs in [0 0 1] orientation simulated by the JEMS software [112].

2.5.2. Perfluoropentacene: PFP, $C_{22}F_{14}$

Perfluoropentacene is the perfluorinated version of pentacene in which all the hydrogen atoms have been replaced by fluorine atoms (cf. Figure 2.5-2(b), top panel). It was successfully synthesized for the first time in 2004 by Youichi Sakamoto et al. [113] and has a chemical formula of $C_{22}F_{14}$ with a molecular weight of 530 $g \cdot mol^{-1}$ and a density of 2.21 $g \cdot cm^{-3}$. The introduction of fluorine, the highest electronegative of all the elements, favors the attraction of negative charge density, which is accumulated in the outermost molecular structure. This leads to a reduction of electron density onto the conjugated carbon skeleton and therefore, a reversal of the intramolecular dipoles. This effect enables that the conjugated π-system is not only on the carbon backbone but also is extended to the fluorine atoms because they also participate with their p-orbitals. Furthermore, this inversion of the electron distribution yields a change in the type of charge carrier in this compound compared to the non-perfluorinated counterpart PEN. PFP is therefore an n-type OSC with an electron mobility reported to date up to 0.220 $cm^2 \cdot V^{-1} \cdot s^{-1}$ [114].

Similar to PEN, PFP also exhibits several polymorphs: the thin film (TF) structure, the bulk phase and the PS-polymorph. Their lattice constants and angles are provided in Table 2.5-2. The TF and bulk structures have been found on oxidized silicon [113,115] and alkali halides [31] substrates, and adopt the HB motif with the P $2_1/c$ triclinic space group (cf. the PFP TF polymorph in Figure 2.5-2(b), lower panel). In addition, a PFP polymorph with a parallel π-stacked geometry has been observed on metals [116] and graphene/graphite [22] substrates. This structure has been denoted as PS-polymorph and is the particular interest because this geometry enhances the overlap of the π-orbitals, enabling a more efficient charge transport for such configurations [117].

Since, the PFP TF and bulk structures differ only slightly in unit cell dimensions and angles, the PFP material deposited on SiO_2 and KCl substrates in the results part of this dissertation is only compared to the PFP TF phase for reasons of simplicity. Additionally, the PS-polymorph is addressed in this dissertation when graphene substrate is used.

PFP polymorph	a (Å)	b (Å)	c (Å)	α (°)	β (°)	γ (°)	Space group
Bulk [113]	15.51	4.49	11.45	90.00	91.57	90.00	P 2_1/c
Thin film [115]	15.76	4.51	11.48	90.00	90.40	90.00	P 2_1/c
PS-polymorph [22]	15.13	8.94	6.51	78.56	108.14	92.44	P $\bar{1}$

Table 2.5-2. Unit cell parameters of different PFP polymorphs.

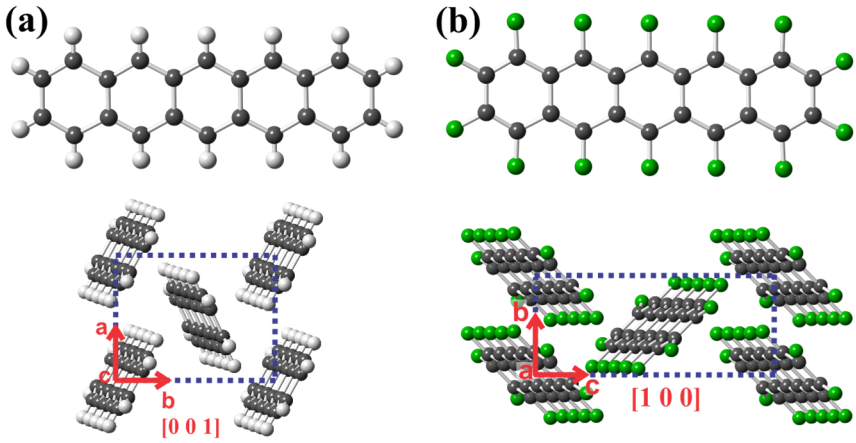

Figure 2.5-2. Top panel: (a) PEN and (b) PFP molecule. Lower panel: Crystal structure of (a) PEN and (b) PFP with axes denotation, both in their thin film phase. These arrangements show the HB ordering.

2.5.3. Heterostructures of organic semiconductors

2.5.3.1. Current interest in heterostructures of organic semiconductors

OSCs are relevant for several electronic and optoelectronic applications such as: OFET [118–120], OLED [121,122] and OPVs [123–125]. In such compounds, the fundamental understanding of the structures is rather difficult because of the weak Van der Waals binding forces and the major conformational and orientational degrees of freedom. Since the mixing behavior has influence on the electronical and optical properties, its knowledge is very important. This section is adapted from [25].

A typical architecture of these binary systems formed by simultaneous deposition of the two compounds are those composed by a donor compound (electron conduction) and an acceptor compound (hole conduction) giving an heterojunction.

The degree of intermixing between both (phase separation or good intermixing) on the molecular level depends strongly on the structural compatibility of both molecules and thermodynamic properties, and is prime of interest. An organic blend without steric compatibility between the two compounds (dissimilar molecular shape and size) often exhibits phase separation. The thermodynamic properties of these organic blends can be described using the mean-field approach given by the 'regular solution model' [126]. The free energy of mixing of two different compounds A and B can be described as follows:

$$\Delta F_{mix} = k_B T[(x_A\, ln x_A + \, x_B\, ln x_B) + \chi x_A x_B)] \tag{2.5-1}$$

where x_A and x_B are the respective relative concentrations. As can be seen, there are two driving forces for mixing or phase separation. First, there is an entropy term (ln terms), which always favors mixing. The second term is due to the different interaction energies between the molecules of species A and B (inter-particle interaction), which can either favor or disfavor mixing. The χ is the dimensionless interaction parameter, which is determined using equation (2.5-2):

$$\chi = \frac{Z}{k_B T}\,(W_{AA} + \, W_{BB} - 2W_{AB}) \tag{2.5-2}$$

where Z is the coordination number and W_{AA}, W_{BB} and W_{AB} are the different interaction energies. Depending on the entropy contribution and the inter-particle interaction (which in turn depends on the interaction parameter χ) terms of equation (2.5-1), different mixing scenarios can take place [25,127]:

I) Entropy dominated, high temperatures

At high temperatures, the entropy term will dominate the system ΔF_{mix}, giving a continuously mixed crystal, that is, molecules of B are randomly replaced by molecules of A in a B crystal (Figure 2.5-3(a)). This system is also known as 'solid solution' or 'mixing by substitution'. The lattice parameters of this mixture change continuously depending on the mixing ratio. A requirement for the formation of a solid solution is the sterical compatibility.

II) Inter-particle dominated, low temperatures

At low temperatures, the inter-particle interaction term becomes noticeable, and the ΔF_{mix} will depend on the balance of the interaction parameter value χ, leading the following mixing scenarios:

(a) $\chi > 2$ Phase separation: the interaction between the two species (W_{AB}) is unfavorable or there is no sterical compatibility between both (Figure 2.5-3(b)).

(b) $\chi \approx 0$ Random mixing: at low temperatures a 'solid solution' determined by entropy can also be formed if the interaction energy between the two species ($2W_{AB}$) is similar to those in pure states ($W_{AA} + W_{BB}$). The two organic species should present sterical compatibility to reach this scenario (Figure 2.5-3(c)).

(c) $\chi < 0$ Intermixing: the interaction energy between the species A and B (W_{AB}) is stronger than the attraction energy in their pure states ($W_{AA} + W_{BB}$), that is, the A-B pairing is more favorable and an ordered complex is formed. (Figure 2.5-3(d)). Blends of this kind are preferentially equimolecular ([1:1] ratio). If the mixing ratio is deviated from the equimolar [1:1] ratio, a phase separation (of the species in excess) from the equimolecular ordered crystal is expected (Figure 2.5-3(e)). This is because the incorporation of additional molecules will deform the complex leading to an increase of the lattice energy.

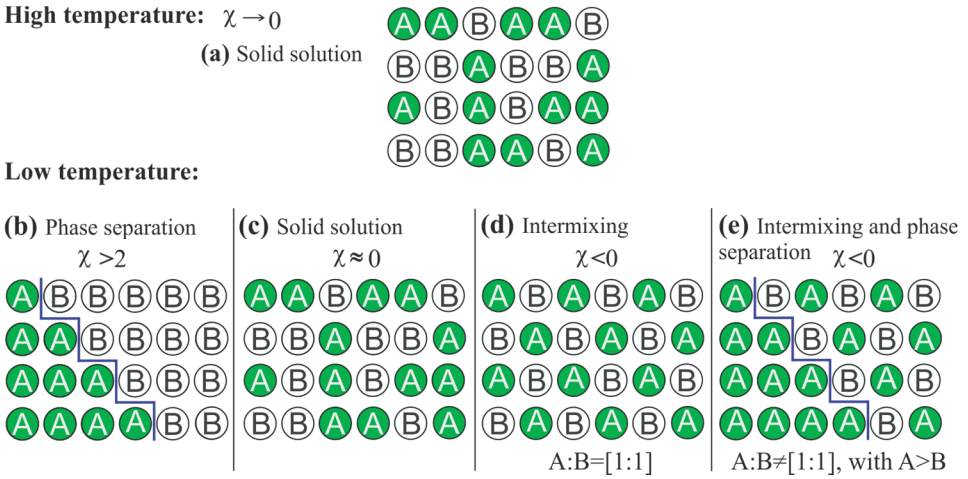

Figure 2.5-3. Mixing scenarios of molecular crystals depending on the entropy contribution and the inter-particle interaction: (a) and (c) Solid solution. (b) Phase separation. (d) Intermixing. (e) Intermixing and phase separation (specie A in excess). The illustration is adapted from [25].

2.5.3.2. PEN and PFP heterostructures

The interest in PEN and PFP heterostructures in the OSC field arises with the need for producing ambipolar transistors [128,129] and complementary circuits [130,131] that can transport both electron and holes in their channels (p-n junctions). PEN has shown high hole mobilities hence this material is a good candidate for that p-type semiconductor proposal. In turn, to address this request, the n-type organic semiconductor PFP has been suggested as a compatible compound with PEN mainly due to two reasons: the relative small size and the electronegativity of fluorine atoms. The small fluorine atoms do not introduce big changes into the molecular structure suggesting that continuous crystal growth at the PEN/PFP interface is possible [114], whereas the incorporation of the electronegative fluorine atoms to the carbon backbone changes the charge transport behavior, they lower the HOMO levels facilitating the electron injection [132]. Nevertheless, for good optical and structural properties of these junctions, a coupling between PEN and PFP at molecular levels is needed; for this reason, the mixing behavior of the PEN:PFP blends has been investigated in the experimental stage of this dissertation (cf. chapter 5).

2.5.3.3. **Literature review of PEN and PFP heterostructures**

Previous studies regarding the binary blends formed by PEN and PFP are briefly described in this part and in chronological order to give an overview of the current status of this mixture.

First preliminary studies of PEN and PFP mixtures date back to 2004, when Sakamoto et al. [113] synthetized PFP for the first time and demonstrated its structural similarities to PEN. They showed that the combination of PEN and PFP could be promising for ambipolar devices due to the similar shapes and sizes of both constituents PEN and PFP.

Later in 2008, codeposited PEN and PFP was structurally studied by Salzmann et al. using grazing incidence X-ray diffraction (GIXD) [115], atomic force microscopy (AFM), and Fourier-transform infrared (FTIR) spectroscopy. They revealed that PEN and PFP forms a '*new mixed-crystal structure*' with no detectable phase separation. Consequently, the mixing between PEN and PFP on molecular level was proved for the first time. In the same year, Salzmann et al. [133] also evidenced the presence of a differently oriented mixed film phase with a lattice spacing regardless of the mixing ratio by using specular XRD. This phase was attributed to the [1:1] phase of PEN and PFP. Moreover, FTIR tools proved the intercalation of PEN and PFP on the molecular scale.

In 2010, Kowarik et al. [134] also observed the formation of the new crystal between PEN and PFP by scanning transmission X-ray microscopy (STXM). They reported that for the coevaporated PEN:PFP a complete mixing of the two types of molecules without any phase separation of PEN and PFP domains is found. This reference again corroborated the mixing on the molecular scale, with one PFP and one PEN molecule per unit cell.

In 2011, Hinderhofer et al. studied the structure and morphology of coevaporated PEN:PFP blends with different mixing ratios grown on SiO_2 by X-ray reflectivity (XRR) and GIXD [135]. They found not only the development of a mixed structure between the PEN and PFP, but also that the crystal structure of this PEN:PFP blend did not change continuously depending on the mixing ratio. Hence, this mixed crystal

between PEN and PFP was formed with only [1:1] mixing ratio. For other mixing ratios, different that [1:1], a phase separation between the excess of molecules (PEN or PFP) and the mixed [1:1] structure was found. Besides, two different polymorphs for this [1:1] mixed crystal were detected: (i) [1:1] mixed λ-phase, and (ii) [1:1] mixed σ-phase. The λ-phase (molecular plane parallel to the substrate) was metastable and induced by low growth temperature. The σ-phase (molecular plane nearly perpendicular to the substrate) was thermally stable and nucleated predominantly at high growth temperatures.

Another reference about PEN and PFP blends was also published in 2011 by Broch et al. [136]. They found evidences for the intermolecular coupling in mixed films of PEN and PFP grown on SiO_2 with different mixing ratios by analyzing samples with variable angle spectroscopic ellipsometry (VASE), differential reflectance spectroscopy (DRS) and X-ray photoelectron spectroscopy (XPS). By comparison with the pure film spectra of PEN and PFP, a new transition arose at 1.6 eV (related to charge transfer) which was not found in the pure film spectra and which was assigned to the coupling of PFP and PEN. Furthermore, the effects of coupling were also visible through the appearance of new transitions in both components of the dielectric tensor and also small blueshifts of the whole spectra, which were interpreted as changes in the intermolecular polarizability.

Anger et al. (2012) [137] reported studies of photoluminescence (PL) spectra of PEN, PFP and codeposited PEN:PFP grown on SiO_2. They observed an optical transition at 1.4 eV in PL spectra of mixed PEN:PFP films, which was attributed to the coupling between the PEN and PFP. They discussed the possible charge transfer between the PEN and PFP and provided a possible scheme of the optical transitions in these binary systems.

Later, Breuer et al. [26] in 2013 studied the thermal stability of PEN and PFP blends by means of thermal desorption spectroscopy (TDS). They used different preparation methods and proved that the mixture of PEN and PFP yielded thermally stabilized heterostructures. This stabilization depended on the preparation method and did not only happen in codeposition of PEN and PFP but also in multi-stacks and subsequently PEN/PFP grown stacks (and not in the other way round, i.e. PFP/PEN

stacks). In addition, they played with different substrate temperatures, demonstrating that the intermixture was caused by a thermally activated diffusion during film growth and not due to post-deposition diffusion introduced by TDS analyses. Finally, optical absorption showed new absorption bands evidencing the mixing on a molecular level.

In 2013, there was also another paper covering this topic: Broch et al. [138] delved into PEN:PFP blends. They reported the relation between the optical properties and the average molecular tilt angle of these blends for different substrate temperatures by near-edge X-ray absorption fine-structure spectroscopy (NEXAFS) and VASE. They observed larger average tilt angles at 180 K than at higher substrate temperatures.

A new study on PEN:PFP [1:1] mixed films was carried out by Haas et al. [139] in 2014, the KCl substrate was utilized for the first time with these heterostructures. PEN:PFP blends were analyzed by TEM techniques. The sample presented a different growth morphology from that previously reported on SiO_2 substrates. They observed an underlying film with a 4-fold symmetry in contact with the substrate and some fibers on top of this oriented film. The authors pointed out that the underlying film was presumably formed by PEN excess, while the fibers seemed to be made of codeposited PEN:PFP.

All these studies above described form the framework in which the PEN:PFP mixtures grounded and they have served as a starting point for the experimental work.

3. Theoretical and experimental methods

‘Do not follow where the path may lead. Go, instead, where there is no path and leave a trail’ — Ralph Waldo Emerson

3.1. Basics of transmission electron microscopy

This section is devoted to the main methodology used throughout this thesis: (S)TEM. Fundamental parts and theoretical aspects, including the main interactions between the electron beam and the specimen, are described.

3.1.1. General aspects

Characterization techniques based on accelerated and transmitted electrons constitute a powerful set of tools to study a wide range of materials from the micron to the atomic level. The knowledge of the physics properties of electrons is prime of interest to success in the study of a specimen since results provided by microscopes can be understood in terms of electron-specimen interactions.

The development of electron microscopes was based on the theoretical work done by Louis de Broglie [140], who showed that every particle or matter propagates like a wave (wave-particle duality). The wavelength of a particle or a matter can be calculated as: $\lambda = h/p$, where h is Planck's constant and p is the particle momentum. Apart from the wavelength, the most relevant physical property of an electron in electron microscopy is its non-zero electric charge, since this fact allows modifying and focusing electron's trajectories by electric and magnetic fields. Due to electron's charge in electron microscopes, a series of physical phenomena occur when electrons interact within the specimen, obtaining a valuable information about sample's nature for each of these events. This issue will be addressed in section 3.1.4.

There are three basic types of microscopes depending on the working mode: the transmission electron microscope (TEM), the scanning transmission electron microscope (STEM) and the scanning electron microscope (SEM). The TEM and STEM will be described in the following section 3.1.2, while the SEM will be briefly shown in section 3.4.3.

3.1.2. Overview of the instrument

In a conventional TEM, an electron transparent sample is irradiated by a parallel electron beam generating several signals which can be collected and related to the specimen properties. The main parts of a TEM are depicted in Figure 3.1-1(a).

Electrons are generated from a source by thermionic emission - tungsten wire or lanthanum hexaboride (LaB_6) are usually the used materials - or by tunneling effect in a field emission gun (FEG), and they are directed to the condenser lenses. This lens system is also known as illumination system. It consists of two or more lenses and is followed by an aperture, the condenser lens aperture (CLA). The function of the lenses is to form the beam and to control the diameter of the electron beam (spot size). The CLA is located behind the condenser lenses to eliminate off-axis rays and to determine the illumination intensity onto the specimen.

Next, the electron beam interacts with the specimen, and electrons leaving the specimen are collected by the objective lens (OL), which is the most important lens for conventional TEM since it generates the first intermediate image and therefore determines the resolution of the TEM. This lens also forms a diffraction pattern in the back focal plane (BFP) and an image of the specimen in the image plane. The objective aperture (OA) is located in the BFP and selects the electrons which will contribute to the image. In the image plane, the selected area diffraction (SAD) aperture is used to select a part of the sample, thereby limiting the area from which diffraction patterns are acquired. The next lens system is the intermediate lens which allows focusing onto either the back focal plane or the image plane. Finally, the first image produced by the OL is further magnified by the intermediate and projector lenses, which project the image onto the fluorescent screen.

The conventional TEM used for sample's characterization in the framework of this thesis is the JEOL JEM-3010 equipped with a LaB_6 electron source (thermionic gun). Additionally, a second transmission electron microscope has been utilized: the JEOL JEM-2200FS equipped with a FEG. This is a combined TEM/STEM instrument which offers the possibility to work in either TEM or STEM mode.

The setup of a STEM mode is schematically illustrated in Figure 3.1-1(b). In STEM operation mode, the electron beam is focused into a very small spot and scanned over the specimen. The condenser lens system together with the upper part of the objective lens form the convergent beam, which is systematically guided line-by-line on the sample. The convergence angle of the beam is determined by condenser lens aperture[I]. Unlike conventional TEM, no further electromagnetic lenses are required for imaging in STEM mode. Hence, image intensities are generated pixel per pixel by collecting the scattered electrons with either the upper or lower annular dark field (ADF) detector.

In the next subsection, the lenses of (S)TEM machines and their aberrations will be discussed.

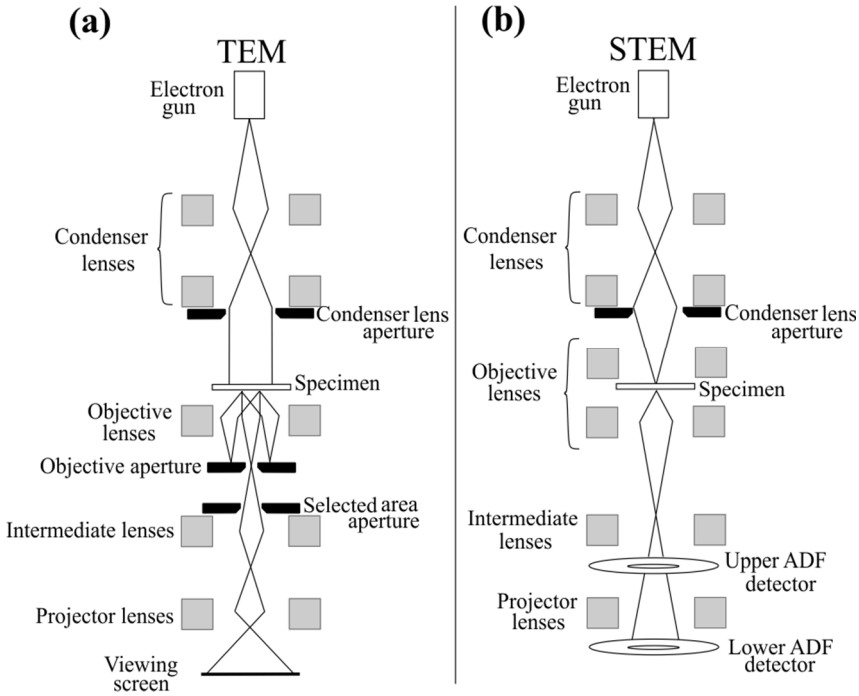

Figure 3.1-1. Brief description of a (a) TEM instrument and (b) STEM instrument.

[I] In pure STEM machines, this aperture is also referred to as objective aperture.

3.1.3. Lens aberrations: types and corrections

As it has been mentioned, (S)TEM machines use magnetic lenses to focus the electron beam towards the optical axis. However, they are not perfect and have aberrations that impair their performance. Although there are different types of aberrations, only the most important will be mentioned in this subsection, i.e. spherical aberration, astigmatism, coma and chromatic aberration [141,142].

Spherical aberrations (C_s) occur when the incoming rays do not converge at the same point after passing through the lens, creating different focal points (cf. Figure 3.1-2(a)). As a result, a point object is imaged as a disk of finite size, which limits the ability to resolve features. The minimum radius of the disk for spherical aberration is known as 'disc of least confusion' d_s and depends of different factors, i.e. the degree of spherical aberration C_s and the aperture angle of the lens α_{OA} [141,143]:

$$d_s = 0.5 \cdot C_s(\alpha_{OA})^3. \tag{3.1-1}$$

Astigmatism occurs when a lens does not have perfect cylindrical symmetry. The focusing strength of the lens then varies with an angle θ (cf. Figure 3.1-2(b)), leading to a spread of focus and a 'disc of least confusion'. The aberration is manifested by the off-axis image of a specimen point, appearing as a line or ellipse instead of a point [141,143].

Coma aberration is related to off-axis rays emitted from an object. The rays which travel through the center of the lens are focused on a point focus off the optic axis. This point focus is different from that of the peripheral rays (cf. Figure 3.1-2(c)). The resulting shape of the image distorted by coma aberration resembles that of a comet with its tail, hence the name coma [143].

Chromatic aberrations take place when electrons with different energies, entering a lens along the same path, come to different focal points forming a disc image (cf. Figure 3.1-2(d)). There are two main sources of this energy distribution: the electron gun and the specimen. The effect of chromatic aberration increases with (i) decreasing electron energy and (ii) increasing energy spread of the beam. Thus, a FEG minimizes the chromatic aberrations of about < 1 eV due to the narrow energy

spread, and thin specimens minimize the blurring of (S)TEM images caused by chromatic aberrations. The disc of least confusion d_c for chromatic aberrations can be related to the coefficient of chromatic aberration C_c, the aperture angle of the lens α_{OA}, the energy spread of the beam (ΔE) and the energy of the primary beam (E_0) by [141,143]:

$$d_c = C_c \cdot \alpha_{OA} \cdot \Delta E / E_0 \tag{3.1-2}$$

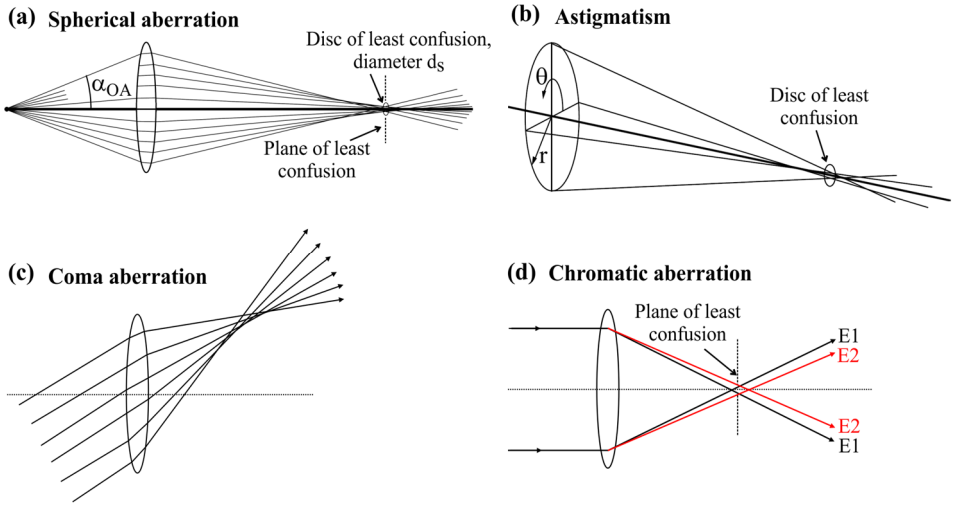

Figure 3.1-2. Lens aberrations. (a) Spherical aberration. (b) Astigmatism. (c) Coma aberration. (d) Chromatic aberration of rays with different energies, $E_1 < E_2$. The illustrations (a) and (b) are adapted from [143], and (c) and (d) are based on [141].

In a (S)TEM instrument, coma aberration and astigmatism can be easily corrected by using coils to a very low residual effect. In contrast, chromatic and spherical aberrations need magnetic multipole lenses to be corrected. These multipole lenses consist of an even number of magnetic poles arranged in equidistant angles around the optical axis. So far, there are essentially two types of correctors in use: those which use the effect of two extended magnetic hexapoles, and the ones which are based on combining quadrupole and octupole elements.

The hexapole corrector has the simplest structure and is the most stable, however this corrector only eliminates the spherical aberration, and therefore, cannot be extended to chromatic aberration; per contra, the quadrupole-octupole corrector is able to correct the chromatic aberration as well but its configuration is much more complex and exhibits large off-axis aberrations [144].

Concerning the instruments used along the experimental work, only the JEOL JEM-2200FS (S)TEM is fitted with correctors, in particular with two hexapole correctors (from CEOS GmbH). The first one is located behind the condenser lenses in the probe-forming side and is used for STEM mode, whereas the second one is positioned behind the objective lenses and is used for high resolution TEM imaging.

3.1.4. Interaction of electrons with specimen

Different interactions can occur when an incident beam enters a specimen, the main resulting signals are depicted in Figure 3.1-3. Electrons can be scattered by a variety of process or they may remain unaffected. The scattered electrons can be forward scattered (< 90°) or backscattered (> 90°) depending on their deflection angle. (S)TEM instruments collect forward scattered electrons, while backscattered signals are acquired by SEM machines.

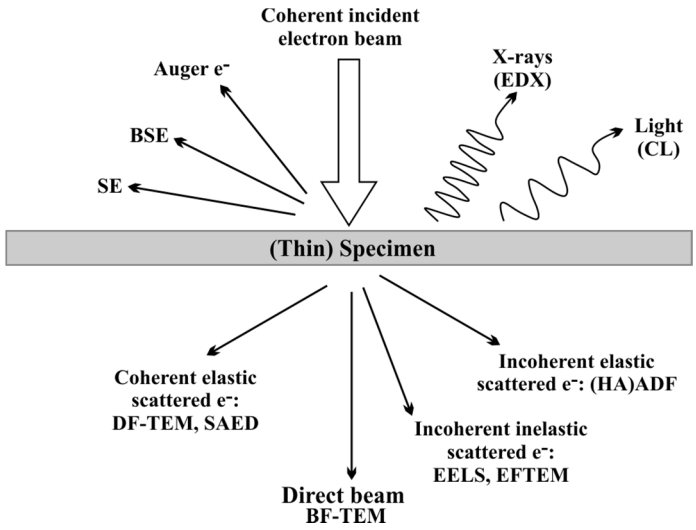

Figure 3.1-3. Scheme of electron-matter interactions arising from the impact of an electron beam onto the specimen. The signals below the specimen are only visible if the thickness of the sample is small enough.

Scattered electrons in turn can be can be classified into: (i) coherently and incoherently scattered electrons according to their wave nature, and (ii) elastically and inelastically scattered electrons whenever they preserve their energy or they do not (respectively).

The direct beam and the coherently elastically scattered electrons are exploited in conventional TEM for: BF- and DF-TEM imaging (cf. sections 3.4.1.1 and 3.4.1.2), electron diffraction (cf. section 3.4.1.3) and high resolution TEM (HRTEM, cf. section 3.4.1.4). In contrast, incoherent quasi-elastically scattered electrons are used to form ADF and high-angle annular dark field (HAADF) images (cf. section 3.4.2) in STEM mode. There is another type of electrons, those incoherent inelastically scattered, which can be utilized for electron energy loss spectroscopy (EELS) in STEM or energy-filtered TEM (EFTEM) but they lie outside the scope of this dissertation.

Apart from forward scattered electrons, backscattered events are produced upon interaction of the incident beam with the sample. The most important signals for this thesis are: secondary electrons (SE, cf. section 3.4.3) and characteristic X-rays which are used for energy dispersive X-ray (EDX) spectroscopy (cf. section 3.4.4). Additionally, auger electrons, light known as cathodoluminescence (CL) and back-scattered electrons (BSE) can be generated.

3.2. Electron scattering

As it has been mentioned in the previous subsection, electron scattering can be divided in elastic and inelastic scattering. For a particular electron, the probability of scattering of both elastically and inelastically can be expressed in terms of either cross-section (σ) or mean free path (MFP). In the following, these terms will be described. Next, the physic background and/or mechanisms of elastic and inelastic scattering will be introduced.

Cross-section (σ)

The derivations of this subsection are mainly adapted from [145] and [146]. The cross-section σ deals with the 'target area' presented by each scatterer (atom). Thereby, if an electron passes within this area, an interaction will take place and its probability will be higher if the cross-section increases. The total cross-section σ_{tot} will be the sum of the events that occur as elastic and inelastic interactions, $\sigma_{tot} = \sigma_{elast} + \sigma_{inelast}$. For every interaction, the cross-section depends on the effective radius r of each scattering center in this way: $\sigma = \pi \cdot r^2$. The radius r has different forms for each scattering process. For instance, for elastic scattering, the radius depends on the atomic number Z, the electron charge e, the acceleration voltage V and the scattering angle θ:

$$r_{elast} = Ze \,/\, V\theta. \tag{3.2-1}$$

As shown in equation (3.2-1), the radius will increase with the atomic number Z. Hence, the total scattering and the probability of the interaction will be higher for heavier atoms (higher Z). From equation (3.2-1), one can also deduce that the elastic scattering events are reduced at high voltages V and high angles θ. However, the angular details are missing in the total cross-section σ. These angular details are described by the differential cross section $d\sigma/d\Omega$. Rutherford calculated the differential cross section $d\sigma/d\Omega$ and its details will be shown in section 3.2.2, 'unscreened Coulomb potential'.

If the specimen in total is taken into account (instead of an isolated atom), the total cross-section Q_{tot} for a sample thickness t is:

$$Q_{tot} \cdot t = N \cdot \sigma_{tot} = \frac{N_0 \cdot \sigma_{tot} \cdot \rho \cdot t}{A} \quad (3.2\text{-}2)$$

Where N is the number of atoms in the sample, N_0 is the Avogadro number, ρ is the density of specimen and A is the atomic weight of atoms. The term $\rho \cdot t$ is also known as mass-thickness.

Mean free path (MFP) λ

The derivations of this subsection are mainly adapted from [145] and [146]. Another way to describe the probability of scattering is the MFP, which is the average distance traveled by an electron between two scattering events. The MFP is inversely proportional to the total cross-section Q_{tot} of the sample. Considering the thickness of the specimen, the probability p of scattering is:

$$p = t/\lambda = t \cdot Q_{tot}. \quad (3.2\text{-}3)$$

3.2.1. Inelastic scattering

This subsection is mainly adapted from [143,147]. The inelastic scattering concentrates on events that result in energy losses even at small scattering angles. The following mechanisms are known to produce energy losses:

Phonon excitation and molecule vibrations. Electrons generating phonons usually lose energies in the order of 20 meV-1 eV. These energy losses are relatively low and can only be observed if a monochromated primary electron beam is used. These interaction processes can also be generated by using infrared light.

Intra- and interband transitions. These energy losses cover excitations of electrons within an energy band or from outer to inner bands, and are around 2 eV.

Plasmons. They usually exhibit relatively broad energy-loss maxima in the energy-loss range of E = 1-50 eV. In some materials such as metals, the plasmon losses depend on the concentration of valence and conduction electrons. If the bonding

of electrons is imaged as a gas of free electrons (free electron gas model [148]), plasmons are created when the incident electrons pass through this gas. Plasmons are then longitudinal oscillations of the free-electron gas, which create regions of varying electron density.

Ionization of core electrons in inner atomic shells. Incident electrons can excite core electrons of atoms to higher energy states (above the Fermi level in the band theory or in the antibonding orbitals in the molecular orbital theory) causing an ionization of the atom. Hence, incident electrons experiment energy losses which are higher than the ionization energy of the atom (ranging between 10^2 and 10^4 eV) and are characteristics of each element of the specimen, 'fingerprinting'.

The energy losses of electrons, mainly plasmons and core excitations, can be measured in a (S)TEM instrument by a EELS spectrometer located after the projector lens.

Secondary electrons (SE). They are caused from the collision between the incident electrons and the loosely bonded outer electrons. The incoming electrons transfer part of their energy to a lower energy electron causing the ionization of the electron in the specimen atom. This ionized electron leaves the atom with a very small kinetic energy (5–50 eV) and gives information about the surface topography (cf. section 3.4.3).

Bremsstrahlung[II] X-rays. These signals result when the electron beam interacts inelastically with the nucleus of the specimen atoms. Electrons will exit the material with less energy and the energy loss depends on the strength of interaction (is undetermined). Hence bremsstrahlung X-rays can have any energy up to the beam energy.

Characteristic X-rays. These signals result when the electron beam ejects inner shell electrons of the specimen atoms leaving a vacancy, which can be filled by an electron from an outer shell. If this process occurs, characteristic X-rays are emitted.

[II] Also referred to as continuum or background X-rays.

They contain chemical information of the sample and can be collected using an EDX detector (cf. section 3.4.4).

Auger electrons. As it has been above mentioned, the incident beam can eject electrons leaving a vacancy which can be filled by an outer shell electron. Instead of emission of X-rays, the superfluous energy can be transferred to another electron, causing the ejection of the electron. Thus, this electron is known as Auger electron.

Cathodoluminescence (CL). This signal occurs when the primary beam has sufficient energy to promote electrons from the valence band to the conduction band[III]. This process leaves a hole in the valence band that can be filled by a conduction-band electron. When the electron and hole recombine, a photon will be emitted whose energy can be related to the band gap of the material.

3.2.2. Elastic scattering

Elastic scattering of electrons upon interaction with a specimen is the most important interaction that contributes to image contrast. In this subsection, firstly, the derivations needed to get the expression of the elastically scattered wave are briefly described. Next, the potential responsible for electron scattering and its equations depending on the scattering angle are discussed. The derivations of this subsection are mainly adapted from [143].

The incident electron can be treated as a plane wave that interacts with the nucleus and the electron cloud of the atom, giving a spherical scattered wave which is collected in a detector. The intensity of the scattered wave is not isotropic. A sketch showing the positions of the scatterer ($\boldsymbol{r}'$) and the detector ($\boldsymbol{r}$), together with the incident ($\boldsymbol{k}_0$) and scattered ($\boldsymbol{k}$) wavevectors is depicted in Figure 3.2-1.

[III] In the case of an organic material, an electron excited from HOMO to LUMO is concerned.

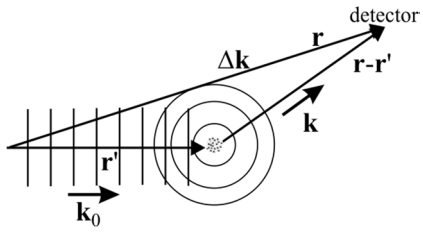

Figure 3.2-1. Position of wavevectors and detector for electron scattering. Figure adapted from [143].

The plane incoming wave ψ_{inc} and the spherical scattered wave ψ_{sca} can be deduced as following:

$$\psi_{inc} = \exp[i(\boldsymbol{k}_0 \cdot \boldsymbol{r}' - \omega t)] \tag{3.2-4}$$

$$\psi_{sca} = f(\boldsymbol{k}_0, \boldsymbol{k}) \frac{\exp\,[i\boldsymbol{k}|\boldsymbol{r} - \boldsymbol{r}'|]}{|\boldsymbol{r} - \boldsymbol{r}'|} \tag{3.2-5}$$

where ω is the angular frequency and the difference $\boldsymbol{r} - \boldsymbol{r}'$ is the distance from the scatterer to the detector. Moreover, if elastic scattering is considered, the magnitudes of the incident and scattered wavevectors are equal ($\boldsymbol{k} = \boldsymbol{k}_0$).

The total wave at $\boldsymbol{r}$, $\psi(\boldsymbol{r})$, will be the sum of the incident and scattered components: $\psi = \psi_{inc} + \psi_{sca}$. The incident wave ψ_{inc} can be easily solved, however to obtain the scattered wave ψ_{sca}, the term $|f(\boldsymbol{k}_0, \boldsymbol{k})|$ should be solved. This is done by using the Schrödinger equation for the incident electron inside the scattering atom. The Schrodinger equation has the following form:

$$-\frac{\hbar}{2m}\nabla^2\,\psi(\boldsymbol{r}') + V(\boldsymbol{r}')\,\psi(\boldsymbol{r}') = E\,\psi(\boldsymbol{r}'), \tag{3.2-6}$$

where $\hbar$ is the reduced Planck constant, m is the electron mass, $V\,(\boldsymbol{r}')$ is the potential, E is the total energy, $\psi(\boldsymbol{r}')$ is the wave function of incident electron, ∇ is the Nabla operator and $\nabla^2 = \Delta$ is the Laplace operator. If the Green's functions are used to solve the Schrödinger equation and the following approximations are applied:

- ❖ The 'first Born approximation', which assumes that *the 'wave is undiminished and scattered only once by the material'*. This assumption is valid when the scattering is weak.
- ❖ The detector is far away from scatterer. It allows working with plane waves at detector instead of scattered spherical waves.
- ❖ The origin is near the scatterer, so that $|\boldsymbol{r}|>>|\boldsymbol{r}'|$.

Then, the solution of the total wave at r, $\psi(\boldsymbol{r})$, can be approached to the expression of equation (3.2-7):

$$\psi(\boldsymbol{r}) \cong exp\,[i\boldsymbol{k}_0 \cdot \boldsymbol{r}] - \underbrace{\frac{m}{2\pi\hbar^2}\int V(\boldsymbol{r}')\ exp\,[i\boldsymbol{k}_0 \cdot \boldsymbol{r}']\frac{exp\,[i\boldsymbol{k}\,(\boldsymbol{r}-\boldsymbol{r}']}{|\boldsymbol{r}|}\,d^3\,\boldsymbol{r}'}_{\psi_{sca}} \tag{3.2-7}$$

where, the scattered part of the wave ψ_{sca} if $\Delta\boldsymbol{k} = \boldsymbol{k} - \boldsymbol{k}_0$ is:

$$\psi_{sca}(\Delta\boldsymbol{k}, \boldsymbol{r}) = \frac{\exp\,[i\boldsymbol{k}\cdot\ \boldsymbol{r}]}{|\boldsymbol{r}|} f(\Delta\boldsymbol{k}). \tag{3.2-8}$$

The factor $f(\Delta\boldsymbol{k})$ is the scattering factor which depends on the incident and scattered wave vector only through their difference ($\Delta\boldsymbol{k}$). The $f(\Delta\boldsymbol{k})$ has the following form:

$$f(\Delta\boldsymbol{k}) = -\frac{m}{2\pi\hbar^2}\int V(\boldsymbol{r}')\ \exp\,[-i\Delta\boldsymbol{k}\cdot\ \boldsymbol{r}']\ d^3\,\boldsymbol{r}'. \tag{3.2-9}$$

The integral of equation (3.2-9) is the Fourier transform[IV] of the potential 'seen' by the incident electron when is directed to the scatterer. If $V(\boldsymbol{r}')$ is the potential of an atom ($V_{at}(\boldsymbol{r})$[V]), $f(\Delta\boldsymbol{k})$ will be the '*atomic form factor*' for electrons $f_{el}(\Delta\boldsymbol{k})$. Thus, one can say that *the scattered wave is proportional to the Fourier transform of the scattering potential.* The atomic form factor of equation (3.2-9) is only valid in

[IV] Notice that the Fourier transform is a mathematical operation that decomposes a signal into its constituent frequencies, therefore, the atomic form factor is the Fourier transform of the shape of the scattering potential: $F(\omega) = \int f(x)\exp[-2\pi i x\omega]\ dx$.

[V] Note that $\boldsymbol{r}'$ has been changed by $\boldsymbol{r}$. This designation will be maintained in the following.

case of 'kinematical diffraction'. Hence, when $V(\boldsymbol{r})$ is extended to the whole crystal, equation (3.2-9) may fail. This situation is overcome by using 'the dynamical theory' of electron diffraction, which is based on higher order Born approximations.

The potential $V(\boldsymbol{r})$ responsible for electron scattering has a Coulombic nature: electrons travel on hyperbolic trajectories due to the attractive Coulomb force between electron and nucleus, but there are surrounding atomic electrons which modify and partly screen the positive charge of the nucleus. On balance, the atom is electrically neutral since there is a cancellation of the electric fields from the nucleus and the atomic electrons. The incident electron is therefore unaffected by this neutral atom and the scattering process occurs when it penetrates in the electron cloud of the atom.

Depending on the effect of the surrounding atomic electrons on the incident electron, two different model potentials for electron scattering can be applied, i.e. the screened Coulomb potential and the unscreened Coulomb potential, they will be briefly described in the following.

Screened Coulomb potential

When the screening by the atomic electrons becomes important, the incident electrons are deflected from its straight-line trajectory at low angles. This Coulomb potential $V(\boldsymbol{r})$ has the following form:

$$V(\boldsymbol{r}) = \frac{-Ze^2}{\boldsymbol{r}} \exp\left[-\boldsymbol{r}/\boldsymbol{r}_0\right], \tag{3.2-10}$$

substituting the Coulomb potential of equation (3.2-10) in the atomic form factor of equation (3.2-9), and doing a series of intermediate steps, the atomic form factor for the coherent elastic scattering at low angles is obtained as:

$$f_{el}(\Delta\boldsymbol{k}) = \frac{2Za_0}{\Delta\boldsymbol{k}^2 a_0^2 + Z^{2/3}}, \tag{3.2-11}$$

where Z is the atomic number, r_0 is the effective Bohr radius ($r_0 = a_0 Z^{-1/3}$), and a_0 is the Bohr radius of H atom in its ground state. One can see from equation (3.2-11) that the electron scattering factor of the atom $f_{el}(\Delta\boldsymbol{k})$ increases slower

than Z^1. This model potential is particularly important in conventional TEM, where the elastic scattering events occur at very low angles due to the screening of incident electrons. At these low angles, the elastic scattering is coherent (if the incident beam is also coherent), this part will be described in more detail in section 3.2.3.

Unscreened Coulomb potential

In this situation, the incident electrons pass close to the nucleus and they are deflected at high angles since the screening by the surrounding electrons is somehow neglected. In consequence, the difference in the wave vector becomes larger: $\Delta\boldsymbol{k}^2 a_0^2 \gg Z^{2/3}$ in equation (3.2-11), and $f_{el}(\Delta\boldsymbol{k})$ is approximately proportional to Z^1.

The scattering at high angles was investigated by Rutherford by using the α-particle (He nuclei) on a gold foil [149]. The differential cross-section for the Rutherford scattering of electrons, $d\sigma_R/\,d\Omega$, if there is no screening of incident electrons ($r_0 \to \infty$) is:

$$\frac{d\sigma_R}{d\Omega} = |f_{el}(\Delta\boldsymbol{k})|^2 = \frac{4\,Z^2}{a_0^2\,\Delta\boldsymbol{k}^4}\,, \tag{3.2-12}$$

taking into account the following expressions: $\Delta\boldsymbol{k} = 4\pi\,sin\theta/\lambda$, $E = p^2/(2m)$ and $p = h/\lambda$, and doing a series of intermediate steps, the 'familiar' form of the 'Rutherford scattering cross-section' is obtained as:

$$\frac{d\sigma_R}{d\Omega} = \frac{Z^2\,e^4}{16\,E^2\,\,sin^4\,\theta} = \left(\frac{Z\,e^2}{4\,E\,sin^2\,\theta}\right)^2. \tag{3.2-13}$$

Hence, the probability that an incident electron is scattered at high angles increases with the charge of the nucleus to the power of two (Z^2) and decreases with the energy of the incident electrons to the power of two (E^2). This model potential becomes important in STEM when electrons scattered into high or very high angles are collected by detectors. At these high angles, the (quasi)-elastic scattering is mostly incoherent. High-angle scattering contributes to mass-thickness contrast, but not to the diffraction contrast.

3.2.3. Electron diffraction from crystals

This subsection is based on elastically coherently scattered electrons, which are those used in electron diffraction. In this part, the expressions derived in the previous section will be extended to the periodic arrangement of atoms in a crystal. In addition, the basic concepts of Bragg's Law, reciprocal lattice and Laue Condition and their relationship with electron diffraction will be explained. These concepts are particularly important to understand the results part of this thesis. Finally, the excitation error term will be introduced.

The derivations of this subsection are mainly adapted from [143]. Equation (3.2-9) relates the electron in the same atom (only one scattering center). However, there are a certain number of atoms in a unit cell of a crystal. In consequence, equation (3.2-8) needs to be adapted for the case of more than one scattering center. In this case, new coordinates are added: the set of vectors $\{\boldsymbol{R}_j\}$, which determine the center of the atoms in the material. Hence, the vector $\boldsymbol{r}' - \boldsymbol{R}_j$ will be the distance of $\boldsymbol{r}'$ from the center of the nth atom (cf. Figure 3.2-2 for clarification). Then, the potential $V(\boldsymbol{r}')$ is determined by the sum of the individual atomic potentials V_{at} of atoms centered at site $\boldsymbol{R}_j$:

$$V(\boldsymbol{r}') = \sum_{\boldsymbol{R}_j} V_{at}(\,\boldsymbol{r}' - \boldsymbol{R}_j). \tag{3.2-14}$$

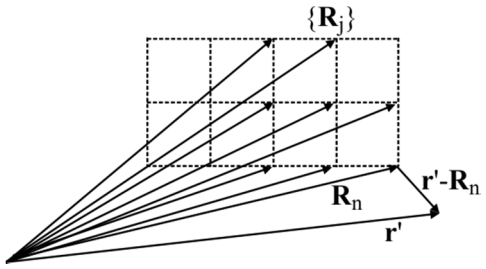

Figure 3.2-2. Sketch showing the center of atoms placed at positions $\{R_j\}$ and their relation with the vector $\boldsymbol{r}'$. Figure adapted from [143].

The term for the potential of equation (3.2-14) is introduced in equation (3.2-8), obtaining the scattered wave as:

$$\psi_{sca}(\Delta \boldsymbol{k}, \boldsymbol{r}) = -\frac{m}{2\pi\hbar^2}\frac{exp\,[i\boldsymbol{k}\cdot\boldsymbol{r}]}{|\boldsymbol{r}|}\int \sum_{\boldsymbol{R}_j} V_{at}(\,\boldsymbol{r}' - \boldsymbol{R}_j)\; exp\,[-i\Delta\boldsymbol{k}\cdot\,\boldsymbol{r}']\; d^3\,\boldsymbol{r}'. \qquad (3.2\text{-}15)$$

Additionally, if the following assumptions are done: r-dependent outgoing wave in front of the integral is ignored, a new coordinate is defined as $\boldsymbol{r} \equiv \boldsymbol{r}' - \boldsymbol{R}_j$ (so that $\boldsymbol{r}' \equiv \boldsymbol{r} - \boldsymbol{R}_j$), f_{el} is substituted by f_{at}, and the term 2π is included in the exponential, the scattered wave ψ_{sca} from N atoms is derived as the sum of wavelets with amplitude $f_{at}(\boldsymbol{R}_j)$ from atoms at all R_j positions:

$$\psi_{sca}(\Delta\boldsymbol{k}) = \sum_{j}^{N=1} f_{at}(\boldsymbol{R}_j)\,\exp\,[-2\pi i\Delta\boldsymbol{k}\cdot\,\boldsymbol{R}_j]\,. \qquad (3.2\text{-}16)$$

Hence, the diffracted wave is proportional to Fourier transform of the scattering factor distribution in the material.

Since large crystals are considered, another transformation should still be done: the atom positions $\boldsymbol{R}_j$ are decomposed by a sum of vectors to each unit cell $\boldsymbol{r}_g$ and vectors to the atom basis within the unit cell $\boldsymbol{r}_k$, $\boldsymbol{R} = \boldsymbol{r}_g + \boldsymbol{r}_k$. If this term is introduced into equation (3.2-16), the following expression is obtained:

$$\psi_{sca}(\Delta\boldsymbol{k}) = \sum_{\boldsymbol{r}_g}\sum_{\boldsymbol{r}_k} f_{at}\left(\boldsymbol{r}_g + \boldsymbol{r}_k\right)\exp\left[-2\pi i\Delta\boldsymbol{k}\left(\boldsymbol{r}_g + \boldsymbol{r}_k\right)\right]. \qquad (3.2\text{-}17)$$

So that, the atoms basis is the same for all unit cells, f_{at} does not depend on $\boldsymbol{r}_g$ and therefore: $f_{at}\,(\boldsymbol{r}_g + \boldsymbol{r}_k) \cong\; f_{at}\,(\boldsymbol{r}_k)$. Doing this change in equation (3.2-17):

$$\begin{aligned}\psi_{sca}(\Delta\boldsymbol{k}) &= \sum_{\boldsymbol{r}_g}\exp[-2\pi i\Delta\boldsymbol{k}\cdot\boldsymbol{r}_g]\cdot\sum_{\boldsymbol{r}_k} f_{at}(\boldsymbol{r}_k)\exp[-2\pi i\Delta\boldsymbol{k}\cdot\boldsymbol{r}_k] = \\ &= S(\Delta\boldsymbol{k})\cdot F(\Delta\boldsymbol{k}).\end{aligned} \qquad (3.2\text{-}18)$$

The first summation term of equation (3.2-18) is known as '*shape factor*' $S(\Delta \boldsymbol{k})$, while the second summation term is called '*structure factor*' $F(\Delta \boldsymbol{k})$. As it can be seen, the shape factor is over the whole lattice. The structure factor applies on the atoms within a unit cell and is the Fourier transform of the atomic form factor distribution $f_{at}(\boldsymbol{r}_k)$. The shape factor and structure factor are defined by equation (3.2-19) and equation (3.2-20), respectively:

$$S(\Delta \boldsymbol{k}) = \sum_{\boldsymbol{r}_g}^{\boldsymbol{lattice}} \exp\left[-2\pi i \Delta \boldsymbol{k} \cdot \boldsymbol{r}_g\right], \tag{3.2-19}$$

$$F(\Delta \boldsymbol{k}) = \sum_{\boldsymbol{r}_k}^{\boldsymbol{basis}} f_{at}(\boldsymbol{r}_k) \exp[-2\pi i \Delta \boldsymbol{k} \cdot \boldsymbol{r}_k]. \tag{3.2-20}$$

Thus, the scattered wave $\psi_{sca}(\Delta \boldsymbol{k})$ of an infinite large crystal can be written as:

$$\psi_{sca}(\Delta \boldsymbol{k}) = \sum_{\boldsymbol{r}_g}^{\boldsymbol{lattice}} F(\Delta \boldsymbol{k}) \exp\left[-2\pi i \Delta \boldsymbol{k} \cdot \boldsymbol{r}_g\right], \tag{3.2-21}$$

and the intensity of the scattered wave is defined as the square of the absolute value of $\psi(\Delta \boldsymbol{k})$, hence:

$$I = |\psi(\Delta \boldsymbol{k})|^2 = |S(\Delta \boldsymbol{k})|^2 \cdot |F(\Delta \boldsymbol{k})|^2. \tag{3.2-22}$$

One can see from equation (3.2-22) that the square of the structure factor is proportional to the diffracted intensity. This concept becomes important in practice when the intensity of reflections in a diffraction pattern are analyzed.

3.2.3.1. **Bragg's Law**

The scattered waves of all atoms arranged periodically in a crystal can interfere when they are irradiated by a coherent incident beam. Diffraction will take place only under certain angles (the so called Bragg angles) if the scattered waves interfere in a constructive way, and therefore, the Bragg condition is fulfilled.

The Bragg's Law relates the spacing of atomic planes in crystals d_{hkl} and the angles θ of incidence of radiation [150] in the following way:

$$2d_{hkl} \cdot sin\theta = n \cdot \lambda, \tag{3.2-23}$$

where the integer, n (n =1, 2, 3 etc.) indicates the order of reflection. The use of electrons that satisfy the Bragg's equation allow the determination of unit cell parameters, bond-lengths, bond-angles, ordering and arrangement of the crystalline material. In particular, they are important for techniques such as SAED patterns and BF- and DF- imaging, all of them based on conventional TEM. They will be discussed in section 3.4.1.

3.2.3.2. **Reciprocal lattice**

A reciprocal lattice is a Fourier transformed real lattice, where the set of real lattice planes is conserved into a point in reciprocal lattice. The reciprocal space has length-dimensions in reciprocal order, that is [length]$^{-1}$. The knowledge of reciprocal space is essential to understand several issues of the results part in this thesis: The main characteristics of reciprocal space are [147,151]:

(i) A lattice vector in real space is usually denoted as $\boldsymbol{T} = n_1\boldsymbol{a}_1 + n_2\boldsymbol{a}_2 + n_3\boldsymbol{a}_3$, hence the reciprocal lattice can be constructed with the reciprocal lattice vector of $\boldsymbol{g} = h\boldsymbol{a}_1^* + k\boldsymbol{a}_2^* + l\boldsymbol{a}_3^*$, where, $\boldsymbol{a}_1^*$, $\boldsymbol{a}_2^*$, $\boldsymbol{a}_3^*$ are primitive vectors of real lattice (cf. equation (3.2-24)), $\boldsymbol{b}_1$, $\boldsymbol{b}_2$, $\boldsymbol{b}_3$ are the corresponding primitive vectors of reciprocal lattice, and n_1, n_2, and n_3 are integers. The primitive vectors in both spaces can be related by the following expression: $\boldsymbol{a}_i^* \cdot \boldsymbol{b}_j = \delta_{ij}$, where $\delta_{ij} = 1$ when $i = j$, and $\delta_{ij} = 0$ when $i \neq j$ (with i, j=1,2,3). In turn:

$$\boldsymbol{a}_1^* = \frac{\boldsymbol{a}_2 \times \boldsymbol{a}_3}{\boldsymbol{a}_1 \cdot \boldsymbol{a}_2 \times \boldsymbol{a}_3}; \quad \boldsymbol{a}_2^* = \frac{\boldsymbol{a}_3 \times \boldsymbol{a}_1}{\boldsymbol{a}_2 \cdot \boldsymbol{a}_3 \times \boldsymbol{a}_1}; \quad \boldsymbol{a}_3^* = \frac{\boldsymbol{a}_1 \times \boldsymbol{a}_2}{\boldsymbol{a}_3 \cdot \boldsymbol{a}_1 \times \boldsymbol{a}_2}. \tag{3.2-24}$$

(ii) If the vector $\boldsymbol{g}_{hkl} = h\boldsymbol{a}_1^* + k\boldsymbol{a}_2^* + l\boldsymbol{a}_3^*$ is a reciprocal lattice vector pointing from origin to a reciprocal lattice point hkl, then the $\boldsymbol{g}_{hkl}$ is always perpendicular to the crystal plane (hkl) in real space.

(iii) Each reciprocal lattice point represents a set of lattice planes in real space, where the distance between the origin and the reciprocal lattice point is reciprocal of the plane spacing in real space: $|\boldsymbol{g}_{hkl}| = 1/d_{hkl}$. Where, d_{hkl} is the interplanar spacing of the plane (hkl).

(iv) The reciprocal lattice can be defined as the Fourier transform of the crystal real lattice. The Fourier integral of the 3D real lattice is the sum of the discrete lattice points $\boldsymbol{T}$ (with $\boldsymbol{T} = n_1\boldsymbol{a}_1 + n_2\boldsymbol{a}_2 + n_3\boldsymbol{a}_3$):

$$F(\boldsymbol{g}) = \sum_{n_1\, n_2\, n_3} \exp\left[-2\pi i \boldsymbol{g}(n_1\boldsymbol{a}_1 + n_2\boldsymbol{a}_2 + n_3\boldsymbol{a}_3)\right]. \tag{3.2-25}$$

3.2.3.3. **Laue Condition**

The Laue condition relates the incoming and outgoing waves in the process of diffraction by a crystal lattice, in this sense, the Laue diffraction law can be expressed as [143,145,147]:

$$\Delta\boldsymbol{k} = \boldsymbol{g}. \tag{3.2-26}$$

Laue condition states that diffraction occurs when $\Delta\boldsymbol{k}$ is a vector of the reciprocal lattice; notice that $\boldsymbol{g}$ is an arbitrary reciprocal lattice vector ($\boldsymbol{g} = h\boldsymbol{a}_1^* + k\boldsymbol{a}_2^* + l\boldsymbol{a}_3^*$). The three Laue equations, for integer values of a reflection with reciprocal lattice indices (hkl) by considering the wave vector, $\boldsymbol{k} = 1/\lambda$, can be also written as:

$$\boldsymbol{a}_1 \cdot \Delta\boldsymbol{k} = \boldsymbol{h}\,; \quad a_2 \cdot \Delta\boldsymbol{k} = \boldsymbol{k}\,; \quad \boldsymbol{a}_3 \cdot \Delta\boldsymbol{k} = \boldsymbol{l}\,. \tag{3.2-27}$$

Despite the Bragg's Law (equation (3.2-23)) and the Laue condition (equation (3.2-26)) seem different, both are equivalent, and therefore, both describe the conditions to be satisfied by an incident wave to be diffracted by a crystal.

Ewald's construction gives a geometrical interpretation of the Laue condition in 3D and is depicted in Figure 3.2-3. The Ewald's sphere is constructed on the corresponding reciprocal lattice in the following way: the incoming wave vector $\boldsymbol{k}_0$ is drawn with one end at the origin O of the reciprocal lattice. The other end C of $\boldsymbol{k}_0$ is

taken at the center of a sphere of radius $1/\lambda$. Hence the length of $|\boldsymbol{k}_0|$.is $1/\lambda$. The Laue condition is fulfilled, and therefore diffraction occurs, when Ewald's sphere intersects a lattice point of reciprocal lattice (G point in the example of Figure 3.2-3). The direction of $\boldsymbol{k}$ is the direction of the scattered wave vector and $\boldsymbol{g}$ connects the endpoints of $\boldsymbol{k}$ and $\boldsymbol{k}_0$, where $\boldsymbol{g} = \boldsymbol{k} - \boldsymbol{k}_0 = \Delta\boldsymbol{k}$. The angle 2θ is defined as the angle between $\boldsymbol{k}$ and $\boldsymbol{k}_0$.

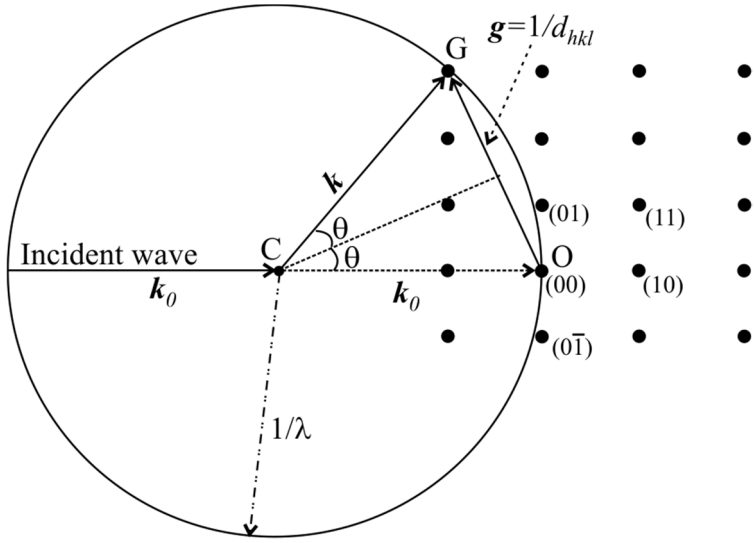

Figure 3.2-3. Geometrical construction of Ewald's circle (in two-dimensional, 2D) with radius 1/λ. The point O (00) represents the origin of the reciprocal space. Constructive interference occurs when the sphere intersects a reciprocal lattice point (e.g. point G).

3.2.3.4. **Bravais lattice**

As mentioned before, a crystal lattice consists of regularly repeating array of unit cells, which are smallest repeating unit in real space lattice. The unit cell is a parallelepiped with edges defined by three non-coplanar fundamental translation vectors $\boldsymbol{a}_1$, $\boldsymbol{a}_2$ and $\boldsymbol{a}_3$ (basic vectors), which when are translationally repeated gives the whole crystal lattice. In 1948, Bravais showed that all crystal structures can be generated by using only 14 types of unit cell. They are kwon as Bravais lattices and are described in Figure 3.2-4.

Bravais lattice cells	Axes and interaxial angles
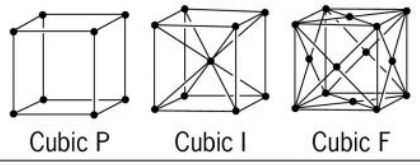 Cubic P Cubic I Cubic F	Three axes at right angles; all equal: $a = b = c$; $\alpha = \beta = \gamma = 90°$
 Tetragonal P Tetragonal I	Three axes at right angles; two equal: $a = b \neq c$; $\alpha = \beta = \gamma = 90°$
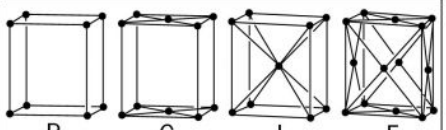 P C I F Orthorhombic	Three axes at right angles; all unequal: $a \neq b \neq c$; $\alpha = \beta = \gamma = 90°$
 Monoclinic P Monoclinic C	Three axes, one pair not at right angles, of any lengths: $a \neq b \neq c$; $\alpha = \gamma = 90° \neq \beta$
 Triclinic P	Three axes not at right angles, of any lengths: $a \neq b \neq c$; $\alpha \neq \beta \neq \gamma \neq 90°$
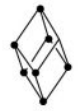 Trigonal R (rhombohedral)	Rhombohedral: three axes equally inclined, not at right angles; all equal: $a = b = c$; $\alpha = \beta = \gamma \neq 90°$
 Trigonal and hexagonal C (or P)	Hexagonal: three equal axes coplanar at 120°, fourth axis at right angles to these: $a_1 = a_2 = a_3 \neq c$; $\alpha = \beta = 90°$, $\gamma = 120°$

Figure 3.2-4. Classification of the 14 Bravais lattices (this figure has been adapted from [152]).

3.2.3.5. **Excitation error / deviation parameter**

In section 3.2.3 the shape factor (cf. equation (3.2-19)) was defined. The importance of this subsection resides in the fact that the effects of the shape factor are sometimes visible in diffraction patterns, since some features similar to streaks appear instead of individual spots or rings. These features may give information on the dimension of the crystal, hence the streaks appear stretched out in the direction of thinness of the sample. These streaked reciprocal lattice points are known as 'relrods'. The Ewald's sphere can intersect with the relrods and diffraction can occur even when the Bragg condition is not exactly satisfied. The deviation parameter $\boldsymbol{s}$ (also called excitation error or deviation vector) measures the deviation from the exact Bragg condition. Thus, to determine the influence of relrods on Shape factor (equation (3.2-19)) and Structure factor (equation (3.2-20)), the diffraction vector $\Delta\boldsymbol{k}$ should be slightly modified:

$$\Delta\boldsymbol{k} = \boldsymbol{g} - \boldsymbol{s} \;\rightarrow \boldsymbol{g} = \Delta\boldsymbol{k} + \boldsymbol{s}, \tag{3.2-28}$$

where $\Delta\boldsymbol{k}$ is the difference between the exact reciprocal lattice vector $\boldsymbol{g}$ and the deviation parameter $\boldsymbol{s}$. If equation (3.2-28) is introduced in equation (3.2-19), and taking into account that $\boldsymbol{g} \cdot \boldsymbol{r}_g$ is an integer, the Shape factor is modified as follows:

$$S(\Delta\boldsymbol{k}) = \sum_{\boldsymbol{r}_g}^{\boldsymbol{lattice}} \exp[+2\pi i \cdot \boldsymbol{s} \cdot \boldsymbol{r}_g] = \boldsymbol{S}(-\boldsymbol{s}). \tag{3.2-29}$$

If equation (3.2-28) is also introduced into the equation of Structure factor and considering that $\boldsymbol{s} \cdot \boldsymbol{r}_k$ is small, equation (3.2-20) is modified as:

$$F(\Delta\boldsymbol{k}) = \sum_{\boldsymbol{r}_k}^{\boldsymbol{basis}} f_{at}(\boldsymbol{r}_k) \exp[-2\pi i\, \boldsymbol{g} \cdot \boldsymbol{r}_k] = F(\boldsymbol{g}). \tag{3.2-30}$$

From equation (3.2-29), it can be seen that the shape factor only depends on the excitation error $\boldsymbol{s}$ and not on the reciprocal lattice vector $\boldsymbol{g}$. In contrast, equation (3.2-30) shows that the structure factor depends only on $\boldsymbol{g}$. The excitation error $\boldsymbol{s}$ is minimum on the exact reciprocal lattice point.

3.3. Contrast mechanisms in (S)TEM

The previous sections have described different electron scattering mechanisms and the particular case of diffraction. They generate different kind of contrasts which are useful for imaging. The contrast is defined as the difference in intensity between two adjacent areas [153]:

$$C = \frac{I_2 - I_1}{I_1} = \frac{\Delta I}{I_1} \tag{3.3-1}$$

It has been shown that the electron wave can change its amplitude and phase passing through a specimen. According to this fact, the different contrast mechanisms can be classified as:

Amplitude-contrast:

The change into the amplitude of electron wave results in mass-thickness contrast, and diffraction contrast.

Mass-thickness contrast: thicker sample regions or with heavier atoms will scatter the electrons more strongly making that these areas appear darker in the image.

Diffraction contrast: crystalline regions of the specimen oriented at the Bragg angle for diffraction will excite diffracted beams, giving a reduction of the undiffracted beams. In particular, this image mechanism is used for the formation of BF-TEM and DF-TEM images that will be discussed in section 3.4.1.

Phase contrast:

The image is formed by the interference of the scattered beams with the unscattered beam generating an interference pattern. This is visible at high magnifications and reflects the lattice periodicity. The lattice planes and therefore atomic positions are imaged but may appear bright or dark depending on the microscope conditions (objective lens defocus, beam energy…) and the sample thickness. Phase contrast is the main contrast mechanism in HRTEM (cf. section 3.4.1.4).

3.4. Experimental techniques

This section introduces the experimental (S)TEM and SEM methods used to characterize the samples as well as the procedure utilized to prepare the organic films. Firstly, the different conventional TEM techniques, i.e. BF-TEM, DF-TEM, SAED patterns and HRTEM, are presented. Next, the HAADF method used in the STEM instrument is described. This is followed by the explanation of the SEM machine together with its comparison with the TEM, and the description of the EDX and the ET techniques. Finally, basics details of the organic molecular beam deposition (OMBD) procedure are introduced.

3.4.1. Conventional TEM techniques

In conventional TEM of crystalline materials, coherently elastically scattered electrons as well as the unscattered electrons (named as direct beam, primary beam or transmitted beam) contribute to the formation of images. As it has been explained in section 3.1.4, a parallel and broad electron beam is used to illuminate a region of the sample in conventional TEM. The direct beam is used to create a BF-TEM image and the diffracted beam(s) are selected for the DF-TEM images. In order to do that, the OA is inserted in the back focal plane of the objective lens and the beams are selected from the SAED patterns. In the following subsections the BF-TEM and DF-TEM imaging together with SAED and HRTEM methods are described in detail. This section is based on [143,145,147].

3.4.1.1. **Bright field-TEM (BF-TEM)**

The direct beam on the optic axis is selected by the OA for imaging as shown in Figure 3.4-1. Hence, only the electrons transmitted through the specimen contribute to generate the BF-TEM image. Therefore, mass-thickness and diffraction contrast contribute to image formation, so thicker areas, regions with heavier atoms and crystalline areas oriented at the Bragg angles for diffraction present dark contrast.

3.4.1.2. **Dark field-TEM (DF-TEM)**

DF-TEM images are formed using electrons diffracted at angles other than those collected in the primary beam. When the OA is introduced into the diffraction plane of the objective lens and select diffracted beams, areas diffracting toward the aperture appear brighter than the ones diffracting in other directions. This happens since crystalline particles obeying the Bragg condition appear bright, while the ones which do not fulfil Bragg condition are dark. This technique gives the real space distribution of the part of the phase which fulfills the Bragg condition for the selected reflections. In addition, any microstructural feature which changes the corresponding diffraction condition (such as grain boundary, stacking fault, strain field or a line defect) will, in principle, show up in diffraction contrast.

If the direct beam is on the optic axis, one option to create a DF-TEM image is to move the OA to select the diffracted beam(s) which contributes to the DF-TEM image (cf. Figure 3.4-1). In this case, the electrons selected for the DF-TEM image travel off the optic axis, so that they will be more affected by the spherical aberrations and astigmatism, resulting in a poor quality image. This operation mode is sometimes referred as 'dirty' DF (cf. Figure 3.4-1(b)). In order to retain the direct beam parallel to the optic axis and get the diffracted electrons on the optic axis too, the illumination incident on the specimen should be tilted is such a way that the diffracted electrons travel along the optic axis (cf. Figure 3.4-1(c)). This working mode is known as centered DF and is the conventional way to do DF imaging.

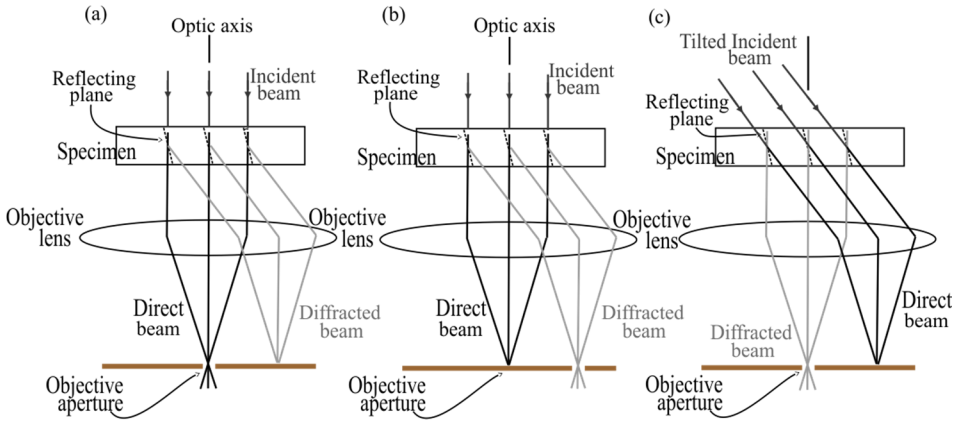

Figure 3.4-1. Ray diagram showing the position of the OA of (a) BF operation, (b) 'dirty' DF operation and (c) centered DF operation. Figure adapted from [145].

3.4.1.3. **Selected area electron diffraction (SAED)**

Electron diffraction is a basic tool for obtaining important quantitative structural and crystallographic information about crystalline materials. The diffraction pattern is formed in the back focal plane of objective lens and consists of the direct beam and all the diffracted beams. The direct beam is located in the center of the pattern and is the most intense beam since most of electrons appear to travel straight through the specimen. This technique is known as SAED since a small aperture (SAD aperture) is inserted in the image plane of objective lens to delimit the area from which the diffraction pattern is recorded.

The diffraction pattern of a crystalline material may consist of: (i) a series of concentric rings in the case of polycrystalline materials or randomly oriented crystals, or (ii) individual spots for a single crystal or when the SAD aperture solely includes an orientation of the crystal.

The separation of the diffracted spots with respect to the direct beam in a SAED pattern can be related to the interplanar lattice spacings d_{hkl} of the crystalline material by using the Bragg's Law and the geometry for electron diffraction. Figure 3.4-2 illustrates the relationship between the direct beam and one of the diffracted beams, where L is the camera length (distance from the sample to the projected image), and r^* is the distance from the diffracted beam to the direct beam. Thus, according to the geometry described in Figure 3.4-2, one can say that:

$$r^*/L = tan2\theta. \tag{3.4-1}$$

Combining equation (3.4-1) with the Bragg's Law (equation (3.2-23)) and considering that the diffraction angle in electron diffraction is very small (typically $\theta < 1°$, hence $sin\theta \approx \theta$ and $tan2\theta \approx 2\theta$), the interplanary spacings can be calculated as:

$$d_{hkl} = \frac{\lambda \cdot r^*}{L}. \tag{3.4-2}$$

The use of equation (3.4-2) for the analysis of SAED patterns has allowed determining the lattice planes associated with each reflection observed in the experimental diffraction patterns, and therefore, it has allowed the resolution of the crystalline materials and phases present in each sample.

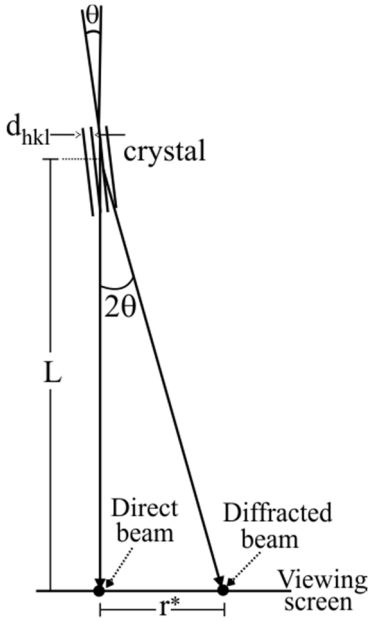

Figure 3.4-2. Geometry for electron diffraction. L is the camera length and r^* is the distance from the diffracted beam to the direct beam. Figure adapted from [143].

3.4.1.4. **High resolution TEM (HRTEM)**

HRTEM images formation is based on the interference between the transmitted beam and two or several diffracted beam. A large OA can be used to limit the number of the diffracted beams which contribute in the HRTEM image, as well as, to restrict the high angle noise and the transfer shift of the contrast transfer function (CTF). Crystalline materials present well defined diffraction angles, and their interference generates a periodic pattern corresponding to the sample atomic structure, which can be imaged under high magnification and a suitable sample orientation. However, HRTEM images cannot be readily interpreted, since they can be affected for thickness variation, orientation and the scattering factor of the specimen. In addition, variations of the focus and lens aberrations alter the contrast. This section is adapted from [143,145,147].

In general, image simulations are needed to interpret the contrast mechanisms and the complicated interference patterns, usually referred to as HRTEM images.

The wave leaving the specimen is modified by the aberrations of the objective lens (mostly spherical aberration), which impose an additional phase factor. This additional factor is the CTF. Hence, the microscope transforms each point of the specimen into some extended regions due to the aberrations. Since each point of the specimen can be different, it is possible to describe it with the specimen function $f(x,y)$ whenever the sample is thin and therefore the changes in z direction are neglected. In the same way, the extended region can be described with the function $g(x,y)$. Another function should be introduced which describes how a point spreads into a disc, the function $h(x,y)$ called blurring or point-spread function. Mathematically, the image formation in HRTEM can be formulated as the convolution of functions $f(x,y)$ and $h(x,y)$:

$$g(\boldsymbol{r}) = \int f(\boldsymbol{r}')h(\boldsymbol{r}-\boldsymbol{r}')d\boldsymbol{r}' = f(\boldsymbol{r}') \otimes h(\boldsymbol{r}-\boldsymbol{r}'). \tag{3.4-3}$$

Working with convolution of functions in real space is not an easier task, hence the reciprocal space is preferred and high resolution images are best understood in terms of Fourier transform. The real space convolution of equation (3.4-3) can be replaced by a simple multiplication in Fourier space, so that:

$$G(\boldsymbol{u}) = F(\boldsymbol{u})\, H(\boldsymbol{u}), \tag{3.4-4}$$

where $\boldsymbol{u}$ is the corresponding vector in the reciprocal space, which is also called spatial frequency, and $G(\boldsymbol{u})$, $F(\boldsymbol{u})$ and $H(\boldsymbol{u})$ are the Fourier transform of $f(\boldsymbol{r})$, $h(\boldsymbol{r})$ and $g(\boldsymbol{r})$.

The function $H(\boldsymbol{u})$ shows how the contrast information is transferred through the microscope, hence it is the CTF. The factors that contribute to the CTF are: the aperture function $A(\boldsymbol{u})$, the envelope function $E(\boldsymbol{u})$ and the aberration function $B(\boldsymbol{u})$:

$$H(\boldsymbol{u}) = A(\boldsymbol{u})\, E(\boldsymbol{u})\, B(\boldsymbol{u}). \tag{3.4-5}$$

The $A(\boldsymbol{u})$ is related to a cut-off spatial frequency higher than a certain value which depends on the radius of the objective aperture. $A(\boldsymbol{u})$ is equal to 1 for electrons which pass through the aperture and 0 otherwise. The $E(\boldsymbol{u})$ acts equal to $A(\boldsymbol{u})$ but it is a property of the lens itself. The $B(\boldsymbol{u})$ is usually expressed as $B(\boldsymbol{u}) = \exp[i\chi(\boldsymbol{u})]$. Because only the imaginary term contributes to the intensity, $B(\boldsymbol{u})$ can be simplified as $B(\boldsymbol{u}) = 2\ sin\ \chi(\boldsymbol{u})$. A new term is then defined, the intensity transfer function $T(\boldsymbol{u})$, which is:

$$T(\boldsymbol{u}) = A(\boldsymbol{u})\ E(\boldsymbol{u})\ 2\ sin\ \chi(\boldsymbol{u}), \tag{3.4-6}$$

depending on the sign of $T(\boldsymbol{u})$, different image contrasts are observable:

- If $T(\boldsymbol{u}) > 0$, the phase contrast is negative and the atoms appear bright against a dark background.
- If $T(\boldsymbol{u}) < 0$, the phase contrast is positive and the atoms appear dark against a bright background.
- If $T(\boldsymbol{u}) = 0$, no contrast is observable.

Including defocus Δf, spherical aberrations C_s and astigmatism and assuming that astigmatism can be properly corrected, it can be shown that $\chi(\boldsymbol{u})$ is:

$$\chi(\boldsymbol{u}) = \pi\ \Delta f\ \lambda\ u^2 + \frac{1}{2}\pi\ C_s\ \lambda^3\ u^4. \tag{3.4-7}$$

In 1949, Scherzer realized that the CTF could be optimized by adjusting the defocus such that it counteracts the effect of spherical aberration. This is known as 'Scherzer defocus' and is formulated as [154]:

$$\Delta f_{Sch} = -\sqrt{\frac{4}{3} C_s \lambda}\,, \tag{3.4-8}$$

at this defocus, the best resolution that can be obtained is known as 'Scherzer resolution' and it can be calculated as:

$$d_{Sch} = \sqrt[4]{\frac{3}{16} C_s \lambda^3}. \quad (3.4\text{-}9)$$

The Scherzer resolution limit becomes especially important in uncorrected TEM. However in microscopes coupled with correctors, this Scherzer defocus does not play a role since in these cases the aberration function is close to cero.

3.4.2. High-angle annular dark field (HAADF) STEM

In HAADF imaging, the specimen is scanned by a convergent electron beam and the incoherently scattered electrons are collected by a geometrically large annular detector, which is located beyond the specimen. A sketch illustrating the technique is displayed in Figure 3.4-3.

The electrons scattered at high angles hit the detector and their total intensity is recorded and displayed as a function of the position of the illuminating probe. The collection semi-angle for the detector is called θ, which is determined by the inner θ_{in} and outer θ_{out} detector angles. The convergence semi-angle of the probe is called α, which is determined by the condenser aperture.

This technique is also referred as Z-contrast, since the intensity of a HAADF image is proportional to the thickness t of the sample and the atomic number of the specimen atoms Z^c, where $1 \leq c \leq 2$. The value of c depends on the screening by the atomic electrons, the detector angles and the sample thickness [156,157]. The vacuum in HAADF images appears dark since the detector only receives a signal when the specimen is present.

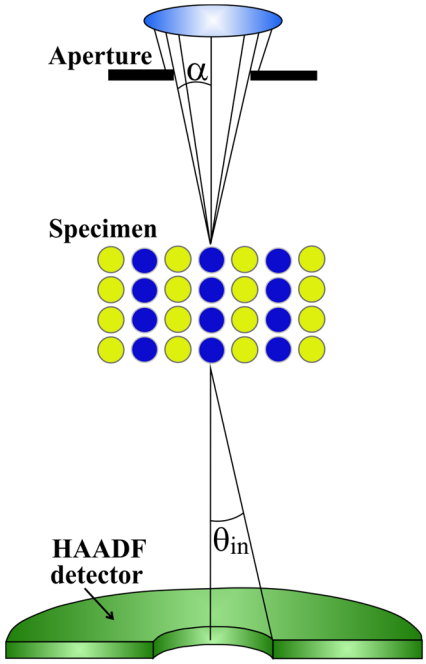

Figure 3.4-3. Schematic representation of a STEM coupled with a HAADF detector. The convergence semi-angle of the probe θ shown. The electrons scattered are collected by the HAADF detector. The inner θ_{in} detector angle of the detector is also represented. Figure adapted from [155].

3.4.3. Scanning electron microscopy (SEM)

There are few similarities between SEM and TEM. Both are types of electron microscopes, give the possibility of analyzing materials up to nanometer scale and share certain features such as the electron gun, condenser lenses and the vacuum system. However, they also present some differences, hence in a SEM: (i) the electrons are accelerated to the energy ranging between 1 keV and 50 keV, (ii) the electron beam is focused by the objective lens to a very fine spot (1 nm-5 nm) and scans the sample surface in a raster pattern, and (iii) electrons belong to the surface, or near the surface, of specimen.

An important consideration in SEM is that specimens must be electrically conductive, at least at the surface. This means that non-conductive materials have to be coated before analysis, being gold, and platinum the most used materials [145].

When electrons penetrate into the sample, the region of interaction between the specimen and the beam is known as *interaction volume*, which extends from less than 100 nm up to approximately 5 µm into the surface. Different signals can be obtained depending on the depth of penetration of electron beam into the material, i.e. auger electrons, SE, BSE, X-ray and CL. They have been mentioned in previous sections and are illustrated in Figure 3.4-4. The size of the interaction volume depends on the acceleration voltage, the size of the electron beam, the atomic number of the material and the specimen's density.

Only the SE and X-ray signals have been used to characterize the samples during the experimental stage of this thesis.

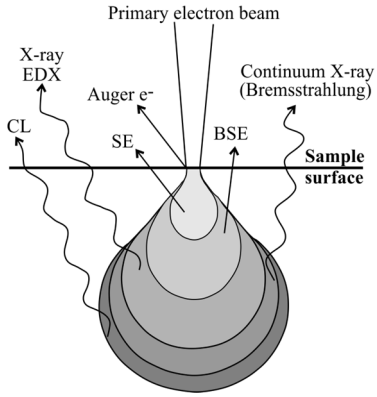

Figure 3.4-4. Electron interaction volume within the specimen. Notice the different regions where Auger electrons, SE, BSE, X-ray and CL come from.

3.4.4. Energy dispersive X-ray (EDX) spectroscopy

EDX also referred to as EDS or EDAX, is an analytical X-ray technique used to identify the elemental composition of materials in individual points, line scans or an imaged area. The EDX method can be coupled with a STEM or a SEM instrument.

The X-rays generated are collected in an energy dispersive detector, which displays the signal as an X-ray spectrum. The intensity (number of X-rays or X-ray count rate) are plotted versus the X-ray energy in the X-ray spectrum. The energies of the characteristic X-rays allow the identification of elements of the sample. This energy can be related to the transition energy between the inner shells of the specimen atoms, which are specific of each element.

The characteristic X-rays lines are named according to the transition between the shell from which the electron 'jumps' and the shell of the vacancy. In this way, if the transition is from the L to the K shell (L-K transition), the X-rays emitted are named as K_α. The X-rays emitted from an M-K transition are named as K_β, or from a M-L transition are named as L_α. More transitions are possible, however, the most probable is the L-K transition (K_α X-rays) since the K and L shells are the most adjacent ones, and therefore, the K_α will always be more intense than the K_β radiation.

3.4.5. Electron tomography (ET)

Real shape, connectivity, location, size, morphology and 3D orientation of many structures cannot be directly derived by conventional (S)TEM techniques. In contrast, ET overcomes this limitation providing 3D reconstructions of objects at nanometer length scales from a series of images acquired [158–160]. The ET technique can be divided in two stages: firstly the 2D image acquisition at several angles (cf. Figure 3.4-5(a)), and secondly the correlation and reconstruction of these images to obtain 3D information (Figure 3.4-5(b)). The typical workflow for an ET experiment is described in Figure 3.4-5(c).

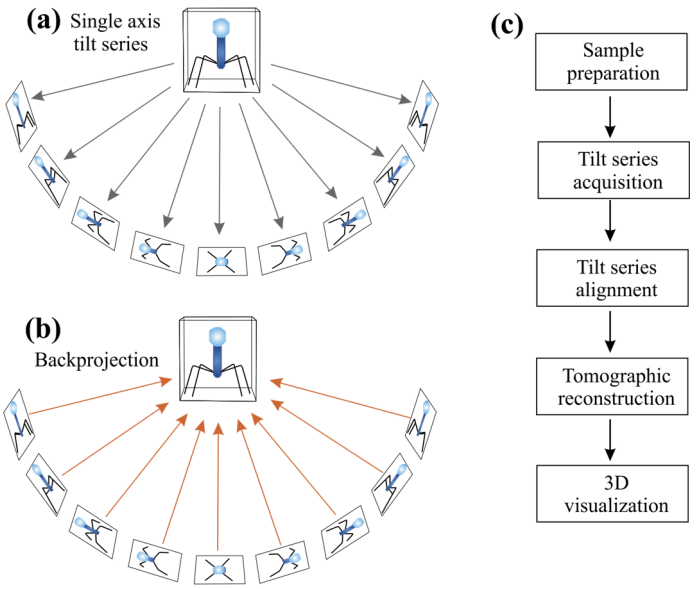

Figure 3.4-5. (a) Projections recorded from a tilt series of a 3D image. (b) backprojections treated to retrieve the 3D volume. (c) Steps involved in an ET experiment. (a) and (b) are adapted from [161].

The acquisition of the tilt series can be carried out by sequential tilting of the specimen around an axis perpendicular to the electron beam (single-axis tomography), or taking a second tilt series of the same area after a 90° in-plane rotation of the specimen (dual-axis tomography) to overcome the missing wedge of data effect (loss of information in the x-y plane) [162]. In this dissertation, the ET technique will be referred considering only the single-axis mode, which is the most commonly used acquisition mode.

These individual projection images are shifted onto a common tilt axis (alignment step) by sequential cross-correlation [163], which can be combined with the least-squares tracking of fiducial markers [164]. This process also requires that the intensity in the images shows, at least, a monotonic measurement of any property of the specimen in each tilting data sets (projection requirement). In this thesis, gold particles have been used providing high-contrast reference points and making easier the alignment.

The mathematical principles of tomographic reconstruction are based on a combination of the Radon transform theory and the projection theorem (also named as the Fourier slice theorem), which states that *the Fourier transform of a 2D projection of a 3D object is a central section of the 3D Fourier transform of the object* [165]. Thus, the 3D Fourier transform of the specimen can be computed by assembling the 2D Fourier transforms of the images under the appropriate angle in the tilt series, which yields the 3D structure of the specimen by an inverse Fourier transform. These approaches are described in detail in the following part.

3.4.5.1. **The Radon transform and Fourier slice theorem**

The Radon transform [166] can convert the real space data in (x, y) coordinates system to its Radon space, which is in (θ, t) coordinates system. From the Radon transform, a projection can be defined as collection of several integrals (cf. Figure 3.4-6). The object in the figure is represented by a 2D function $f(x, y)$ and each line integral by the (θ, t) parameters. The equation of the line integral is:

$$x \cos\theta + y \sin\theta = t. \tag{3.4-10}$$

The function $P\,(\theta, t)$ is called Radon transform of the function $f(x, y)$, the formulation of Radon transform can be represented by transforming the function of $f(x, y)$ through an object to the function which has the parameters θ (tilting angle) and t in Radon space:

$$P_\theta(t) = \int_{(\theta,t)} f(x, y)\ \mathrm{d}s, \tag{3.4-11}$$

using a delta function, and introducing equation (3.4-10) into equation (3.4-11):

$$P_\theta(t) = \int_{-\infty}^{+\infty} \int_{-\infty}^{+\infty} f(x, y)\ \partial\ (x\cos\theta + y\sin\theta - t)\, dx\, dy. \tag{3.4-12}$$

In addition to the Radon transform, the Fourier slice theorem (see [167] for details and demonstration) is also fundamental in tomographic reconstruction. The Fourier slice theorem describes the relationship between the Radon transform and the Fourier transform of a 3D object. In the Fourier slice theorem, the 1D Fourier transform $S_\theta(\omega)$ of a parallel projection $P_\theta(t)$ is equal to a central slice through the 2D Fourier transform $F(u, v)$ of the original object $f(x, y)$ at a tilting angle of θ (described with the u axis). Mathematically, it can be written as:

$$F(u, v) = \int_{-\infty}^{+\infty} \int_{-\infty}^{+\infty} f(x, y) \exp\left[-i2\pi(ux + vy)\right]\ dx\, dy, \tag{3.4-13}$$

$F(u, v)$ is the 2D Fourier transform of an object function $f(x, y)$. The Fourier transform $S_\theta(\omega)$ of a projection $P_\theta(t)$ is therefore:

$$S_\theta(\omega) = \int_{-\infty}^{+\infty} P_\theta(t)\ \exp\left[-i2\pi\omega t\right]\ dt. \tag{3.4-14}$$

According to the Fourier slice theorem, the Fourier transform of a projection is equal to a central slice through the 2D Fourier transform of the object, so it can be written as:

$$S_\theta(\omega) = F(\omega\cos\theta\,, \omega\sin\theta). \tag{3.4-15}$$

This important result is known as the Fourier Slice theorem or central projection theorem and is illustrated in Figure 3.4-6.

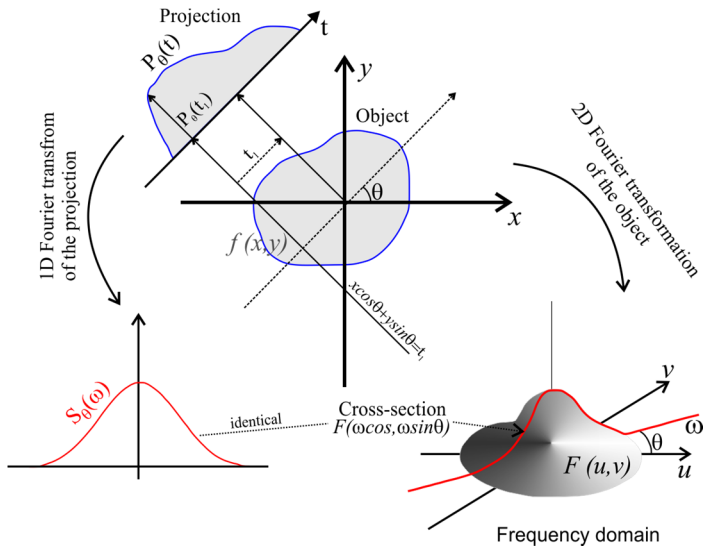

Figure 3.4-6. Graphic representation of Radon transform and Fourier slice theorem statement. Figure adapted from [168,169].

The projections acquired at different tilt angles $(\theta_1, \theta_2, \dots, \theta_n)$ give information about the Fourier transform of the 3D object along central slices. In theory, if enough projections are acquired, the $F(u,v)$ should be known at all points in the frequency domain, and the object function $f(x,y)$ could be recovered by 2D inverse Fourier transforming $F(u,v)$. However, only a finite number of projections and samples per projections are taken, and then $F(u,v)$ is known just on a finite number of points and its transformation into Cartesian coordinates leads to high errors. Hence, some approximations should be considered to improve its performance. So far, the most widely accepted algorithms are the weighted backprojection (WBP) [165], the algebra reconstruction technique (ART) [170], the simultaneous algebra reconstruction technique (SART) [171], and the simultaneous iterative reconstruction technique (SIRT) [172]. In the following, only the SIRT mechanism will be explained since this is the one selected for improving the acquired data of the experimental series. Finally, when the reconstruction is finished, it is usually exported to a visualization package for 3D rendering or extraction of 2D cross-sectional views. In this thesis, Avizo Fire version 8.1.0 [173] (from FEI Visualization Sciences Group) has been used.

Simultaneous iterative reconstruction technique (SIRT)

The original projections are iteratively compared with linear re-projections of a reconstruction to remove artefacts from the final representation of the object. The comparison operation must be repeated iteratively until a 'best' solution is reached. However, an excessive number of iterations could result in deficient reconstructions, since the process tends to converge to a local minimum after 20–30 iterations before the reconstruction quality degrades with more refinement steps. SIRT is now a common reconstruction technique and is known to succeed reducing reconstruction artefacts for sets of projections and improving the signal-to-noise ratio of the reconstructions, but they are still subject to missing wedge artefacts. It requires a relatively large number of projections with a small missing wedge tilt steps (usually angles of ±70° and tilt steps of 1°–2° are used) to produce the best results. Recently, a hybrid method combining WBP and SIRT, called W-SIRT, was shown as a new improvement [174].

3.4.6. Organic molecular beam deposition (OMBD)

The samples used within this work have been prepared by OMBD. An example of a typical chamber used for the deposition process is depicted in Figure 3.4-7. The chamber is evacuated to a base pressure of about 10^{-9} mbar (UHV) to avoid any contamination and oxidation of the source materials and deposited films. The source of the materials is evaporated from effusion cells at temperatures ranging between 373 K and 723 K, depending on the organic material utilized. For the chamber utilized in the growth of the samples of this dissertation, Knudsen cells heated by means of a heating coil were employed. The geometry of the effusion cells allows the condensation of the vapored organic molecules on the substrate of interest. To control the flux of each organic molecular beam, the effusion cells are provided with mechanical shutters. In addition, a shutter (main shutter) in front of the sample controls the growth of the organic film. The deposition rate is monitored by a quartz-crystal microbalance (QCM).

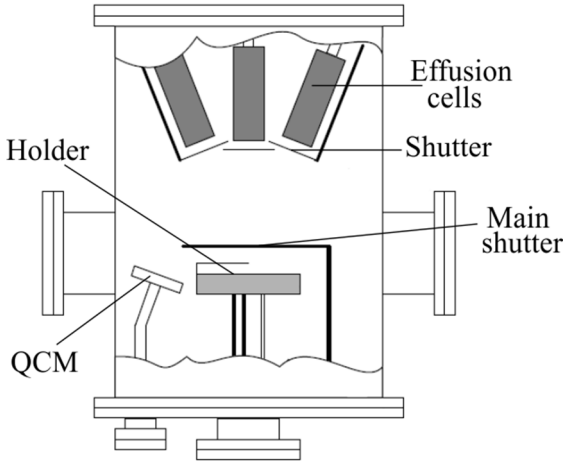

Figure 3.4-7. Sketch of the mains parts of an OMBD chamber. Figure adapted from [175].

4. Microstructural characterization of PFP grown on graphene

‘If you want something you have never had, you must be willing to do something you have never done’ — Thomas Jefferson

4.1. Introduction

This study has been performed as a collaborative research among three different groups of the Philipps-Universität Marburg, i.e. the Structure and Technology Research Laboratory Group (group leader Prof. Dr. Kerstin Volz), the Molecular Solid State Physics Group (group leader Prof. Dr. Gregor Witte) and the Complex Systems Group (group leader Prof. Dr. Bruno Eckhardt). The Molecular Solid State Physics Group carried out the growth of the samples and the XRD, STM and AFM characterizations, whereas the Complex Systems Group performed the theoretical calculations. The main focus of this work has been the (S)TEM characterization, which has been performed by the author of this thesis in the Structure and Technology Research Laboratory Group. The structure of this chapter is as follows: firstly, the importance of the graphene substrate (cf. section 4.1.1), the relevance of the organic compound PFP grown on this substrate (cf. section 4.1.2), as well as the motivation of this study (cf. section 4.2) are explained. Subsequently, the experimental conditions and some important remarks are discussed (cf. section 4.3). Finally, the results are presented divided in three different parts: (i) overview of the morphology of the sample (cf. section 4.4), (ii) determination of the lateral orientation of the PFP molecules relative to the graphene substrate by a combination of TEM and other techniques (cf. section 4.5), and (iii) study of the faceting observed in the growth of PFP in island shapes by TEM and ET (cf. section 4.6). The general conclusions obtained in this chapter are presented in section 4.7.

4.1.1. Current interest in graphene

Graphene is the name given to a flat monolayer of carbon atoms tightly packed into a 2D honeycomb lattice made of sp^2 hybridized carbon. Graphene is probably the best known of all 2D materials, with properties that make it attractive for a whole range of mechanical [176–178], optical [179,180] and electronical [181,182] applications. In particular, its optical transparency together with its large charge carrier mobility and low sheet resistance [183–185] have enabled that it can be directly integrated into optoelectronic devices [186–189]. In this sense, efficient thin films and flexible devices based on graphene have been achieved [190–193]. For instance,

graphene is a promising candidate to replace high-cost tin-doped indium oxide (ITO) [185,194,195] as standard transparent cathode. For such potential applications, one of the important factors that determines the performance of organic devices is the interface structure between the organic molecules and the electrode material [196–198]. Therefore, understanding and knowing the configuration of organic molecules on graphene is one of the key-research for the development of graphene-based organic devices [196–198].

4.1.2. Current interest in PFP deposited on graphene

As it has already been mentioned in section 2.4, weak substrate-adsorbate interactions lead to upright (HB) geometries of the adsorbate. In contrast, strong interactions favor lying down (π-stacked) arrangements of the organic film. Although the HB arrangement (characterized by non π-π overlapping of neighboring molecules) is more common in OSC compounds, it is not a priori the most favorable packing for transport. As a result, many efforts have been devoted to achieve the π-stacked structure. Surprisingly, PAH molecules have been found to adopt frequently a lying down orientation deposited on graphene/graphite [199–202] due to π-π interactions between the molecules and graphene/graphite surfaces. This is the case of PFP grown on graphene: while PFP forms a HB arrangement in bulk crystals and in thin films on oxidized silicon, glass and alkali halides; it adopts a parallel π-stacked geometry on metals and graphene/graphite surfaces, the called '*PS-polymorph*'. Since this configuration of PFP enhances its charge transport properties, a detailed understanding of the morphology and alignment of the PFP molecules on the graphene substrate is prime of interest.

4.2. Motivation

The first target of this chapter deals with the characterization of the morphology and lateral orientation of PFP grown on graphene substrate. While previous experiments of PFP films prepared on graphene and highly oriented pyrolytic graphite (HOPG) substrates have allowed studying the film morphology and resolving the crystal structure of the PS-polymorph [22,23], the exact lateral alignment of PFP molecules deposited on graphene/graphite substrates has not yet been resolved. In this regard, Salzmann et al. suggested that the long axis of PFP molecules is aligned along the two-high symmetry directions of graphene lattice, i.e. ⟨1 1 $\bar{2}$ 0⟩ (also referred to as the '*zig-zag*' directions) and ⟨1 0 $\bar{1}$ 0⟩ (also referred to as the '*armchair*' directions). However, that work could not determine if the PFP molecules are: (i) equivalently aligned along these high symmetry directions or (ii) solely along one of both.

These high symmetry directions are crystallographically and energetically highly different. The alignment of the long axis of PFP molecules along the zig-zag direction vs the armchair direction can be seen in Figure 4.2-1. As illustrated in the case of zig-zag alignment (Figure 4.2-1(a)), the centers of the PFP phenyl units are positioned on top of a carbon atom of the graphene lattice. This stacking cannot be achieved along the, obviously different, armchair direction (Figure 4.2-1(b)), where the individual phenyl units have to be placed inequivalently relative to the substrate lattice. Within this thesis, the issue concerning the alignment of PFP molecules along the high symmetry graphene directions is clarified (cf. section 4.5).

The second aim of this work is to study the morphology of the PFP film on graphene. In a first stage, a characteristic growth of PFP in islands with some faceting is found. In general, side facets appear on many growing crystals because some surfaces grow much more slowly than others do. Therefore, it is required a detailed study that can provide information on the crystal habitus that follows PFP deposited on graphene substrate. Section 4.6 shows this study, which gains insight on these island facets and analyze the planes that are the potential candidates for forming the faceting.

The determination of the relative alignment of PFP molecules on graphene substrate together with the deep knowledge of the growth habitus of PFP film in island shapes will delve into the understanding of the epitaxial growth of the OSC PFP on a graphene lattice. Considering the novelty and technological relevance of a substrate such as graphene, this piece of information is rather relevant for future device applications since: (i) the efficiency of transport in OSCs is intimately related to the relative positions of the interacting molecules, and (ii) any faceting effect cannot be ignored since the faceting phenomena could affect the physical properties of materials.

Finally, the contribution of this study to the science framework has been fulfilled with the publication of a paper in the journal *Crystal Growth and Design*, which includes the majority of the content presented in this chapter just excluding the electron tomography analysis (cf. reference [32]).

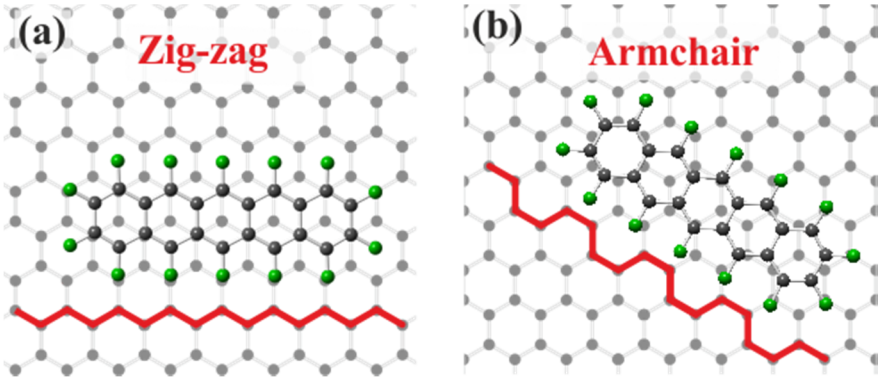

Figure 4.2-1. Long axis of PFP molecule oriented (a) along zig-zag direction and (b) armchair direction of a graphene lattice.

4.3. Experimental

The graphene substrate used for (S)TEM analyses is commercially available as graphene-Quantifoil TEM grid from Graphenea S.A. [203]. It consists of a suspended monolayer of graphene (theoretical thickness of 0.345 nm) grown by chemical vapor deposition (CVD) and transferred to gold-coated Quantifoil TEM-grids. The Quantifoil grid substrate exhibits holes with sizes of 2 μm diameter separated by a distance of 4 μm. The graphene layer consists of single-crystalline graphene domains in-plane rotated. The PFP was supplied from Kanto Denka Kogoyo Co. with a purity ≥ 99 %. The PFP is directly grown on the graphene-Quantifoil TEM grid under UHV conditions (base pressure ≤ 5.7×10^{-8} mbar) by OMBD from a resistively heated Knudsen cell at typical deposition rates of 8 Å/min as determined by a QCM. The samples were grown at 330 K onto the graphene TEM grid with a nominal total thickness of approximately 40 nm.

Two samples of PFP on graphene were initially grown for the investigations: in one of them, the substrate was preheated to 570 K for 10 min prior to the organic deposition to clean it. In the other one, the organic deposition was performed without any preheating process. When the first sample (PFP on graphene with preheating process) was investigated in TEM, a different morphology from that previously reported for PFP grown on such substrates was observed [23]. This anomalous growth of PFP on graphene led to the conclusion that the high temperature of the preheating process damaged the substrate. Therefore, that sample was neglected and just the sample without any preheating is considered in the results part of this chapter.

Although this thesis is mainly focused on TEM measurements, other analyses - such as XRD, STM and AFM - were performed in the Molecular Solid State Physics Group in order to obtain complementary information of the samples. Contrary to TEM analysis, these measurements were carried out onto freshly exfoliated graphite single crystal (SC) substrates (purchased in Naturally Graphite, Michigan, USA) instead of graphene substrate. Graphite SC substrates were selected since their surfaces exhibit only one exclusive orientation over the entire surface area.

Furthermore, it has already been evidenced that PFP adopts identical growth on graphene and graphite SC surfaces [22,23]. Notice that *graphite SC* will be alternatively referred to as only *graphite* in the content of this thesis. The XRD and STM measurements were carried out by means of a Bruker D8 Discovery diffractometer (using monochromatized Cu K_α radiation with $\lambda = 1.541$ Å and a LynxEye silicon strip detector) and an Omicron VT-STM XA system (operated under UHV conditions at 110 K and using etched tungsten tips), respectively. The AFM analyses were performed in the Agilent SPM 5500 equipment operated in tapping mode at ambient conditions and room temperature. AFM tips with resonance frequencies of about 325 kHz, radii of 7 nm, and force constants of 40 N/m were used.

SEM images were acquired at the JEOL JIB-4610F scanning electron microscope, implemented in a SEM/focused ion beam dual beam system, at an acceleration voltage of 5 kV. Whereas, conventional BF-TEM images and SAED patterns were recorded at the JEOL JEM-3010 operated at its maximum acceleration voltage, i.e. 300 kV. HAADF-STEM images and ET series were acquired using the JEOL JEM-2200FS operated at its maximum acceleration voltage of 200 kV. For ET investigations, the sample was mounted on a tomography holder (Fischione 2030). Moreover the size of the grid had to be reduced (by means of a simple cutter, leaving a final size of around 1 mm and 3 mm of width and length, respectively) due to the limitations of the tip of the tomography holder. The single-tilt series were acquired in HAADF-STEM mode with tilt angles ranging from -70° to +64° (tilted in the minus/plus direction of the x-axis of the sample holder) in a continuous tilt scheme with increments of 2° (image size 512 pixel x 512 pixel: pixel size 2.93 nm). The software Recorder (version 2.48.1.1) was used for the single-tilt series acquisition in an automated manner. IMOD version 4.7.15 software [204] has been utilized for post-processing. Before tomographic reconstruction, the tilt series had to be precisely aligned with respect to a common tilt axis, thereby minimizing both blurring of small features and artefacts in the reconstruction. This was achieved by a combination of rough cross-correlation alignment and least squares fitting, but in addition, fiducial gold markers (BBI solutions, Gold EM.GC15/4) have been used to reach an accurate and robust cross-correlation. Typically 5-30 markers with size of 15 nm (well

distributed over the imaged area) were tracked throughout the tilt series. In the last step, the reconstruction was obtained by alignments with SIRT algorithm using 20 iterations as optimum value. The visualization of the reconstructed volume was performed using Avizo Fire version 8.1.0 [173] (from FEI Visualization Sciences Group) by Dr. Katharina I. Gries (AG Volz, Philipps-Universität Marburg).

4.4. Morphology of the sample

Firstly, an overview SEM image shows a global idea about the morphology of the sample. As can be seen in Figure 4.4-1, the PFP deposited on graphene exhibits a characteristic growth in island shapes which has not been observed before by PFP on other substrates. The holes mentioned in the experimental section 4.3 are also clearly visible here enclosed by a white dotted circle. The density of the islands is around $8.5x10^{-1}$ N/μm^2 (where N is the number of islands), while the diameter size of them is around (0.5-2) μm. After the morphology of the sample, the epitaxial relationship (relative orientation) between PFP molecules and the underlying graphene substrate (cf. section 4.5) are discussed. Next the analysis of the characteristic growth in island shapes by TEM characterization and ET are presented (cf. section 4.6).

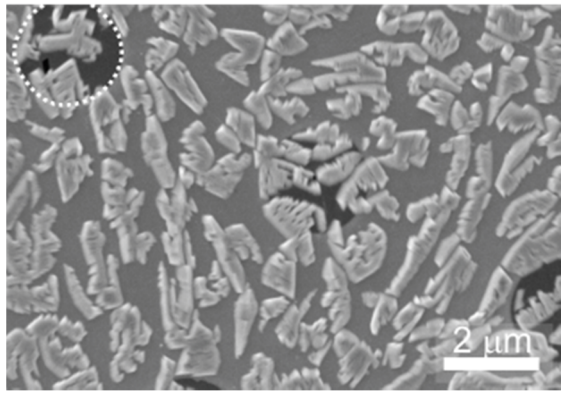

Figure 4.4-1. Morphology overview of PFP film deposited on graphene by SEM analysis.

4.5. Epitaxial relation between PFP and graphene substrate

4.5.1. TEM characterization

The aim of this section is the determination of the rotational alignment of the PFP molecules in the multilayer crystalline films with respect to the graphene substrate via (S)TEM techniques. Therefore, electron diffraction experiments play an important role, since they give information on crystal structures and orientations. The distances between the diffracted reflections and the (0 0 0) reflection in the SAED pattern are measured (r^*), and introduced in equation (3.4-2). From that, the interplanar lattice spacing (d_{hkl}) of each reflection is calculated and compared to the one reported in the literature for the PS-polymorph [22]. The sample is studied in a plan-view orientation with the electron beam directed perpendicular to the substrate surface, consequently, such diffraction experiments allow recording the orientation of PFP and graphene simultaneously in the same micrograph. Note that the sample is initially analyzed at **cooling conditions** (T ≈ 89 K) to minimize the damage caused by electron beam irradiation. This experimental procedure may influence the results, a fact that will be discussed in the development of this chapter (section 4.5.2.4).

Figure 4.5-1(upper) displays two diffraction patterns of the sample. The black dotted circle (lower panel) represents the size and position of the SAD aperture used to record the SAED patterns. The reciprocal lattice spacing distances r^* of the reflections found in these diffraction patterns are measured and, from that, the d_{hkl} values are calculated. The geometry of the experimental SAED patterns, as well as the respective interplanar spacings d_{hkl} obtained, are compared to those determined for graphene and PFP by using the simulation software for electron microscopy JEMS [112]. This comparison allows assigning reflections originated by graphene and PFP in the experimental SAED pattern (cf. pink and blue circles for graphene and PFP, respectively, in Figure 4.5-1). For graphene, the diffraction pattern has been simulated through a graphite structure in [0 0 0 1] zone axis (Z.A.) [205].

The graphene reflections that appear in the experimental SAED patterns belong to the 1 1 $\bar{2}$ 0 family. The 6-fold symmetry of the graphene lattice causes that the six visible reflections are equivalent, and therefore, they cannot be directly distinguished by the current diffraction experiments. In case of PFP, as it was above mentioned (cf. section 4.1.2), Salzmann et al. [22] determined the unit cell parameters and full structure solution of the PFP PS-polymorph by combining GIXD and theoretical structure modeling. This PS-polymorph is the one expected on graphene/graphite structures in the multilayer regime. Based on these results, the PFP crystal has been simulated by JEMS [112] as a triclinic structure described by unit cell parameters of **a** = 15.13 Å, **b** = 8.94 Å, **c** = 6.51 Å, α = 78.56°, β = 108.14° and γ = 92.44°. This PFP PS-polymorph has been compared to the experimental data.

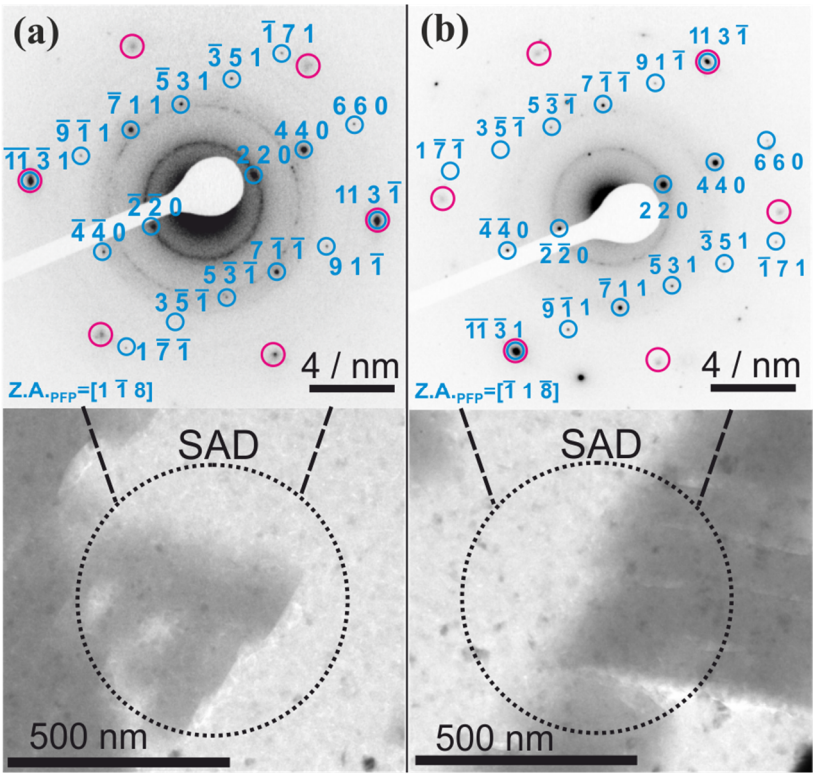

Figure 4.5-1. (a) and (b) SAED patterns with their corresponding BF-TEM image. Upper panel: SAED patterns; blue circles represent the reflections of PFP whereas pink circles belong to the 1 1 $\bar{2}$ 0 family of reflections for graphene. Lower panel: BF-TEM images, where the black dotted circle points out the size and position of the SAD aperture used to create the corresponding SAED pattern. These micrographs were taken at cooling conditions (T ≈ 89 K).

The best fit between the experimental SAED patterns and the simulated model is obtained for a zone axis perpendicular to the (0 0 1) plane of the PFP crystal. This corresponds to the [1 $\bar{1}$ 8] viewing direction in this triclinic system, which agrees with the determined orientation in the previous XRD study carried out by Salzmann et al. [22]. Note that the signal recorded from the graphene layer is very weak (spots are diffuse) due to the low thickness of the graphene layer in comparison to the PFP layer. Furthermore, some rings originated from polycrystalline material are also visible in the SAED patterns. They belong to the small particles (ranging between 10 nm-30 nm) observed in the BF-TEM pictures (cf. Figure 4.5-1, lower panel). Their measured interplanar distances match with the (1 1 1), (2 2 0), (3 1 1), and (3 3 1) planes of cubic ice at 100 K [206], indicating that some residual water was frozen during the cooling process of the sample.

As far as it has been afore-mentioned, the interplanar lattice spacings d_{hkl} of reflections exhibited by the SAED patterns have been measured and compared to the values obtained for the PFP PS-polymorph by Salzmann et al. from XRD analysis [22]. This comparison is displayed in Table 4.5-1. Both measurements deviate only few Angstroms, confirming the good concordance between the lattice spacing values calculated from experimental SAED patterns and the ones determined via XRD for the PFP PS-polymorph. The uncertainties in the measurements of experimental SAED patterns have been estimated using at least 20 diffraction patterns. Once, the SAED patterns have been indexed and contrasted with previous results, they are analyzed in detail revealing an important outcome of this study: the overlapping of two of the 1 1 $\bar{2}$ 0 graphene reflections and the 11 3 $\bar{1}$ and $\overline{11}$ $\bar{3}$ 1 PFP reflections (encircled concentrically in pink and blue in Figure 4.5-1, respectively) when cooling conditions are used. The coincidence of these two reflections allows finding the relative orientation between graphene and PFP.

h k l Reflections	**Experimental SAED patterns, d_{hkl} (Å)**	**PFP PS-polymorph [22], d_{hkl} (Å)**
2 2 0	3.74 ± 0.06	3.78
4 4 0	1.87 ± 0.03	1.89
6 6 0	1.25 ± 0.02	1.26
$\bar{1}\bar{1}$ $\bar{3}$ 1	1.22 ± 0.02	1.23
$\bar{9}$ $\bar{1}$ 1	1.62 ± 0.03	1.64
$\bar{7}$ 1 1	2.09 ± 0.03	2.12
$\bar{5}$ 3 1	2.13 ± 0.03	2.17
$\bar{3}$ 5 1	1.68 ± 0.03	1.71
$\bar{1}$ 7 1	1.27 ± 0.02	1.28

Table 4.5-1. Lattice spacing d_{hkl} comparison of reflections collected in experimental SAED patterns and those reported for the PFP PS-polymorph by Salzmann et al. [22].

The rotational alignment of the PFP molecules with respect to the graphene substrate is deduced in this way:

The overlapping between two of the $1\ 1\ \bar{2}\ 0_{graphene}$ and the $11\ 3\ \bar{1}_{PFP}$ and $\overline{11}\ \bar{3}\ 1_{PFP}$ reflections indicates that one of the $\{11\ 3\ \bar{1}\}_{PFP}$ planes (for instance the $(11\ 3\ \bar{1})_{PFP}$ plane) is parallel to one of the $\{1\ 1\ \bar{2}\ 0\}_{graphene}$ planes (for instance the $(1\ 1\ \bar{2}\ 0)$ plane) in real space (observe that the width of these $11\ 3\ \bar{1}_{PFP}$ reflections leave an uncertainty of around ± 1°). This concept is transferred to a sketch where a layer of PFP molecules of the PFP PS-polymorph is superimposed on a layer of graphite (graphene). The crystal structure visualization software Mercury [207] is used to simulate the PFP and graphene.

The PFP molecules are rotated on the graphene lattice until the $(11\ 3\ \bar{1})_{PFP}$ plane lies parallel to the $(1\ 1\ \bar{2}\ 0)_{graphene}$ plane. Then, the long molecular axis of PFP results aligned nearly parallel to the high-symmetry zig-zag directions of the graphene lattice. This is summarized in Figure 4.5-2, where the graphene layer in [0 0 0 1] orientation and PFP in $[1\ \bar{1}\ 8]$ arrangement are plotted together. Additionally, the two different high-symmetry directions of graphene (zig-zag and armchair) are also marked for clarification. As visible, when the $(11\ 3\ \bar{1})_{PFP}$ plane (marked as blue line) is parallel to the $(1\ 1\ \bar{2}\ 0)_{graphene}$ plane (marked as pink line), the plane parallel to the **long**

molecular axis of PFP[I] (marked as orange line) **is aligned almost parallel** to the **graphene zig-zag directions** with an offset of ca. +1.5°[(II)]. Notice that the blue arrow of Figure 4.5-2 represents direction which is oriented normal to the $(11\ 3\ \bar{1})_{PFP}$ plane ($[n(11\ 3\ \bar{1})]$), which is in turn parallel to the $\langle 1\ 1\ \bar{2}\ 0\rangle_{graphene}$ direction marked by the pink arrow.

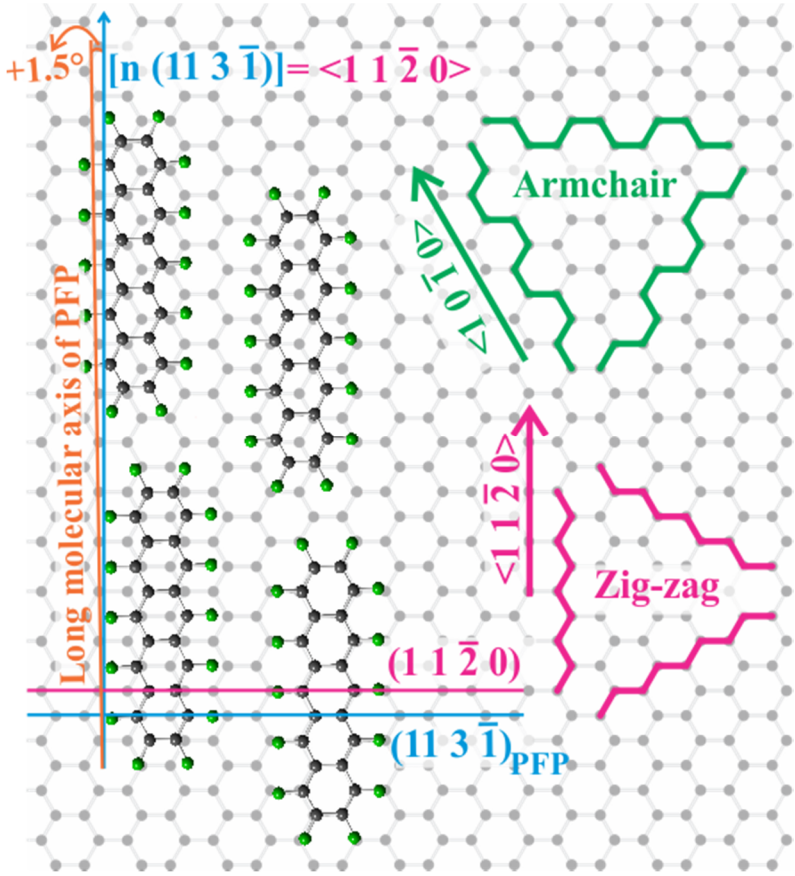

Figure 4.5-2. Sketch that shows the rotational alignment of the PFP molecules (in the multilayer films) with respect to the graphene lattice, according to the measurements performed by TEM tools at liquid nitrogen temperatures. The graphene zig-zag and armchair directions have been marked in pink and green, respectively.

[I] The plane denoted by an orange line in Figure 4.5-2 is parallel to the long molecular axis of PFP and perpendicular to the $(0\ 0\ 1)_{PFP}$ plane.

[II] **Criterion of the sign**: The offset angle is positive if the in-plane rotation with respect to the $\langle 1\ 1\ \bar{2}\ 0\rangle$ zig-zag direction marked by a pink arrow in Figure 4.5-2 is anticlockwise (the zig-zag direction is considered as the origin).

This study shows that the long axis of PFP molecules is aligned nearly parallel to the graphene zig-zag directions. In this way, this outcome allows resolving the so far remaining question whether the PFP molecules are equivalently aligned along the armchair or zig-zag directions of graphene, or solely along one of both.

4.5.2. Additional results obtained by other methods

Although TEM gives important data about PFP in the multilayer film, some other techniques have also been used to gain information on substrate−film epitaxy and compare their outcomes to TEM analyses. They are: (i) XRD which also applies on the multilayer regime, (ii) STM which gives information on the monolayer of PFP, and (iii) MM calculations which provide theoretical information on the first monolayers and multilayers of PFP. Graphite SC is the substrate utilized for experimental XRD and STM analyses.

Since the main focus of this thesis is concentrated on the TEM characterization, just a brief overview of the results achieved by these other methods will be described in the following subsections. In this regard, the publication wthat includes this work [32] offers more detailed information and exhaustive description of these additional results.

4.5.2.1. X-ray diffraction (XRD)

XRD scans (2θ and φ scans) have been performed on a PFP thin film grown on graphite SC at room temperature. The 2θ scans have been carried out in Bragg-Brentano geometry, while rotational scans (φ scans) have been conducted on lattice planes which are not oriented parallel to the sample surface.

In the 2θ XRD scans (cf. Figure 4.5-3(a)), signals for the graphite substrate ($0\ 0\ 0\ 2_{graphite}$), the glue used to mount the sample, the X-ray radiation (copper Cu and tungsten W) and the PFP ($(0\ 0\ 2)_{PFP}$ whose 2θ is equal to 29.2°) are visible. The signal detected for PFP, which corresponds to a lattice spacing of 3.06 Å, indicates that PFP exhibits the (0 0 1) orientation normal to the substrate surface. This orientation agrees with the one obtained by TEM in this thesis as well as Salzman's studies [22].

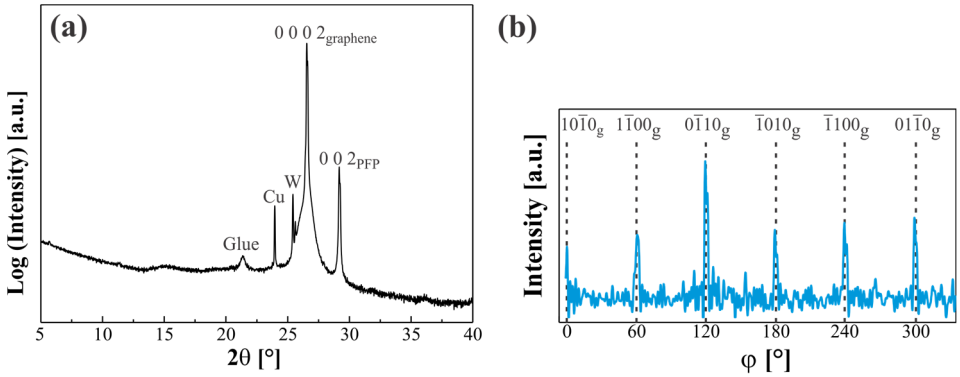

Figure 4.5-3. (a) 2θ XRD scans of a PFP film grown on graphite SC. (b) rotational φ XRD scans of the diffraction peak 2 $\bar{2}$ 0 of PFP (in blue) compared to the signals of graphite zig-zag directions (indicated by the dashed lines and the subscript 'g')[III]. The sample has been tilted by 72° for this analysis.

Further information about the lateral orientation of the PFP molecules relative to the graphite lattice has been obtained in the following way:

(i) First, rotational φ scans have been performed using PFP lattice planes which are not oriented parallel to the substrate plane. The selected planes are: $(\bar{1}\ 1\ \bar{1})_{PFP}$, $(1\ \bar{1}\ \bar{1})_{PFP}$, $(6\ 0\ \bar{2})_{PFP}$, $(2\ \bar{2}\ 0)_{PFP}$, $(0\ \bar{1}\ \bar{1})_{PFP}$, $(4\ 3\ \bar{1})_{PFP}$, $(1\ 1\ \bar{1})_{PFP}$ and $(1\ \bar{2}\ 0)_{PFP}$. Discrete signals with a separation of 60° have been observed in the φ scans. The deviation between the signals and the graphite zig-zag direction has been measured. As an example, the rotational φ scan of the $2\ \bar{2}\ 0_{PFP}$ diffraction peak is shown in Figure 4.5-3(b). Hence, the position of the signals for PFP (in blue) is compared to the position of the graphene zig-zag direction (dashed lines).

(ii) Second, the relative orientation of the PFP molecules with respect to: the intersection line of the selected lattice planes and the $(0\ 0\ 1)_{PFP}$ plane, has been measured. Using the example of the $(2\ \bar{2}\ 0)_{PFP}$ plane, the relative orientation measured is: that between the long molecular axis of the PFP and the intersection line of the $(2\ \bar{2}\ 0)_{PFP}$ and $(0\ 0\ 1)_{PFP}$ planes.

[III] Notice that the $\langle 1\ 1\ \bar{2}\ 0\rangle$ zig-zag directions are running parallel to the intersection line between the $\{1\ 0\ \bar{1}\ 0\}_{graphite}$ and the $(0\ 0\ 0\ 1)_{graphite}$ planes.

The combination of the information from (i) and (ii) allows determining the PFP molecules relative to the graphite lattice in such a way that: the PFP molecules lie with their long molecular axis deviated around -3.7° with respect to the zig-zag direction of graphite (the direction of this rotation is clockwise).

Although both XRD and TEM experiments agree that the long axis of the PFP molecules is rotated slightly with respect to the zig-zag direction of the substrate, they differ in the offset angle (-3.7° vs +1.5°, respectively). This incongruity will be discussed in the subchapter 4.5.2.4 'Deviation between XRD and TEM analyses'.

4.5.2.2. **Scanning tunneling microscopy (STM)**

TEM and XRD analyses reveal that the long molecular axis of PFP molecules is aligned almost parallel to the graphene/graphite zig-zag directions. Both are measurements in the multilayer regime, therefore STM analysis has been performed to obtain information on the first and second monolayer of the PFP film. The aim is to check if this non-perfect alignment of the PFP molecules along the zig-zag direction occurs from the PFP/substrate interface. In this analysis, the identified unit cell parameters for the monolayer are: $\mathbf{a} = 17.8\ \text{Å} \pm 0.5\ \text{Å}$ and $\mathbf{b} = 8.7\ \text{Å} \pm 0.4\ \text{Å}$, enclosing an angle of $\theta = 63° \pm 2°$. The study of the first monolayer shows that the long molecular axis of the PFP molecules is aligned along the $\langle 1\ 1\ \bar{2}\ 0 \rangle$-substrate zig-zag direction[IV] (cf. visualization in Figure 4.5-4(a)) with a deviation of $(4 \pm 3)°$. In addition, a second layer of PFP is deposited to check if the first monolayer acts as orientational precursor for the subsequent layers, or if the first monolayer relaxes and transforms into the multilayer structure. The analysis of this second monolayer evidences the first fact mentioned, i.e. the first monolayer acts as orientational precursor for the next layer transferring its molecular orientation (cf. Figure 4.5-4(b)).

[IV] Notice that the $\langle 1\ 1\ \bar{2}\ 0 \rangle$-graphite zig-zag direction has been determined by removing the PFP molecules via increasing the tunneling current from the tip to the PFP monolayer. It has allowed imaging the graphite surface.

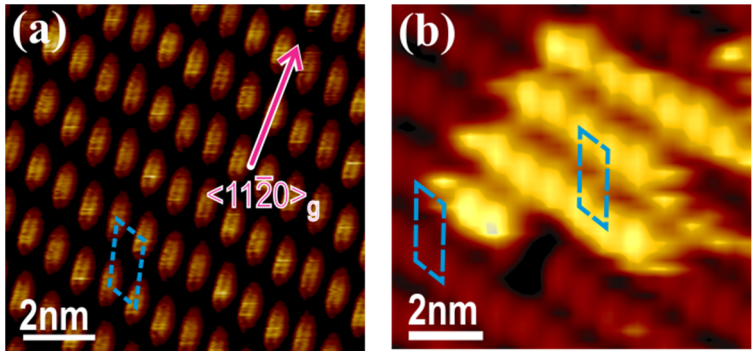

Figure 4.5-4. STM analysis. (a) First monolayer of PFP film. The dashed blue rhomboid describes the PFP unit cell, while the pink arrow indicates the zig-zag direction of the substrate. (b) Deposition of a second PFP monolayer on the first one. The dashed blue left and right rhomboids are the unit cells of the first and second monolayer, respectively.

4.5.2.3. Molecular mechanics (MM) calculations

MM calculations have been applied to gain insight on the lateral position of the PFP molecules with respect to the graphene/graphite lattice. The calculations have been carried out by the TINKER software package version 7.1.3 [208] and they complement the information received by the experimental data (TEM, XRD and STM).

Firstly, the potential energy of an adsorbed PFP molecule is determined on a grid of 40×64 points in the 2.46×4.27 Å^2 rectangular area. The position of the PFP molecule is fixed in these points and the rotation around the center of the molecules is optimized for every point. The most stable configuration results with the centers of the PFP phenyl units situated on top of a carbon atom in the graphite lattice (cf. Figure 4.5-5(a)). Afterward, the angle between the long molecular axis of PFP and the graphene zig-zag direction is varied from 0° to 360° (with steps of 1º in between). The potential energy is calculated for all rotation angles in three cases: an isolated adsorbed molecule, a monolayer film and multilayer regime. In case of the adsorption of just one molecule, the minimum energy is found at angles of φ = 0°, 60°, 120°, 180°, 240° and 300°. These angles correspond to the exact substrate zig-zag directions (cf. Figure 4.5-5(b))[V]. For the first monolayer of PFP, the most energetically favorable

[V] Note that the energetic minima in Figure 4.5 5(b) are rather broad instead of sharp peaks since small rotations of single molecules from the ideal alignment along the zig-zag direction are energetically not expensive.

configuration appears for the long axis of PFP molecules lying parallel to the graphene zig-zag direction with a small deviation of +2.3°. This result is in line with the STM experiments (recall 4 ± 3°). Additionally, two more configurations appear as energetically favorable with offsets of +9° and -4.1°. This fact can be attributed to the interaction between the lattice structures of PFP and graphene (cf. Figure 4.5-5(c)). Finally in the case of the multilayer structure of PFP, a bottom slice of the PS-polymorph is selected for the theoretical calculations. The energetic minima are found for an orientation approximately along the graphene zig-zag direction with three offset peaks at -4.5°, +2.4° and +10° (cf. Figure 4.5-5(d)). In particular, the higher offset peak at -4.5° is in agreement with the experimental XRD data (recall -3.7°).

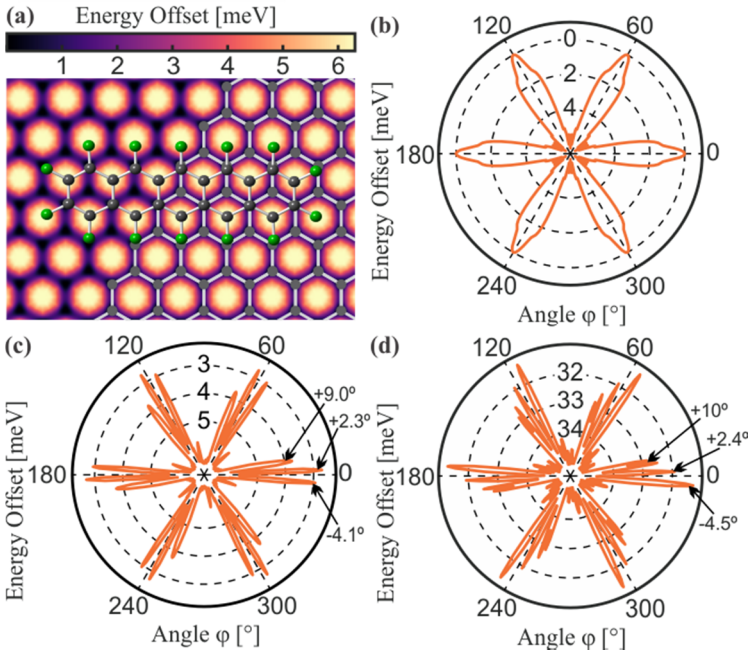

Figure 4.5-5. MM calculations. (a) 2D map of the adsorption energy dependence of a PFP molecule on the graphene lattice. Analyses of the minimum potential energy of (b) a single PFP molecule, (c) a PFP monolayer and (d) multilayers of PFP. Notice the 'inverted' energy scale used to show more clearly angular positions of energetic minima.

In summary, the MM calculations studies determine that only isolated PFP molecules are perfectly aligned along the graphene/graphite zig-zag directions. For the monolayer and multilayer films, the PFP long molecular axis is slightly rotated, which is in line with the outcomes observed by XRD, STM and TEM measurements.

4.5.2.4. **Deviation between XRD and TEM analyses**

XRD and TEM investigations (both measurements give information on the multilayer regime) lead to the same outcome: the long axis of PFP molecules is non-perfectly aligned with respect to the graphene/graphite zig-zag direction. However, there is still a discrepancy between both methods, i.e. the determined offset angle between the long molecular axis of PFP and the graphene/graphite zig-zag direction. TEM and XRD measurements have derived an offset angle of +1.5° and -3.7°, respectively. This discrepancy is attributed to the different temperatures used for both experiments, since lattice parameter variations as a function of low temperatures were previously manifested by similar materials [108,209–212]. Thereby, complementary TEM experiments are also conducted at **room temperatures** (≈293 K).

A SAED pattern together with its respective BF-TEM micrograph (indicating the area selected for the SAED pattern) acquired at room temperature are presented in Figure 4.5-6.

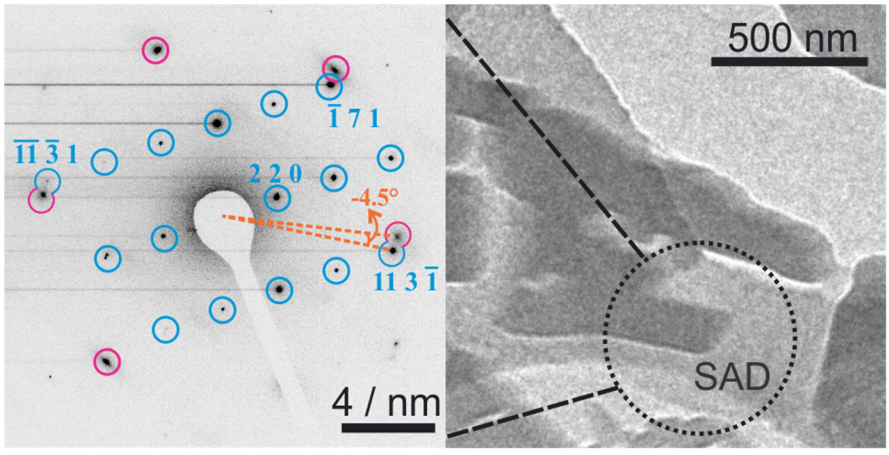

Figure 4.5-6. TEM micrographs recorded at **room temperature**. Left: SAED pattern where pink and blue circles represent graphene and PFP reflections, respectively. As displayed, the 11 3 $\bar{1}_{PFP}$ reflections are rotated by -4.5° clockwise relative to two of the 1 1 $\bar{2}$ $0_{graphene}$ reflections. Right: BF-TEM picture where the dotted black circle marks the size of the SAD aperture used to collect the SAED pattern.

As can be seen, the family of $11\,3\,\bar{1}_{PFP}$ reflections does not overlap with the closest $1\,1\,\bar{2}\,0_{graphene}$ reflections, instead they enclose an angle of -4.5°[VI] with respect to the center of the diffraction pattern. This fact is in contrast to that observed by the SAED patterns recorded at cooling conditions (cf. Figure 4.5-1).

Hence, the rotation of the long axis of PFP molecules and the graphene zig-zag direction at room temperature is deduced representing the data from the SAED pattern at room temperature in a sketch, which is shown in Figure 4.5-7. A similar procedure to the one presented in Figure 4.5-2 is followed for the deduction. The findings of Figure 4.5-6 are taken into account to correlate the $(11\,3\,\bar{1})_{PFP}$ plane with the $(1\,1\,\bar{2}\,0)_{graphene}$ plane. Thus, the four PFP molecules in Figure 4.5-7 are rotated in such a way that the $(11\,3\,\bar{1})_{PFP}$ plane (marked as blue line) and the $(1\,1\,\bar{2}\,0)_{graphene}$ (marked as pink line) describe an angle of -4.5° clockwise. Therefore, the normal direction to the $(11\,3\,\bar{1})_{PFP}$ plane ($[n(11\,3\,\bar{1})_{PFP}]$, marked as a blue arrow) also exhibits a deviation of -4.5° relative to the $\langle 1\,1\,\bar{2}\,0\rangle$ zig-zag direction (marked as a pink arrow). Taking into account that the long molecular axis of the PFP (marked by the orange line) presents an offset of -1.5° (clockwise if the graphite $\langle 1\,1\,\bar{2}\,0\rangle$ zig-zag direction is considered as the origin) with respect to the $[n(11\,3\,\bar{1})_{PFP}]$ direction (cf. section 4.5.1, Figure 4.5-2), the offset between the long axis of the PFP molecules and the graphene zig-zag direction is therefore: -3° (-4.5°-(-1.5°) = -3°, cf. Figure 4.5-7).

Thus, TEM and XRD experiments performed at room temperatures lead to equivalent results. Both analyses display a similar offset between the PFP long molecular axis and the zig-zag direction, i.e. values of -3° and -3.7° are found for TEM and XRD measurements, respectively; solving in this way the issue about the discrepancy between TEM and XRD methods.

[VI] The sign of -4.5° is negative due the criterion stated in footnote II, section 4.5.1. As shown in Figure 4.5-6, the shift of the $11\,3\,\bar{1}_{PFP}$ reflections around the $1\,1\,\bar{2}\,0_{graphene}$ reflections is clockwise (offset angle negative).

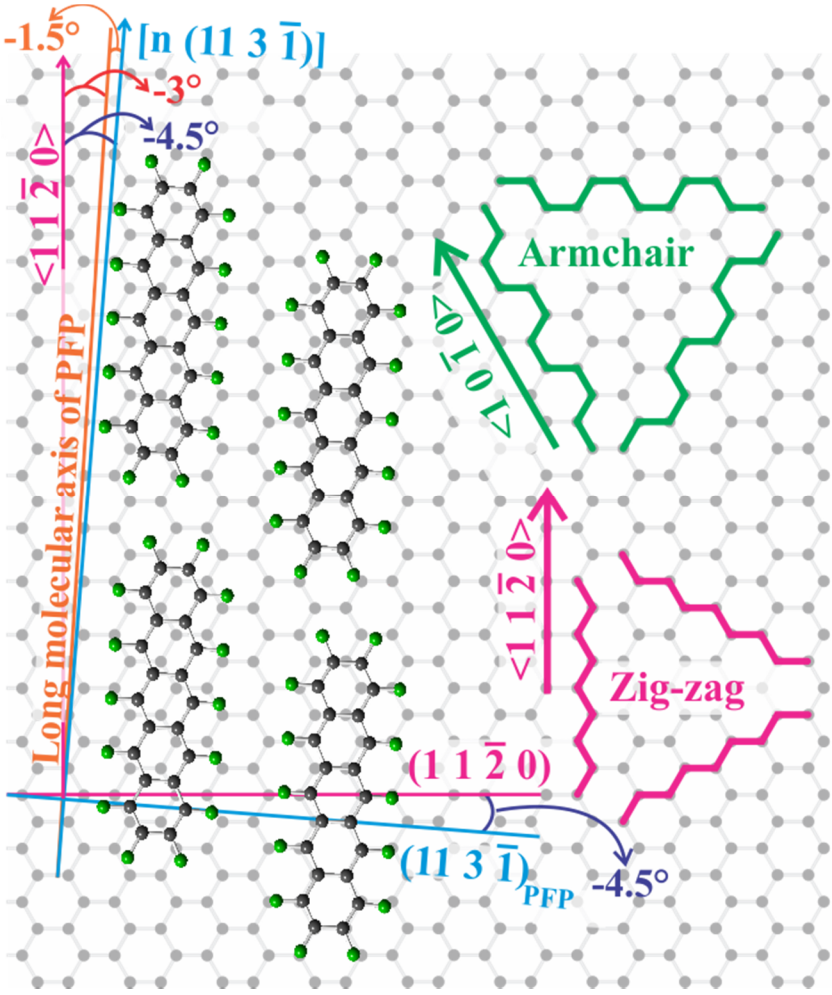

Figure 4.5-7. Sketch showing the rotational alignment of the PFP molecules (in the multilayer films) with respect to the graphene lattice, according to the measurements performed by TEM tools at **room temperature**. The graphene zig-zag and armchair directions have been marked in pink and green, respectively. As displayed, when the $(11\ 3\ \bar{1})_{PFP}$ plane (marked in blue) is in-plane rotated by 4.5° relative to the $(1\ 1\ \bar{2}\ 0)_{graphene}$ plane, the long molecular axis of PFP (marked as orange line) exhibits an offset of -3° with respect to the $\langle 1\ 1\ \bar{2}\ 0\rangle_{graphene}$ zig-zag direction.

4.6. Faceting of the PFP islands

The morphology of the sample has been presented in a previous section (cf. section 4.4), hence PFP exhibits a growth in island shapes on graphene substrates. In this section, the morphology of the PFP in islands will be further investigated. Firstly, AFM analysis is shown giving new knowledges of the PFP island morphology. Next, SAED pattern analysis and its correlation with BF-TEM imaging allow deriving some of the possible crystallographic planes for forming the side facets of the PFP islands. Finally ET experiments provide further knowledge on the PFP side facets.

4.6.1. Previous results obtained by AFM analysis

The morphology of the surface of PFP islands has been analyzed by AFM. This study reveals that the side facets of PFP islands are inclined with respect to the substrate surfaces. Figure 4.6-1(a) and (b) present two AFM pictures where some islands have been selected and their profiles along the side facets have been measured (purple, pink, green and blue profiles). The side facets of the islands describe the following inclination angles relative to the substrate surface in Figure 4.6-1(c): 18°-20° (green (τ_3) and blue (χ_1) profiles), 30°-35° (purple (γ_1), pink (δ_1 and δ_2), green (τ_2) and blue (χ_3) profiles), 45°-46° (purple (γ_2) and green (τ_1) profiles) and 66° (blue (χ_2) profile).

This analysis has been extended to many PFP islands, concluding that only certain inclination angles are exhibited by the side facets relative to the (0 0 1) substrate surface. The most representative are the ones above mentioned (those described in Figure 4.6-1). After this AFM analysis, TEM characterization has been conducted in order to obtain further information about the morphology and shape of the side facets of the PFP islands.

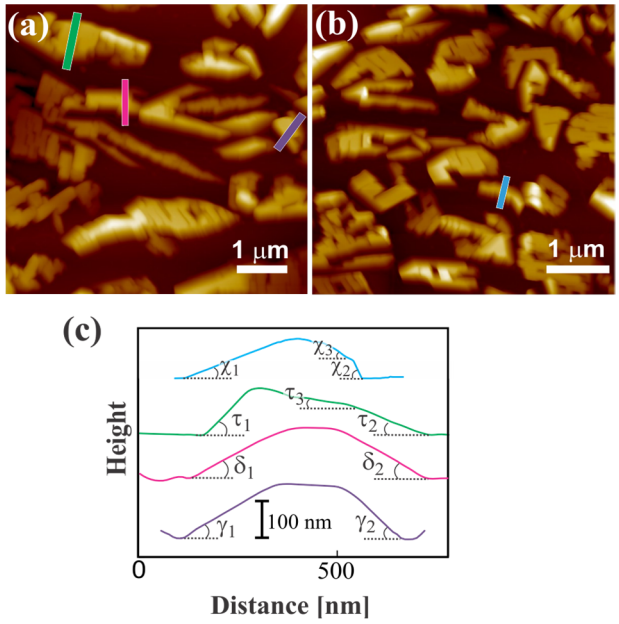

Figure 4.6-1 (a) and (b) AFM pictures of PFP grown on graphene. (c) Height profiles of the PFP islands along the colored lines in (a) and (b). The inclination angles of the PFP islands relative to the (0 0 1) surface have been measured. Purple profile: $\gamma_1 = 33°$ and $\gamma_2 = 45°$. Pink profile: $\delta_1 = 30°$ and $\delta_2 = 35°$. Green profile: $\tau_1 = 46°$, $\tau_2 = 30°$ and $\tau_3 = 18°$. Blue profile: $\chi_1 = 20°$, $\chi_2 = 66°$ and $\chi_3 = 32°$. The error of the angles has been estimated to be ±3°.

4.6.2. (S)TEM characterization

SEM and (S)TEM analyses (cf. Figure 4.6-2(a) and (b), respectively) have been carried out to inspect the PFP island shapes. Upon detailed analysis, it is found that edges of PFP islands enclose angles between 66° and 69° in many cases (ca. 65 % of the PFP islands present these 'characteristic confining edges'). Several of these edges are marked by dashed pink lines in the SEM and STEM micrographs displayed in Figure 4.6-2(a) and (b), respectively. Despite the focus of both images was optimized, some edges of the PFP islands still appear blurred. An explanation for this fact is found in the AFM pictures shown in the previous subsection (cf. Figure 4.6-1): the side facets of the PFP islands do not exhibit abrupt shapes, but they are inclined with respect to the substrate surface. Whenever the surface of the PFP islands is in focus, the inclined side facets are slightly out of focus because of the different heights of the edges and the PFP island surfaces.

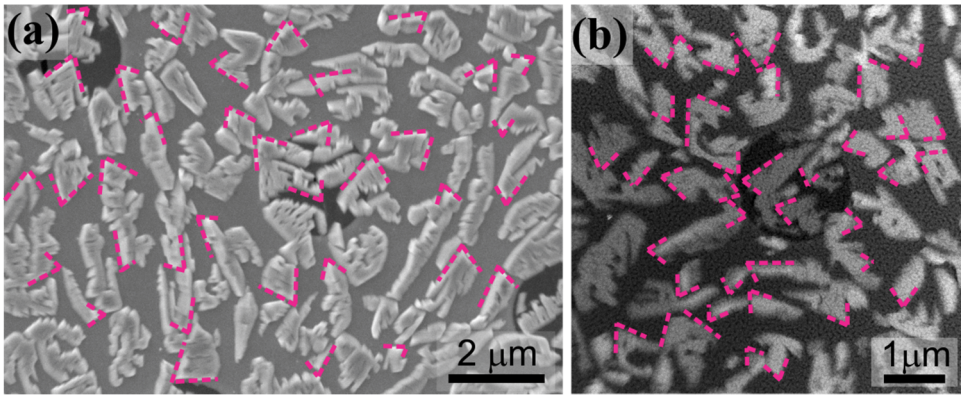

Figure 4.6-2. (a) SEM and (b) HAADF-STEM overview images of PFP islands on graphene substrate. The confining edges that include angles between 66°-69° are highlighted by dashed pink lines. Note that figure (a) without the dashed pink lines corresponds to Figure 4.4-1.

To clarify the concept of terms '**edges**' and '**side facets**' used in this thesis, Figure 4.6-3 is provided. The side facets are described by planes which define the real shape of the PFP islands. The edges are given by the borders of the PFP islands that are visible in $[1\,\bar{1}\,8]$ viewing direction.

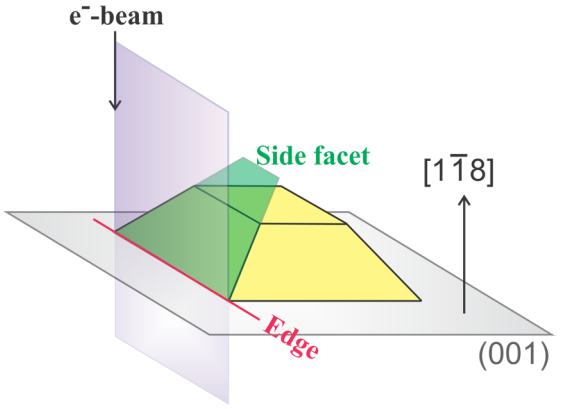

Figure 4.6-3. Sketch describing the concepts of edge and side facet. An edge is given by the border of the PFP island visible in $[1\,\bar{1}\,8]$ viewing direction as a line. A side facet is described by the plane inclined with respect to the $(0\,0\,1)_{PFP}$ plane. The side facets define the shape of the PFP islands.

The microstructural TEM characterization presented in the following lines is based on the determination of the planes (h k l indices) which run parallel to the characteristic confining island edges in the $[1\,\bar{1}\,8]_{PFP}$ viewing direction (plane highlighted in purple in Figure 4.6-3).

Firstly, the correlation between SAED patterns and micrographs collected in real space for PFP islands was examined via conventional TEM and SAED patterns (cf. Figure 4.6-4). The confining edges of the PFP islands have been highlighted by purple and red dashed lines. As displayed, they describe an angle of 68° in both images (measured experimentally and denoted by angle α).

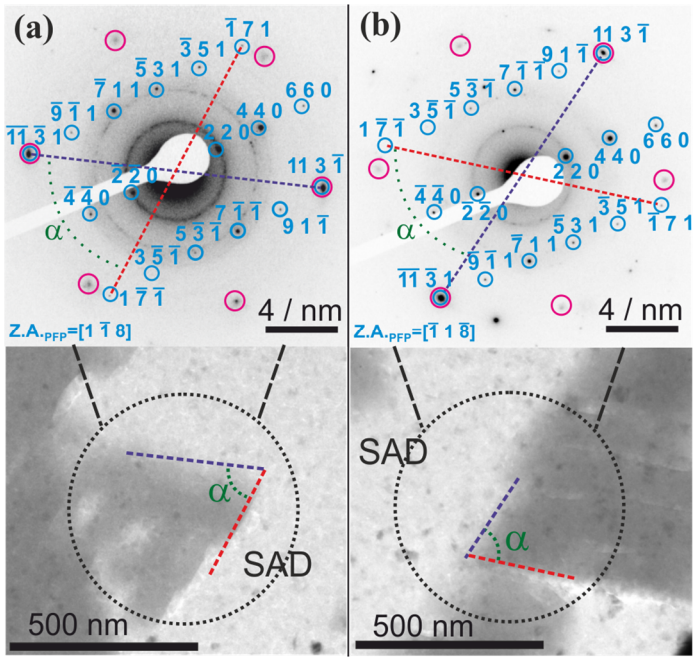

Figure 4.6-4[VII]. (a) and (b) SAED patterns with their corresponding BF-TEM image. Upper panel: PFP reflections are enclosed by blue circles, whereas the $1\,1\,\bar{2}\,0_{\text{graphene}}$ family reflections are enclosed by pink circles. Lower panel: the black dotted circles point out the size and position of the SAD aperture used to create the corresponding SAED pattern.

A detailed analysis of the micrographs of Figure 4.6-4 shows that the dotted purple and red lines in the SAED patterns (which join the $11\,3\,\bar{1}_{\text{PFP}}$ and $\overline{11}\,\bar{3}\,1_{\text{PFP}}$ reflections and the $\bar{1}\,7\,1_{\text{PFP}}$ and $1\,\bar{7}\,\bar{1}_{\text{PFP}}$ reflections, respectively) are parallel to the planes running along the confining PFP island edges in these BF-TEM images. This evidences a correlation between the $\overline{11}\,\bar{3}\,1_{\text{PFP}}$ and $1\,\bar{7}\,\bar{1}_{\text{PFP}}$ reflections[VIII] in reciprocal

[VII] Note that Figure 4.6-4 is an adaptation of Figure 4.5-1.

[VIII] To simplify the process, only $\overline{11}\,\bar{3}\,1_{\text{PFP}}$ and $1\,\bar{7}\,\bar{1}_{\text{PFP}}$ reflections have been mentioned, but likewise by symmetry, same correlation applies for the $11\,3\,\bar{1}_{\text{PFP}}$ and $\bar{1}\,7\,1_{\text{PFP}}$ reflections.

space and the confining edges of a PFP island in real space. Upon this finding, the Miller-indices of the planes that run parallel to the island edges and to the $[1\,\bar{1}\,8]$ viewing direction are determined[IX]. This derivation is presented in the following lines.

In high symmetry crystal systems, such as cubic systems, the assignment between reflections in reciprocal space and planes in real space is almost a direct process. However, this process becomes more difficult whenever lower symmetry crystal systems are involved. This is the case of the triclinic system adopted by the PFP molecules, where the angles of the unit cell are different from each other and not equal to 90°. In these situations, only general crystallographic relations can be applied. The expression used in the evaluations of the SAED patterns is the Weiss Zone Law (WZL) [213], which is a general expression valid for all crystal lattices. The WZL states that if a direction $[u\ v\ w]$ is contained in a plane $(h\ k\ l)$, then:

$$hu + kv + lw = 0\,. \tag{4.6-1}$$

Likewise, if two planes $(h_1\ k_1\ l_1)$ and $(h_2\ k_2\ l_2)$ intersect in a line, the direction $[u\ v\ w]$ of the intersection line can be found if:

$$\begin{aligned} h_1u + k_1v + l_1w &= 0 \\ h_2u + k_2v + l_2w &= 0\,. \end{aligned} \tag{4.6-2}$$

Then:

$$\begin{aligned} u &= k_1l_2 - k_2l_1 \\ v &= l_1h_2 - l_2h_1 \\ w &= h_1k_2 - h_2k_1 \end{aligned} \tag{4.6-3}$$

as can be seen, this expression can be formulated as the scalar product of $[u\ v\ w]$ and the plane normal $(h\ k\ l)$ in a cubic system. But the WZL also applies in the form

[IX] Note that these planes are equivalent to that highlighted in purple in the sketch of Figure 4.6-3.

above to all lattices to determine if a direction lies in a plane (including those that do not have orthogonal **a**, **b** and **c** axes).

The WZL is applied on the set of lattice planes that correspond to the $\overline{11}\ \overline{3}\ 1_{PFP}$ and $1\ \overline{7}\ \overline{1}_{PFP}$ reflections, and the $(0\ 0\ 1)_{PFP}$ plane. In this way, the WZL in the form of equation (4.6-3) is used to find the intersection line (direction $[u\ v\ w]$) of the $(\overline{11}\ \overline{3}\ 1)_{PFP}$ and $(0\ 0\ 1)_{PFP}$ planes, and the $(1\ \overline{7}\ \overline{1})_{PFP}$ and $(0\ 0\ 1)_{PFP}$ planes. These directions are calculated as: $[\overline{3}\ 11\ 0]_{PFP}$ and $[\overline{7}\ \overline{1}\ 0]_{PFP}$, respectively. The planes that are oriented normal to these directions are those that run parallel to the island edges in the 2D TEM projection. To identify the Miller-indices $(h\ k\ l)$ of these planes in the triclinic system, the following equations need to be fulfilled:

$$\begin{aligned} h &= ua^2 + vab\ cos\gamma + wca\ cos\beta \\ k &= uab\ cos\gamma + vb^2 + wba\ cos\alpha \\ l &= uca\ cos\beta + vbc\ cos\alpha + wc^2 \end{aligned} \tag{4.6-4}$$

where $[u\ v\ w]$ are the indices of the direction which stands normal to the $(h\ k\ l)$ plane ($[\overline{3}\ 11\ 0]_{PFP}$ and $[\overline{7}\ \overline{1}\ 0]_{PFP}$ directions in this case), and a, b and c, and α, β and γ, are the lattice constants and angles (respectively) of the PFP PS-polymorph. When equation (4.6-4) is applied and the values obtained are normalized and approached to integer values, the planes that run parallel to the confining island edges in the $[1\ \overline{1}\ 8]_{PFP}$ viewing direction are determined as: $(\overline{7}\ 8\ 2)_{PFP}$ and $(\overline{40}\ \overline{1}\ 5)_{PFP}$. Notice that they are the planes normal to the $[\overline{3}\ 11\ 0]_{PFP}$ and $[\overline{7}\ \overline{1}\ 0]_{PFP}$ directions, respectively.

TEM experiments produce images that are *2D projections* of an object. Thus in the $[1\ \overline{1}\ 8]_{PFP}$ viewing direction, the projections of the $(\overline{7}\ 8\ 2)_{PFP}$ and $(\overline{40}\ \overline{1}\ 5)_{PFP}$ planes onto the $(0\ 0\ 1)_{PFP}$ plane will be displayed in BF-TEM micrographs as lines running parallel to the confining island edges (see clarification in Figure 4.6-3, the plane highlighted in purple corresponds to the $(\overline{7}\ 8\ 2)_{PFP}$ and/or $(\overline{40}\ \overline{1}\ 5)_{PFP}$). In other words, the determined $(\overline{7}\ 8\ 2)_{PFP}$ and $(\overline{40}\ \overline{1}\ 5)_{PFP}$ planes in the $[1\ \overline{1}\ 8]_{PFP}$ viewing direction will be visible as a line lying parallel to the purple and red marked edges in Figure 4.6-4, respectively.

Moreover, the $(\bar{7}\ 8\ 2)_{PFP}$ and $(\bar{4}\bar{0}\ \bar{1}\ 5)_{PFP}$ planes are drawn in a crystallographic model of the PS-polymorph (simulated by the software Mercury [207]) in order to interpret the meaning of the determined indices. Figure 4.6-5 shows a single-layer of the PS-polymorph which contains six PFP molecules lying in the $(0\ 0\ 1)_{PFP}$ plane.

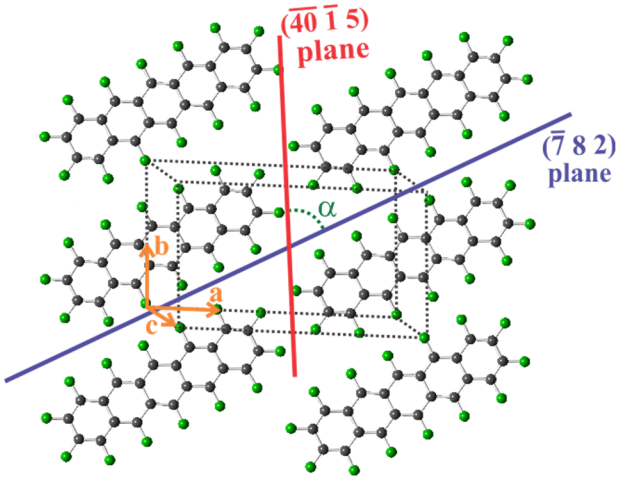

Figure 4.6-5. Sketch of a layer of the PFP PS-polymorph in the $[1\ \bar{1}\ 8]_{PFP}$ viewing direction, visualizing the $(\bar{7}\ 8\ 2)_{PFP}$ (marked in purple) and the $(\bar{4}\bar{0}\ \bar{1}\ 5)_{PFP}$ planes (marked in red) in the model. The angle α equal to 67° is also included.

The $(\bar{7}\ 8\ 2)_{PFP}$ and $(\bar{4}\bar{0}\ \bar{1}\ 5)_{PFP}$ planes (purple and red lines, respectively) are visualized as lines since the $[1\ \bar{1}\ 8]_{PFP}$ viewing direction is used. As can be seen, the $(\bar{7}\ 8\ 2)_{PFP}$ plane (purple color) results aligned parallel to the long molecular axis of the PFP molecules. Conversely, the $(\bar{4}\bar{0}\ \bar{1}\ 5)_{PFP}$ plane passes approximately between the fluorine atoms at the end of neighboring PFP molecules. The angle between the $(\bar{7}\ 8\ 2)_{PFP}$ and $(\bar{4}\bar{0}\ \bar{1}\ 5)_{PFP}$ planes has been calculated as $\alpha = 67°$, which of course agrees with the angles enclosed by the confining edges of the PFP islands and the angle measured for the $\bar{1}1\ \bar{3}\ 1_{PFP}$ and $1\ \bar{7}\ \bar{1}_{PFP}$ reflections of SAED patterns in Figure 4.6-4. The small deviation between both of just 1° is attributed to the approaches used during the calculations of the $(\bar{7}\ 8\ 2)_{PFP}$ and $(\bar{4}\bar{0}\ \bar{1}\ 5)_{PFP}$ planes by normalization and rounding to integer values of Miller-indices.

The data visualization in the sketch presented in Figure 4.6-5 allows gaining a deeper understanding about why certain angles (the ones of around 68°) have been formed between some confining edges of the PFP islands. The $(\bar{7}\ 8\ 2)_{PFP}$ and $(\overline{40}\ \bar{1}\ 5)_{PFP}$ planes are some of the most favorable planes which can form the island edges since they can pass through PFP molecules without cutting them.

Once the projected facet areas 'seen' by the electron beam in the BF-TEM image ($(\bar{7}\ 8\ 2)_{PFP}$ and $(\overline{40}\ \bar{1}\ 5)_{PFP}$ planes) are characterized, the crystallographic planes that can form the side facets are analyzed. In order to do that, the $(\bar{7}\ 8\ 2)_{PFP}$ and $(\overline{40}\ \bar{1}\ 5)_{PFP}$ planes are plotted in the PFP PS-polymorph crystal model (using the software Mercury [207]) and visualized from a viewing direction different from the $[1\ \bar{1}\ 8]_{PFP}$ (cf. Figure 4.6-6 and Figure 4.6-7 for $(\bar{7}\ 8\ 2)_{PFP}$ and $(\overline{40}\ \bar{1}\ 5)_{PFP}$ planes, respectively).

To find the planes of the side facets, one needs to focus on planes whose *intersection line* with the $(\bar{7}\ 8\ 2)_{PFP}$ and the $(\overline{40}\ \bar{1}\ 5)_{PFP}$ planes do not 'cut' the PFP molecules, but they have to pass between the gaps of the PFP molecules instead. In this way, the $(\bar{1}\ 1\ 1)$, $(3\ \bar{4}\ 4)$, $(2\ \bar{3}\ 6)$ and $(\bar{1}\ 1\ 3)$ planes of PFP are found as candidates for forming the side facets associated with the $(\bar{7}\ 8\ 2)_{PFP}$ plane (cf. Figure 4.6-6(a), (b), (c) and (d), respectively). These planes describe angles of 46°, 30°, 18° and 16°, respectively, with respect to the $(0\ 0\ 1)_{PFP}$ plane.

Similarly, the $(1\ 0\ 0)$, $(1\ 0\ 2)$ and $(\bar{1}\ 0\ 2)$ planes are found as plausible side facets of PFP islands associated with the $(\overline{40}\ \bar{1}\ 5)_{PFP}$ plane (cf. Figure 4.6-7(a), (b) and (c), respectively). These planes exhibit angles of 70°, 12° and 11°, respectively, relative to the $(0\ 0\ 1)_{PFP}$ plane.

Complementary videos, where the side facets are shown, can be seen in the Microsoft videos (AVI) of the Supporting Information of the paper '*Microstructural Analysis of Perfluoropentacene Films on Graphene and Graphite: Interface-Mediated Alignment and Island Formation*' [32].

The angles which describe the side facet planes with respect to the $(0\ 0\ 1)_{PFP}$ plane have been compared to the inclinations observed in the AFM profile measurements presented in section 4.6.1. Angles of 18°-20°, 30°-35°, 45°-46° and 66° have been found in the AFM measurements. Some of these values are in congruence with the possible side facets determined from the visualization of the facet planes in the PFP PS-polymorph crystal model. Notice that not all of the determined side facets may necessarily be found in the AFM analyses. In addition, the steeper side facets - for instance the (1 0 0) plane which describes an angle of 70° relative to the $(0\ 0\ 1)_{PFP}$ plane - becomes difficult to obtain in the AFM measurements since the finite size of the AFM tips limit the resolution of steep edges.

The TEM study of the edges and facets of the PFP islands has allowed addressing several issues which remained open after AFM and STEM measurements. For instance, phenomena concerning the appearance of blurred edges and the angle of about 66°-69º enclosed by the confining edges of the PFP islands in SEM and STEM images have been clarified. Moreover, the microstructural characterization by TEM has allowed determining the Miller-indices of the planes parallel to the island edges in the 2D TEM projection. Additional information on the inclination of the islands relative to the substrate surface observed in AFM experiments has been obtained by finding some of the possible crystallographic planes which are candidates for the side facets of the PFP islands.

Studies via electron tomography have also been carried out to obtain 3D information on the faceting of the PFP islands, they are presented in section 4.6.3.

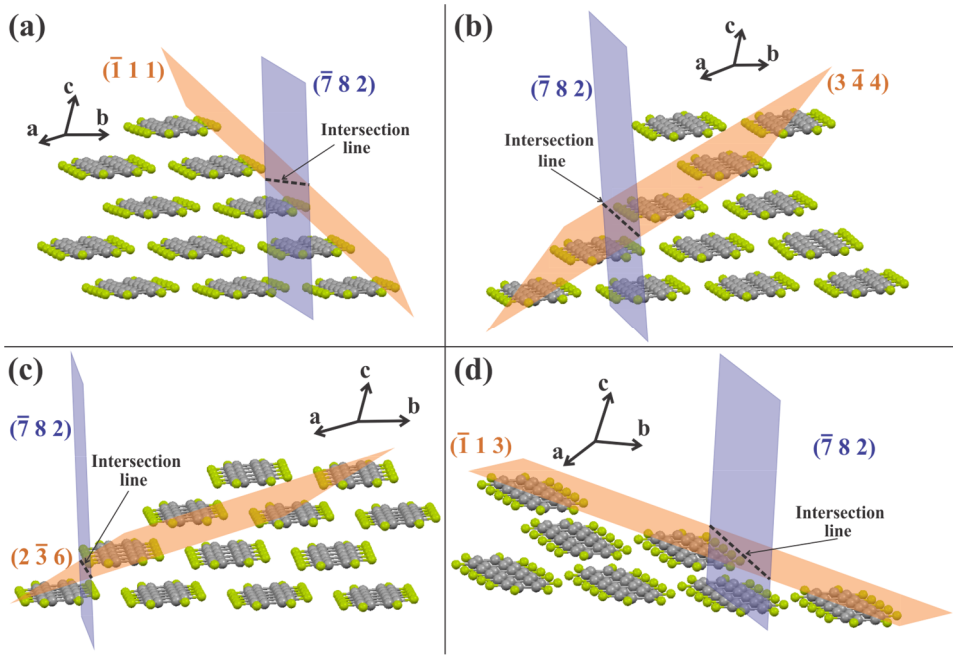

Figure 4.6-6. Visualization of the planes which are candidates for forming the side facets (marked in orange) associated with the $(\bar{7}\ 8\ 2)_{PFP}$ plane (marked in purple). (a) $(\bar{1}\ 1\ 1)$ plane, (b) $(3\ \bar{4}\ 4)$ plane, (c) $(2\ \bar{3}\ 6)$ plane and (d) $(\bar{1}\ 1\ 3)$ plane.

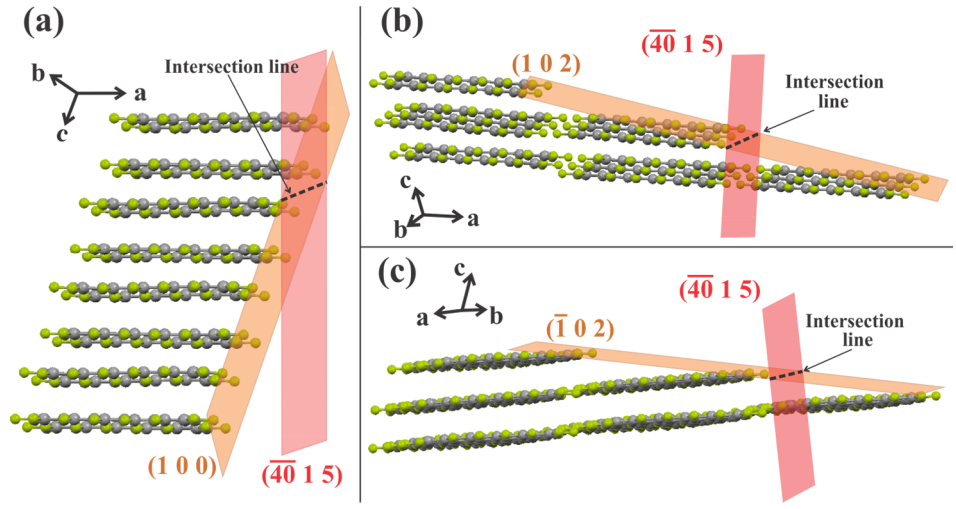

Figure 4.6-7. Visualization of the planes which are candidates for forming the side facets (marked in orange) associated with the $(\overline{40}\ \bar{1}\ 5)_{PFP}$ plane (marked in red). (a) (1 0 0) plane, (b) (1 0 2) plane and (c) $(\bar{1}\ 0\ 2)$ plane.

4.6.3. Electron tomography (ET)

The HAADF-STEM image displayed in Figure 4.6-8(a) presents a typical PFP island that exhibits an angle of about 68° (α) between the confining edges (blue dashed lines). The brighter features in the STEM image correspond to gold particles - they possess a diameter of 15 nm - utilized to facilitate the alignment of the acquired tilt-series data. ET has been carried out to elucidate the shape and morphology of the side facets. The focus has been put on the edges that enclose the angle of 68° in the 2D (S)TEM projection. As described in experimental section 4.3, the sample has been titled every 2° from -70° to +64° (around the x-axis of the sample holder) and the tilt-series data have been computationally aligned. The reconstructed images have been segmented forming virtual slices. The edges of the islands have been manually marked in different slices of the reconstructed data. Then, the traces have been interpolated to obtain the visualization of a 3D model of the island.

The angles of the confining edges at different positions (heights) have been analyzed from a 3D reconstructed island by (virtual) slices parallel to the substrate surface ((0 0 1) slices). This analysis has been performed to check if the angle of the confining edges remains constant along the height of the island. Figure 4.6-8(b) corresponds to the reconstructed island whose height is defined as the normal to the (0 0 1)-substrate surfaces. Two different heights, 'height 1' and 'height 2', have been selected to study such angle. The (0 0 1)-slice of height 1 (named as 'slice 1') intersects the island at the basal plane, while the (0 0 1)-slice of height 2 (named as 'slice 2') intersects the island at the upper part. The reconstructed data of slice 1 and slice 2 can be seen in Figure 4.6-8(c) and (d), respectively. Likewise, the 3D structures segmented from slice 1 and slice 2, which contain all reconstructed data above each slice, are visualized in Figure 4.6-8(e) and (f), respectively. The angles formed between the characteristic confining edges are marked as α_1 for slice 1 and α_2 for slice 2. They have been measured as: $\alpha_1 = (68\pm2)°$ and $\alpha_2 = (90\pm2)°$. Thus, the angle α is not constant at different heights of the island but increases at the upper part of the island.

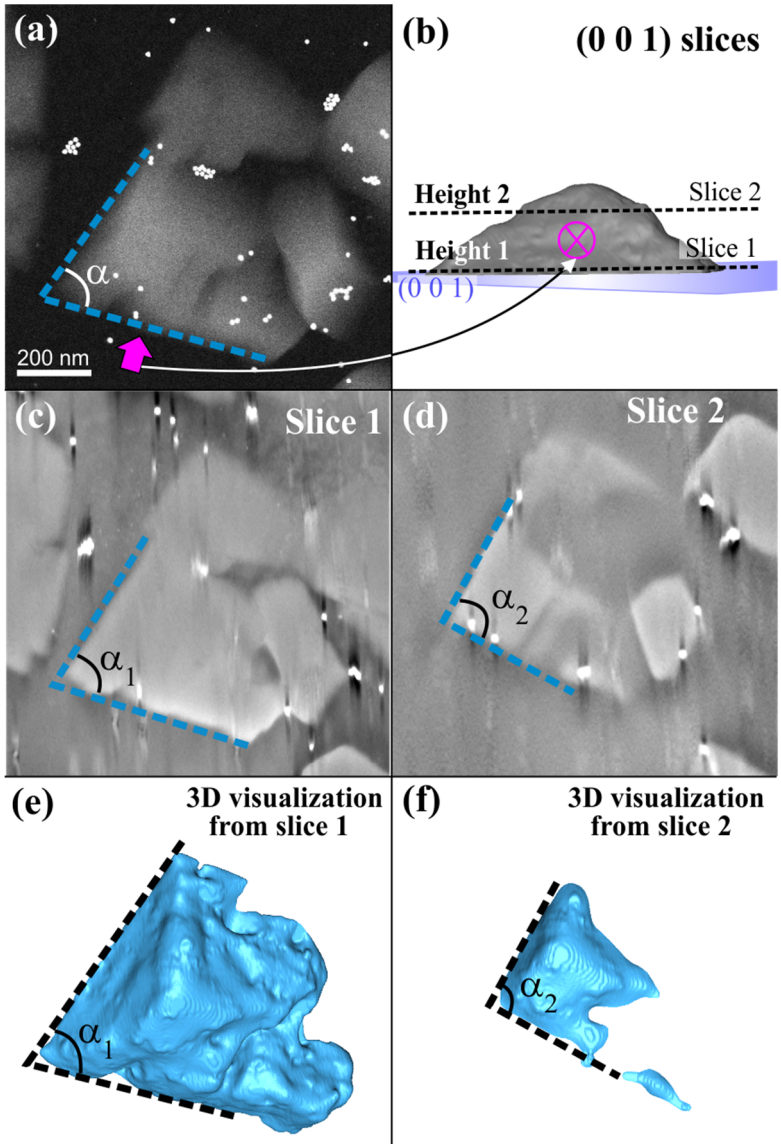

Figure 4.6-8. (a) HAADF-STEM image of a PFP island. The confining edges which describe an angle α of about 67° are highlighted by blue dashed lines. The brighter particles correspond to the gold particles. (b) 3D visualization of the island along the viewing direction marked by the pink arrow in (a). (c) and (d) Virtual slices 1 and 2 through the reconstructed data. (e) and (f) 3D visualizations of reconstructuted data lying above slice 1 and slice 2, respectively. α_1 is equal to (68±2)° and α_2 is equal to (90±2)°.

In order to have a closer look on the side facets, the 3D visualization of Figure 4.6-8(e) has been tilted in such a way that one of the respective side facets of the confining edges and the (0 0 1)-surface substrate plane appear as lines in projection. This allows measuring the inclination of the side facet relative to the (0 0 1)-substrate surface.

Figure 4.6-9(a) displays the same 3D visualization of the island as Figure 4.6-8(e) where the viewing direction used for Figure 4.6-9(b) and Figure 4.6-9(c) is marked by the pink and the green arrows, respectively. The side facets, which form the confining edges, describing the angle α, are named as facet 1 and facet 2.

In Figure 4.6-9(b), the face of facet 1 is visible, while facet 2 and the (0 0 1)-basal plane are displayed as lines in projection. The inclination angle between facet 2 and the (0 0 1)-basal plane (angle β) has been measured, resulting in an angle of around (66±3)°.

Likewise, the face of facet 2 is shown in Figure 4.6-9(c), and facet 1 and the (0 0 1)-basal plane are visible as lines in projection. This orientation allows determining the inclination angle(s) between facet 1 and the (0 0 1)-basal plane. As shown, two different angles have been measured at different heights of the 3D model of the island, i.e. $\phi_1$and $\phi_2$which correspond to values of (45±3)° and (20±3)°, respectively. This fact explains the issue observed in Figure 4.6-9(c-d) regarding the increasing of the angle α in the upper part of the island compared to the basal plane. The inclination angle β of facet 2 with respect to the (0 0 1)-basal plane remains constant, while facet 1 exhibits a flatter inclination angle (relative to the (0 0 1)-basal plane) in the upper part than in the lower part of the island, $\phi_2 < \phi_1$. The flatter angle ϕ_2 causes in the upper part of the island a bigger angle (α_2) between the confining edges than the one at the lower part (α_1).

All these measured angles are summarized in Figure 4.6-9(d), where a sketch of a PFP island in perspective is displayed. As it can be seen, whereas one side facet remains constant (facet 2) along the different heights of the island, the inclination angle of the other side facet (facet 1) becomes flatter along the height of the island yielding that $\alpha_1 < \alpha_2$.

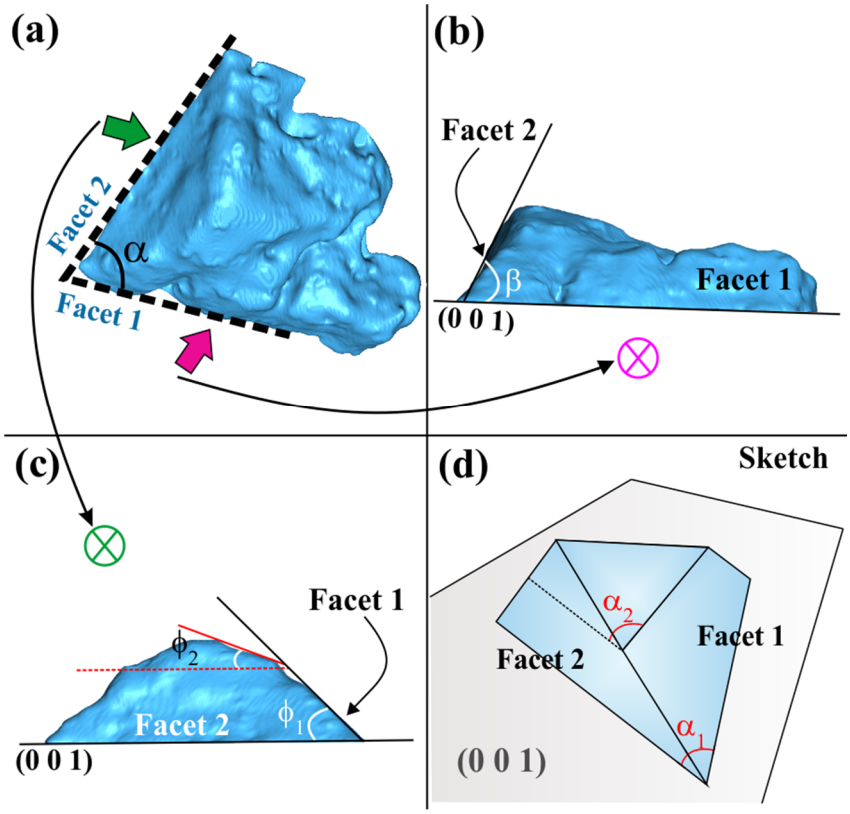

Figure 4.6-9. (a) 3D visualization of a PFP island. (b) 3D model of a PFP island oriented along the viewing direction marked by the pink arrow in (a). (c) 3D visualization of a PFP island oriented along the viewing direction marked by the green arrow in (a). (d) Sketch summarizing the measured angles.

Table 4.6-1 presents a brief summary of the inclination angles of the side facets determined by ET, TEM and AFM.

For TEM characterization, plausible angles of around 46°, 30°, 18° and 16° are found for one of the side facet associated with the $(\bar{7}\ 8\ 2)_{PFP}$ plane. For the other side facet associated with the $(\overline{40}\ \bar{1}\ 5)_{PFP}$ plane, the possible angles are 70°, 12° and 11°. The comparison of the ET with TEM data shows that:

(i) The angle $\phi_1 = (45\pm3)°$ (measured in ET) agrees with the angle of 46º formed between the $(\bar{1}\ 1\ 1)_{PFP}$ side facet and the $(0\ 0\ 1\ )_{PFP}$ plane (found in TEM).

(ii) The angle $\phi_2 = (20\pm3)°$ (measured in ET) agrees with the angle of 18º formed between the $(2\ \bar{3}\ 6)_{PFP}$ side facet and the $(0\ 0\ 1\ )_{PFP}$ plane (found in TEM analysis).

(iii) The angle β of (66±3)° measured in ET fits with the angle of 70° which is found between the side facet $(1\ 0\ 0)_{PFP}$ and the $(0\ 0\ 1)_{PFP}$ plane in TEM experiments.

Additionally, when ET data are compared to AFM experiments, it can be seen that these angles named as β, ϕ_1 and ϕ_2 observed in ET also agree with those detected by AFM measurements, i.e. 18°-20°, 30°-35°, 45°-46°and 66°.

ET		TEM		AFM
ϕ_1 ϕ_2	(45±3)° (20±3)°	$(\bar{7}\ 8\ 2)_{PFP}$	46°, 30°, 18°,16°	18°-20°, 30°-35°, 45°-46°, 66°
β	(66±3)°	$(\bar{4}\bar{0}\ \bar{1}\ 5)_{PFP}$	70°, 12°, 11°	

Table 4.6-1. Inclination angles for the side facets relative to the $(0\ 0\ 1)_{PFP}$ plane determined by ET, TEM and AFM.

Based on the ET characterization, ten PFP islands that exhibit the angle α of around (68±2)° between confining edges have been selected and reconstructed. When the virtual slides of the reconstructed islands have been analyzed, 70 % of the investigated islands presented an angle α of ca. 68° at their basal plane and of (90±2)° at their upper part. An example of these reconstructed data of the PFP islands together with its 3D model is shown in Figure 4.6-8 and Figure 4.6-9. In view of the results, it could be said that the 3D modelled PFP island is common to the 70 % of those that exhibit the angle of approx. 68º between the confining edges.

Summarizing, the faceting exhibited by the PFP islands has directly been visualized in a 3D model by means of the tomography reconstruction. The inclination angles found for the side facets are in line with those formerly predicted by AFM and TEM measurements. An additional fact that could not be previously detected in 2D projections has been observed: the different angles of the confining edges at the lower and upper part of an island. When these angles are analyzed in detail, it is found that a side facet (the steepest one) remains constant along the different heights of the island, while for the other facet, two inclination angles are detected along the height of the island. The inclination angle at the upper part is flatter than the one at the basal plane of the island.

4.7. Conclusions

The first aim of this chapter is focused on the determination of the exact lateral alignment of PFP molecules with respect to the graphene substrate. TEM measurements have been initially performed at cooling conditions, revealing that the PFP molecules grow epitaxially on graphene substrate with their long molecular axis slightly rotated with respect to the graphene zig-zag directions (offset value = +1.5°).

XRD analysis (performed also in multi-stack structure) has reached the same outcome as TEM but with discrepancies in the offset rotation value, i.e. -3.7°. A later TEM study at room temperature has led to a similar result as XRD experiments, i.e. the offset value between the long molecular axis of the PFP molecules and the graphene zig-zag direction is -3° in the multilayer films.

Further STM analyses have been carried out to know the relative alignment between the PFP molecules and graphene beyond the first and second PFP monolayers. These analyses have revealed that the small misalignment already starts at the interface between the PFP molecules and the substrate.

To obtain complementary information, MM calculations have also been performed to compare the potential energy of different adsorption scenarios. The theoretical calculations have shown that only for the isolated PFP molecules, the most stable configuration is the one with their long axis oriented exactly parallel to the graphene zig-zag direction. This geometry is not accessible for the PFP monolayer and multilayer films due to their different lattice-matching with regard to the hexagonal structure of the graphene structure. The growth in island shapes can be attributed to the difficulty of the first monolayer(s) of PFP to accommodate the crystalline structure of the subsequent PFP layers deposited on top of them. Thus, making the thin film unstable and leading to the break-up of the film into islands that lower the total energy of the system.

Precisely, this growth of PFP in island shapes involves a certain faceting which has also been studied. AFM analyses have revealed side facets inclined with respect to the substrate surfaces by angles of around 18°-20°, 30°-35°, 45°-46° and 66°.

Furthermore, SEM and STEM micrographs have shown that many of these islands have confining edges enclosing angles of around 66°-69°. A correlation between BF-TEM images and their corresponding SAED patterns of selected islands have enabled the determination of the crystallographic planes that form these confining edges in the 2D TEM projections, together with the identification of the possible planes that are candidates for the side facets. The Miller-indices of the planes that run parallel to the island edges in the 2D TEM projection have been deduced as $(\bar{7}\ 8\ 2)_{PFP}$ and $(\overline{40}\ \bar{1}\ 5)_{PFP}$ planes. From that, the plausible planes that can form some side facets of the PFP islands have been identified as: $(\bar{1}\ 1\ 1)_{PFP}$, $(3\ \bar{4}\ 4)_{PFP}$, $(2\ \bar{3}\ 6)_{PFP}$ and $(\bar{1}\ 1\ 3)_{PFP}$ when associated with the $(\bar{7}\ 8\ 2)_{PFP}$ plane, and $(1\ 0\ 0)_{PFP}$, $(1\ 0\ 2)_{PFP}$ and $(\bar{1}\ 0\ 2)_{PFP}$ when associated with the $(\overline{40}\ \bar{1}\ 5)_{PFP}$ plane. The inclination of these suggested planes with respect to the substrate surface agrees with some of the inclinations previously measured by AFM experiments, providing additional evidence as potential candidates to form the side facets of the PFP islands.

In a further step, the shape of the PFP islands has been investigated by ET to gain insight on the faceting formation at different island heights and to receive detailed information on the 3D structure of the PFP islands. Particular attention has been paid to the confining side facets of these islands that exhibit a confining angle of around 68° in the 2D TEM projection. These experiments have revealed that the angle between the confining edges is smaller at the lower part compared to the upper part of the PFP islands. This issue is caused by different inclinations of the side facets of the islands. While the inclination with respect to substrate surface of one of the side facet remains constant, the other side facet presents a flatter inclination angle at the upper part of the island compared to the lower part.

At the heart of materials science is the need to understand and control the microstructure of the materials examined. Aiming to do that techniques providing information are required not only at global length scales but also at the nanometer level. In particular, electron microscopy has been used within this work as a powerful tool to characterize organic structures when suitable conditions are applied.

The π-stacking is an ordering desirable for OSC materials since this arrangement enhances the π-π overlapping, and therefore, leads to desirable electronic characteristics including charge carrier mobilities. For such potential applications, the structural properties of a PFP film prepared on graphene have to be known. In this sense, the characterization performed in this chapter has provided a valuable information on the morphology, arrangement, orientation and faceting of the PFP film:

- The determination of the exact lateral alignment of the PFP film on graphene substrates is fundamental to understand the physical properties of the PFP/graphene system.
- Analysis of PFP island faceting 'sheds light' on the shape of PFP structures and reveals the role in promoting growth of preferred facet inclinations. Since the side facets are key parameters to control the surfaces and interfaces, theoretical models for facet formation and competition during the growth of a PFP island will help to explain the experimental observations.

5. Microstructural characterization of PEN and PFP blends grown on SiO_2 and KCl

‘The top of one mountain is always the bottom of another’

— Marianne Williamson

5.1. Introduction

The current study describes an investigation performed as a collaborative research between the Structure and Technology Research Laboratory Group and the Molecular Solid State Physics Group of the Philipps-Universität Marburg. The sample growth was carried out by the Molecular Solid State Physics Group. The (S)TEM characterization has been performed by the author of this thesis in the Technology Research Laboratory Group. This chapter describes the (S)TEM analyses.

Section 5 is organized as follows: firstly, the importance of the binary mixtures of OSCs is provided together with the motivation of the work (see in 5.2). Next, the chapter is divided in two parts: PEN:PFP blends grown on the amorphous substrate SiO_2 (cf. in section 5.3), and PEN:PFP mixtures grown on the crystalline substrate KCl (cf. in section 5.4). These investigations have been mainly carried out by EDX experiments and conventional TEM analyses. DF-TEM micrographs and SAED patterns have been of prime interest since they have allowed resolving the arrangement and distribution of the phases observed in the samples. In case of SiO_2 substrates, PEN:PFP blends with mixing ratios of [2:1], [1:1] and [1:2] are described. In contrast, PEN:PFP blends with mixing ratios of [2:1] and [1:2] are presented for KCl substrate.

5.2. Motivation

As it has already been mentioned in the introduction part (cf. chapter 2.5.3), OSC heterostructures which consist of two types of organic molecules where one acts as ‘donor’ and the other one as ‘acceptor’ for electrons, have gained a significant interest in the last years [118–124]. Their production has increased to cover the needs of producing novelty devices with ambipolar character (p-n junctions) that can replace the conventional inorganic semiconductors. Among other organic heterostructures, mixtures of PEN (p-type OSC) and PFP (n-type OSC) are a promising alternative to other organic heterostructures because these compounds have structural compatibility and offer intermixing at a molecular level [113,115,135–138], which is essential for good optical, electronic and structural properties.

The mixing on the molecular level in these heterostructures of PEN and PFP has been proven by averaging characterization techniques such as GIXD [133,135], FTIR spectroscopy [115], PL [137], VASE [136,138], DRS [136], STXM [134] and TDS [26], using SiO_2 as substrate. This mixing behavior has been evidenced by the formation of a mixed crystal structure with a [1:1] mixing ratio of the PEN:PFP blend. This mixed crystal structure will be referred to as '***mixed phase***' in the content of this thesis. For other mixing ratios, a phase separation has been found between the molecules in excess that remain in their pure states and the mixed phase [135]. So far, PEN and PFP binary systems have only been studied by global characterization techniques. However, the spatial resolution of these methods is not enough to provide information about the samples up to nanometer scale. The studies presented in this chapter pursue the overcome of this limitation using (S)TEM analyses, providing information on the crystallographic orientations, element distribution and phase segregation of PEN:PFP mixtures.

The influence of the substrate is a key parameter that determines the crystal orientations and molecular packings of deposited OSCs. In these experiments, two different substrates have been chosen, i.e. SiO_2 and KCl. On the one hand, SiO_2 is an inert substrate that is known to minimize the substrate-film interactions leading to polycrystalline character of the organic layers [27]. On the other hand, KCl is a crystalline substrate that leads to epitaxial growth and crystalline films [28–31]. Thus, one purpose of this chapter is to study and compare the influence of the substrate on the morphology and arrangement of PEN:PFP blends.

Additionally, different mixing ratios have been selected for the analyses, i.e. PEN:PFP [2:1], [1:1] and [1:2] for organic mixtures grown on SiO_2 substrates, and PEN:PFP [2:1] and [1:2] for organic blends deposited on KCl substrates. Hence, a second target of these studies deals with the analysis of the morphology, crystal structure, arrangement and distribution of codeposited mixtures.

Considering the importance of OSC heterostructures due to their applications in organic optoelectronics, the investigation of codeposited mixed films becomes relevant. It is clear that organic heterostructures have an important role in the development of novel organic materials. In particular, they are a key for further

progress in achieving efficient donor-acceptor interfaces. However, OSCs exhibit a wide variety of structures and morphologies whose changes affect their physical properties and have severe influence on the device performance. A deeper knowledge of mixing scenarios and behaviors, together with arrangements and distribution of different phases in OSC heterostructures, are of prime interest for the understanding of their structure formation and behavior, playing a capital role that will help to improve the architecture of future devices.

The contribution of this research to the scientific framework has been fulfilled with the publication of two papers in the *Journal of Crystal Growth* [33,34], which include the results presented in section 5.3 (PEN and PFP blends grown on SiO_2), and section 5.4 (PEN and PFP blends grown on KCl).

5.3. Microstructural characterization of PEN and PFP blends grown on SiO_2

Here, the growth conditions of PEN and PFP mixtures on SiO_2 substrate are shown. Next, their morphology and characterization studied by (S)TEM techniques are presented and discussed.

5.3.1. Experimental

All organic blend films of PEN (Sigma-Aldrich, purity ≥ 99.9 %) and PFP (Kanto Denka Kogoyo Co., purity ≥ 99 %) were grown under UHV conditions (≤ $1.00x10^{-8}$ mbar base pressure) by OMBD from a resistively heated Knudsen cell at typical deposition rates of 6 Å/min as determined by a QCM. The samples were grown at typical temperatures of 330 K with a nominal total thickness of approximately 40 nm onto SiO_2 TEM grids (Pelco [214]). As illustrated in Figure 5.3-1, the TEM grids possess a central part consisting of a silicon nitride support with free standing electron transparent silicon dioxide windows of a thickness ca. 8 nm. The SiO_2 TEM grid was preheated to 570 K for 15 min prior to the organic film deposition in order to clean it from carbon, hydrogen and some other impurities. Once the organic films were grown on these substrates, they were studied by (S)TEM without any additional preparation method since the silicon dioxide windows fulfill the condition of electron transparency. The following blend ratios were grown on these substrates: PEN:PFP [2:1], [1:1] and [1:2].

The film morphology of these samples was characterized by a JEOL JIB-4601F SEM microscope operated at an acceleration voltage of 5 kV and a JEOL JEM-2200FS microscope operated at an acceleration voltage of 200 kV for STEM analysis. TEM measurements, such as SAED patterns, BF- and DF-TEM imaging were performed in the JEOL JEM-3010 operated at its maximum acceleration voltage of 300 kV. In order to reduce the beam damage caused on the sample, low electron doses of (1-2)$x10^{-3}$ $C \cdot s^{-1} \cdot cm^{-2}$ were applied. These low dose conditions were achieved by reducing the beam current, using a small condenser aperture and increasing the

spot size of the beam. The EDX analyses were performed using a Bruker XFlash 5060 detector attached to the JEOL JEM-2200FS microscope.

The samples were studied in all cases in plan-view orientation with the electron beam perpendicular to the sample surface at **room temperature** (≈293 K).

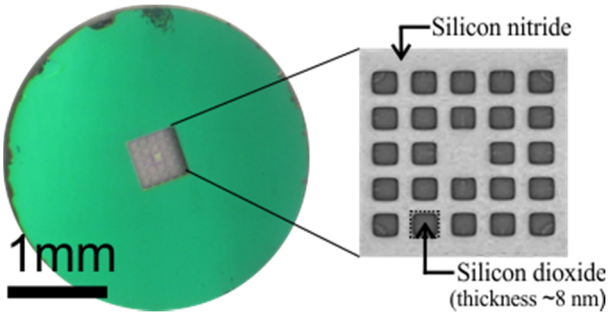

Figure 5.3-1. Image of the SiO_2 TEM grid support used for the deposition of the organic film.

5.3.2. Morphology of the samples

The influence on the morphology of the different ratios used for the PEN:PFP blends grown on SiO_2 is analyzed by SEM and HAADF-STEM micrographs. The PEN:PFP [1:1] mixture is presented first. Next, the PEN:PFP [2:1] and [1:2] mixtures are described. Finally, these morphologies are compared to the pure phases of PEN and PFP grown on the same substrate.

Figure 5.3-2(a) corresponds to a SEM overview of the PEN:PFP [1:1] blend showing that this sample consists of fibers whose lengths are ranging between 0.5 µm and 2 µm. Furthermore, the HAADF-STEM image (cf. Figure 5.3-2(b)) displays that these fibers have well-defined shapes. Conversely the SEM micrograph of the PEN:PFP [2:1] blend (cf. Figure 5.3-3(a)) is dominated by low intensity variations, leading to smooth and homogeneous images. The corresponding HAADF-STEM picture (cf. Figure 5.3-3(b)) displays some grainy structures. Likewise in the SEM micrograph of the PEN:PFP [1:2] blend (cf. Figure 5.3-4(a)), just few fibers are observed on top of a smooth background. The HAADF-STEM image (cf. Figure 5.3-4(b)) shows that these fibers in the foreground are very sharp and have a well-defined shape (needle-shape) with typical lengths of (1-2) µm.

Although the pure phases of these materials - pure PEN and PFP - on SiO_2 substrate have already been reported [209,215–219], some images have been recorded and they are presented in Figure 5.3-5 in order to compare them with the heterostructures. Pure pentacene deposited on SiO_2 crystallizes in flat islands with densities of around 3.8 $N/\mu m^2$ (where N is the number of islands) and average grain diameters of 0.5 µm (cf. Figure 5.3-5(a)). In contrast, pure PFP exhibits isotropically distributed spicular fibers with typical sizes of about 1 µm×150 nm (cf. Figure 5.3-5(b)). Comparing to the PEN:PFP mixtures, the PEN:PFP [2:1] blend clearly exhibits a more PEN-like character, while the PEN:PFP [1:2] blend shows a PFP-like morphology. In contrast, the PEN:PFP [1:1] blend is very different from that identified for pure PEN and pure PFP phases.

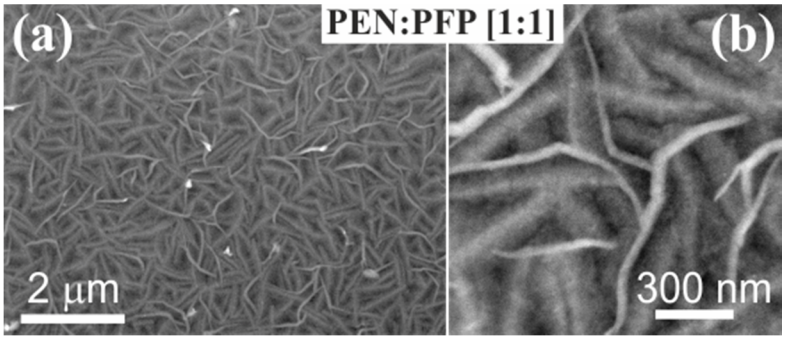

Figure 5.3-2. (a) SEM and (b) HAADF-STEM images of the PEN:PFP [1:1] mixture grown onto SiO_2 substrate.

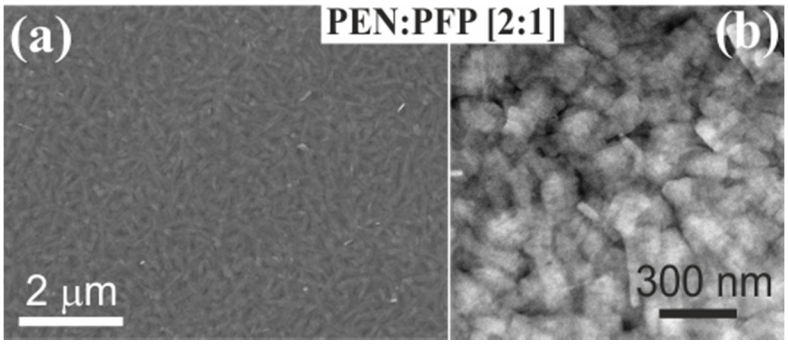

Figure 5.3-3. (a) SEM and (b) HAADF-STEM images of the PEN:PFP [2:1] mixture grown onto SiO_2 substrate.

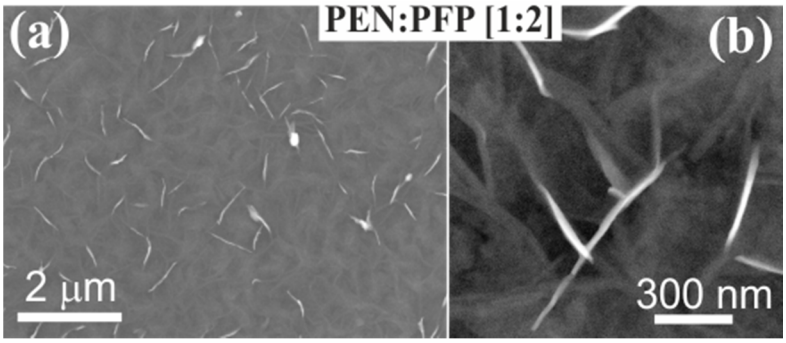

Figure 5.3-4. (a) SEM and (b) HAADF-STEM images of the PEN:PFP [1:2] mixture grown onto SiO_2 substrate.

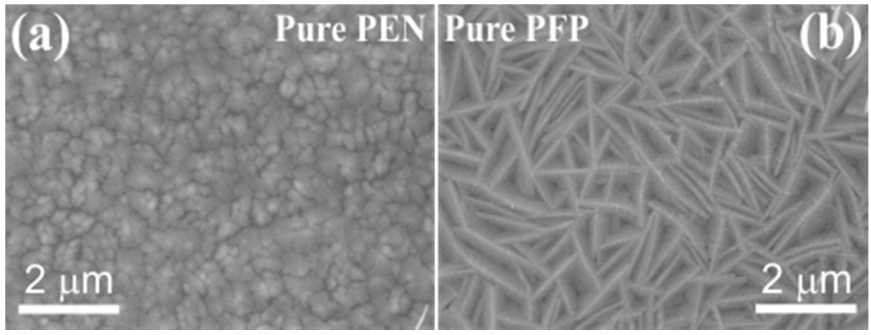

Figure 5.3-5. SEM images of (a) pure PEN and (b) pure PFP films grown onto SiO_2 substrate.

In the following subsections, the different morphologies observed by changing the mixing ratio are analyzed by microstructural and compositional characterization using EDX measurements, SAED patterns and DF-TEM analyses.

5.3.3. TEM characterization: EDX analysis

Since EDX is a suitable tool to determine the local elemental distribution, the mixtures with one component in excess, i.e. PEN:PFP [2:1] and [1:2] blends, are analyzed first by EDX experiments in order to check if different phases might be distinguished in such samples.

5.3.3.1. PEN:PFP [2:1] blend

Figure 5.3-6(a) shows a HAADF-STEM image of the PEN:PFP [2:1] blend, where the positions of the electron probe for local EDX analysis are marked in different colors (from point 1 to point 6). Their corresponding spectra are displayed in Figure 5.3-6(b). Since the composition of PEN and PFP is very similar, just varying hydrogen atoms by fluorine atoms, the carbon-to-fluorine (C/F) ratio has been used to check if the presence of PFP or of the mixed phase (formed by PEN and PFP) may be detected within the blend (cf. Figure 5.3-6(c)). Regions consisting of pure PFP or of the mixed phase provide smaller C/F ratios than regions formed by only PEN. As shown in Figure 5.3-6(c), no high variations of C/F ratios can be detected and, therefore, no hints for the distribution of PFP or of the mixed phase are obtained by EDX measurements. It leads to inspect the sample with other techniques, which can supply information on the phases.

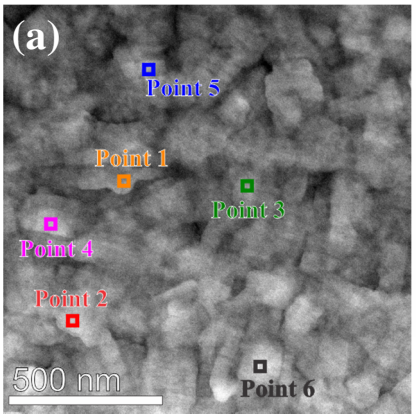

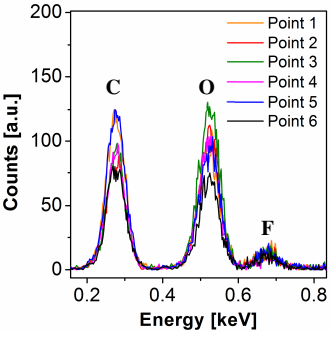

(b)

Point	C/F ratio
1	5.6
2	4.9
3	5.4
4	6.0
5	6.2
6	5.1

(c)

Figure 5.3-6. EDX analysis of the PEN:PFP [2:1] blend. (a) HAADF-STEM image with local positions for EDX acquisition (points 1-6). (b) EDX spectra. (c) C/F ratio from the EDX measurements.

5.3.3.2. **PEN:PFP [1:2] blend**

Figure 5.3-7(a) shows a HAADF-STEM image of the PEN:PFP [1:2] blend. The localization of the EDX measurements is marked: positions 1, 4, 5 and 7 correspond to the area extended between the fibers, while positions 2, 3 and 6 belong to measurements performed on the sharp fibers. The spectra collected for these points can be seen in Figure 5.3-7(b). Additionally, some areas have been magnified to clearly observe the exact positions where the EDX data are acquired (Figure 5.3-7(c) and (d)). The C/F ratio is provided in the table contained in Figure 5.3-7(e). Observing the data, it is not possible to predict any trend, whether the ratio is bigger or smaller in the fibers or in the area extended between the fibers. Hence, EDX analysis performed cannot elucidate the issue concerning the distribution of the different phases in the PEN:PFP [1:2] blend.

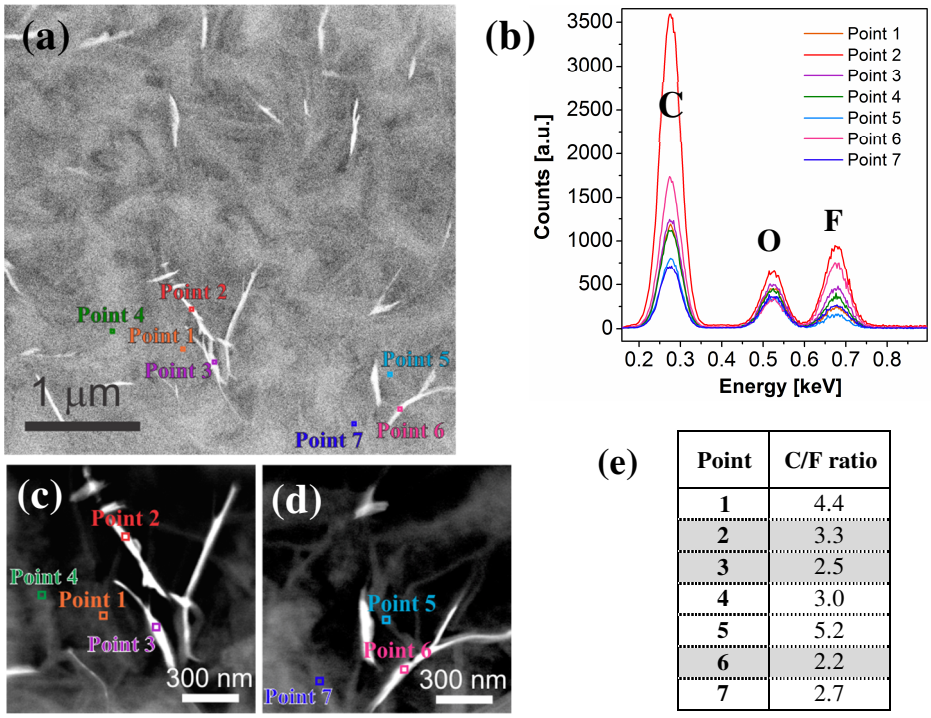

(e)

Point	C/F ratio
1	4.4
2	3.3
3	2.5
4	3.0
5	5.2
6	2.2
7	2.7

Figure 5.3-7. EDX analysis of the PEN:PFP [1:2] blend. (a) HAADF-STEM image with local positions for EDX acquisition (points 1-7). (b) EDX spectra. (c) and (d) magnified images of the areas used for the EDX analysis. (e) C/F ratio of the EDX measurements.

The spectra collected for the PEN:PFP [2:1] and [1:2] blends only reveal that the samples are mainly composed by carbon and fluorine. Notice that the oxygen peak observed in both cases is due to the oxygen content of the TEM support grid (SiO_2 substrate). Higher amount of fluorine is found in the PEN:PFP [1:2] mixture compared to the [2:1] blend. This fact is expected since the PEN:PFP [1:2] mixture is grown with excess of PFP. However, no hints for the distribution of the different phases in the blends are obtained. For this reason, a second technique which provides local information on structure and crystallography of materials is considered, i.e. a TEM characterization via SAED patterns.

5.3.4. TEM characterization: SAED patterns

As it has been mentioned in the motivation of this chapter (cf. section 5.2), PEN:PFP mixtures have been previously studied by averaging techniques. These studies reported the formation of a stabilized *mixed phase* between codeposited PEN and PFP only with stoichiometrically [1:1] mixing ratio of these compounds. For other mixing ratios, a phase separation appears between the mixed phase and the component in excess which remains in its pure state.

In a first step, the crystallinity of the three different blends is analyzed by electron diffraction to check and prove: (i) the existence of this mixed phase regardless of the mixing ratio and (ii) the presence of the compounds in their pure states when a non-stoichiometric ratio is used. Hereby, the biggest SAD aperture available in the microscope with diameter size equal to 1.3 µm (enclosing a specimen area of 1.33 μm^2) is utilized to acquire SAED patterns.

Afterward, a microstructural characterization is performed to get information of the sample on a local scale. The single crystalline character in the PEN:PFP blends is investigated by using the smallest SAD aperture available in the microscope (with diameter size equal to 143 nm enclosing a specimen area of 0.0160 μm^2).

Furthermore, similar to the microstructural characterization by SAED patterns in section 4.5.1, the distances between the diffracted reflections and the (0 0 0) primary beam in the SAED patterns (r^*) are measured, and from that, the interplanary spacings d_{hkl} are calculated using equation (3.4-2). These values are compared to the ones reported in the literature.

It is important to point out that all SAED patterns displayed in this chapter have been acquired at room temperature (≈293 K). Consequently, all interplanary spacings $\mathbf{d_{hkl}}$ values are provided at **room temperature**.

5.3.4.1. SAED patterns using SAD apertures with 1.3 µm diameter

As it has already been mentioned, SAED patterns acquired from specimen areas of about 1.33 μm^2 are shown in this section. The SAED patterns are composed by a series of concentric diffraction rings[I] rather than distinct spots. This is due to the selection of a relatively large area of several micrometers squared which involves crystalline phases with different orientations.

PEN:PFP [1:1] blend

Figure 5.3-8(a) shows the SAED pattern of the PEN:PFP [1:1] blend recorded with a SAD aperture of 1.3 µm diameter. Just five diffraction rings are clearly visible in this mixture. The r^* distances of each concentric diffraction ring are measured and they are labelled with numbers[II] according to their d^*_{hkl} obtained values (where $d^*_{hkl} = 1/d_{hkl}$), i.e. numbers 1, 2, 4, 6 and 8 are assigned for d^*_{hkl} values equal to (0.133-0.135) $Å^{-1}$, (0.151-0.156) $Å^{-1}$, (0.208-0.213) $Å^{-1}$, (0.263-0.270) $Å^{-1}$ and (0.303-0.313) $Å^{-1}$, respectively[III]. The diffraction rings are highlighted by red dotted lines and labelled with the respective number in Figure 5.3-8(b). From the d^*_{hkl} distances, the values of interplanar lattice spacings in real space d_{hkl} are calculated for this sample as the average of at least 20 different SAED patterns acquired. These interplanar spacing values are presented in Table 5.3-1 ('experimental SAED patterns' column) and they are compared to the ones reported for the mixed phase [135] (cf. Table 5.3-1, 'mixed phase' column) and those expected for pure PEN [102,107] (cf. Table 5.3-1, 'PEN TF' and 'PEN Campbell' columns). The experimental data do not fit with values reported for PFP [115], hence this comparison is not shown in Table 5.3-1.

[I] Note that the term '*concentric diffraction rings*' will be often replaced by only '*diffraction rings*' for reasons of simplicity throughout the content of this dissertation.

[II] Note that the term '*diffraction rings labelled with numbers*' will be often replaced by '*diffraction rings numbers*' or by only '*diffraction rings*' throughout the content of this dissertation.

[III] The reason why the diffraction rings are not labelled by consecutive numbers (1, 2, 3, 4 and 5 instead of 1, 2, 4, 6 and 8) is clarified below (cf. footnote V, subsection 5.3.4.1).

Although the experimental d_{hkl} data agree better with the d_{hkl} values of the mixed phase, they may also match with some values reported for the TF and Campbell phases of pure PEN, especially for diffraction rings numbers 4, 6 and 8. Thus, the following question arises: how can it be assured that all diffraction rings observed in the SAED pattern displayed in Figure 5.3-8 correspond to the mixed phase and none of them belong to any phase of pure PEN?

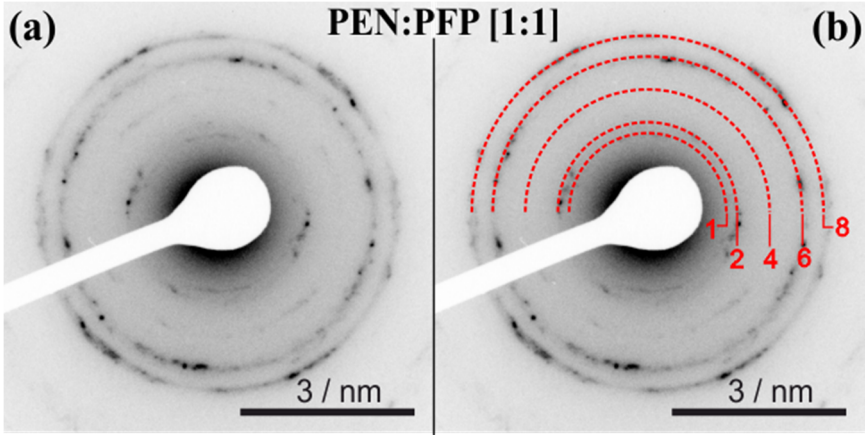

Figure 5.3-8. SAED pattern of the PEN:PFP [1:1] blend using a SAD aperture of 1.3 µm in diameter. The concentric diffraction rings visible in (a) are highlighted by red dotted lines in (b), and according to their d^*_{hkl} values the numbers of the diffraction rings have been assigned.

Diffraction ring No.	**Experimental SAED patterns d_{hkl} (Å)**	**Mixed phase** [135] **d_{hkl} (Å)**	**PEN TF** [115]		**PEN Campbell** [102]	
			hkl	**d_{hkl} (Å)**	**hkl**	**d_{hkl} (Å)**
1	7.43	7.40	0 1 0[a]	7.51	1 0 0	7.29
2	6.53	6.53	1 0 0[b]	5.95	0 1 0	5.93
4	4.78	4.80	1 1 0	4.65	1 1 0	4.59
6	3.73	3.74	0 2 0	3.75	2 0 0	3.65
8	3.27	3.27	1 2 0	3.17	2 1 0	3.10

[a] This reflection is forbidden and it will only be visible in the SAED patterns if plural (dynamical) scattering events are present.
[b] This reflection has a very weak intensity, therefore it is not always visible in experimental SAED patterns.

Table 5.3-1. The experimental d_{hkl} values determined for each ring in the experimental SAED patterns of the PEN:PFP [1:1] blend are compared to those reported in the literature for: the mixed phase by GIXD [135] (in the PEN:PFP [1:1] mixture), and the PEN TF [115] and Campbell phases [102] in [0 0 1] zone axis. The error of the d_{hkl} experimental values was estimated to be less than 3 % for the first two diffraction rings and less than 2 % for the rest of the rings.

In principle, a phase separation between PEN and PFP is not expected in the PEN:PFP [1:1] blend since the mixed phase is favorable over the pure phases. However, the similitude between some experimental d_{hkl} values with those corresponding to the PEN phases does not allow attributing the experimental rings to the mixed phase at first glance. The similar values are: the experimental d_{hkl} values of diffraction rings 4, 6 and 8, and those associated with the PEN TF 1 1 0, 0 2 0 and 1 2 0 reflections, and the PEN Campbell 1 1 0, 2 0 0 and 2 1 0 reflections.

To clarify whether the experimental diffraction rings observed in the SAED patterns belong to the mixed phase or the PEN phase, the focus should be put on: (i) the experimental d_{hkl} values determined for diffraction ring number 1, and those corresponding to the PEN TF 0 1 0 and the PEN Campbell 1 0 0 reflections. (ii) The experimental d_{hkl} values determined for diffraction ring number 2 and the ones corresponding to the PEN TF 1 0 0 and PEN Campbell 0 1 0 reflections.

The d_{hkl} value of experimental diffraction ring number 1 may fit with the d_{hkl} value of the PEN TF 0 1 0 reflection. However, this reflection should be forbidden in the PEN TF[IV] SAED pattern (cf. Figure 2.5-1(a), section 2.5.1). Since the reflection is present, it does not belong to the PEN TF. Furthermore, the d_{hkl} value of diffraction ring number 1 may also fit with the 1 0 0 refection of the PEN Campbell phase. But if this reflection appears, it should have a d_{hkl} spacing of 7.3 Å in a weak intensity (cf. Figure 2.5-1(b), section 2.5.1). The d_{hkl} spacing of 7.3 Å is slightly deviated from the experimental d_{hkl} value of 7.4 Å determined for ring number 1.

The d_{hkl} value of diffraction ring number 2 may fit with the d_{hkl} value of PEN TF 1 0 0 and PEN Campbell 0 1 0 reflections. However, these reflections should appear in the SAED pattern with a d_{hkl} spacing of 5.9 Å in a weak intensity (cf. Figure 2.5-1 (a) PEN TF and (b) Campbell polymorphs, section 2.5.1). This d_{hkl} value differs from the one corresponding to the experimental diffraction ring number 2, i.e. the d_{hkl} spacing of 6.5 Å.

[IV] This reflection is forbidden and it will only be visible if plural (dynamical) scattering events are present, which are not expected for a PEN total thickness of 20 nm.

In this way, all these facts evidence that diffraction rings numbers 1 and 2 belong to the mixed phase, and therefore, the rest of the rings (numbered as 4, 6 and 8) should correspond to the mixed phase as well. This is in line with the observations by global characterization techniques, which demonstrated that the diffraction rings observed in the experimental SAED pattern of the PEN:PFP [1:1] blend are associated with the mixed phase [135].

PEN:PFP [2:1] blend

The PEN:PFP [2:1] blend is also analyzed by using a SAD aperture of 1.3 µm in diameter, detecting five concentric diffraction rings (cf. Figure 5.3-9(a)). Their r^* distances are measured and the d^*_{hkl} and d_{hkl} values are calculated from the average of at least ten SAED patterns. The experimental d_{hkl} values are compared to those observed for diffraction rings labelled with numbers 1, 2, 4, 6 and 8 in the PEN:PFP [1:1] blend. Only if a deviation smaller than ±0.0045 $Å^{-1}$ of the d^*_{hkl} distances between both the PEN:PFP [2:1] and [1:1] blends is obtained, the diffraction ring of the PEN:PFP [2:1] is labelled with the same number used for its equivalent in the PEN:PFP [1:1] blend.

Figure 5.3-9(b) shows the five diffraction rings detected in the PEN:PFP [2:1] blend. They are highlighted by red dotted lines and labelled with the same number as the ones observed in the PEN:PFP [1:1] blend since they appear at similar d^*_{hkl} distances in both samples. The experimental d_{hkl} interplanar spacings are collected in Table 5.3-2. The d_{hkl} spacings of the mixed phase observed in the PEN:PFP [2:1] blend by Hinderhofer et al. [135] and those corresponding to the pure PEN TF and Campbell phases are also provided to be compared with the experimental ones. Note that the d_{hkl} values of PFP are not included since they are different from those determined experimentally. At first glance, the experimental d_{hkl} spacings of these five experimental diffraction rings fit with the mixed phase or either PEN phases. However, taking into account previous works for the non-equimolecular PEN:PFP blends [135], d_{hkl} values for the mixed phase and the pure PEN phase should be present in the PEN:PFP [2:1] blend. For this reason a deeper analysis of these five experimental diffraction rings has been performed in order to find out whether both,

the mixed phase and the pure PEN phase, contribute to these five experimental diffraction rings.

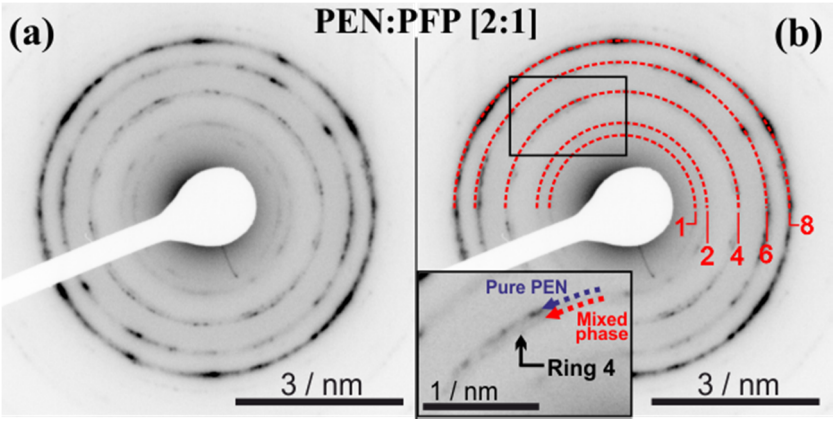

Figure 5.3-9. SAED pattern of the PEN:PFP [2:1] blend using a SAD aperture of 1.3 μm in diameter. The concentric diffraction rings visible in (a) are highlighted by red dotted lines and labelled with numbers in (b). The inset in (b) displays the splitting of ring 4.

Diffraction ring No.	**Experimental SAED patterns d_{hkl} (Å)**	**Mixed phase** [135] **d_{hkl} (Å)**	**PEN TF** [115]		**PEN Campbell** [102]	
			hkl	**d_{hkl} (Å)**	**hkl**	**d_{hkl} (Å)**
1	7.54	7.42	0 1 0[a]	7.51	1 0 0	7.29
2	6.56	6.49	1 0 0[b]	5.95	0 1 0	5.93
4	4.67	---	1 1 0	4.65	1 1 0	4.59
	4.78	4.79	---	---	---	---
6	3.74	3.72	0 2 0	3.75	2 0 0	3.65
8	3.22	3.27	1 2 0	3.17	2 1 0	3.10

[a] This reflection is forbidden and it will only be visible in the SAED patterns if plural (dynamical) scattering events are present.

[b] This reflection has a very weak intensity, therefore it is not always visible in experimental SAED patterns.

Table 5.3-2. The experimental d_{hkl} values determined for each ring in the experimental SAED patterns of the PEN:PFP [2:1] blend are compared to those reported in the literature for: the mixed phase by GIXD [135] (in the PEN:PFP [2:1] mixture) and the PEN TF [115] and Campbell phases [102] in [0 0 1] zone axis. The error of the d_{hkl} experimental values was estimated to be less than 3 % for the first two diffraction rings and less than 2 % for the rest of the rings.

As it has already been discussed for the PEN:PFP [1:1] blend, the diffraction rings with numbers 1 and 2 observed in the PEN:PFP [2:1] blend should belong to the mixed phase due to the same reasons above stated, i.e. the diffraction rings numbers

1 and 2 exhibit a higher intensity than the one expected for the PEN phases and appear at positions correlated to the mixed phase. Thus, the focus should be put on diffraction rings 4, 6, and 8 in order to answer the question whether they belong only to the mixed phase or if they have contributions of the two phases, the mixed phase and the pure PEN phase.

For diffraction rings 4, 6, and 8, the mixed and the PEN phases may not be directly recognized in the current SAED pattern experiments at first glance due to their similar d_{hkl} values. Nevertheless, if the focus is concentrated on these experimental diffraction rings, the following phenomena are observed:

- Diffraction rings 4, 6 and 8 are broader and more intense in the PEN:PFP [2:1] blend compared to those in the PEN:PFP [1:1] blend. This may indicate that diffraction rings of the mixed phase and the PEN phase overlap in the PEN:PFP [2:1] blend.
- A split of the experimental diffraction ring number 4 (see in the inset of Figure 5.3-9(b)). When the d_{hkl} spacings of these two diffraction rings are calculated, one agrees better with the mixed phase and the other one fits with the PEN phase (these two different d_{hkl} values for diffraction ring number 4 are also collected in Table 5.3-2).

In this way, these signs might indicate that two different phases, the mixed phase and the PEN phase, coexist in this PEN:PFP [2:1] mixture.

PEN:PFP [1:2] blend

For the investigated PEN:PFP [1:2] blend, eight concentric diffraction rings are observed in the SAED patterns when a SAD aperture with diameter size of 1.3 µm is used (cf. Figure 5.3-10(a)). As described earlier, their r^* distances are measured to calculate the d^*_{hkl} and d_{hkl} distances by averaging at least ten different SAED patterns. The resulting values are compared to those collected for the PEN:PFP [1:1] and PEN:PFP [2:1] blends. When a similar d^*_{hkl} value is obtained, the diffraction ring is labelled with the same number reported for the other blends considering a deviation of ± 0.0045 $Å^{-1}$.

Apart from the previously observed diffraction rings labelled with numbers 1, 2, 4, 6 and 8 (highlighted by red dotted lines), some extra rings appear (cf. Figure 5.3-10(b)). They are highlighted in purple and labelled with numbers 3, 5 and 7 since their associated d^*_{hkl} distances are in between the diffraction ring number 2 and 4, 4 and 6, and 6 and 8, respectively[V]. The corresponding d_{hkl} values of each diffraction ring are provided in Table 5.3-3. The d_{hkl} values of the diffraction rings highlighted with purple color (diffraction ring numbers 3, 5 and 7) match with the corresponding interplanar distances of the (0 0 2), (0 1 1) and (0 1 2) planes of pure PFP in both TF phase and bulk[VI].

The diffraction rings numbers 1 and 2 belong to the mixed phase due to the reasons already mentioned: i.e. the diffraction rings number 1 and 2 exhibit a higher intensity than the one expected for the PEN phases and appear at positions correlated to the mixed phase. The d_{hkl} values associated with diffraction rings 4, 6 and 8 may fit with the mixed phase or the PEN phase. Nevertheless in principle, the pure PEN phase is not expected as phase separated from PFP in this blend, since the attraction force between the PEN and PFP compounds to form the heterostructure is stronger than the one in their pure systems. In addition, there are no hints for the presence of the PEN phase as happens in the PEN:PFP [2:1] blend (mainly, the split of diffraction ring 4 is not observed). For these reasons, the diffraction rings 1, 2, 4, 6 and 8 are attributed to the mixed phase.

Hence, in the PEN:PFP [1:2] blend contributions of the mixed phase and the pure PFP phase (compound in excess) are recognized via the diffraction rings marked in red and purple color in Figure 5.3-10(b), respectively.

[V] In this PEN:PFP [1:2] blend the assignation of the diffraction number is according to their d^*_{hkl} value measured in a consecutive manner. This explains why the assignment of the observed diffraction rings of the PEN:PFP [1:1] and PEN:PFP [1:2] blends are not labelled with consecutive numbers.

[VI] For simplicity only the PFP TF phase is shown in Table 5.3-3, since the lattice parameters of both PFP polymorphs slightly differ (cf. Table 2.5-2, section 2.5.2). This designation of PFP as PFP TF will be maintained within the whole chapter.

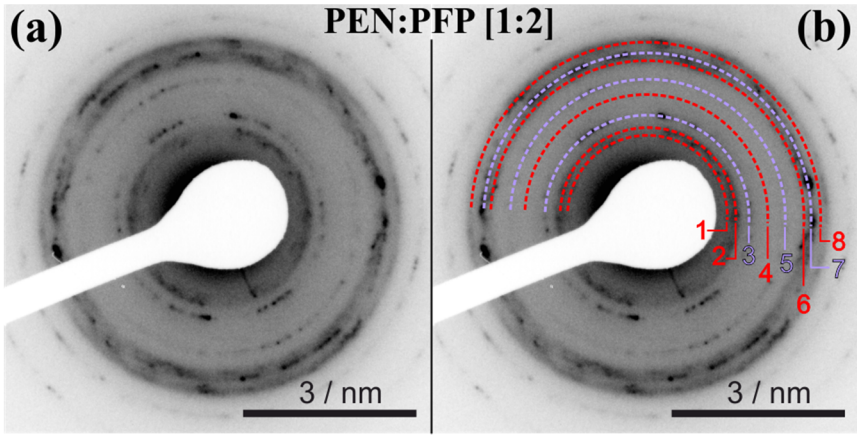

Figure 5.3-10. SAED pattern of the PEN:PFP [1:2] blend using a SAD aperture of 1.3 μm in diameter. The concentric diffraction rings visible in (a) are highlighted by red dotted lines for the mixed phase and by purple dotted lines for the PFP phase in (b).

Diffraction ring No.	**Experimental SAED patterns d_{hkl} (Å)**	**Mixed phase** [135] **d_{hkl} (Å)**	**PFP TF** [115]	
			hkl	**d_{hkl} (Å)**
1	7.43	7.38	---	---
2	6.60	6.60	---	---
3	5.80	---	0 0 2	5.74
4	4.82	4.80	---	---
5	4.26	---	0 1 1	4.20
6	3.79	3.73	---	---
7	3.59	---	0 1 2	3.55
8	3.31	3.29	---	---

Table 5.3-3. The experimental d_{hkl} values determined for each ring in the experimental SAED patterns of the PEN:PFP [1:2] blend are compared to those reported in the literature for: the mixed phase by GIXD [135] (in the PEN:PFP [1:2] mixture) and the PFP TF [115] in [1 0 0] zone axis. The error of the d_{hkl} experimental values was estimated to be less than 3 % for the first two diffraction rings and less than 2 % for the rest of the rings.

In summary, just five diffraction rings are observed in the PEN:PFP [1:1] and [2:1] blends. They are associated with the mixed phase for the PEN:PFP [1:1] mixture, whereas for the PEN:PFP [2:1] mixture signs of the contribution of the mixed phase and the PEN phase have been are found. Analogously, up to eight diffraction rings have been identified in the PEN:PFP [1:2] blend and they have been assigned to the mixed phase and the pure PFP phase.

5.3.4.2. SAED patterns using SAD apertures with 143 nm diameter

So far, the SAED pattern experiments have been acquired by selecting relative large areas of the specimen (in the order of microns squared). They have confirmed the same results as those previously reported by global characterization techniques.

Furthermore, the microstructural characterization has also been performed at a nanometer scale by selecting the smallest SAD aperture available in the microscope, it means that the SAED patterns have been acquired in an area of 0.0160 μm^2 by using a SAD aperture of 143 nm in diameter. In consequence, the SAED patterns mainly display individual spots since they belong to a single-crystalline region. This local characterization will be presented following the same order as before for the micrometer scale.

PEN:PFP [1:1] blend

Figure 5.3-11(a) displays the SAED pattern of the PEN:PFP [1:1] blend. Although its polycrystalline character is still visible, distinct and discrete reflections manifest the single-crystal nature of the region selected. The d_{hkl} spacings associated with each reflection have been calculated, finding similar values as reported for this blend in Table 5.3-1 (when the larger SAD aperture is used to acquire the SAED patterns). Consequently, they are labelled using the same numbers: 1, 2, 4, 6 and 8.

Two interesting features are detected in this SAED pattern: (i) a split of reflection number 4 in actually two reflections. The one closer to the center of the diffraction pattern presents a d_{hkl} distance which corresponds to the one expected for the mixed phase. This reflection is named '*inner reflection*' and is marked with a red semi-circle.

The other reflection further away from the center of the diffraction pattern is associated with a d_{hkl} spacing which belongs to the pure PEN phase. This reflection is named '*outer reflection*' and it is marked with a blue semi-circle. (ii) The reflection number 8 is broad and elongated, although a split is not clear visible. These issues concerning the identification of PEN reflections in this mixture are explained by the fact that the exact [1:1] ratio during the growth of the codeposited blends is difficult to obtain, and a negligible deviation of this ratio may lead to a slight excess of PEN[VII].

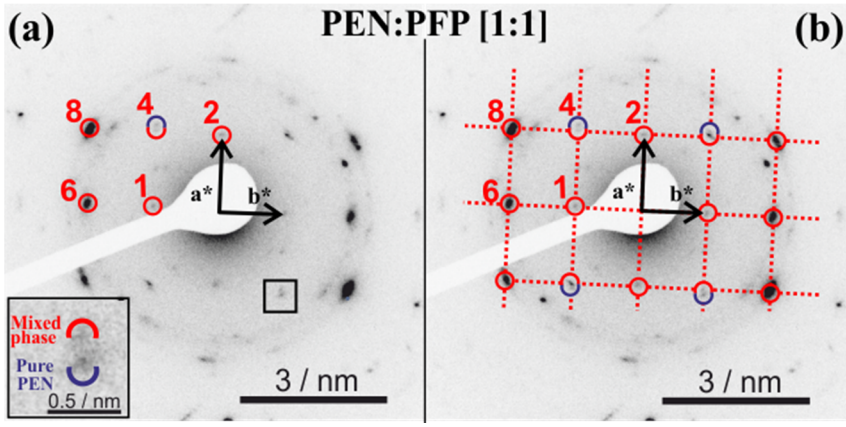

Figure 5.3-11. (a) SAED pattern of the PEN:PFP [1:1] blend. The inset shows a magnification in which two spots are actually detected for the reflection number 4. (b) Same diffraction pattern as (a) showing that the reflections of the mixed phase enclosed by red (semi-)circles are linear combinations of **a*** and **b*** vectors. Note that **a** and **b** directions were arbitrarily chosen (cf. footnote VIII, section 5.3.4).

The dashed lines drawn in Figure 5.3-11(b) illustrate that the reflections numbered with 1, 2, 4 (only the *inner* ones), 6 and 8 consist of a periodic array of spots in diffraction plane, in such a way that they are linear combinations of **a*** and **b*** vectors[VIII]. Thus, one may consider that these reflections belong to the same zone axis of the mixed phase. Thereby, the electron **diffraction pattern** of the **mixed phase** is displayed for the **first time**: it exhibits a similar geometry to the one of pure PEN in [0 0 1] orientation (cf. Figure 2.5-1(a), section 2.5.1).

[VII] The split of reflection number 4 as well as the elongation of reflection number 8 are not obvious at all positions and they only appear in some images recorded for this blend.

[VIII] Since the **a*** and **b*** axes are still unknown for the mixed phase, these axes have been arbitrarily assigned according to the known PEN TF phase (this designation will be maintained in the following for the mixed phase).

PEN:PFP [2:1] blend

In Figure 5.3-12, the microstructural characterization for the PEN:PFP [2:1] blend using the smallest SAD aperture is displayed (with diameter of 143 nm). As it has been previously shown, the mixed phase and the PEN phase should be present and phase separated from each other in this mixture. Hence, the local characterization is performed in such a way that individual crystals of the different phases are acquired. In Figure 5.3-12(a), the SAED pattern of mainly the mixed phase, whose reflections are highlighted by red (semi-)circles, is shown. The mixed phase can be distinguished from any pure PEN phase by the presence and the intensity of reflections numbered with 1 and 2[IX]. The blue semicircles highlight the contributions of the pure PEN phase, which can be observed by the split of reflections labelled with numbers 4 and 8 (cf. the inset for clarification). Notice that the split of the reflection number 4 has also been observed in the SAED pattern of the PEN:PFP [1:1] blend (Figure 5.3-11(a)). However, this split is more clearly distinguishable for the PEN:PFP [2:1] blend. Additionally, the reflection labelled with number 8 also exhibits a significant split, which cannot be clearly observed in the equimolecular blend.

Thus, the individual SAED pattern of the mixed phase has also been detected in the PEN:PFP [2:1] blend, together with hints which indicate the presence of a PEN phase. The signs associated with the PEN phase are more clearly visible in the PEN:PFP [2:1] blend (cf. Figure 5.3-12(a)) than in the PEN:PFP [1:1] blend (cf. Figure 5.3-11(a)), which is reasonable since the PEN:PFP [2:1] blend has intentionally PEN in excess. The reflections of the mixed phase highlighted by the red (semi-)circles are combinations of **a*** and **b*** vectors (cf. Figure 5.3-12(b)). This indicates that the reflections of the mixed phase lie closer to the primary reflection (at least in **a*** direction of the reciprocal space) compared to the ones of the PEN phase. Likewise, the pure PEN phase without any contribution of the mixed phase is also detected in the PEN:PFP [2:1] blend (cf. Figure 5.3-12(c)). The plausible polymorph

[IX] As previously stated, reflections labelled with numbers 1 and 2 should not appear for pure PEN unless multiple scattering effects are present. However, if they appear their intensity should be very low, which is not the case in this SAED pattern. Additionally, the d_{hkl} values calculated for these reflections match better for the mixed phase than for any pure PEN phase, especially values for reflection number 2.

of PEN is the TF since the first two reflections (0 1 0) and (1 0 0) are not visible and the d_{hkl} values determined from the experimental SAED pattern agree slightly better with that polymorph. This PEN phase exhibits the same orientation as reported for pure PEN grown on SiO_2 substrates, i.e. [0 0 1] zone axis [107].

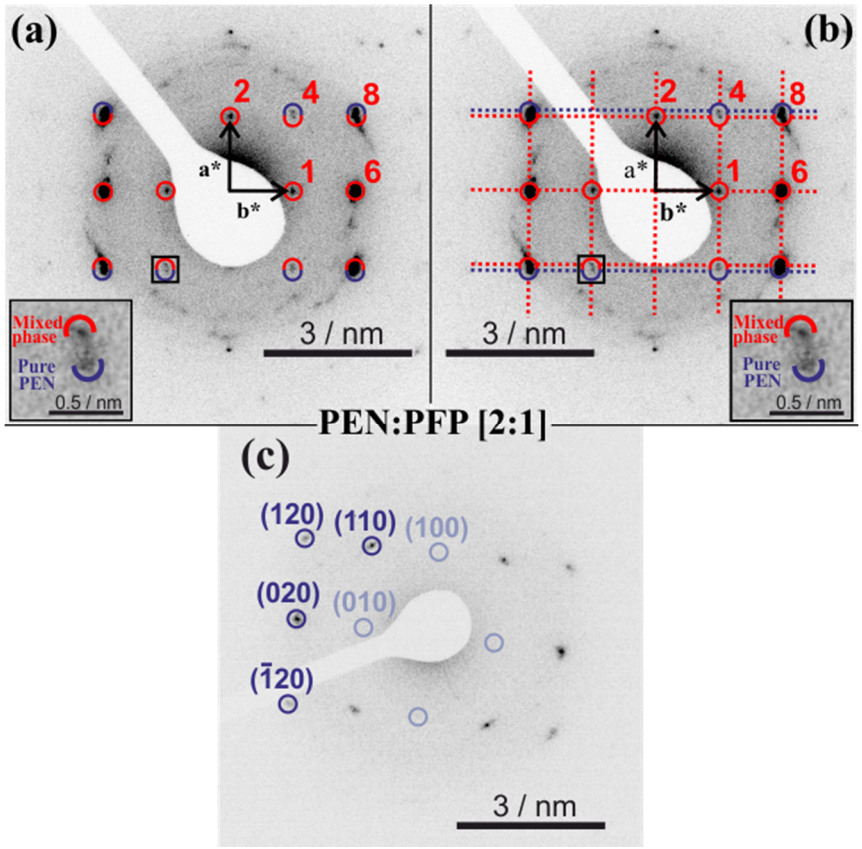

Figure 5.3-12. SAED patterns of the PEN:PFP [2:1] blend. (a) mixed phase whose reflections are marked with numbers (in red) according to their corresponding d_{hkl} spacings. The inset shows a magnification in which one reflection belongs to pure PEN (*outer* reflection enclosed by a blue semi-circle) and the other one corresponds to the mixed phase (*inner* reflection, enclosed by a red semi-circle). (b) Same diffraction pattern as (a) showing that the reflections of the mixed phase enclosed by red (semi)-circles are linear combinations of the vectors **a*** and **b***. The dashed lines are added to show that the reflections belong to one zone axis. Note that **a** and **b** directions have been chosen arbitrarily (cf. footnote VIII, section 5.3.4). (c) PEN phase detected in this sample. The diffraction pattern is indexed assuming the PEN TF phase in [0 0 1] zone axis.

PEN:PFP [1:2] blend

The microstructural characterization of the PEN:PFP [1:2] blend is displayed in Figure 5.3-13. In accordance with previous reports [135], reflections of the mixed phase and the PFP phase should be observed as separated from each other in this mixture.

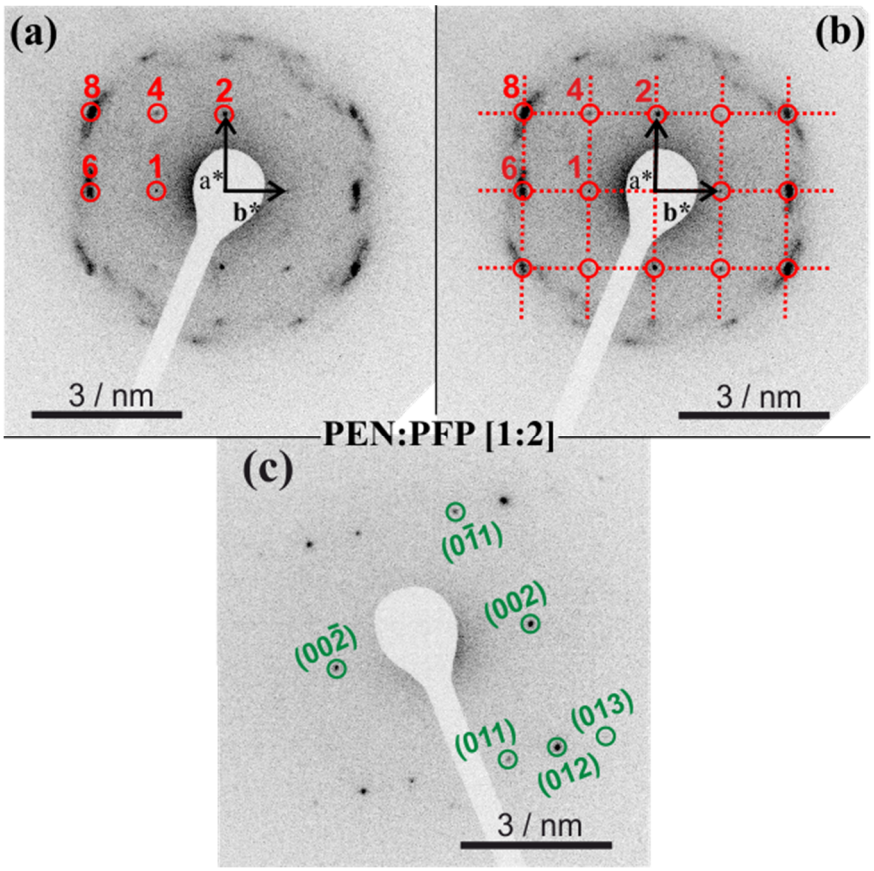

Figure 5.3-13. SAED patterns of the PEN:PFP [1:2] blend. (a) mixed phase whose reflections are marked with numbers (in red) according to their corresponding d_{hkl} spacings. (b) Same diffraction pattern as (a) showing that the reflections of the mixed phase enclosed by red (semi)-circles are linear combinations of the vectors **a*** and **b***. The dashed lines are added to show that the reflections belong to one zone axis. Note that **a** and **b** directions have been chosen arbitrarily (cf. footnote VIII, section 5.3.4). (c) PFP phase in [1 0 0] zone axis.

In this way, Figure 5.3-13(a) shows the individual SAED pattern of the mixed phase (SAD aperture of 143 nm in diameter). The mixed phase is shown exclusively without any contribution of the PEN phase. The arrangement of reflections in the SAED pattern and their associated d_{hkl} values agree with those observed for the mixed phase in the PEN:PFP [1:1] and [2:1] blends (cf. in Figure 5.3-13(b)). This fact clearly confirms that this is the SAED pattern exhibited by the mixed phase on this type of substrate. As explained above, the **SAED pattern** of the **mixed phase** has a **similar symmetry as** the one exhibited by the **PEN phase in [0 0 1] zone axis**. In addition, the single-crystalline SAED pattern of the pure PFP is shown in Figure 5.3-13(c). PFP adopts the same orientation as previously reported for pure PFP grown on SiO_2 substrate: the $[1\ 0\ 0]_{PFP}$ zone axis normal to the substrate surface [115].

The results of this subsection 5.3.4.2 are in line with those of subsection 5.3.4.1 'SAED patterns using SAD apertures with 1.3 µm diameter', and with those previously announced by global characterization techniques [135]: the mixed phase has always been found exhibiting the same crystalline structure, while the pure phase of the compound in excess is also present separated from the mixed phase. The pure phase adopts the same crystal orientation and structure as grown on SiO_2.

One of the important findings of this subsection is the revelation of the **mixed phase SAED pattern** for the first time, which exhibits quite similar symmetry and lattice constants as the one of pure PEN in [0 0 1] direction, suggesting a close similarity in the crystal structures between both compounds (the mixed phase and the PEN phase).

Once the microstructural characterization by SAED patterns is performed, further studies to gain knowledge about the arrangement and distribution of each phase in the blends are required. In this way, conventional DF-TEM is used for this purpose. This analysis is presented in the next subsection 5.3.5 only for the non-equimolecular blends, since mainly one phase is formed, i.e. the mixed phase, in the PEN:PFP [1:1] mixture.

5.3.5. TEM characterization: DF-TEM analyses

The non-equimolecular blends are presented in a different order in this section, since the DF-TEM analyses were performed in a different manner in both mixtures. The conventional DF-TEM analysis in the PEN:PFP [1:2] blend is presented first. Afterward, time sequence DF-TEM experiments are discussed for the PEN:PFP [2:1] blend.

5.3.5.1. PEN:PFP [1:2] blend

Figure 5.3-14 displays the DF-TEM pictures acquired for the PEN:PFP [1:2] blend. As it has previously been mentioned, diffraction rings numbers 3, 5 and 7 are associated with the PFP phase within this sample. Nonetheless, the only diffraction rings that can be chosen by the OA without selecting any reflection from the mixed phase are rings numbers 3 and 5. If diffraction ring number 7 is selected, the DF-TEM micrograph obtained will have contribution not only from the PFP phase but also from the mixed phase, since the diameter size of the smallest OA available in the microscope (1.1 nm^{-1} in the diffraction plane) is not small enough to avoid enclosing other diffraction rings. In principle, the same reason may apply to diffraction rings numbers 3 and 5 due to the presence of diffraction ring number 4 attributed to the mixed phase, but the reflections in this diffraction ring are hardly visible (cf. Figure 5.3-10) and, in consequence, their contribution to the DF-TEM picture is negligible. In this way, the DF-TEM images of the PFP phase are recorded using the diffraction ring number 5, since the handling to set the OA and select the diffraction ring number 5 was easier than the handling of the OA to select the diffracting ring number 3.

As illustrated in Figure 5.3-14(a), a fiber appears in bright contrast when the diffraction ring number 5 associated with PFP is selected, revealing that the **PFP phase** can be found **in the fibers**. In addition, a second image of this area is recorded illustrating that this bright intensity disappears after 18 seconds of beam irradiation (cf. Figure 5.3-14(b)). This fact indicates that the bright contrast of the fibers is caused by the fulfillment of the Bragg conditions rather than any diffuse scattering effect that may play a role because of the large thickness of these fibers. The corresponding BF-TEM image, where the fiber is more clearly distinguishable due to its black contrast, is shown in Figure 5.3-14(c).

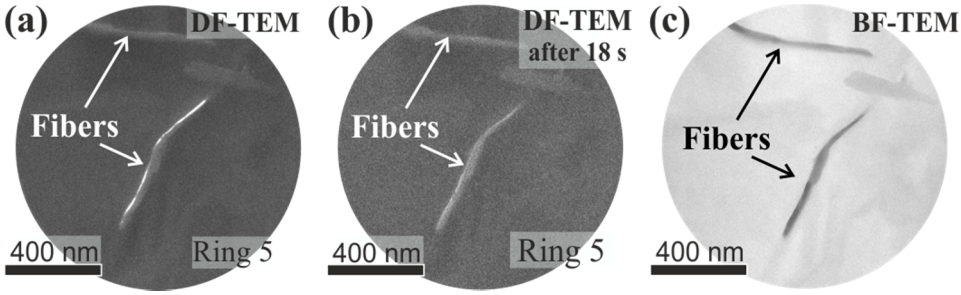

Figure 5.3-14. PEN:PFP [1:2] blend. (a) and (b) Sequential DF-TEM images acquired by selecting reflections of the diffraction ring number 5 with the OA (time step equal to 18 s between both). (c) Their corresponding BF-TEM image.

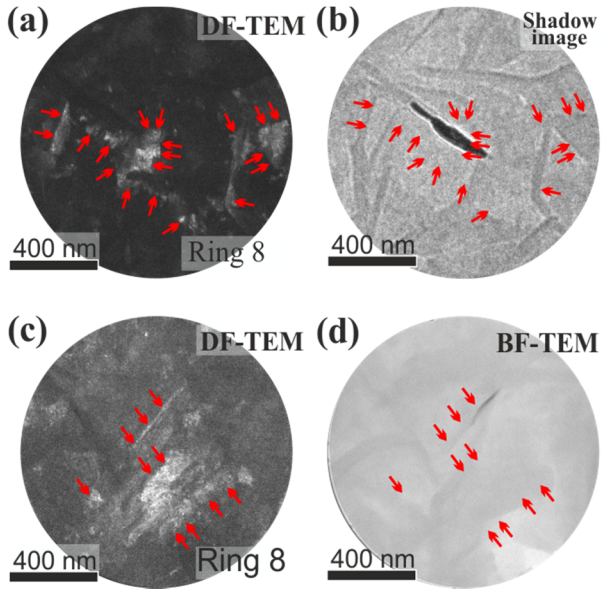

Figure 5.3-15. PEN:PFP [1:2] blend. (a) and (c) DF-TEM images acquired by selecting reflections of the diffraction ring number 8 with the OA. (b) and (d) The corresponding BF-TEM images to (a) and (c), respectively. The red arrows indicate the same diffracting areas in the DF-TEM images and their corresponding BF-TEM images.

Moreover, diffraction rings corresponding to the mixed phase have been selected to image the DF-TEM micrograph. In particular, diffraction ring number 8 (associated with the mixed phase) has been chosen since it is bright enough to image contrast in the DF-TEM picture and allows enclosing diffraction rings of the mixed phase exclusively (cf. Figure 5.3-15). As illustrated, the bright regions, and therefore, the **mixed phase** is found in the **area extended between the fibers**.

This analysis clarifies the unresolved issue about the arrangement of the different phases in this sample. Thus, the bright contrast exhibited by the fibers when PFP reflections are selected manifests that the fibers are formed by PFP. In contrast, the bright contrast displayed by the area extended between the fibers when reflections of the mixed phase are selected reveals that these regions correspond to the mixed phase.

5.3.5.2. **PEN:PFP [2:1] blend**

DF-TEM studies have also been performed in the PEN:PFP [2:1] blend, but they have been conducted in a different manner since the diffraction rings of the PEN phase and the mixed phase are almost overlapped, and therefore, the selection of reflections associated exclusively with one of the compounds is not possible. In consequence, the PEN:PFP [2:1] blend has been analyzed by time-dependent sequences, which have been performed firstly via electron diffraction and next via DF-TEM. By acquiring consecutive SAED patterns, the degradation times of the mixed phase and the PEN phase have been studied in order to check if the different stabilities presented for each phase could be used to distinguish both in further DF-TEM analysis.

Degradation analysis via electron diffraction

In the *degradation analysis via electron diffraction*, the radiation effects can be linked to the properties of the sample. The electron beam is used for causing degradation in the material. This degradation can be observed as changes in the diffraction pattern and allows obtaining information about the crystallinity of the sample.

The stability of the PEN:PFP [1:1] blend is analyzed firstly by acquiring a time series of SAED patterns from a constant illuminated sample region. This allows describing the time dependence behavior of the mixed phase with the exposure to electron beam irradiation, addressing the question whether all reflections are equally affected by the electron beam or not. Once the degradation behavior in this sample is known, the PEN:PFP [2:1] sample is inspected based on the idea that: if two different phases coexist in a material (the mixed phase and the PEN phase), different degradation times of each phase might occur since different phases could present different stabilities under the electron beam.

The SAED pattern series for the PEN:PFP [1:1] blend acquired under an electron dose of $1.3x10^{-3}$ $C \cdot s^{-1} \cdot cm^{-2}$ are displayed in Figure 5.3-16. In the beginning (Figure 5.3-16 (a)), five diffraction rings are detected. They are labelled with numbers 1, 2, 4, 6 and 8 according to their d_{hkl} values. The diffraction ring number 1 is the one most rapidly affected by the exposure to radiation, disappearing after 18 seconds. However, the rest of the diffraction rings remain in their respective positions although in a lower intensity compared to the beginning (cf. Figure 5.3-16(b)). After 30 seconds, the diffraction rings numbers 2, 4, 6 and 8 are almost gone (cf. Figure 5.3-16(c)). Finally, after 60 seconds all diffraction rings, and therefore the complete crystallinity of the sample, fully disappear (cf. Figure 5.3-16(d)). Thus, this examination shows that the lattice planes associated with the diffraction ring number 1 are degraded by the electron beam the fastest, while the rest of the diffraction rings exhibits similar degradation rates, disappearing almost simultaneously.

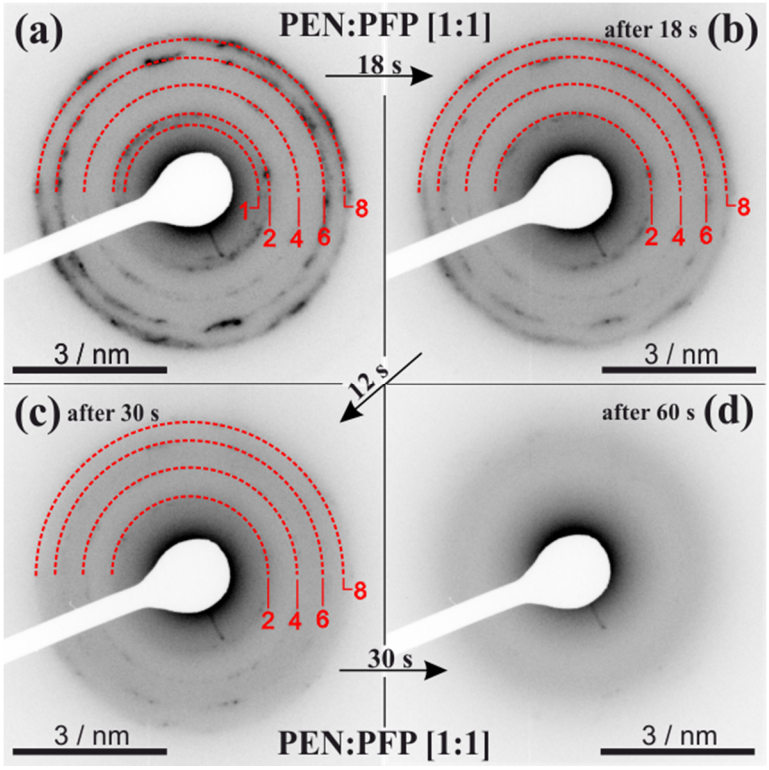

Figure 5.3-16. SAED patterns of PEN:PFP [1:1] over time. (a) Initially, (b) after 18 s, (c) after 30 s, and (d) after 60 s. The electron-dose and the SAD aperture used were $1.3x10^{-3}$ $C \cdot s^{-1} \cdot cm^{-2}$ and 1.3 µm in diameter, respectively. The exposure time per image was 1 s.

The same degradation analysis has been performed in the PEN:PFP [2:1] blend (cf. Figure 5.3-17) at similar conditions as in the PEN:PFP [1:1] blend (electron dose of $1.1x10^{-3}$ $C \cdot s^{-1} \cdot cm^{-2}$) to compare both mixtures. As displayed in Figure 5.3-17(a), five diffraction rings are detected at the beginning of the SAED pattern time series acquisition. They are labelled with numbers 1, 2, 4, 6 and 8. After ca. 32 seconds, the diffraction rings numbers 1 and 2 are completely degraded and they disappear (Figure 5.3-17(b)), whereas the rest of the diffraction rings remain in their respective positions but in a lower intensity. Even after 60 seconds (Figure 5.3-17(c)), these rings can still be identified giving evidence that their associated crystal structure is not destroyed yet. Just after approx. 120 s these diffraction rings are no longer visible in the SAED patterns.

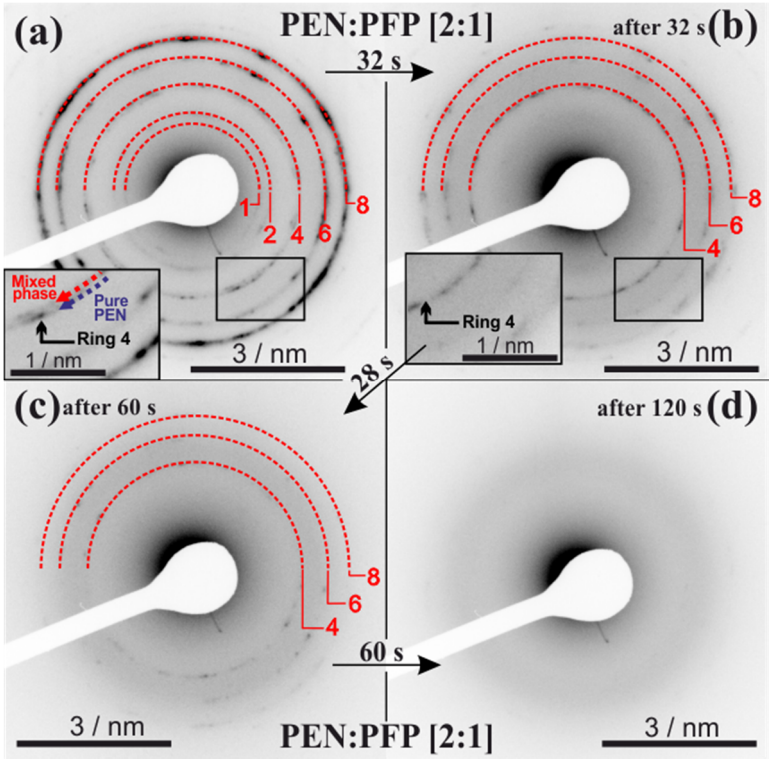

Figure 5.3-17. SAED patterns of PEN:PFP [2:1] over time. (a) Initially, (b) after 32 s, (c) after 60 s, and (d) after 120 s. The electron dose and the SAD aperture used were $1.1x10^{-3}$ $C \cdot s^{-1} \cdot cm^{-2}$ and 1.3 µm in diameter, respectively. The inset in (a) shows the split of diffraction ring number 4. The exposure time per image was 1 s.

In a closer inspection of the SAED pattern time series, some interesting features are additionally observed: firstly, a split of diffraction ring number 4 (cf. inset of Figure 5.3-17(a)). This split cannot be longer identified in Figure 5.3-17(b) (see the inset), (c) and (d). Secondly, the diffraction rings numbers 6 and 8 are more intense and broader in Figure 5.3-17(a) compared to Figure 5.3-17(b) and (c), indicating that a higher spread of spatial frequencies contributes to these rings in Figure 5.3-17(a).

To sum up, the following outcomes are found after 32 seconds of SAED pattern time series acquisition in the PEN:PFP [2:1] blend: (i) diffraction rings numbers 1 and 2 disappear. (ii) The split of diffraction ring number 4 is no longer detected. (iii) The width of diffraction rings 6 and 8 changes. In combination with the information from the PEN:PFP [1:1] blend, these three facts can be explained by the initial presence of both, the mixed phase and the PEN phase, in this PEN:PFP [2:1] blend. The mixed phase is destroyed after ~30 seconds, and the remained diffraction rings correspond to the PEN phase.

Thus, the PEN phase and mixed phase present in the PEN:PFP [2:1] blend exhibit a different stability when they are irradiated under the electron beam. This different degradation time will be used to study de arrangement and distribution of the two phases in the mixture.

Time-dependent DF-TEM sequences

The degradation analysis via electron diffraction has revealed that the diffraction rings of the mixed phase disappear faster than those corresponding to the PEN phase. According to these results, if diffraction rings for the mixed phase and the PEN phase are selected by the OA (diameter size of 1.1 nm^{-1}) diameter and imaged in a time dependent DF sequence, the mixed phase should disappear first and the pure PEN phase should remain in a brighter contrast. This fact could be used to obtain information on the arrangement and distribution of the mixed phase and the PEN phase in the PEN:PFP [2:1] blend.

The time dependent DF sequence is presented in Figure 5.3-18. Diffraction rings numbers 6 and 8 (both have contributions of the PEN phase and the mixed phase) were selected for the acquisition of the DF sequence. To observe changes in the

intensity, regions that are brighter at the beginning and at the end of the sequence are marked and labelled from A to F. The total intensity of these regions is measured and evaluated (cf. graphic of Figure 5.3-19[X]). As it can be seen, there are areas (A, C, D and F) whose intensity decreases very fast in the beginning, but after a while, the decay rates are reduced. On the other hand, there are some other areas where this decay of intensity occurs in a progressive manner along the time-dependent DF-TEM sequence. These outcomes can be explained by a strong contribution of the mixed phase with only small amounts of the PEN phase in the regions marked with A, C, D and F. In contrast, the areas highlighted with B and E are expected to have a majority of PEN phase. Thus, the mixed phase contributing in areas A, C, D and F is destroyed faster in the beginning, leading to an unavoidable decrease of the intensity. The PEN phase is not destroyed so fast under the electron beam, causing a gradual decay of brightness.

An additional conclusion can be extracted from the time-dependent DF-TEM sequence presented in Figure 5.3-18, that is, the mixed phase and the PEN phase are distributed in a grainy structure with domains in the order of (10-60) nm. Thus, no evidence for single domains at a relative large scale (in the order of micrometers) is found for the PEN phase and the mixed phase. The lower value of the grain size is in consonance with those reported by Hinderhofer et al. [135] for such domains, i.e. (10-20) nm, determined by GIXD experiments. However, larger grain sizes ((10-60) nm vs (10-20) nm) are found in this time-dependent DF-TEM sequence. This small discrepancy may be explained by the method itself: the coherence length which was determined from GIXD experiments gives the averaged size of crystalline areas that are restricted by defects or crystallographic orientations, whereas for DF-TEM measurements defects could not be visible or not taken into account in the grain size.

In addition, an effect that should not be neglected in DF-TEM sequences of beam sensitive materials is that a few areas which appear dark in the beginning could become brighter in the consecutive DF-TEM series. This effect has been reported and

[X] Note that the electron doses used for the acquisition of the DF-TEM sequence is different than that used for the acquisition of the degradation analysis via electron diffraction (1.7×10^{-3} $C \cdot s^{-1} \cdot cm^{-2}$ vs 1.1×10^{-3} $C \cdot s^{-1} \cdot cm^{-2}$, respectively). Hence, the time at which the phases disappear is not comparable.

ascribed to two possible sources [220]: the small bending of the sample or the strain caused by the amorphization during the electron beam irradiation. Even though this effect cannot be fully prevented, one might assume that it has a minimal impact on the evaluation of the DF-TEM sequence images because no hints for this effect are visible in the areas selected (cf. Figure 5.3-18).

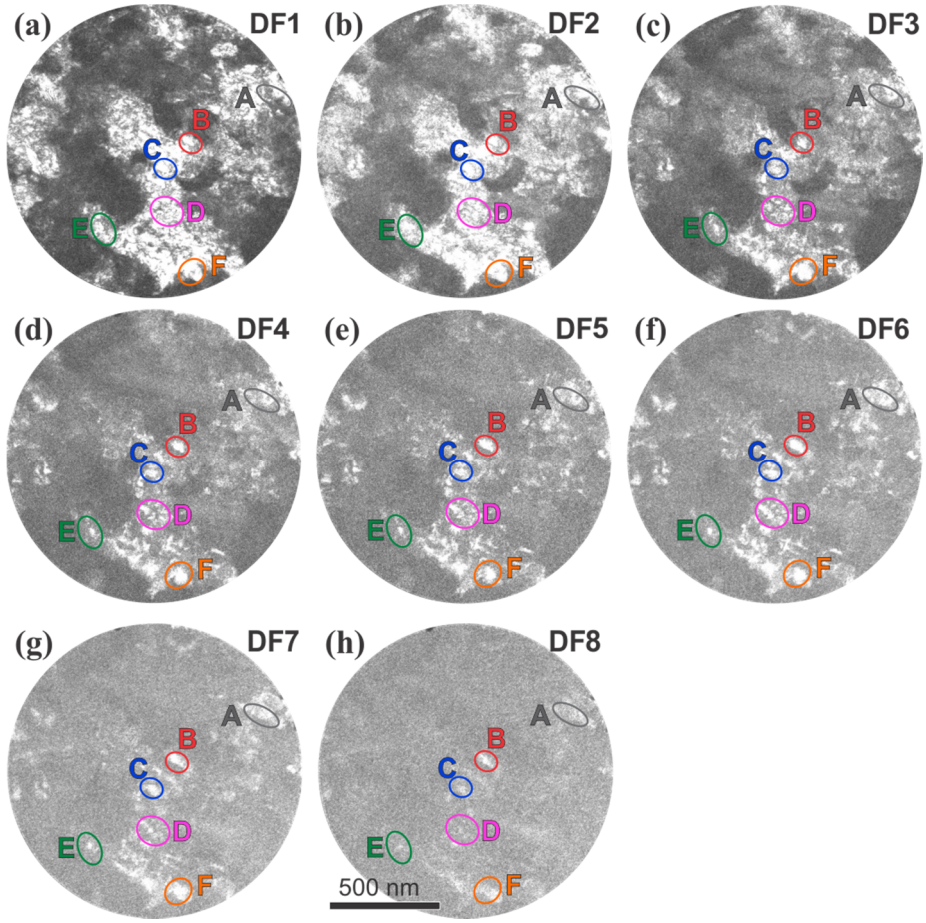

Figure 5.3-18. Sequence of DF-TEM images of the PEN:PFP [2:1] blend selecting rings numbers 6 and 8: (a) in the beginning, from (b) to (e) after time steps of 4 s, (f) after a time step of 10 s, and (g) and (h) after time steps of 12 s. The sample was irradiated with an electron dose of 1.74×10^{-3} $C \cdot s^{-1} \cdot cm^{-2}$. The areas enclosed by coloured ellipses (from A to F) mark the regions used for the intensity profiles shown in Figure 5.3-19.

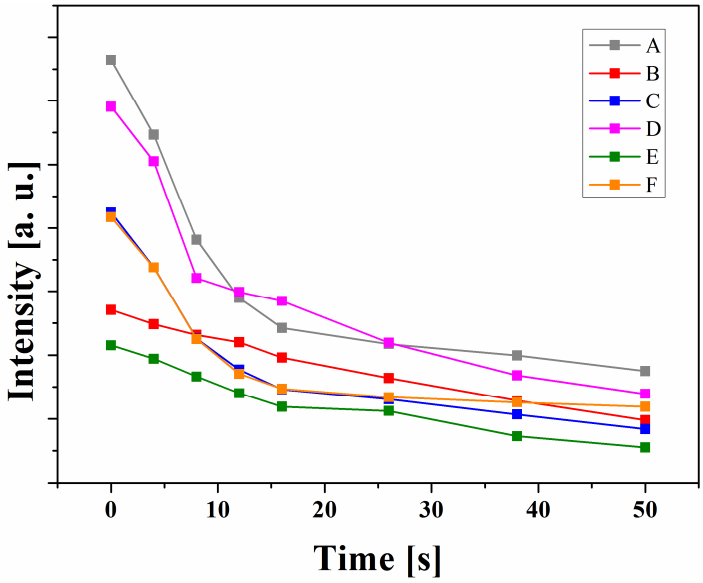

Figure 5.3-19. Intensity profiles of the areas marked from A to F in Figure 5.3-18. The intensity profiles were normalized to an exposure time of 1 second.

5.3.6. Conclusions

Previous studies on codeposited PEN and PFP mixtures grown on SiO_2 substrates were performed by global characterization techniques. They reported the coupling between PEN and PFP at a molecular level by the formation of a mixed phase crystal structure with a stoichiometrically equal [1:1] mixing ratio of both compounds PEN and PFP. For other different mixing ratios, a phase separation was found between the molecules of the excessive pure phase and the mixed phase.

In the current study, codeposited blends of PEN and PFP with mixing ratios of [2:1], [1:1] and [1:2] have been grown on SiO_2 substrates. The morphology of the three different blends has been studied by SEM and STEM techniques. It has also been compared to the pure phases grown on the same substrate. The PEN:PFP [1:1] blend exhibits a tangle of fibers. This morphology is very different from that identified for pure PEN and/or PFP phases. In contrast, the PEN:PFP [2:1] and [1:2] blends clearly reveal a more PEN-like and PFP-like character, respectively. Less sharp and grainy fibers are observed in the mixture with the excess of PEN, while some fibers on top of a background layer are visible in the blend with excess of PFP.

Next, EDX measurements have been performed with the aim of achieving a local elemental distribution, in such a way that it could be linked to different phases that coexist in each mixture. However, results obtained by EDX have not been conclusive requiring additional analyses by other techniques, i.e. SAED experiments and DF-TEM analyses.

SAED experiments have been performed by using two different diameters of SAD apertures, 1.3 μm and 143 nm, on the three different blends. Focusing on the SAED pattern experiments with larger SAD apertures, concentric diffraction rings denote the polycrystalline character of the mixtures. In the SAED pattern of the PEN:PFP [1:1] blend, the diffraction rings associated with the mixed phase formed between PEN and PFP have been identified. In the PEN:PFP [2:1] mixture, the diffraction rings of the PEN phase and the mixed phase have not been fully recognized at first glance. However, some signs for the presence of the two different phases have been detected in an extensive analysis of the mixture: some diffraction rings are broad,

and one of the diffraction rings is actually split in two rings, indicating that two different phases, i.e. the mixed phase and the PEN phase, may coexist in the PEN:PFP [2:1] mixture. In the PEN:PFP [1:2] mixture, the diffraction rings that correspond to the mixed phase together with those that belong to the PFP have been detected easily.

SAED patterns performed with the smaller SAD aperture available have revealed the monocrystalline SAED pattern of the mixed phase for the first time on this substrate. The diffraction pattern is rather similar to the one of the pure PEN in [0 0 1] direction, suggesting crystal-structural similarities between both, the mixed phase and the pure PEN phase. Likewise, it has also been illustrated that the reflections of the mixed phase are closer to the primary reflection (at least in **a*** direction) than the reflections associated with the PEN phase. This fact is easier to see in the SAED pattern of the blend with PEN in excess than in the equimolecular blend. These findings indicate that the molecules in the unit cell of the mixed phase may exhibit a similar arrangement to the ones of the pure PEN TF phase, only differing in the lattice parameters. The mixed phase should exhibit slightly larger lattice spacings than the pure PEN TF polymorph.

The microstructural characterization by SAED patterns has been followed by DF-TEM analyses in order to study the arrangement and distribution of the different phases in the non-equimolar blends. The DF-TEM analyses have not been performed in the equimolecular blend [1:1] since this mixture exhibits mainly one phase; i.e. the mixed phase. In the case of the PEN:PFP [1:2] blend, this investigation has revealed that the fibers of the foreground consist of pure PFP while the mixed phase is found in the region extended between these fibers. In the PEN:PFP [2:1] blend, similar DF-TEM characterization could not be carried out since the reflections of the mixed phase and the pure PEN phase almost overlap. Hence, the PEN:PFP [2:1] blend has been analyzed by means of time-dependent sequences, which have been performed first via electron diffraction and next via DF-TEM. The characterization by electron diffraction has shown that the mixed phase is degraded faster than the PEN phase when they are irradiated under the electron beam, and consequently, the diffraction rings attributed to the mixed phase disappear earlier in the SAED pattern.

The different degradation time between the mixed phase and the PEN phase has been used to study the PEN:PFP [2:1] blend by time-dependent DF-TEM sequences. This study has provided information on the arrangement and distribution of the mixed phase and the PEN phase, revealing that both phases are distributed in a grainy structure with domains in the order of (10-60) nm.

Once again, DF-TEM characterization has been shown as a powerful tool to study the arrangement of different phases whenever reflections of each phase can be selected by the OA. The DF-TEM micrographs have provided a valuable information on the distribution of the different phases in the samples. Hereby, the possible scenarios of the arrangements of the two different phases in these non-equimolecular mixtures are illustrated in the sketches of Figure 5.3-20(a) and (b) for the PEN:PFP [1:2] and [2:1] mixtures, respectively.

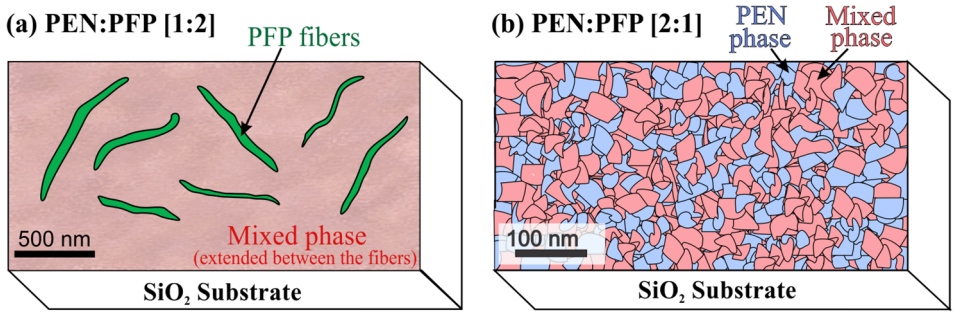

Figure 5.3-20. (a) Sketch of the PEN:PFP [1:2] blend. The fibers in green represent the PFP phase while the slightly red background consists of the mixed phase. (b) Sketch of the PEN:PFP [2:1] blend. This sample exhibits randomly oriented grains of PEN and the mixed phase which are marked in blue and red color, respectively.

In the field of the new materials that can satisfy the needs of the donor-acceptor junctions, heterostructures of PEN and PFP are promising candidates. However, their physical properties, and in particular their crystalline structure, should be fully known in order to obtain a high efficiency of the device. In this regard, TEM techniques have been proven as a suitable tool to characterize these organic molecular films, even though damage by electron beam radiation cannot be entirely prevented. This study has tried to 'shed light' on this matter delving into the arrangement of the mixed phase and the distribution of the different phases present in such materials.

5.4. Microstructural characterization of PEN and PFP blends grown on KCl

The microstructural characterization of PEN and PFP heterostructures grown on an amorphous substrate such as SiO_2 has already discussed (cf. section 5.3). However, it is known that the substrate can influence on the arrangement and orientation of the deposited organic film, KCl has been chosen as substrate since alkali halide supports have been found to lead to epitaxial growth and large crystalline OSC films [28–31]. The aim of this chapter is the analysis of the influence of the KCl substrate on the arrangement of the PEN:PFP blends. Two different mixing rations will be shown, one with excess of PEN ([2:1]) and another one with excess of PFP ([1:2]).

This section is organized as follows: the experimental conditions, particularly the sample preparation procedure for (S)TEM analyses, are presented first. Afterward, this subchapter is divided in two parts: one for the PEN:PFP [2:1] blend and another one for the PEN:PFP [1:2] blend. The morphology of the samples together with their characterization via (S)TEM analyses are presented and discussed in each section.

5.4.1. Experimental

The organic blend films consisting of PEN (Sigma-Aldrich, purity ≥ 99.9 %) and PFP (Kanto Denka Kogoyo Co., purity ≥ 99 %) were grown under UHV conditions (≤ 1.00×10^{-8} mbar base pressure) by OMBD from a resistively heated Knudsen cell at typical deposition rates of 6 Å/min as determined by a QCM. The samples were grown at typical temperatures of 330 K with a nominal total thickness of approximately 40 nm onto (0 0 1) faces of freshly cleaved KCl substrates (Korth Kristalle, Germany) of approximately 3 mm of thickness. The PEN:PFP ratios deposited on KCl substrates were: PEN:PFP [2:1], [1:1] and [1:2]. However, when the PEN:PFP [1:1] mixture was characterized, an anomalous growth of the organic layer was observed: the layer consisted of a discontinuous film and presented many different morphologies. This unexpected behavior was ascribed to the steps presented by the KCl substrate surface after the cleaving process. For this reason, the PEN:PFP [1:1] mixture was neglected, and therefore, this mixture is not part of this investigation.

In the content of this thesis, when the PEN:PFP mixtures grown on KCl are referred, only the [2:1], and [1:2] blend ratios are considered.

After the organic film deposition, a preparation procedure was required to study the samples by (S)TEM techniques since they were not electron transparent. In the case of inorganic materials, there are several ways to thin down the sample: from conventional methods like milling, polishing and ion milling steps [221,222], to the use of the focused ion beam (FIB) technique [223–225]. However, the sensitivity of organic materials to high temperatures and beam radiation makes such techniques unsuitable to get the electron transparency. To overcome these drawbacks, a distinct preparation method was used. This alternative procedure is based on a reported sample preparation method by Fryer and Holland [226] and some preceding works carried out in the Structure and Technology Research Laboratory Group by Benedikt Haas [220] and Wiebke Witte [227]. The procedure used is described in Figure 5.4-1 and consists of the following steps:

- First, the sample formed by the OSC layer of codeposited PEN:PFP and the KCl substrate (cf. Figure 5.4-1(a)) is cleaved to small pieces of ca. 3x3x3 mm^3 (cf. Figure 5.4-1(b)).
- Second, the KCl substrate is backside thinned down up to about 1 mm by means of a silicon carbide grinding paper (Buehler, Grit 320/P400).
- Third, a plastic box with a hydrophobic membrane is used (cf. Figure 5.4-1(c)). A typical holey carbon copper support grid is placed onto the hydrophobic membrane. Furthermore, a droplet of ultrapure water is deposited on the copper support grid with the help of a syringe. The hydrophobic membrane is utilized since water tends to 'bead' on hydrophobic surfaces forming discrete droplets (Figure 5.4-1(c)).
- Fourth, the thinned piece of the OSC layer on KCl is immersed into the droplet of water (Figure 5.4-1(d)). Due to the good solubility of KCl in water, it dissolves very fast until the solution reaches the saturation level.

- Fifth, the KCl saturated solution is carefully removed in order to avoid damages of the OSC layer and replaced with fresh ultrapure water. When the substrate is dissolved, the OSC layer is detached from the KCl and it floats on top of the droplet of water (Figure 5.4-1(e)).
- Sixth, the majority of water is removed and the remaining water is sponged with a small piece of filter paper (Figure 5.4-1(g)). In this stage, a careful handling is required since the OSC layer could quickly be damaged.
- Seventh, once the water is completely removed, the OSC layer is attached on the copper support grid (Figure 5.4-1(h)). In addition, the OSC layer on the TEM grid is washed two or three times with ultrapure water to prevent from a possible recrystallization due to the presence of remaining dissolved KCl. The water is again removed by the syringe and the filter paper. When the TEM grid is dried, it is collected with a tweezer and stored under vacuum conditions, avoiding an exposure to light that could decrease the lifetime of the sample.

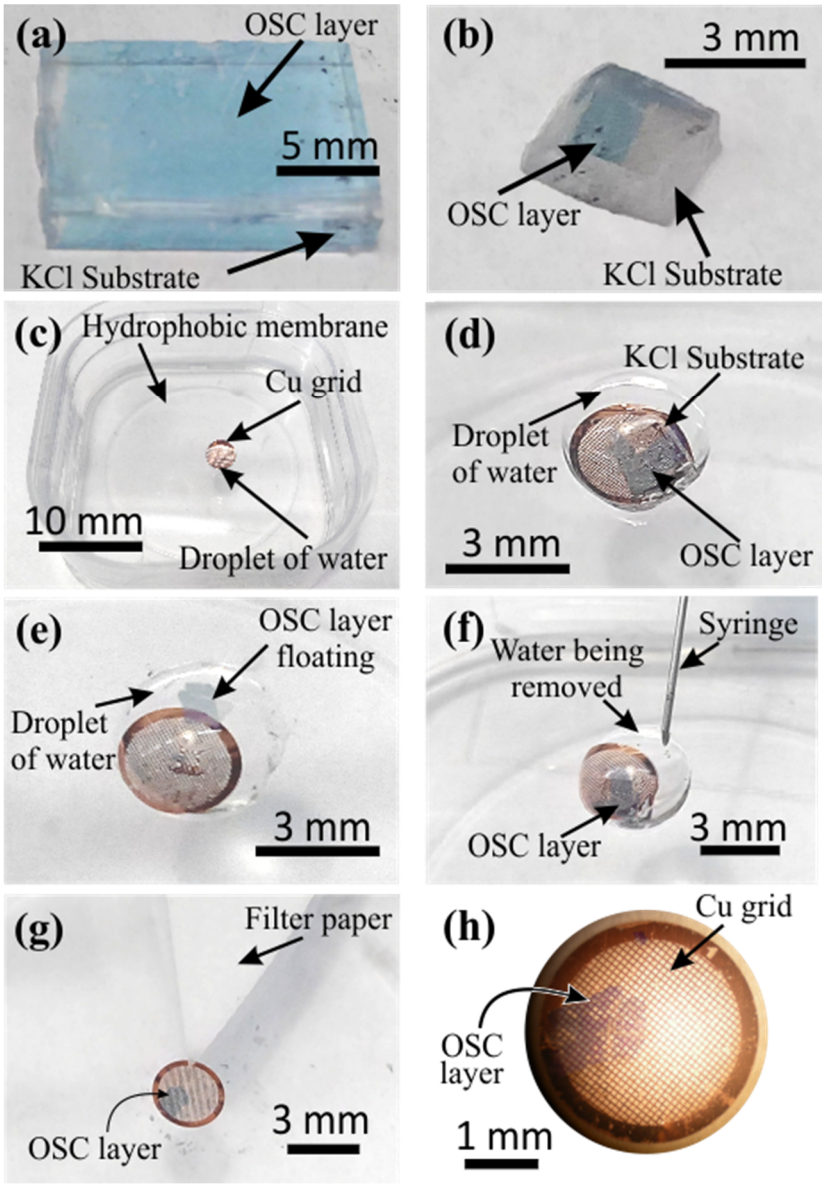

Figure 5.4-1. Steps for sample preparation. (a) OSC layer on the KCl substrate. (b) Sample cleaved in a small piece. (c) Assembling used to dissolve the KCl substrate. (d) Sample immersed into the droplet of water. (e) OSC layer detached from the KCl substrate and floating onto the droplet of water. (f) Water removed by a syringe. (g) Remaining water sponged with a filter paper. (h) OSC layer placed onto the TEM grid.

The film morphology was characterized by the JEOL JIB-4601F operated at 5 kV for SEM imaging. The SEM measurements were performed when the organic films were still attached to the KCl substrate and after the preparation process (when the OSC layers were placed onto the copper support grid). In the first case, a platinum coating layer of a thickness ca. 5 nm was required. This coating creates a conductive layer of metal on the sample that not only inhibits charging effects caused by the low conductivity of the KCl substrate, but also reduces thermal damage and improves the secondary electron signal required for topographic examination in the SEM.

TEM techniques such as SAED patterns, DF- and BF-TEM imaging, and HRTEM were performed in the JEOL JEM-3010 operated at its maximum acceleration voltage of 300 kV. In order to reduce the beam damage, low electron doses of $(0.5\text{-}2)\text{x}10^{-3}$ $\text{C}\cdot\text{s}^{-1}\cdot\text{cm}^{-2}$ were applied. These low dose conditions were achieved by reducing the beam current, using a small condenser aperture and increasing the spot size of the beam. The EDX analyses were performed in the JEOL JEM-2200FS equipped with a Bruker XFlash 5060 detector. The samples were studied in all cases in plan-view orientation with the electron beam directed perpendicular to the sample surface at **room temperature** (≈293 K). In addition, all investigated blends used for (S)TEM examinations - with the exception of those used for EDX analyses - were vapor coated with approx. (5-10) nm of amorphous carbon for better stability during electron beam irradiation.

5.4.2. PEN:PFP [2:1] blend

5.4.2.1. Morphology of the sample

Figure 5.4-2(a) and (b) correspond to SEM micrographs of the PEN:PFP [2:1] blend after preparing the sample for TEM analyses (with the OSC layer placed onto the copper support grid). As can be seen in Figure 5.4-2(a), this mixture consists of a uniform and homogeneously distributed layer with domains rotated in-plane in two orthogonal directions. When the same area of the sample was tilted by 55º relative to the surface normal (cf. Figure 5.4-2(b)), the uniform layer exhibits a flat lying orientation on the support grid (there are no hints of any upright orientation). Since Figure 5.4-2(a) and (b) belong to the same area of the sample, the two regions highlighted by the black dotted circles correspond to the same hole presented by the holey carbon film of the non-tilted/tilted sample, respectively. Per contra, Figure 5.4-2(c) and (d) were acquired when the organic films were still attached to the KCl substrate with the aim of correlating the direction of the elongation of the domains with respect to the substrate. The KCl edges are marked in these pictures by black dotted lines, they correspond to the substrate ⟨1 0 0⟩ directions[I]. The elongation of the domains is aligned in-plane parallel or perpendicular to the KCl edges, denoting that the elongated domains point along the KCl ⟨1 0 0⟩ directions.

In the following subsections, a deep analysis of the crystallinity and composition of this sample is presented. The local composition is analyzed by EDX. Next, electron diffraction analyses (SAED patterns) as well as DF/BF-TEM imaging are used to study the local orientation and crystalline properties of the mixture. Complementary analyses by HRTEM are also presented below.

[I] Within the scope of this chapter, the notation $\langle 1\ 0\ 0 \rangle_{KCl}$ only considers $[1\ 0\ 0]_{KCl}$ and $[0\ 1\ 0]_{KCl}$ directions, since the $[0\ 0\ 1]_{KCl}$ is normal to the KCl surface.

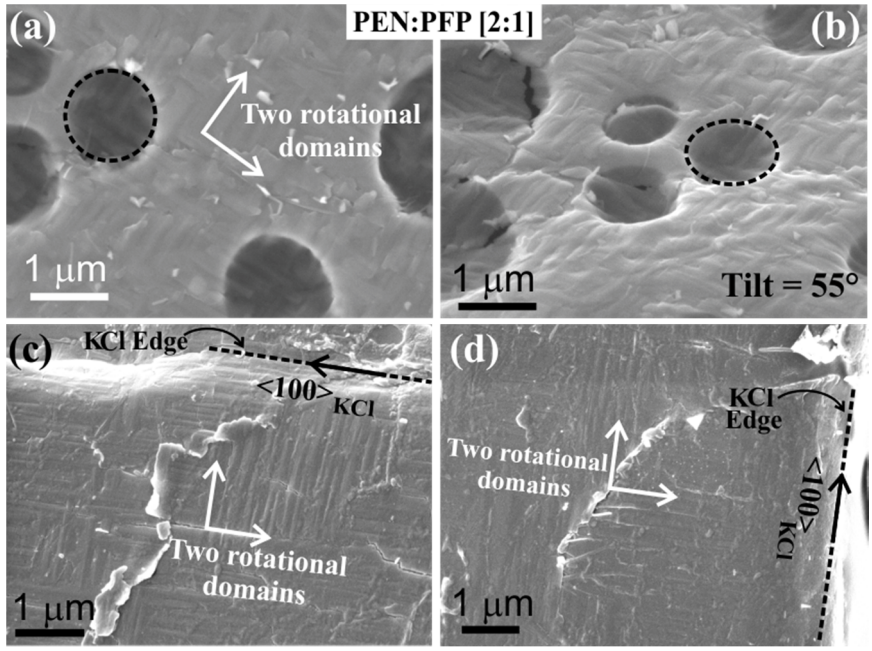

Figure 5.4-2. SEM images of the PEN:PFP [2:1] blend. Upper panel has been acquired after the sample preparation process. (a) Non-tilted sample. (b) Sample tilted by 55º relative to the surface normal. The black dotted circles highlight the same region in (a) and (b). Lower panel: (c) and (d) have been acquired with the organic layers still attached to the KCl substrate.

5.4.2.2. TEM characterization: EDX analysis

The sample has been studied in a hole to avoid misleading results due to the influence of the carbon coming from the holey carbon film. The area of the PEN:PFP [2:1] blend used for the EDX analysis in STEM mode operation is shown in Figure 5.4-3(a). The electron probe has been placed on some features visible in the sample (points 3, 4 and 5) and on some positions chosen randomly (points 1, 2, 6, 7 and 8) to check if point-spectra with and without fluorine atom contribution are detected. The spectra collected for these points are presented in Figure 5.4-3(b). The inset is a magnified region of the signal registered for the fluorine peak. Just small amounts of fluorine with very noisy signals are detected. Hence, the determination of the C/F is not possible. In addition, measurements performed in the identified features (points 3, 4 and 5) exhibit a very high content of carbon atoms. This fact only indicates that they correspond to thicker regions. Thus, the spectra collected for these points have just revealed that the samples are mainly composed by carbon and very small

amounts of fluorine, but no additional information can be obtained. Note that only few measurement points are shown for the PEN:PFP [2:1] blend, but the sample has exhaustively been studied and in all cases similar results have been obtained.

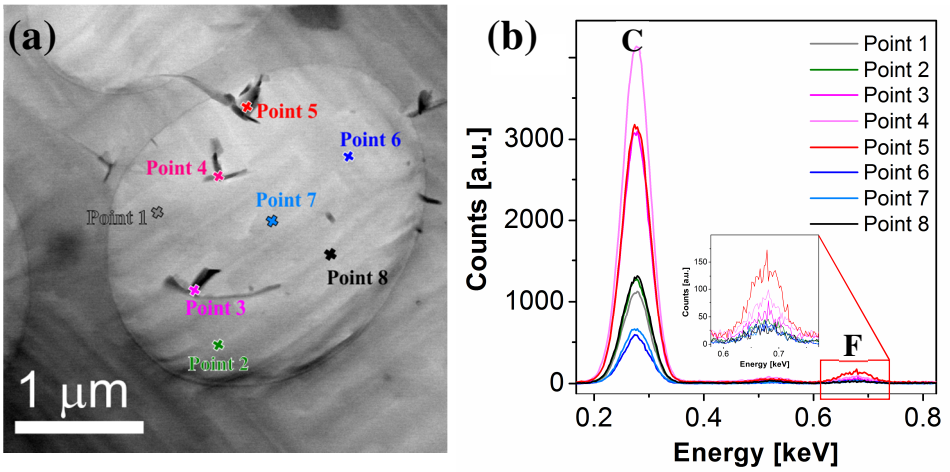

Figure 5.4-3. EDX analysis of the PEN:PFP [2:1] blend. (a) STEM overview where the positions used for the acquisition of EDX measurements are marked. (b) EDX spectra. The inset shows a magnified region of the fluorine peak.

5.4.2.3. TEM characterization: SAED patterns

Since different compositions cannot be detected by EDX measurements, another characterization is needed in order to get local information on the different phases and arrangements present, i.e. TEM characterization via SAED patterns. For this purpose, a specimen area of about 0.0491 μm^2 (SAD aperture with diameter size equal to 250 nm) has been selected to acquire electron diffraction patterns. It needs to be emphasized that all SAED patterns displayed in this section have been acquired at room **temperature** (≈293 K). In consequence, the **interplanary spacing d_{hkl}** values are given at **room temperature** too.

The electron diffraction pattern acquired for the PEN:PFP [2:1] blend is displayed in Figure 5.4-4(a), and a zoom on the 2 1 0 and 2 0 0 reflections can be seen in its inset. A double pattern can be distinguished at several positions, indicating that two separate crystalline structures with slightly different lattice constants coexist.

Similar to the microstructural characterization by SAED patterns in sections 4.5.1 and 5.3.3, the distances between the diffracted reflections and the (0 0 0) primary beam in the SAED patterns (r^*) are measured, and the interplanar lattice spacings d_{hkl} are calculated using equation (3.4-2). The d_{hkl} values obtained are compared to those: (i) previously collected in section 5.3.3 for the PEN:PFP [2:1] blend on SiO_2, (ii) determined by Hinderhofer et al. via GIXD [135] for the PEN:PFP [2:1] blend on SiO_2, and (iii) reported for the TF [107] and Campbell [102] phases of PEN.

Upon comparison, it is found that the experimental d_{hkl} spacings match with PEN in $[0\ 0\ 1]$ zone axis and the mixed phase. The PEN phase is associated with the set of reflections that are more far away from the center of the SAED pattern (highlighted in blue in Figure 5.4-4(a)), while the mixed phase corresponds to the diffraction pattern with the set of reflections closer to the primary reflection, at least closer in **a*** direction (highlighted in red in Figure 5.4-4(a)).

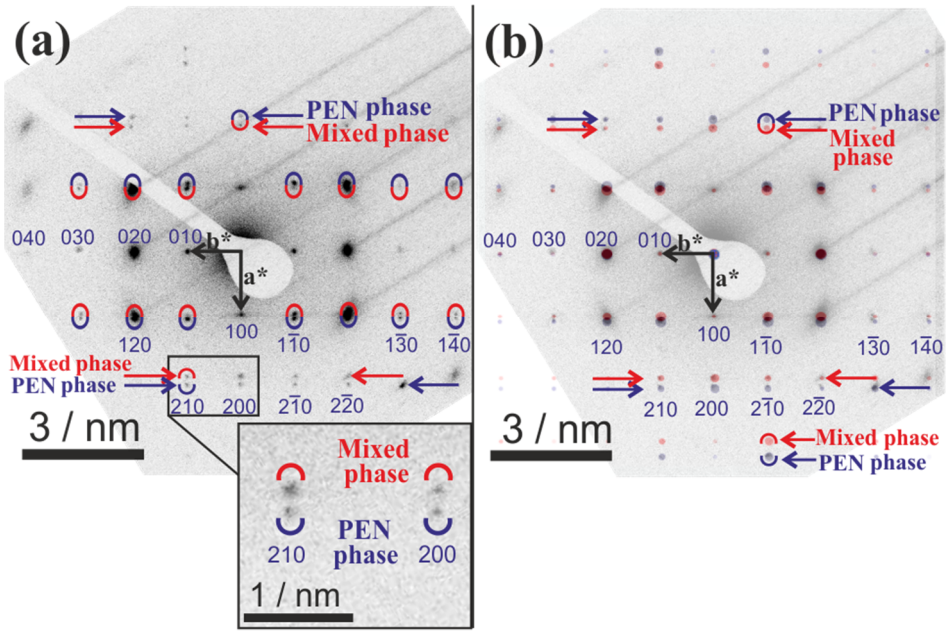

Figure 5.4-4. (a) SAED pattern of the PEN:PFP [2:1] blend on KCl with reflections of the mixed phase (highlighted in red) and of the PEN phase (highlighted in blue). (b) Overlay of the simulated diffraction pattern for PEN (TF phase in [0 0 1] direction, in blue) and the mixed phase (in red) on the experimental SAED pattern of (a). The simulated diffraction pattern for the mixed phase was achieved by compressing the simulated [0 0 1] PEN TF diffraction pattern in **a*** direction. The electron dose for the SAED pattern acquision was 0.86×10^{-3} $C \cdot s^{-1} \cdot cm^{-2}$.

Table 5.4-1 provides the experimental d_{hkl} values calculated for the PEN phase in the PEN:PFP [2:1] blend grown on KCl (column 2), in addition to the values reported for the PEN TF [107] (column 3) and Campbell [102] (column 4) phases. As visible in the table, the d_{hkl} values determined from the experimental SAED pattern agree slightly better with the TF phase. Thus, the hkl indices for the PEN phase (found in the experimental SAED pattern) have been assigned according to the PEN TF phase. The experimental d_{hkl} values are calculated as the average of at least five different SAED patterns acquired at room temperature (≈293 K).

Assigned hkl reflections	**Experimental SAED patterns d_{hkl} (Å)**	**PEN TF** [107]		**PEN Campbell** [102]	
		hkl	**d_{hkl} (Å)**	**hkl**	**d_{hkl} (Å)**
0 1 0	---	0 1 0[a]	7.51	1 0 0	7.29
1 0 0	---	1 0 0[b]	5.95	0 1 0	5.93
1 $\bar{1}$ 0	4.67	1 $\bar{1}$ 0	4.65	1 $\bar{1}$ 0	4.59
0 2 0	3.81	0 2 0	3.75	2 0 0	3.65
1 2 0	3.17	1 2 0	3.17	2 1 0	3.10
2 0 0	2.95	2 0 0	2.97	0 2 0	2.96
2 $\bar{1}$ 0	2.75	2 $\bar{1}$ 0	2.77	1 $\bar{2}$ 0	2.74
1 $\bar{3}$ 0	2.31	1 $\bar{3}$ 0	2.31	$\bar{3}$ 1 0	2.25
2 $\bar{2}$ 0	2.46	2 $\bar{2}$ 0	2.34	2 $\bar{2}$ 0	2.31
1 $\bar{4}$ 0	1.79	1 $\bar{4}$ 0	1.79	$\bar{4}$ 1 0	1.75

[a] This reflection is forbidden and it will just be visible in the SAED patterns if plural (dynamical) scattering events are present.
[b] This reflection has a very weak intensity, therefore it is not always visible in experimental SAED patterns.

Table 5.4-1. The experimental d_{hkl} values determined for reflections associated with the PEN phase in the PEN:PFP [2:1] blend (column 2) are compared to those of the PEN TF [107] (column 3) and the PEN Campbell [102] (column 4) phases in [0 0 1] zone axis. The error was estimated to be less than 3 % in the case of 0 1 0 and 1 0 0 reflections, and less than 2 % for the remaining reflections.

Likewise, Table 5.4-2 collects the d_{hkl} values calculated for the mixed phase in this PEN:PFP [2:1] blend grown on KCl (column 2). They are compared to those previously calculated in section 5.3.3 (column 3) and the ones determined by Hinderhofer et al. [135] (column 4), both for the PEN:PFP [2:1] blend grown on SiO_2. The **a*** and **b*** axes in Figure 5.4-4 and the hkl indices in Table 5.4-2 have been assigned for the mixed phase in consonance with the ones of the PEN TF phase for the same reasons mentioned in section 5.3 (cf. footnote VIII, section 5.3.4): the crystal

structure of the mixed phase is not yet fully resolved, and therefore, the **a*** and **b*** axes are still unknown and have been arbitrarily assigned. The experimental d_{hkl} values are calculated as the average of at least five different SAED patterns acquired at room temperature (≈293 K).

Assigned hkl reflections	**Experimental SAED patterns d_{hkl} (Å)**	**Experimental SAED pattern of section 5.3.3, d_{hkl} (Å)**	**Mixed phase** [135] **d_{hkl} (Å)**
0 1 0	7.57	7.54	7.42
1 0 0	6.48	6.56	6.49
1 $\bar{1}$ 0	4.87	4.78	4.78
0 2 0	3.81	3.74	3.72
1 2 0	3.25	3.22	3.27
2 0 0	3.23	---	---
2 $\bar{1}$ 0	2.95	---	---
1 $\bar{3}$ 0	2.35	---	---
2 $\bar{2}$ 0	2.33	---	---
1 $\bar{4}$ 0	1.81	---	---

Table 5.4-2. The experimental d_{hkl} values calculated for each reflection of the mixed phase in the PEN:PFP [2:1] blend (column 2) are compared to those assigned to the mixed phase in section 5.3.3 (column 3) and those reported for the mixed phase by GIXD [135] (column 4), both in the PEN:PFP [2:1] blend on SiO_2. Note that there are no data collected for reflections 2 0 0 to the end for columns 3 and 4. The error was estimated to be less than 3 % for 0 1 0 and 1 0 0 reflections, around 4 % for 2 $\bar{2}$ 0 reflections and less than 2 % for the remaining ones.

Since the experimental d_{hkl} values of the PEN phase agree better with the PEN TF polymorph, the SAED pattern recorded in Figure 5.4-4(a) has been overlaid with the PEN TF diffraction pattern simulated in the [0 0 1] zone axis by JEMS [112] (cf. blue simulated diffraction pattern in Figure 5.4-4(b)). This superposition shows the very good fitting between both. Furthermore, this simulated PEN TF polymorph (in [0 0 1] orientation) is also utilized to highlight the reflections of the mixed phase in the experimental SAED pattern by comprising its **a*** direction around 8 %. (cf. red simulated diffraction pattern in Figure 5.4-4(b)). The good fit with the mixed phase's reflections underlines once more the similarities between the SAED pattern of the PEN TF phase and the mixed phase just differing in a compression around 8 % in **a*** direction.

5.4.2.4. **TEM characterization: BF/DF-TEM analyses**

BF and DF-TEM analyses have been performed in the PEN:PFP [2:1] blend pursuing two goals. Firstly, clarifying the details about the direction in which the observed domains are elongated. This inspection has been performed in relative small areas of the sample, in the order of nanometers squared. Secondly, having a closer look on the relative orientation of the different domains with respect to each other. Relative large areas of the sample (in the order of microns squared) have been analyzed for this issue. These two inspections are described in the following in that order.

A typical shadow TEM image acquired for this sample is shown in Figure 5.4-5(a). The two orthogonally rotated domains are visible and their elongation is highlighted by red/blue arrows. The black dotted circle represents the position and size of the SAD aperture (diameter equal to 143 nm) used to acquire the SAED pattern (cf. Figure 5.4-5(b)). The diffraction pattern has been overlaid by the simulated diffraction pattern of the PEN TF polymorph in [0 0 1] zone axis (marked in blue) and the one of the mixed phase[II] (marked in red) to visualize clearly both PEN and mixed phases. By analogy with the SAED pattern displayed in Figure 5.4-4(a), **a*** and **b*** directions are marked in Figure 5.4-5(b) as bigger and smaller distances in reciprocal space, respectively. The reflections enclosed by the black circle in the SAED pattern have been selected to form the DF-TEM image (cf. Figure 5.4-5(c)) and its corresponding BF-TEM image has also been recorded (cf. Figure 5.4-5(d)). The region where the SAED pattern emerges has been highlighted by a black dashed circle in the DF- and BF-TEM micrographs.

Focusing on the DF-TEM image (cf. Figure 5.4-5(c)), the bright contrast allows correlating the elongated direction of the domain with the **a*** and **b*** directions in the SAED pattern. Hence, one can see that the elongation of the domain (marked by a red/blue arrow) points parallel to the **b*** direction of the PEN/mixed phase SAED

[II] Note that the simulated diffraction pattern for the mixed phase was achieved by compressing the simulated [0 0 1] PEN TF phase diffraction pattern in **a*** direction (similar to Figure 5.4-4(b)).

pattern (with **b*** < **a***, cf. Figure 5.4-5(b)). This means that the in-plane long unit cell axis (**b** > **a** in real space) points along the elongation of the domains.

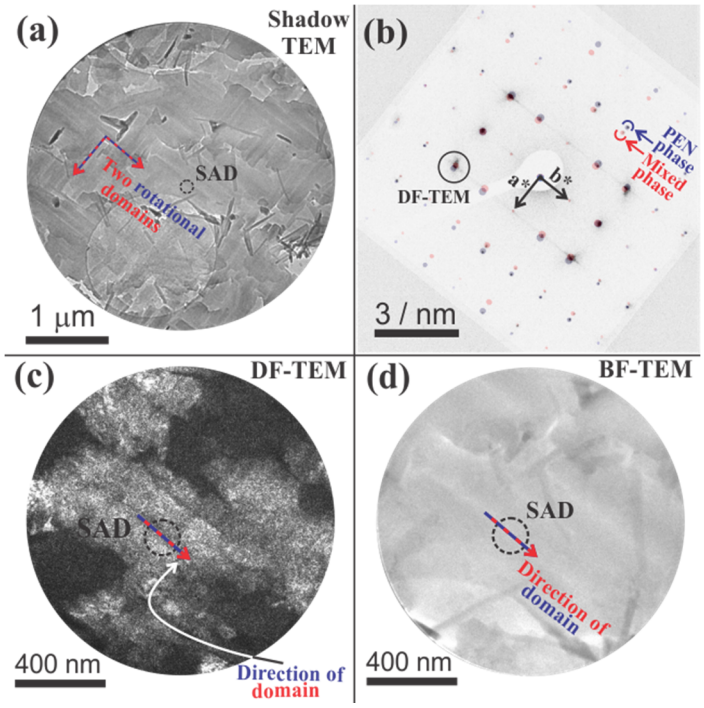

Figure 5.4-5. (a) Shadow TEM image of the PEN:PFP [2:1] blend. (b) Overlay of the simulated diffraction pattern for PEN TF in [0 0 1] direction (in blue) and the mixed phase (in red) on the experimental SAED pattern. (c) DF-TEM image and its corresponding (d) BF-TEM image. The area used to create the SAED pattern is highlighted by black dotted circles in (a), (c) and (d).

To address the second part of this study, a bigger SAD aperture has been utilized with diameter size equal to 1.3 µm. Figure 5.4-6(a) shows the shadow TEM image used for this purpose, two rotational domains (highlighted by red/blue arrows) have been enclosed by the SAD aperture (black dashed circle) and their corresponding SAED pattern has been acquired (Figure 5.4-6(b)). It can be seen that the 4-fold ordering of the domains results in the overlap of two diffraction patterns rotated by 90º. In order to visualize clearly the SAED patterns, they have been overlaid by two simulated diffraction patterns (rotated by 90º) of the PEN TF phase in [0 0 1] zone axis (marked in red and blue). Similar to the SAED pattern of Figure 5.4-4(a), **a*** and **b*** directions have been marked as bigger and smaller distances in reciprocal space, respectively.

The reflections enclosed by the red and blue circles are selected to form the DF-TEM micrographs presented in Figure 5.4-6(c) and (d), respectively. As illustrated, this selection yields complementary DF-TEM images, hence proving that they correspond to different rotational domains and giving additional proofs of the direction of the elongation of the domains in the film.

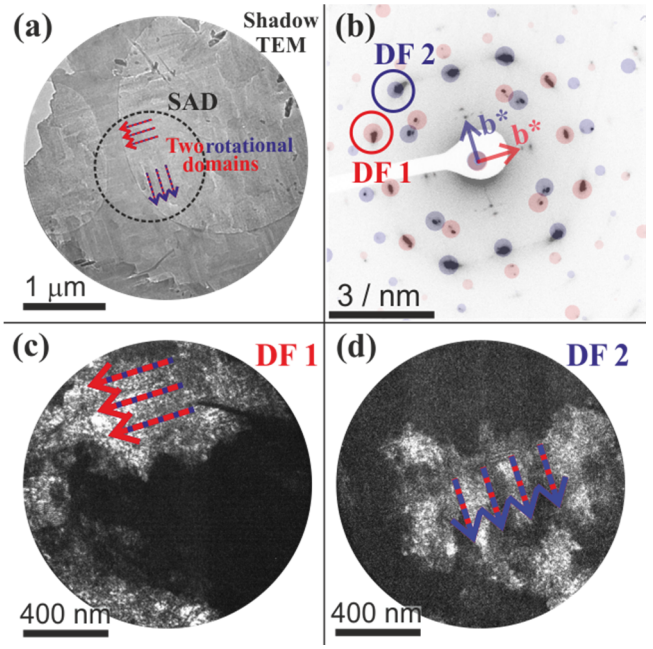

Figure 5.4-6. (a) Shadow TEM image of the PEN:PFP [2:1] blend. (b) Overlay of simulated PEN TF diffraction patterns in [0 0 1] direction on the experimental SAED pattern. (c) and (d) DF-TEM images recorded by using the reflections enclosed in (b).

When the information concerning the correlation between the SAED patterns and the elongation of the domains is combined with the SEM data[III], the relationship between the uniform pentacene and/or mixed phase layer and the underlying KCl substrate can be determined, i.e. the [0 1 0] axis of the mixed phase and/or PEN phase points along the elongation of the organic domains, which in turn, are aligned along the $<1\ 0\ 0>_{KCl}$ directions.

[III] Notice that the SEM data have revealed that the elongation of the domains is aligned along the substrate <1 0 0> directions.

5.4.2.5. **TEM characterization: High resolution (HR)**

In addition to the diffraction analyses, the two different phases that coexist in the PEN:PFP [2:1] blend can also be distinguished by HRTEM. Figure 5.4-7 illustrates two HRTEM images with their corresponding line profiles (bottom panels) and fast Fourier transform (FFT) patterns (insets in the upper parts). Two slightly different lattice spacings are extracted from the measurements of spots found in the FFT patterns of panels (a) and (b). Likewise, slightly different distances are detected by measuring the periodicity of the plane separations via the red and blue linescans of Figure 5.4-7(a) and (b), respectively.

The measured lattice spacings correspond to d_{hkl} distances equal to 4.84 Å and 4.65 Å with an error in the range of ±0.04 Å for Figure 5.4-7(a) and (b), respectively. They match with the interplanar lattice spacings of the $(1\ \bar{1}\ 0)$ planes determined for the mixed phase and the PEN phase in the electron diffraction experiments of section 5.4.2.3 (cf. Table 5.4-2 and Table 5.4-1 for the mixed phase and the PEN phase, respectively). Although no clear contours and/or features can be distinguished, the phase contrast images display a region where high resolution could be exclusively obtained for the mixed phase and the PEN phase.

The lattice plane periodicities of the mixed phase are only weakly visible in comparison to the PEN phase since the mixed phase might have been partly destroyed due to the action of the electron beam. There are not many works reporting HRTEM imaging in PEN and its derivatives because the HRTEM is mostly limited in OSCs by the beam damage. Thus, despite the fact that HRTEM has some restrictions, this technique has been successfully applied to illustrate lattice planes that correspond to the two different structures, i.e. the mixed phase and the PEN phase, in the mixture.

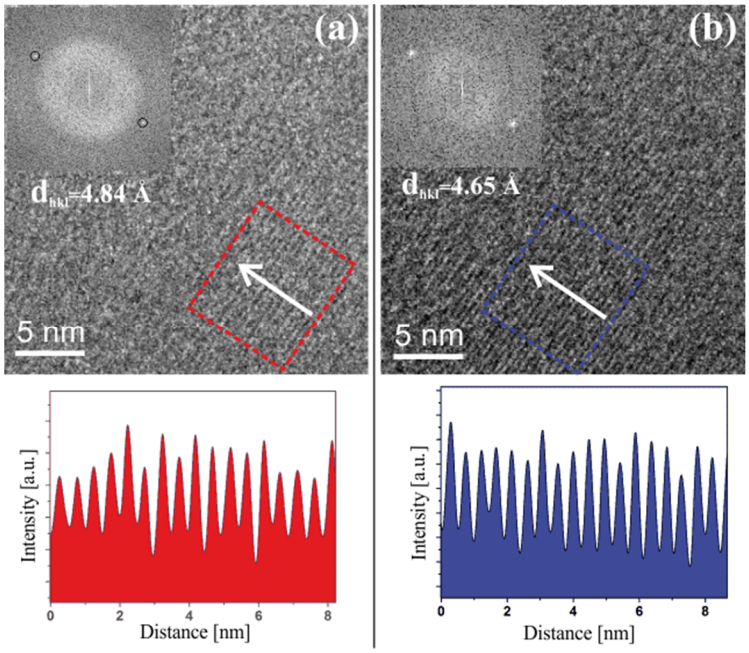

Figure 5.4-7. HRTEM micrographs of (a) the mixed phase and (b) the PEN TF phase in the PEN:PFP [2:1] blend. Upper insets: fast Fourier transform (FFT) pattern. Bottom: corresponding profiles of lattice plane periodicities.

5.4.3. PEN:PFP [1:2] blend

5.4.3.1. Morphology of the sample

The morphology of the PEN:PFP [1:2] blend is rather different from that exhibited by its counterpart [2:1] mixture. Figure 5.4-8(a) and (b) correspond to SEM micrographs after the preparation process of the sample for TEM analyses (with the OSC layer placed onto the copper support grid). Panels (c) and (d) belong to images collected when the organic films are still attached to the KCl substrate. As can be seen in Figure 5.4-8(a), spicular or needle-like fibers[IV] are visible on top of a background layer on the substrate. The spicular fibers ranging between (0.5-1) μm in length tend to be mainly aligned along two orthogonal in-plane directions (cf. inset of Figure 5.4-8(a)). The needles do not exhibit a completely flat lying geometry since many of them are tilted and/or bent as shown in the image acquired when the sample is tilted by 55º relative to the surface normal (cf. Figure 5.4-8(b)). The holes of the holey carbon film can also be observed in the micrographs. The two dotted black curves mark the same position in the non-tilted/tilted samples, Figure 5.4-8(a) and (b), respectively.

Figure 5.4-8(c) and (d) have been recorded to check the lateral alignment between the spicular fibers and the KCl substrate. In panel (c), the KCl edge, which denotes the $\langle 1\ 0\ 0 \rangle_{KCl}$ directions, is highlighted by a black dotted line. In contrast, panel (d) corresponds to a region far away from the KCl edge, thus the $\langle 1\ 0\ 0 \rangle_{KCl}$ directions are indicated according to the direction of the KCl edge observed when the sample has been investigated. As illustrated, most of the spicular fibers tend to be aligned along two dominant directions which are rotated by 45° with respect to the $\langle 1\ 0\ 0 \rangle_{KCl}$ directions (i.e. along the $\langle 1\ 1\ 0 \rangle_{KCl}$ directions[V]). A background layer is also visible in these images extended under these needles.

[IV] Within this thesis, the terms 'spicular' fibers or 'needles' will be interchangeably used.

[V] Within the scope of this chapter the notation $\langle 1\ 1\ 0 \rangle_{KCl}$ only considers the in-plane directions.

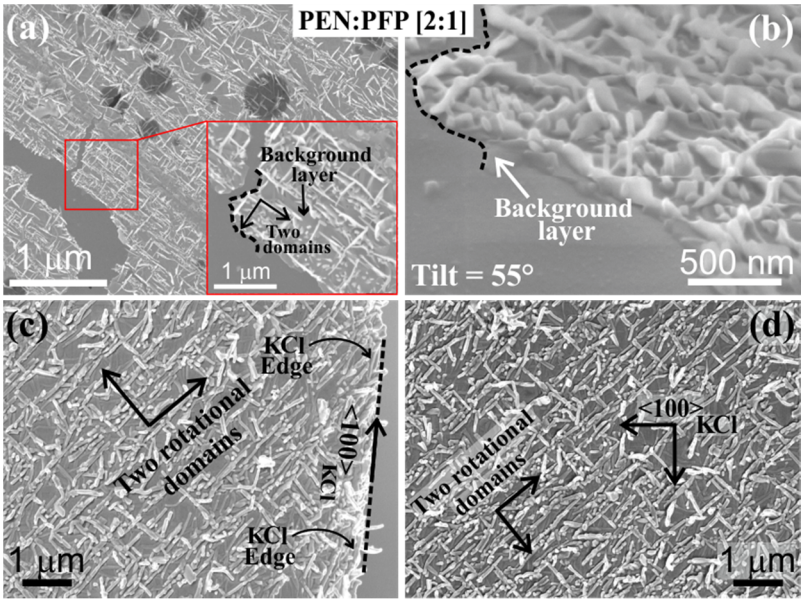

Figure 5.4-8. SEM micrographs of the PEN:PFP [1:2] blend. Upper panel has been acquired after the sample preparation process. (a) Non-tilted sample. (b) Sample tilted by 55° relative to the surface normal. The black dotted lines highlight the same region in (a) and (b). The inset of (a) displays a magnified region. Lower panel: (c) and (d) have been acquired with the organic layers still attached to the KCl substrate.

Additionally, apart from the morphology described above, regions formed by a continuous film (lying in direct contact with the substrate) without spicular fibers on top are also observed in the PEN:PFP [1:2] blend. However, it cannot be directly distinguished from the background layer via SEM methods. This region is presented in the subsection 5.4.3.3, 'TEM characterization: SAED patterns and BF/DF-TEM analyses'.

In the following subsections, the crystalline and composition details of each region/morphology are described. The EDX measurements are introduced first. Next, the local characterization by SAED patterns together with DF/BF-TEM imaging are presented.

5.4.3.2. **TEM characterization: EDX analysis**

EDX analyses have been performed on the PEN:PFP [1:2] blend to check if different compositions can be detected on the fibers and on the background layer extended under the fibers.

Figure 5.4-9(a) shows the area analyzed by STEM-EDX. As it has been explained in section 5.4.2.2, the spectra are recorded in a hole of the holey carbon film in order to include only the freestanding organic film and exclude any amount of carbon coming from the holey carbon film. The hole is highlighted by a dotted white 'circle' in Figure 5.4-9(a). Three different points have been selected for the acquisition of spectra shown in Figure 5.4-9(b):

- A spicular fiber (marked in green)
- The background layer (marked in red)
- The vacuum (marked in blue)

The C/F ratio has been calculated for the three measurements and it is provided in the table contained in Figure 5.4-9(c). It seems clear that the measurement in point 1 contains a higher fluorine fraction, whereas the fluorine amount for the measurement of point 2 is much smaller. Likewise, the F amount is null within the error margins in the vacuum, evidencing the accuracy of the measurement.

Thus, the spectra collected for these points reveal that the spicular fibers exhibit a higher amount of fluorine compared to carbon atoms. It could be a hint for the presence of PFP in the fibers. To a lesser extent, fluorine content is also present in the background layer extended between the fibers. It could be a clue for the presence of the mixed phase consisting of PEN and PFP in this background layer. In this way, a more detailed study is required to clarify the composition detected by the EDX analysis. The samples are inspected in a further analysis by using a combination of SAED patterns with DF/BF-TEM imaging. It provides information on the crystallinity and the distribution of the observed phases.

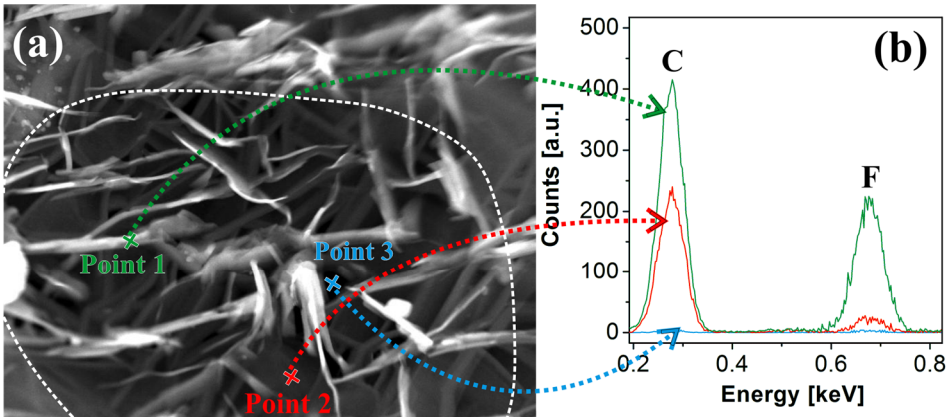

(c)

Point	C/F ratio
1	1.9
2	8.6
3	1.2

Figure 5.4-9. EDX analysis of the PEN:PFP [1:2] blend. (a) STEM overview where the positions used for the acquisition of EDX measurements are marked by different points: in the needles (point 1), in the background layer (point 2) and in the vacuum (point 3). (b) EDX spectra. (c) Table displaying the C/F ratio of the EDX measurements.

5.4.3.3. **TEM characterization: SAED patterns and BF/DF-TEM analyses**

During the TEM characterization by electron diffraction and DF/BF-TEM imaging, it has been possible to distinguish two different regions in the PEN:PFP [1:2] blend. The majority of the sample exhibits some spicular fibers on top of a background layer lying on the KCl substrate. This region is the one presented in the morphology section 5.4.3.1 by SEM analysis. To a lesser extent, a second region that could not be distinguished in the SEM analysis is also present in the mixture. It consists of a continuous film without spicular fibers on top lying in direct contact with the KCl substrate.

In this subsection, the crystallinity, orientation and arrangement of the phases in the two different regions are described. The measurements have been performed at room temperature (≈293 K). In consequence, the interplanary spacing $\mathbf{d_{hkl}}$ values are also given at **room temperature.**

❖ **Region formed by spicular fibers on a background layer**

This subsection is in turn divided in two different parts: (i) the analysis of the spicular fibers and (ii) the analysis of the background layer beneath the fibers.

Figure 5.4-10(a) shows a shadow TEM image of the area formed by the spicular fibers on the background layer. In order to analyze the crystalline structure and composition details of the spicular fibers, a SAED pattern has been recorded from a region which contains spicular fibers (cf. Figure 5.4-10(b)). The black dotted circle marks the contour and size of the SAD aperture used (with 1.3 μm diameter). Several reflections are visible in the diffraction pattern, but only some of them are highlighted by purple and green circles. The other reflections belong to the mixed phase and will be discussed later (cf. Figure 5.4-11).

The distances between the reflections enclosed by the purple and green circles and the (0 0 0) reflection (r^*) are measured and their d_{hkl} values are calculated using equation (3.4-2). A good match is found between the d_{hkl} spacings of these reflections and those reported for the h 0 0_{PFP} indices. This agreement is visible in Table 5.4-3, where the measured d_{hkl} distances of experimental SAED patterns are compared to the ones associated with the h 0 0_{PFP} reflections[VI] [115].

Two of the reflections enclosed by the purple circles are selected by the OA[VII] with the particular goal of forming the DF-TEM micrograph and checking the features that produce these reflections. The black circle visible in Figure 5.4-10(b) indicates the position and size of the OA used to acquire the DF-TEM micrograph displayed in Figure 5.4-10(c). As shown, some needles appear in a bright contrast indicating that they consist of PFP. The complementary BF-TEM to the DF-TEM image is also displayed in Figure 5.4-10(d). The fibers that appear in a bright contrast in the DF-TEM image are highlighted by purple dashed lines in the BF-TEM image.

[VI] The PFP polymorph is only compared to the PFP TF phase within the whole section for reasons of simplicity, since both polymorphs bulk and TF differ only slightly (cf. section 2.5.2, Table 2.5-2).

[VII] The OA selects not only the reflections enclosed by the purple circles but also some other reflections (cf. Figure 5.4-10(b)). The contribution of these other reflections to the DF-TEM image (shown in Figure 5.4-10(c)) is neglected due to its low intensity.

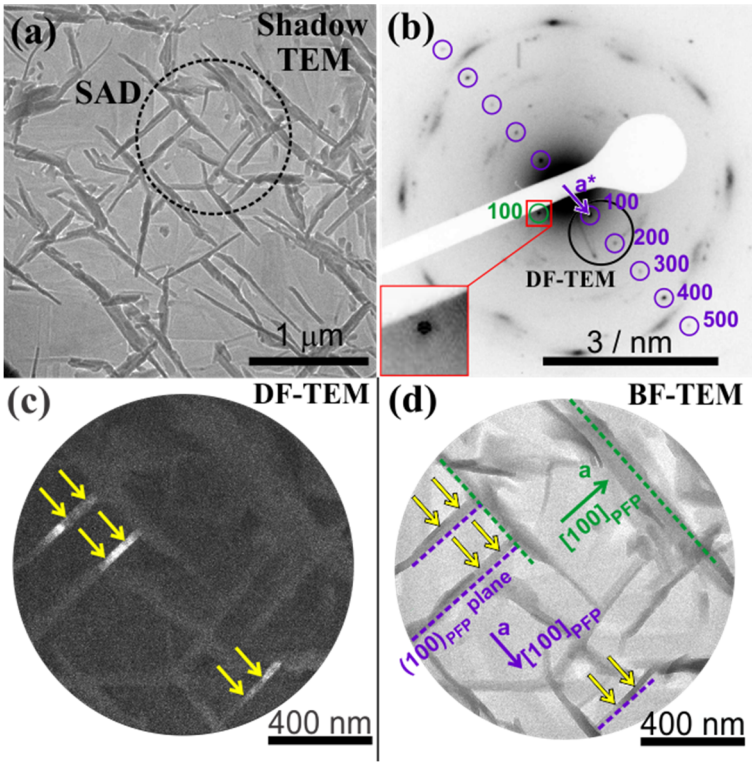

Figure 5.4-10. (a) Shadow TEM image of the PEN:PFP [1:2] blend. (b) SAED pattern with the h 0 0_{PFP} reflections enclosed by purple and green circles. Inset: magnified view of the reflection enclosed by the green circle. (c) DF-TEM image formed by selecting the reflections enclosed by the OA in (b). (d) BF-TEM image corresponding to (c). The (1 0 $0)_{PFP}$ planes associated with the 1 0 0_{PFP} reflections of (b) are highlighted by dotted lines (purple and green, depending on the associated reflection). The yellow arrows mark the same diffracting areas in (c) and (d).

The indexation of the h 0 0_{PFP} reflections in the SAED pattern allows deriving the $[1\ 0\ 0]_{PFP}$ direction and correlating it with the spicular fibers. In this way, the $[1\ 0\ 0]_{PFP}$ direction is (in-plane) perpendicular to the elongation of the needles (cf. Figure 5.4-10(d)). Furthermore, another reflection appears in the SAED pattern and its d_{hkl} value corresponds to the 1 0 0_{PFP} reflection. This reflection is highlighted by a green circle in Figure 5.4-10(b) and should be originated by spicular fibers that are 90º rotated from those marked in purple. The possible needles, which give rise to the reflection highlighted in green, are marked by green dashed lines in the BF-TEM image (cf. Figure 5.4-10(d)). The DF-TEM micrograph with the needles highlighted in green exhibiting a bright contrast could not be acquired since the low stability of the sample did not allow acquiring several DF-TEM micrographs at the same position.

The SAED pattern presented in Figure 5.4-10(b) only shows some of the h 0 0_{PFP} reflections associated with the PFP needles, indicating that a high symmetry zone axis is not satisfied. This fact is attributed to the bending and/or tilting that has been detected in the SEM analysis above discussed (cf. section 5.4.3.1, Figure 5.4-8(b)). Notice that it was not possible to tilt the sample is such a way that the needles fulfil a high symmetry zone axis because their crystallinity was quickly damaged by the electron beam. In this way, it is not possible to determine the exact zone axis exhibited by the needles since only one row of reflections is visible.

hkl Reflections	**Experimental SAED patterns, d_{hkl} (Å)**	**PFP TF** [115] **d_{hkl} (Å)**
1 0 0	15.85	15.76
2 0 0	7.90	7.88
3 0 0	5.24	5.25
4 0 0	3.93	3.94
5 0 0	3.16	3.15

Table 5.4-3. The experimental d_{hkl} values determined for the reflections highlighted by the purple and green circles in the SAED patterns of Figure 5.4-10(b) are compared to the ones of the PFP TF [115]. The error was estimated to be less than 3 %.

In this second part, the crystallinity of the background layer beneath the fibers is described. Figure 5.4-11(a) corresponds to a shadow TEM image of the area used for this investigation. The inset displays a magnified region of the red dotted circle. The black dotted circle represents the position and size of the SAD aperture with diameter equal to 143 nm which has been used for the acquisition of the SAED pattern shown Figure 5.4-11(b). The r^* distances of the diffracted reflections with respect to the (0 0 0) reflection are measured, and from that the interplanar lattice spacings d_{hkl} are calculated. These d_{hkl} values agree with the d_{hkl} spacings previously[VIII] derived for the mixed phase.

[VIII] These d_{hkl} values are in a good agreement with the ones presented in Table 5.4-2 for the mixed phase.

Following the criteria mentioned in previous sections (cf. footnote VIII, section 5.3.4), the **a*** and **b*** axes have been marked in this SAED pattern as bigger and smaller distances in reciprocal space, respectively. The low intensity of the diffraction pattern is due to the use of a very small SAD aperture and the selection of a very low electron dose of 0.77×10^{-3} $C \cdot s^{-1} \cdot cm^{-2}$. The reflection enclosed by the dotted black circle is selected by the OA to image the DF-TEM micrograph. As can be seen in Figure 5.4-11(c), the area that appears brighter is the region extended between the PFP spicular fibers. None of the needles exhibit any bright contrast, confirming that they do not fulfil the Bragg diffraction condition for the selected reflection of the mixed phase. The yellow arrows mark the same positions in the DF-TEM and in the inset of the shadow TEM image. Elongated domains are not fully visible in the TEM micrographs of the mixed phase background layer, hence their direct correlation with the **a*** and **b*** directions in the SAED patterns is not possible.

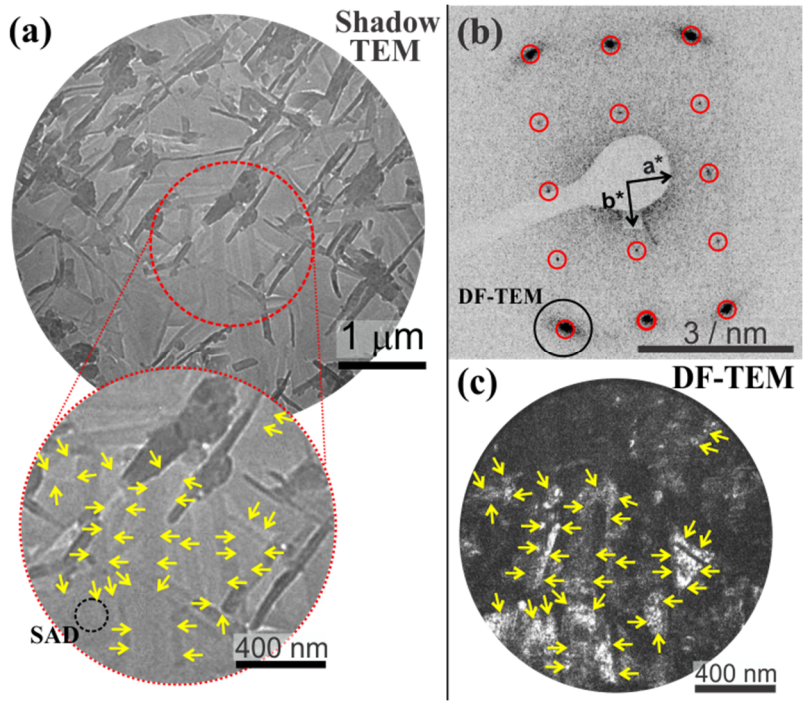

Figure 5.4-11. (a) Shadow TEM image of the PEN:PFP [1:2] blend where the size and position of the SAD aperture is marked by a dotted black circle in the inset. (b) SAED pattern of the mixed phase. The reflection enclosed by the black circle has been selected to form the (c) DF-TEM image. The yellow arrows mark the same diffracting areas in the inset of (a) and (c).

Summarizing, the distribution and orientation of the crystalline structures which form the majority of the PEN:PFP [1:2] blend have been determined. The **background layer** lying in direct contact with the KCl substrate consists of the **mixed phase**. The **needles** placed on top of the background layer are formed by **PFP**, whose in-plane elongated direction is parallel to the $(1\ 0\ 0)_{PFP}$ plane.

❖ **Region formed by a uniform film without spicular fibers on top**

The other arrangement, which is present to a lesser extent, consists of a film without needles on top in direct contact with the KCl substrate. This arrangement could not be distinguished from the background layer described above by SEM measurements, since only analytical techniques that detect different compositions or crystalline structures are able to discern between both.

Figure 5.4-12(a) is a shadow TEM image of the two different regions of the sample. One region, formed by a background layer with spicular fibers on top (region 1), is distinguishable from another one which consists of a continuous film exhibiting elongated domains without needles on top (region 2). The area highlighted by the black dotted circle, which encloses mainly region 2, has been used to record the SAED pattern displayed in Figure 5.4-12(b) as well as the DF/BF-TEM micrographs presented in panels (c) and (d), respectively. The electron diffraction pattern exhibits a polycrystalline character with diffraction rings. The r^* distances have been measured and from that, the interplanar lattice spacings d_{hkl} have been calculated. Table 5.4-4 summarizes the d_{hkl} distances measured, they are in agreement with those reported for the PFP TF in [1 0 0] orientation. This fact demonstrates that this continuous layer without needles on top is made out of pure PFP. The reflections enclosed by the black circle in Figure 5.4-12(b) have been selected to form the DF-TEM micrograph illustrated in Figure 5.4-12(c). The diffracting areas exhibiting a bright contrast denote the regions that originate the reflections selected in the SAED pattern. The complementary BF-TEM micrograph to the DF-TEM micrograph is shown in Figure 5.4-12(d) to observe clearer the regions that appear in bright contrast.

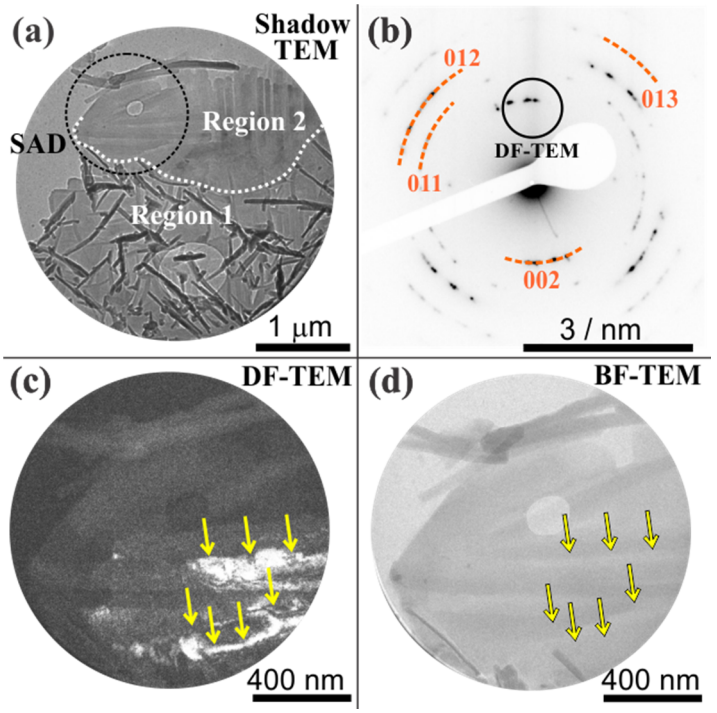

Figure 5.4-12. (a) Shadow TEM image of the PEN:PFP [1:2] blend displaying the two different regions found (region 1 and region 2). The size and position of the SAD aperture is marked by a dotted black circle in region 2. (b) SAED pattern where the reflections enclosed by the black circle have been selected to form the (c) DF-TEM image. (d) BF-TEM image complementary to (c). The yellow arrows mark the same diffracting areas in (c) and (d).

hkl Diffraction rings	**Experimental SAED patterns, d_{hkl} (Å)**	**PFP TF [115] d_{hkl} (Å)**
0 0 2	5.74	5.79
0 1 1	4.20	4.26
0 1 2	3.55	3.56
0 1 3	2.92	2.94

Table 5.4-4. The lattice spacing (d_{hkl}) values determined for the diffraction rings highlighted in orange in Figure 5.4-12(b) are compared to the ones of the PFP TF [115]. The error was estimated to be less than 2 %.

The polycrystalline character of the uniform PFP film (region 2) does not allow correlating the direction of the elongation of the domains with the axes of the SAED pattern. Hence, another SAED pattern exhibiting a single crystalline character has been acquired.

Figure 5.4-13(a) shows a small area where only one PFP domain is selected to create the single crystalline SAED pattern presented in Figure 5.4-13(b). Moreover, one reflection of the diffraction pattern is chosen by the OA and used to image a DF-TEM micrograph (cf. Figure 5.4-13(c)). As can be seen, the PFP exhibits the [1 0 0] orientation and the elongation of the domain forming the layer is parallel to the **b** axis of PFP (parallel to the $[0\ 1\ 0]_{PFP}$ direction).

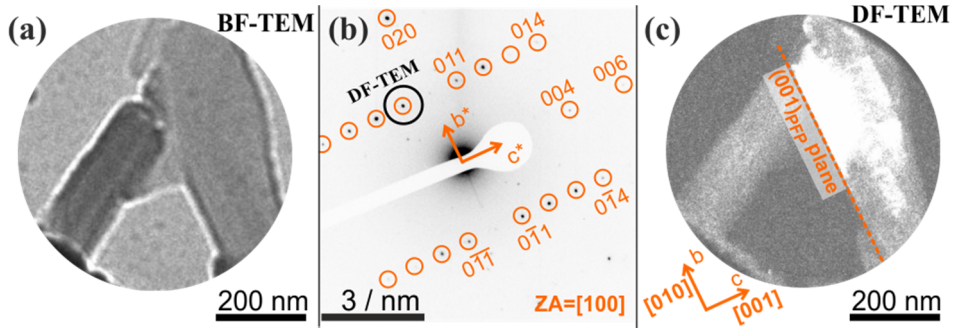

Figure 5.4-13. (a) BF-TEM image of the uniform film present in the PEN:PFP [1:2] blend. (b) Single crystalline SAED pattern of PFP exhibiting the [1 0 0] orientation. This SAED pattern has beeen originated from (a). (c) DF-TEM micrograph recorded by selecting the PFP reflection enclosed by the black circle in (b).

In summary, the **second region** found to a lesser extent in this samples is formed by a **uniform layer of PFP** with domains in direct contact with the KCl substrate. The PFP exhibits the [1 0 0] orientation and the elongation of the domains is parallel to its $[0\ 1\ 0]_{PFP}$ direction.

5.4.4. Conclusions

In this chapter, an alkali halide substrate as KCl has been chosen to study the morphology and arrangement of two codeposited blends of PEN and PFP with mixing ratios of [2:1] and [1:2]. These investigations have been performed by SEM and (S)TEM techniques.

For the PEN:PFP [2:1] blend, the SEM data reveal the formation of a uniform layer with domains rotated by 90° relative to each other. These domains are elongated along the $<1\ 0\ 0>_{KCl}$ directions. Concerning the local compositional analysis, conclusive information could not be obtained by EDX in this blend, hence this sample has been analyzed by electron diffraction and DF/BF-TEM imaging.

The microstructural characterization by SAED pattern reveals that two sets of patterns coexist in the PEN:PFP [2:1] blend. They slightly differ in their lattice parameters. The measurement and comparison of the lattice spacing d_{hkl} values show that one diffraction pattern belongs to the PEN phase in excess, whereas the other one is associated with the mixed phase. The diffraction pattern of the mixed phase presents a compression around 8 % in **a*** direction. This means that the mixed phase has larger lattice parameters (at least along the **a** direction) than the PEN phase. This finding is in line with the results of the non-equimolecular PEN:PFP blends grown on SiO_2 presented in the previous section 5.3.

BF/DF-TEM characterization has also been used to determine the direction along which the domains are elongated within the film. An analysis of relative small areas (in the order of nanometers squared) reveals that the direction of the domain's elongation points out along the **b*** direction of the SAED pattern. In combination with SEM measurements, the lateral rotation between the PEN/mixed phase continuous layer and the underlying KCl substrate has been determined. In this way, the **b** direction of the PEN/mixed phase unit cell points along the elongation of the organic domains, which in turn, are oriented along the $<1\ 0\ 0>_{KCl}$ directions.

These relative orientations between the different phases observed in the PEN:PFP [2:1] mixture and the KCl substrate are summarized in Figure 5.4-14.

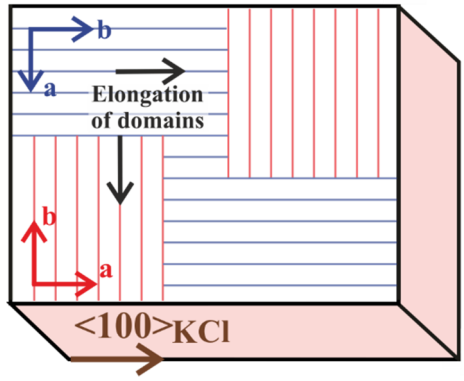

Figure 5.4-14. Sketch of the PEN:PFP [2:1] blend grown on KCl. The two domains, rotated by 90° relative to each other, are highlighted in red and blue. They correspond to the uniform PEN and/or mixed phase layer. The axes of each domain have been marked in their respective colors. The black arrows pointing to the right and down indicate the direction of the domain's elongation. Additionally, the $<1\ 0\ 0>_{KCl}$ direction is marked by a brown arrow.

Additionally, the BF/DF-TEM imaging has been used with the aim of having a closer look on the relative orientation of the different domains with respect to each other. In this study, relative large areas of the sample (in the order of microns squared) have been used. They show that the 4-fold symmetry observed in the SAED pattern is unequivocally associated with the two rotated domains.

HRTEM analyses have also been carried out on the PEN:PFP [2:1] blend to check the atomic structure of the PEN phase and the mixed phase. These high resolution images are specially challenging due to the susceptibility of the organic materials, and more specifically of the PEN:PFP mixtures, to the electron beam irradiation. This fact emphasizes even more the value of displaying lattice plane images in the fast damaged mixed phase. From the atomic planes of the mixed phase and the PEN phase, d_{hkl} values have been measured and they agree with those determined for the $(1\ \bar{1}\ 0)$ planes of both phases in the SAED experiments.

On the other hand, the morphology of the PEN:PFP [1:2] blend is quite different from its counterpart [2:1] mixture. The majority of the sample exhibits some spicular fibers on a background layer lying on top of the KCl substrate. Most of spicular fibers are arranged along the $\langle 1\ 1\ 0 \rangle_{KCl}$ directions and exhibit an uneven geometry where some of the needles tend to be tilted and/or bent. Additionally, regions formed by a continuous film (lying in direct contact with the substrate) without spicular fibers on top are also observed in the PEN:PFP [1:2] blend. This layer could not be directly distinguished from the background layer via SEM methods.

The information of the crystalline structures as well as the composition of these different arrangements have been studied by EDX measurements, SAED patterns and DF/BF-TEM analyses.

Firstly, the arrangement formed by the spicular fibers on the background layer is investigated by EDX. The analyses have detected a very low C/F ratio on the fibers compared to the background, which might be an indication for the presence of PFP in the fibers, and the mixed phase in the background layer beneath the fibers. This issue has been clarified by analyses performed with other techniques.

SAED pattern studies confirm the presence of the PFP phase in the mixture via the detection of the $h\ 0\ 0_{PFP}$ reflections. The combination of SAED patterns with DF/BF-TEM analyses reveals that these $h\ 0\ 0_{PFP}$ reflections are associated with the spicular fibers. In addition, the elongation of the PFP spicular fibers is in-plane perpendicular to its $[1\ 0\ 0]_{PFP}$ direction. SAED patterns also display the presence of the mixed phase. The DF/BF-TEM images show that the mixed phase is found in the background layer extended under the fibers and in direct contact with the KCl substrate. The lateral alignment of the mixed phase background layer cannot be related to the underlying KCl substrate because the elongation of the domains for the mixed phase is not clearly visible in the images recorded for this sample.

The second arrangement, present to a lesser extent in this sample, is associated with regions containing a continuous film with domains. This uniform film is located directly on the KCl substrate and does not have fibers on top. SAED patterns show the polycrystalline character of the uniform film. The reflections recorded in the diffraction pattern agree with those reported for PFP in [1 0 0] orientation, normal to the substrate surface. Thus, this continuous layer without fibers on top is made out of PFP. When the information of the SAED pattern is correlated to DF/BF-TEM micrographs, it is found that the domains of the continuous PFP layer are elongated along its $[0\ 1\ 0]_{PFP}$ direction. No evidence for the presence of spicular fibers on top of this PFP layer is observed. This fact could be explained since adding PFP on top of this PFP layer would result in a thicker layer instead of the formation of spicular fibers.

A sketch illustrating the arrangement and orientation of the different regions and/or phases in the PEN:PFP [1:2] blend is presented in Figure 5.4-15.

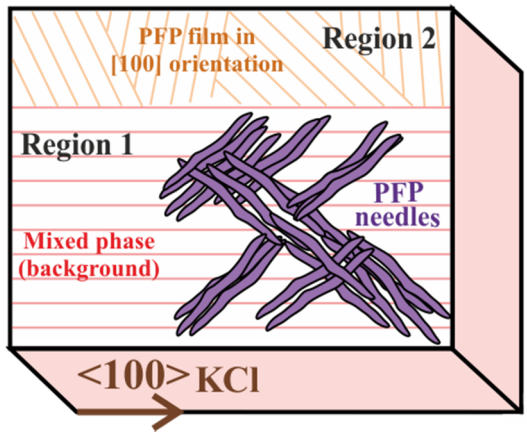

Figure 5.4-15. Sketch of the PEN:PFP [1:2] blend grown on the KCl substrate. Region 1: the sample is mostly formed by PFP needles (marked in purple) on the mixed phase background layer (marked in red), which in turn is lying directly on the KCl substrate. Region 2: to a lesser extent, PFP is also found as a crystalline layer with domains in direct contact with the KCl substrate (marked in orange). Note that the orientation of the organic components with respect to each other and with respect to the KCl substrate has been randomly chosen except for the lateral alignment of the PFP needles relative to the KCl substrate.

The study of OSCs by TEM is challenging due to the low stability of organic crystals under irradiation with the electron beam. Nevertheless, this study has shown that TEM techniques could be a powerful tool to succeed in the characterization of organic blends if suitable conditions are applied. Although the current work provides rather detailed experimental data on the structure and arrangement of the different phases in these blends, further theoretical calculations are needed to obtain information on the mixed phase formation mechanism at the interface together with the exact crystal structure of the mixed phase.

6. Summary and outlook

‘Success is the sum of small efforts, repeated day in and day out’

— Robert Collier

OSC materials have the advantage of flexibility, low cost and ease-of-production. Although some applications from these materials have already been commercialized and are part of our daily life, there is still the need for a deeper scientific understanding of them in order to achieve optimum device performances. This thesis deals with the study of the morphology, epitaxial alignment, orientation and crystalline properties of OSCs grown on different substrates.

Two OSCs have been chosen for this purpose: PFP and heterostructures involving codeposited PEN and PFP. Thereby, the dissertation has been divided in two different works:

- Microstructural characterization of PFP grown on graphene substrate.
- Microstructural characterization of mixtures formed by PEN and PFP grown on KCl and SiO_2 substrates.

The understanding of the microscopic structures of molecular semiconductor films is not only a challenging topic in fundamental research, but also of key importance for organic electronics. In such devices, optoelectronic solid state properties are important parameters for device performance. However, they are highly anisotropic and they critically depend on the degree of crystallinity, the ordering and the arrangement of organic molecules. Within the scope of this thesis, (S)TEM has been established as suitable methods that have allowed the characterization of the above mentioned organic materials at a nanometer scale. Among others, the main focus has been concentrated on SAED patterns and DF- and BF-TEM imaging. In addition, some other techniques such as EDX, STEM and HRTEM have been used.

The first part of this research deals with the study of PFP grown on graphene. Two main targets have been pursued:

- The determination of the lateral alignment between the molecules of PFP and the graphene film.
- The study of the faceting exhibited by the PFP islands deposited on graphene.

Since charge transport properties in PFP depend on an efficient π-orbital overlap between the molecules, it is important to understand the structure and molecular packing in PFP thin films as well as the growth mechanisms at the interface which produce such structures.

The epitaxial relation between the PFP molecules and the graphene substrate has been determined, revealing that the long molecular axis of PFP is aligned along the high symmetry directions of graphene referred to as the 'zig-zag' directions. However, this alignment is not perfect since it exhibits a small offset. XRD experiments have been also applied achieving similar results to TEM characterization, .i.e. the offset value between the long molecular axis of the PFP molecules and the graphene zig-zag direction is ca. -3/-3.7° in the multilayer films.

The alignment of the long axis of the PFP molecules relative to the graphene has been analyzed not only in the multilayer regime but also in the monolayer structure via STM techniques. This inspection has evidenced that the misalignment already starts at the interface between the substrate and the PFP molecules. Further information has been obtained by MM calculations, showing that the molecules adsorbed at the interface behave as orientational precursor and are directly incorporated into the multilayer films upon slight rotation.

PFP grown on graphene exhibits an epitaxial growth in island shapes. This thesis goes insight into the crystal habitus of the PFP islands on the supporting graphene lattice. It has been found that many PFP islands exhibit an angle of around 68° between confining edges. TEM analyses have revealed that the crystallographic planes which run parallel to these confining edges in the 2D TEM projection are the $(\bar{7}\ 8\ 2)_{PFP}$ and $(\overline{40}\ \bar{1}\ 5)_{PFP}$ planes. From that, some of the possible side facts associated with each confining edge have been identified and their Miller-indices have been provided. Moreover, ET has been applied to show detailed information on the side facets of some selected islands, i.e. the angle enclosed by two side facets of the characteristic confining edges changes along the height of the island. This fact is caused by the different inclination relative to the substrate surface that is presented by one of the side facets.

The second part of the results concerns the influence of the mixing ratio and the substrate on the arrangement and ordering of the organic heterostructures formed by PEN and PFP. Two different substrates have been selected for this purpose: SiO_2 an inert substrate, and KCl as crystalline substrate.

On SiO_2 substrate, mixing ratios of PEN:PFP [2:1], [1:1] and [1:2] have been investigated. Electron diffraction experiments have corroborated the presence of a mixed phase formed between PEN and PFP with similar lattice parameters regardless of the mixing ratio. In the equimolecular PEN:PFP [1:1] blend, mainly the mixed phase is formed. In contrast, apart from the mixed phase, the respective pure phase is also found in the mixtures with excess of PEN and PFP. The SAED pattern exhibited by the mixed phase is similar to the one presented by the PEN polymorph in [0 0 1] zone axis, but the mixed phase's reflections are at least in **a*** direction closer to the primary reflection than the PEN's reflections. The morphology and the distribution of the different phases observed in the non-equimolecular blends have also been studied. The PEN:PFP [2:1] blend displays a granular structure with a crystal grain size in the range of (10–60) nm. Per contra, the PEN:PFP [1:2] mixture exhibits a background layer formed by the mixed phase with some fibers on top made out of pure PFP.

On KCl substrate, mixing ratios of PEN:PFP [2:1] and [1:2] have been investigated. In both cases, poly-crystalline layers are formed where molecules adopt an upright orientation.

The PEN:PFP [2:1] blend is composed of elongated domains of pure PEN which coexist with the mixed phase. The elongated domains display a 4-fold ordering. The **b** direction of the PEN/mixed phase unit cell points along the elongation of the organic domains, which in turn, are oriented along the $<1\ 0\ 0>_{KCl}$ directions.

In contrast, the PEN:PFP [1:2] blend exhibits two different arrangements. The majority of the sample is formed by spicular fibers of PFP on a background layer made out of the mixed phase which is lying on the KCl substrate. The long axis of the PFP needles is oriented perpendicular to their $[1\ 0\ 0]_{PFP}$ direction and thus parallel to the KCl substrate surface. Additionally to a lesser extent, regions containing a continuous PFP film located directly on the KCl substrate appear. This PFP layer exhibits the

[1 0 0] orientation normal to the substrate with domains elongated along the $[0\ 1\ 0]_{PFP}$ direction.

The influence of the supporting substrate on the PEN:PFP heterostructures has been evidenced by using SiO_2 and KCl. In the case of PEN:PFP blends grown on SiO_2, the amorphous substrate leads to the formation of tangle of fibers and/or grain structures which are isotropically distributed within the surface plane. On the contrary, the crystalline KCl alkali halide substrate yields epitaxially aligned structures of large sizes. Even though, different structural conformations are formed by the organic films on the different substrates, the mixed phase between PEN and PFP is always found with the same lattice parameters and in the same orientation. This shows that the attraction between the PEN and PFP compounds is stronger than the attraction in their pure systems, and consequently, this attraction is stronger than the molecule-substrate interactions.

In summary, the results presented in this dissertation constitute a comprehensive investigation of orientation, arrangement and distribution of organic films on different substrates.

Concerning future experiments, there are many further works that will delve into the knowledge of PFP/graphene system and that will shed light into the PEN:PFP heterostructures. Since OSCs have vastly different properties compared to inorganic semiconductors, the full understanding of their fundamental properties and the processes that take place at the organic film/substrate interfaces, can contribute to the development of new organic materials, which would satisfy the needs of the market

This thesis underlines the utility of graphene and its high potential for the replacement to ITO as transparent conductive layer. In contrast to the HB molecular orientation exhibited by PFP on ITO-coated glass substrates, the epitaxial growth of PFP on graphene with a π-stacked arrangement is expected to maximize the vertical π-π overlapping improving the charge carrier mobility. Further works regarding the mechanism of carrier transport across the substrate-organic interfaces and faceting formation, as well as a deeper knowledge of the molecular arrangement and

intermolecular interactions will be crucial for opening new possibilities of the use of these organic materials in devices.

Additionally, these results highlight the importance of heterostructures of PEN and PFP as a good way to obtain ambipolar OSCs. The molecular assembling has an impact on optical and electronic properties of heterostructures. The inclusion of organic heterostructures in organic electronic devices is increasing, thus studies that provide routes to understand the arrangement and distribution of molecules in organic blends become important. They constitute a valuable piece of information from both fundamental as well as applications perspective for the production of efficient donor-acceptor interfaces of future organic materials.

However, this is just the beginning, and further progress in the understanding of: (i) structure formation, (ii) processes which occur at various organic/substrate interfaces and (iii) elementary micro- and macroscopy properties will serve as an important milestone for the development of novel organic material systems.

List of acronyms

acronym	meaning
2D	two-dimensional
3D	three-dimensional
ADF	annular dark field
AFM	atomic force microscopy / microscope
ART	algebra reconstruction technique
a.u.	arbitrary units
BFP	back focal plane
BF-TEM	bright field-TEM
BSE	back-scattered electrons
CES	Consumer Electronics Show
C/F	carbon-to-fluorine
CL	cathodoluminescence
CLA	condenser lens aperture
Cs	spherical aberration
CTF	contrast transfer function
CVD	chemical vapor deposition
DF-TEM	dark field-TEM
DRS	differential reflectance spectroscopy
EDX	energy dispersive X ray
EELS	electron energy loss spectroscopy
EFTEM	energy filtered TEM
ET	electron tomography
FEG	field emission gun

acronym	meaning
FFT	fast Fourier transform
FIB	focused ion beam
FTIR	Fourier-transform infrared
GIXD	grazing incidence X-ray diffraction
HAADF	high-angle annular dark field
HB	herringbone
HOMO	highest occupied molecular orbital
HOPG	highly oriented pyrolytic graphite
HRTEM	high resolution TEM
HT	high temperature
ITO	high cost tin doped indium oxide
LaB_6	lanthanum hexaboride
LCD	liquid crystal display
LT	low temperature
LUMO	lowest unoccupied molecular orbital
MFP	mean free path
MM	molecular mechanics
NEXAFS	near edge X ray absorption fine structure spectroscopy
OA	objective aperture
OFET	organic field-effect transistor
OL	objective lens
OLED	organic light-emitting diode
OMBD	organic molecular beam deposition
OPV	organic photovoltaic cell

acronym	meaning
OSC	organic semiconductor
PAH	polycyclic aromatic hydrocarbon
PEN	pentacene
PFP	perfluoropentacene
PL	photoluminescence
PS-polymorph	π-stacked polymorph
QCM	quartz-crystal microbalance
SAD	selected area diffraction
SART	simultaneous algebra reconstruction technique
SC	single crystal
SE	secondary electrons
SEM	scanning electron microscopy / microscope
SIRT	simultaneous iterative reconstruction technique
STEM	scanning transmission electron microscopy / microscope
STM	scanning tunneling microscopy
STXM	scanning transmission X-ray microscopy
TDS	thermal desorption spectroscopy
TEM	transmission electron microscopy / microscope
TF	thin film
TMTSF	tetramethyltetraselenofulvalen
TTF-TCNQ	tetrathiafulvene-tetracyanoquinodimethane
UHV	ultra high vacuum
VASE	variable angle spectroscopic ellipsometry
XPS	X-ray photoelectron spectroscopy

acronym	**meaning**
XRD	X-ray diffraction
XRR	X-ray reflectivity
WBP	weighted backprojection
WZL	Weiss Zone Law
Z.A.	zone axis

References

[1] C.D. Dimitrakopoulos, P.R.L. Malenfant, Organic Thin Film Transistors for Large Area Electronics, Adv. Mater. 14 (2002) 99–117. doi:10.1002/1521-4095(20020116)14:2<99::AID-ADMA99>3.0.CO;2-9.

[2] C. Reese, M. Roberts, M. Ling, Z. Bao, Organic thin film transistors, Mater. Today. 7 (2004) 20–27. doi:http://dx.doi.org/10.1016/S1369-7021(04)00398-0.

[3] T.B. Singh, N.S. Sariciftci, Progress in Plastic electronics Devices, Annu. Rev. Mater. Res. 36 (2006) 199–230. doi:10.1146/annurev.matsci.36.022805.094757.

[4] S.R. Forrest, The path to ubiquitous and low-cost organic electronic appliances on plastic, Nature. 428 (2004) 911–918. doi:10.1038/nature02498.

[5] A. Dodabalapur, Organic and polymer transistors for electronics, Mater. Today. 9 (2006) 24–30. doi:10.1016/S1369-7021(06)71444-4.

[6] N.T. Kalyani, S.J. Dhoble, Organic light emitting diodes: Energy saving lighting technology-A review, Renew. Sustain. Energy Rev. 16 (2012) 2696–2723. doi:10.1016/j.rser.2012.02.021.

[7] J.-H. Jou, S. Kumar, A. Agrawal, T.-H. Li, S. Sahoo, Approaches for fabricating high efficiency organic light emitting diodes, J. Mater. Chem. C. 3 (2015) 2974–3002. doi:10.1039/c4tc02495h.

[8] B.J. Jung, N.J. Tremblay, M.-L. Yeh, H.E. Katz, Molecular Design and Synthetic Approaches to Electron-Transporting Organic Transistor Semiconductors, Chem. Mater. 23 (2011) 568–582. doi:10.1021/cm102296d.

[9] H. Sirringhaus, 25th Anniversary Article: Organic Field-Effect Transistors: The Path Beyond Amorphous Silicon, Adv. Mater. 26 (2014) 1319–1335. doi:10.1002/adma.201304346.

[10] J.E. Anthony, A. Facchetti, M. Heeney, S.R. Marder, X. Zhan, n-Type Organic Semiconductors in Organic Electronics, Adv. Mater. 22 (2010) 3876–3892. doi:10.1002/adma.200903628.

[11] W. Cao, J. Xue, Recent progress in organic photovoltaics: device architecture and optical design, Energy Environ. Sci. 7 (2014) 2123–2144. doi:10.1039/c4ee00260a.

[12] V. Coropceanu, J. Cornil, D.A. da Silva Filho, Y. Olivier, R. Silbey, J.-L. Brédas, Charge Transport in Organic Semiconductors, Chem. Rev. 107 (2007) 926–952. doi:10.1021/cr050140x.

[13] F. Ortmann, F. Bechstedt, K. Hannewald, Charge transport in organic crystals: Theory and modelling, Phys. Status Solidi. 248 (2011) 511–525. doi:10.1002/pssb.201046278.

[14] Z. Bao, J. Locklin, Organic Field-Effect Transistors, 1st ed., CRC Press, Inc., Boca Raton, FL, USA, 2007.

[15] X.C. Li, H. Sirringhaus, F. Garnier, A.B. Holmes, S.C. Moratti, N. Feeder, W. Clegg, S.J. Teat, R.H. Friend, A highly pi-stacked organic semiconductor for thin film transistors based on fused thiophenes, J. Am. Chem. Soc. 120 (1998) 2206–2207. doi:10.1021/ja9735968.

[16] J.E. Anthony, J.S. Brooks, D.L. Eaton, S.R. Parkin, Functionalized pentacene: Improved electronic properties from control of solid-state order, J. Am. Chem. Soc. 123 (2001) 9482–9483. doi:10.1021/ja0162459.

[17] K. Kobayashi, H. Masu, A. Shuto, K. Yamaguchi, Control of face-to-face pi-pi stacked packing arrangement of anthracene rings via chalcogen-chalcogen interaction: 9,10-bis(methylchalcogeno)anthracenes, Chem. Mater. 17 (2005) 6666–6673. doi:10.1021/cm051874t.

[18] A.L. Briseno, Q. Miao, M.M. Ling, C. Reese, H. Meng, Z.N. Bao, F. Wudl, Hexathiapentacene: Structure, molecular packing, and thin-film transistors, J. Am. Chem. Soc. 128 (2006) 15576–15577. doi:10.1021/ja066088j.

[19] Z.H. Chen, P. Muller, T.M. Swager, Syntheses of soluble, pi-stacking tetracene derivatives, Org. Lett. 8 (2006) 273–276. doi:10.1021/ol0526468.

[20] K. Kobayashi, R. Shimaoka, M. Kawahata, M. Yamanaka, K. Yamaguchi, Synthesis and cofacial pi-stacked packing arrangement of 6,13-bis(alkylthio)pentacene, Org. Lett. 8 (2006) 2385–2388. doi:10.1021/ol060679x.

[21] H. Sasaki, Y. Wakayama, T. Chikyow, E. Barrena, H. Dosch, K. Kobayashi, Growth of anthracene derivative thin films with a pi-stacking structure, Appl. Phys. Lett. 88 (2006) 81907. doi:10.1063/1.2178196.

[22] I. Salzmann, A. Moser, M. Oehzelt, T. Breuer, X. Feng, Z.-Y. Juang, D. Nabok, R.G. Della Valle, S. Duhm, G. Heimel, A. Brillante, E. Venuti, I. Bilotti, C. Christodoulou, J. Frisch, P. Puschnig, C. Draxl, G. Witte, K. Muellen, N. Koch, Epitaxial Growth of pi-Stacked Perfluoropentacene on Graphene-Coated Quartz, ACS Nano. 6 (2012) 10874–10883. doi:10.1021/nn3042607.

[23] T. Breuer, I. Salzmann, J. Götzen, M. Oehzelt, A. Morherr, N. Koch, G. Witte, Interrelation between Substrate Roughness and Thin-Film Structure of Functionalized Acenes on Graphite, Cryst. Growth Des. 11 (2011) 4996–5001. doi:10.1021/cg200894y.

[24] K.J. Thorley, C. Risko, Mapping the configuration dependence of electronic coupling in organic semiconductors, J. Mater. Chem. C. 4 (2016) 3825–3832. doi:10.1039/C5TC03765D.

[25] A. Hinderhofer, F. Schreiber, Organic–Organic Heterostructures: Concepts and Applications, ChemPhysChem. 13 (2012) 628–643. doi:10.1002/cphc.201100737.

[26] T. Breuer, G. Witte, Thermally activated intermixture in pentacene-perfluoropentacene heterostructures, J. Chem. Phys. 138 (2013) 114901. doi:10.1063/1.4795004.

[27] R. Ruiz, D. Choudhary, B. Nickel, T. Toccoli, K.C. Chang, A.C. Mayer, P. Clancy, J.M. Blakely, R.L. Headrick, S. Iannotta, G.G. Malliaras, Pentacene thin film growth, Chem. Mater. 16 (2004) 4497–4508. doi:10.1021/cm049563q.

[28] H. Yanagi, T. Morikawa, Self-waveguided blue light emission in p-sexiphenyl crystals epitaxially grown by mask-shadowing vapor deposition, Appl. Phys. Lett. 75 (1999) 187–189. doi:10.1063/1.124314.

[29] Y. Yoshida, H. Takiguchi, T. Hanada, N. Tanigaki, E.M. Han, K. Yase, Control of growth mechanism and optical properties of p-sexiphenyl thin films on ionic crystal substrates, J. Cryst. Growth. 198 (1999) 923–928. doi:10.1016/s0022-0248(98)01186-5.

[30] T. Kiyomura, T. Nemoto, T. Ogawa, T. Minari, K. Yoshida, H. Kurata, S. Isoda, Thin-film phase of pentacene film formed on KCl by vacuum deposition, Japanese J. Appl. Phys. Part 1-Regular Pap. Br. Commun. Rev. Pap. 45 (2006) 401–404. doi:10.1143/jjap.45.401.

[31] T. Breuer, G. Witte, Epitaxial growth of perfluoropentacene films with predefined molecular orientation: A route for single-crystal optical studies, Phys. Rev. B. 83 (2011) 155428. doi:10.1103/PhysRevB.83.155428.

[32] R. Félix, T. Breuer, P. Rotter, F. Widdascheck, B. Eckhardt, G. Witte, K. Volz, K.I. Gries, Microstructural Analysis of Perfluoropentacene Films on Graphene and Graphite: Interface-Mediated Alignment and Island Formation, Cryst. Growth Des. 16 (2016) 6941–6950. doi:10.1021/acs.cgd.6b01117.

[33] R. Félix, K. Volz, K.I. Gries, Codeposited pentacene:perfluoropentacene grown on SiO2: A microstructural study by transmission electron microscopy, J. Cryst. Growth. 458 (2017) 87–95. doi:10.1016/j.jcrysgro.2016.09.077.

[34] R. Félix, T. Breuer, G. Witte, K. Volz, K.I. Gries, Microstructural study of codeposited pentacene:perfluoropentacene grown on KCl by TEM techniques, J. Cryst. Growth. 471 (2017) 29–36. doi:10.1016/j.jcrysgro.2017.05.009.

[35] G.E. Moore, Cramming more components onto integrated circuits, 1965. doi:10.1109/JPROC.1998.658762.

[36] G.E. Moore, Progress in digital integrated electronics, IEEE Conf. Publ. - Int. Electron Devices Meet. 21 (1975) 11–13. doi:10.1109/N-SSC.2006.4804410.

[37] D. House, Expanding Moore's Law, Intel Corp. Prod. TL_002. (2002). http://www.cc.gatech.edu/computing/nano/documents/Intel - Expanding Moore's Law.pdf%0A (accessed April 29, 2017).

[38] J. Bardeen, W.H. Brattain, The Transistor, A Semi-Conductor Triode, Phys. Rev. 74 (1948) 230–231. doi:10.1103/PhysRev.74.230.

[39] W. Brütting, Introduction to the Physics of Organic Semiconductors, in: Phys. Org. Semicond., Wiley-VCH Verlag GmbH & Co. KGaA, 2006: pp. 1–14. doi:10.1002/3527606637.ch.

[40] J. Shinar, Organic light-emitting devices: A survey, Springer, New York, 2004. doi:10.1007/978-0-387-21720-8.

[41] T. Aernouts, P. Vanlaeke, W. Geens, J. Poortmans, P. Heremans, S. Borghs, R. Mertens, R. Andriessen, L. Leenders, Printable anodes for flexible organic solar cell modules, Thin Solid Films. 451–452 (2004) 22–25. doi:10.1016/j.tsf.2003.11.038.

[42] A. Afzali, C.D. Dimitrakopoulos, T.L. Breen, High-Performance, Solution-Processed Organic Thin Film Transistors from a Novel Pentacene Precursor, J. Am. Chem. Soc. 124 (2002) 8812–8813. doi:10.1021/ja0266621.

[43] C.J. Brabec, N.S. Sariciftci, J.C. Hummelen, Plastic Solar Cells, Adv. Funct. Mater. 11 (2001) 15–26. doi:10.1002/1616-3028(200102)11:1<15::AID-ADFM15>3.0.CO;2-A.

[44] H. Letheby, XXIX. On the production of a blue substance by the electrolysis of sulphate of aniline, J. Chem. Soc. 15 (1862) 161–163. doi:10.1039/JS8621500161.

[45] A. Pochettino, A. Sella, Photoelectric behavior of anthracene, Atti Accad. Naz. Lincei. 15 (1906) 355– 363.

[46] M. Volmer, Die verschiedenen lichtelektrischen Erscheinungen amAnthracen, ihre Beziehungen zueinander, zur Fluoreszenz und Dianthracenbildung, Ann. Phys. 345 (1913) 775–796.

[47] H. Naarmann, Polymers, Electrically Conducting, in: Ullmann's Encycl. Ind. Chem., Wiley-VCH Verlag GmbH & Co. KGaA, 2000. doi:10.1002/14356007.a21_429.

[48] R. McNeill, R. Siudak, J.H. Wardlaw, D.E. Weiss, Electronic Conduction in Polymers. I. The Chemical Structure of Polypyrrole, Aust. J. Chem. 16 (1963) 1056–1075. doi:10.1071/CH9631056.

[49] B.A. Bolto, D.E. Weiss, Electronic Conduction in Polymers. II. The Electrochemical Reduction of Polypyrrole at Controlled Potential, Aust. J. Chem. 16 (1963) 1076–1089. doi:10.1071/CH9631076.

[50] B.A. Bolto, R. McNeill, D.E. Weiss, Electronic conduction in polymers. III. Electronic properties of polypyrrole, Aust. J. Chem. 16 (1963) 1090–1103.

[51] H. Shirakawa, E.J. Louis, A.G. MacDiarmid, C.K. Chiang, A.J. Heeger, Synthesis of electrically conducting organic polymers: halogen derivatives of polyacetylene (CH), J. Chem. Soc. Chem. Commun. (1977) 578–580. doi:10.1039/C39770000578.

[52] Nobel Media, The Nobel Prize in Chemistry, (2000). https://www.nobelprize.org/nobel_prizes/chemistry/laureates/2000/ (accessed April 29, 2017).

[53] K.K. Kanazawa, A.F. Diaz, R.H. Geiss, W.D. Gill, J.F. Kwak, J.A. Logan, J.F. Rabolt, G.B. Street, "Organic metals": polypyrrole a stable synthetic "metallic" polymer, J. Chem. Soc. Chem. Commun. (1979) 854–855. doi:10.1039/C39790000854.

[54] A.F. Diaz, K.K. Kanazawa, G.P. Gardini, Electrochemical polymerization of pyrrole, J. Chem. Soc. Chem. Commun. (1979) 635–636. doi:10.1039/C39790000635.

[55] A.F. Diaz, Electrochemical preparation and characterisation of conducting polymers, Chem. Scr. 17 (1981) 145–148.

[56] K. Bechgaard, C.S. Jacobsen, K. Mortensen, H.J. Pedersen, N. Thorup, The properties of five highly conducting salts: (TMTSF)2 X, X = PF 6-, AsF6-, SbF6-, BF4- and NO3-, derived from tetramethyltetraselenafulvalene (TMTSF), Solid State Commun. 33 (1980) 1119–1125. doi:10.1016/0038-1098(80)91088-1.

[57] C.W. Tang, Two-layer organic photovoltaic cell, Appl. Phys. Lett. 48 (1986) 183–185. doi:10.1063/1.96937.

[58] C.W. Tang, S.A. Vanslyke, Organic electroluminescent diodes, Appl. Phys. Lett. 51 (1987) 913–915. doi:10.1063/1.98799.

[59] J.H. Burroughes, D.D.C. Bradley, A.R. Brown, R.N. Marks, K. Mackay, R.H. Friend, P.L. Burns, A.B. Holmes, Light-emitting diodes based on conjugated polymers, Nature. 347 (1990) 539–541. 10.1038/347539a0.

[60] F. Ebisawa, T. Kurokawa, S. Nara, Electrical properties of polyacetylene/polysiloxane interface, J. Appl. Phys. 54 (1983) 3255–3259. doi:10.1063/1.332488.

[61] J.H. Burroughes, C.A. Jones, R.H. Friend, New semiconductor device physics in polymer diodes and transistors, Nature. 335 (1988) 137–141. http://dx.doi.org/10.1038/335137a0.

[62] A. Tsumura, H. Koezuka, T. Ando, Polythiophene field-effect transistor: Its characteristics and operation mechanism, Synth. Met. 25 (1988) 11–23. doi:10.1016/0379-6779(88)90318-9.

[63] A. Assadi, C. Svensson, M. Willander, O. Inganäs, Field-effect mobility of poly(3-hexylthiophene), Appl. Phys. Lett. 53 (1988) 195–197. doi:10.1063/1.100171.

[64] R. Madru, G. Guillaud, M. Al Sadoun, M. Maitrot, J.-J. André, J. Simon, R. Even, A well-behaved field effect transistor based on an intrinsic molecular semiconductor, Chem. Phys. Lett. 145 (1988) 343–346. doi:10.1016/0009-2614(88)80018-6.

[65] C. Clarisse, M.T. Riou, M. Gauneau, M. Le Contellect, Field-effect transistor with diphthalocyanine thin film, Electron. Lett. 24 (1988) 674–675. http://digital-library.theiet.org/content/journals/10.1049/el_19880456.

[66] F. Garnier, G. Horowitz, X. Peng, D. Fichou, An all-organic “soft” thin film transistor with very high carrier mobility, Adv. Mater. 2 (1990) 592–594. doi:10.1002/adma.19900021207.

[67] S. Forrest, Energy efficiency with organic electronics: Ching W. Tang revisits his days at Kodak, MRS Bull. 37 (2012) 552–553. doi:10.1557/mrs.2012.125.

[68] M.A. Green, K. Emery, Y. Hishikawa, W. Warta, E.D. Dunlop, Solar cell efficiency tables (version 47), Prog. Photovoltaics Res. Appl. 24 (2016) 3–11. doi:10.1002/pip.2728.

[69] S. Berny, N. Blouin, A. Distler, H.-J. Egelhaaf, M. Krompiec, A. Lohr, O.R. Lozman, G.E. Morse, L. Nanson, A. Pron, T. Sauermann, N. Seidler, S. Tierney, P. Tiwana, M. Wagner, H. Wilson, Solar Trees: First Large-Scale Demonstration of Fully Solution Coated, Semitransparent, Flexible Organic Photovoltaic Modules, Adv. Sci. 3 (2016) 1500342–n/a. doi:10.1002/advs.201500342.

[70] Y.W. and R.H. and H.-S. Seo, Recent progress in photoactive organic field-effect transistors, Sci. Technol. Adv. Mater. 15 (2014) 24202. http://stacks.iop.org/1468-6996/15/i=2/a=024202.

[71] G. Gelinck, P. Heremans, K. Nomoto, T.D. Anthopoulos, Organic Transistors in Optical Displays and Microelectronic Applications, Adv. Mater. 22 (2010) 3778–3798. doi:10.1002/adma.200903559.

[72] M.D. Angione, R. Pilolli, S. Cotrone, M. Magliulo, A. Mallardi, G. Palazzo, L. Sabbatini, D. Fine, A. Dodabalapur, N. Cioffi, L. Torsi, Carbon based materials for electronic bio-sensing, Mater. Today. 14 (2011) 424–433. doi:10.1016/S1369-7021(11)70187-0.

[73] D. Natali, M. Caironi, 7 - Organic photodetectors, in: B. Nabet (Ed.), Photodetectors, Woodhead Publishing, 2016: pp. 195–254. doi:10.1016/B978-1-78242-445-1.00007-5.

[74] J.M. Shaw, P.F. Seidler, Organic electronics: Introduction, IBM J. Res. Dev. 45 (2001) 3–9. doi:10.1147/rd.451.0003.

[75] S.-S. Sun, L.R. Dalton, S.-S. Sun, L.R. Dalton, Introduction to Organic Electronic and Optoelectronic Materials and Devices (Optical Science and Engineering Series), CRC Press, Inc., Boca Raton, FL, USA, 2008.

[76] D.A. Bernards, G.G. Malliaras, OwensRóisín M., Organic Semiconductors in Sensor Applications, Springer, Berlin and Heidelberg, 2008. doi:10.1007/978-3-540-76314-7.

[77] D.A. Bernards, R.M. Owens, G.G. Malliaras, Organic Semiconductors in Sensor Applications, Springer, Berlin and Heidelberg, 2008. doi:10.1007/978-3-540-76314-7.

[78] Organic Semiconductor World, (2016). https://www.iapp.de/orgworld.de/?Basics:What_are_organic_semiconductors (accessed February 2, 2017).

[79] E.A. Silinsh, V. Capek, Organic Molecular Crystals: Interaction, Localization and Transport Phenomena, American Chemical Society, New York, 1994. doi:10.1021/ja945159o.

[80] N. Zhou, A. Facchetti, Charge Transport and Recombination in Organic Solar Cells (OSCs), in: H. Huang, J. Huang (Eds.), Org. Hybrid Sol. Cells, Springer International Publishing, Cham, 2014: pp. 19–52. doi:10.1007/978-3-319-10855-1_2.

[81] E.A. Silinsh, V. Capek, Organic Molecular Crystals: Interaction, Localization and Transport Phenomena, American Chemical Society, New York, 1994. doi:10.1021/ja945159o.

[82] H.E. Katz, Z. Bao, S.L. Gilat, Synthetic Chemistry for Ultrapure, Processable, and High-Mobility Organic Transistor Semiconductors, Acc. Chem. Res. 34 (2001) 359–369. doi:10.1021/ar990114j.

[83] H. Sirringhaus, Organic semiconductors: An equal-opportunity conductor, Nat Mater. 2 (2003) 641–642. doi:10.1038/nmat988.

[84] A. Pron, P. Rannou, Processible conjugated polymers: from organic semiconductors to organic metals and superconductors, Prog. Polym. Sci. 27 (2002) 135–190. doi:10.1016/S0079-6700(01)00043-0.

[85] F. Cacialli, Organic semiconductors for the new millennium, Philos. Trans. R. Soc. London A Math. Phys. Eng. Sci. 358 (2000) 173–192. doi:10.1098/rsta.2000.0526.

[86] W. Kowalsky, E. Becker, T. Benstem, H.-H. Johannes, D. Metzdorf, H. Neuner, J. Schöbel, Organic semiconductors: fundamentals and applications BT - Advances in Solid State Physics 40, in: B. Kramer (Ed.), Springer Berlin Heidelberg, Berlin, Heidelberg, 2000: pp. 795–808. doi:10.1007/BFb0108396.

[87] G. Horowitz, Organic Semiconductors for new electronic devices, Adv. Mater. 2 (1990) 287–292. doi:10.1002/adma.19900020604.

[88] H. Usta, A. Facchetti, Polymeric and Small-Molecule Semiconductors for Organic Field-Effect Transistors, in: Large Area Flex. Electron., Wiley-VCH Verlag GmbH & Co. KGaA, 2015: pp. 1–100. doi:10.1002/9783527679973.ch1.

[89] G.R. Desiraju, A. Gavezzotti, Crystal structures of polynuclear aromatic hydrocarbons. Classification, rationalization and prediction from molecular structure, Acta Crystallogr. Sect. B. 45 (1989) 473–482. doi:10.1107/S0108768189003794.

[90] J.E. Anthony, Functionalized acenes and heteroacenes for organic electronics, Chem. Rev. 106 (2006) 5028–5048. doi:10.1021/cr050966z.

[91] S. Kera, H. Yamane, N. Ueno, First-principles measurements of charge mobility in organic semiconductors: Valence hole–vibration coupling in organic ultrathin films, Prog. Surf. Sci. 84 (2009) 135–154. doi:10.1016/j.progsurf.2009.03.002.

[92] C.D. Sheraw, T.N. Jackson, D.L. Eaton, J.E. Anthony, Functionalized Pentacene Active Layer Organic Thin-Film Transistors, Adv. Mater. 15 (2003) 2009–2011. doi:10.1002/adma.200305393.

[93] F.J.M. Hoeben, P. Jonkheijm, E.W. Meijer, A.P.H.J. Schenning, About Supramolecular Assemblies of π-Conjugated Systems, Chem. Rev. 105 (2005) 1491–1546. doi:10.1021/cr030070z.

[94] J.Y. Lee, S. Roth, Y.W. Park, Anisotropic field effect mobility in single crystal pentacene, Appl. Phys. Lett. 88 (2006) 252106. doi:10.1063/1.2216400.

[95] H. Huang, S. Chen, X. Gao, W. Chen, A.T.S. Wee, Structural and Electronic Properties of PTCDA Thin Films on Epitaxial Graphene, ACS Nano. 3 (2009) 3431–3436. doi:10.1021/nn9008615.

[96] G. Giri, E. Verploegen, S.C.B. Mannsfeld, S. Atahan-Evrenk, D.H. Kim, S.Y. Lee, H.A. Becerril, A. Aspuru-Guzik, M.F. Toney, Z. Bao, Tuning charge transport in solution-sheared organic semiconductors using lattice strain, Nature. 480 (2011) 504–508. doi:10.1038/nature10683.

[97] S.C.B. Mannsfeld, M.L. Tang, Z. Bao, Thin Film Structure of Triisopropylsilylethynyl-Functionalized Pentacene and Tetraceno[2,3-b]thiophene from Grazing Incidence X-Ray Diffraction, Adv. Mater. 23 (2011) 127–131. doi:10.1002/adma.201003135.

[98] C.D. Dimitrakopoulos, D.J. Mascaro, Organic thin-film transistors: A review of recent advances, IBM J. Res. Dev. 45 (2001) 11–27. doi:10.1147/rd.451.0011.

[99] L.B. Roberson, J. Kowalik, L.M. Tolbert, C. Kloc, R. Zeis, X.L. Chi, R. Fleming, C. Wilkins, Pentacene disproportionation during sublimation for field-effect transistors, J. Am. Chem. Soc. 127 (2005) 3069–3075. doi:10.1021/ja044586r.

[100] O.D. Jurchescu, M. Popinciuc, B.J. van Wees, T.T.M. Palstra, Interface-controlled, high-mobility organic transistors, Adv. Mater. 19 (2007) 688–692. doi:10.1002/adma.200600929.

[101] H. Klauk, M. Halik, U. Zschieschang, G. Schmid, W. Radlik, W. Weber, High-mobility polymer gate dielectric pentacene thin film transistors, J. Appl. Phys. 92 (2002) 5259–5263. doi:10.1063/1.1511826.

[102] R.B. Campbell, J.M. Robertson, J. Trotter, The crystal structure of hexacene, and a revision of the crystallographic data for tetracene and pentacene, Acta Crystallogr. 15 (1962) 289–290. doi:10.1107/S0365110X62000699.

[103] T. Siegrist, C. Kloc, J.H. Schön, B. Batlogg, R.C. Haddon, S. Berg, G.A. Thomas, Enhanced physical properties in a pentacene polymorph, Angew. Chemie-International Ed. 40 (2001) 1732–1736. doi:10.1002/1521-3773(20010504)40:9<1732::aid-anie17320>3.0.co;2-7.

[104] C.C. Mattheus, A.B. Dros, J. Baas, A. Meetsma, J.L. de Boer, T.T.M. Palstra, Polymorphism in pentacene, Acta Crystallogr. Sect. C. 57 (2001) 939–941. doi:10.1107/S010827010100703X.

[105] T. Siegrist, C. Besnard, S. Haas, M. Schiltz, P. Pattison, D. Chernyshov, B. Batlogg, C. Kloc, A polymorph lost and found: The high-temperature crystal structure of pentacene, Adv. Mater. 19 (2007) 2079–2082. doi:10.1002/adma.200602072.

[106] A. Girlando, M. Masino, A. Brillante, T. Toccoli, S. Iannotta, Raman Identification of Polymorphs in Pentacene Films, Crystals. 6 (2016).

[107] S. Schiefer, M. Huth, A. Dobrinevski, B. Nickel, Determination of the crystal structure of substrate-induced pentacene polymorphs in fiber structured thin films, J. Am. Chem. Soc. 129 (2007) 10316–10317. doi:10.1021/ja0730516.

[108] C.C. Mattheus, A.B. Dros, J. Baas, G.T. Oostergetel, A. Meetsma, J.L. de Boer, T.T.M. Palstra, Identification of polymorphs of pentacene, Synth. Met. 138 (2003) 475–481. doi:10.1016/s0379-6779(02)00467-8.

[109] L.F. Drummy, D.C. Martin, Thickness-Driven Orthorhombic to Triclinic Phase Transformation in Pentacene Thin Films, Adv. Mater. 17 (2005) 903–907. doi:10.1002/adma.200400189.

[110] I.P.M. Bouchoms, W.A. Schoonveld, J. Vrijmoeth, T.M. Klapwijk, Morphology identification of the thin film phases of vacuum evaporated pentacene on SIO_2 substrates, Synth. Met. 104 (1999) 175–178. doi:10.1016/s0379-6779(99)00050-8.

[111] H. Akimichi, T. Inoshita, S. Hotta, H. Noge, H. Sakaki, Structure of pentacene/tetracene superlattices deposited on glass substrate, Appl. Phys. Lett. 63 (1993) 3158–3160. doi:10.1063/1.110234.

[112] P.A. Stadelmann, EMS - A Software package for electron-diffraction analysis and HREM image simulation in materials science, Ultramicroscopy. 21 (1987) 131–145. doi:10.1016/0304-3991(87)90080-5.

[113] Y. Sakamoto, T. Suzuki, M. Kobayashi, Y. Gao, Y. Fukai, Y. Inoue, F. Sato, S. Tokito, Perfluoropentacene: High-performance p-n junctions and complementary circuits with pentacene, J. Am. Chem. Soc. 126 (2004) 8138–8140. doi:10.1021/ja0476258.

[114] Y. Inoue, Y. Sakamoto, T. Suzuki, M. Kobayashi, Y. Gao, S. Tokito, Organic thin-film transistors with high electron mobility based on perfluoropentacene, Japanese J. Appl. Phys. Part 1-Regular Pap. Br. Commun. Rev. Pap. 44 (2005) 3663–3668. doi:10.1143/jjap.44.3663.

[115] I. Salzmann, S. Duhm, G. Heimel, J.P. Rabe, N. Koch, M. Oehzelt, Y. Sakamoto, T. Suzuki, Structural order in perfluoropentacene thin films and heterostructures with pentacene, Langmuir. 24 (2008) 7294–7298. doi:10.1021/la800606h.

[116] J. Götzen, C.H. Schwalb, C. Schmidt, G. Mette, M. Marks, U. Hoefer, G. Witte, Structural Evolution of Perfluoro-Pentacene Films on Ag(111): Transition from 2D to 3D Growth, Langmuir. 27 (2011) 993–999. doi:10.1021/la1022664.

[117] J.E. Anthony, The larger acenes: Versatile organic semiconductors, Angew. Chemie-International Ed. 47 (2008) 452–483. doi:10.1002/anie.200604045.

[118] J. Wang, H.B. Wang, X.J. Yan, H.C. Huang, D.H. Yan, Organic heterojunction and its application for double channel field-effect transistors, Appl. Phys. Lett. 87 (2005) 93507. doi:10.1063/1.2037204.

[119] H.B. Wang, J. Wang, H.C. Huang, X.J. Yan, D.H. Yan, Organic heterojunction with reverse rectifying characteristics and its application in field-effect transistors, Org. Electron. 7 (2006) 369–374. doi:10.1016/j.orgel.2006.04.004.

[120] K.M. Lau, J.X. Tang, H.Y. Sun, C.S. Lee, S.T. Lee, D.H. Yan, Interfacial electronic structure of copper phthalocyanine and copper hexadecafluorophthalocyanine studied by photoemission, Appl. Phys. Lett. 88 (2006) 173513. doi:10.1063/1.2198484.

[121] V. Gohri, S. Hofmann, S. Reineke, T. Rosenow, M. Thomschke, M. Levichkova, B. Lussem, K. Leo, White top-emitting organic light-emitting diodes employing a heterostructure of down-conversion layers, Org. Electron. 12 (2011) 2126–2130. doi:10.1016/j.orgel.2011.09.002.

[122] S. Jia, H.D. Sun, J.H. Du, Z.K. Zhang, D.D. Zhang, L.P. Ma, J.S. Chen, D.G. Ma, H.M. Cheng, W.C. Ren, Graphene oxide/graphene vertical heterostructure electrodes for highly efficient and flexible organic light emitting diodes, Nanoscale. 8 (2016) 10714–10723. doi:10.1039/c6nr01649a.

[123] P. Peumans, S. Uchida, S.R. Forrest, Efficient bulk heterojunction photovoltaic cells using small-molecular-weight organic thin films, Nature. 425 (2003) 158–162. doi:10.1038/nature01949.

[124] D.J. Lipomi, H. Chong, M. Vosgueritchian, J.G. Mei, Z.A. Bao, Toward mechanically robust and intrinsically stretchable organic solar cells: Evolution of photovoltaic properties with tensile strain, Sol. Energy Mater. Sol. Cells. 107 (2012) 355–365. doi:10.1016/j.solmat.2012.07.013.

[125] M.C. Scharber, N.S. Sariciftci, Efficiency of bulk-heterojunction organic solar cells, Prog. Polym. Sci. 38 (2013) 1929–1940. doi:10.1016/j.progpolymsci.2013.05.001.

[126] A.J. Pertsin, O.K. Nugmanov, G.N. Marchenko, A.I. Kitaigorodsky, Crystal structure of cellulose polymorphs by potential energy calculations: 1. Most probable models for mercerized cellulose, Polymer (Guildf). 25 (1984) 107–114. doi:10.1016/0032-3861(84)90274-X.

[127] A.I. Kitaigorodsky, Mixed Crystals, Springer-Verlag Berlin Heidelberg, 1984. doi:10.1007/978-3-642-81672-7.

[128] A. Dodabalapur, H.E. Katz, L. Torsi, R.C. Haddon, Organic Heterostructure Field-Effect Transistors, Science. 269 (1995) 1560–1562. doi:10.1126/science.269.5230.1560.

[129] A. Dodabalapur, H.E. Katz, L. Torsi, R.C. Haddon, Organic field-effect bipolar transistors, Appl. Phys. Lett. 68 (1996) 1108–1110. doi:10.1063/1.115728.

[130] A. Dodabalapur, H.E. Katz, L. Torsi, R.C. Haddon, Organic field-effect bipolar transistors, Appl. Phys. Lett. 68 (1996) 1108–1110. doi:10.1063/1.115728.

[131] Y.-Y. Lin, A. Dodabalapur, R. Sarpeshkar, Z. Bao, W. Li, K. Baldwin, V.R. Raju, H.E. Katz, Organic complementary ring oscillators, Appl. Phys. Lett. 74 (1999) 2714–2716. doi:10.1063/1.123946.

[132] F. Babudri, G.M. Farinola, F. Naso, R. Ragni, Fluorinated organic materials for electronic and optoelectronic applications: the role of the fluorine atom, Chem. Commun. (2007) 1003–1022. doi:10.1039/b611336b.

[133] I. Salzmann, S. Duhm, G. Heimel, M. Oehzelt, R. Kniprath, R.L. Johnson, J.P. Rabe, N. Koch, Tuning the ionization energy of organic semiconductor films: The role of intramolecular polar bonds, J. Am. Chem. Soc. 130 (2008) 12870–12871. doi:10.1021/ja804793a.

[134] S. Kowarik, K. Broch, A. Hinderhofer, A. Schwartzberg, J.O. Osso, D. Kilcoyne, F. Schreiber, S.R. Leone, Crystal Grain Orientation in Organic Homo- and Heteroepitaxy of Pentacene and Perfluoropentacene Studied with X-ray Spectromicroscopy, J. Phys. Chem. C. 114 (2010) 13061–13067. doi:10.1021/jp103713z.

[135] A. Hinderhofer, C. Frank, T. Hosokai, A. Resta, A. Gerlach, F. Schreiber, Structure and morphology of coevaporated pentacene-perfluoropentacene thin films, J. Chem. Phys. 134 (2011) 104702. doi:10.1063/1.3557476.

[136] K. Broch, U. Heinemeyer, A. Hinderhofer, F. Anger, R. Scholz, A. Gerlach, F. Schreiber, Optical evidence for intermolecular coupling in mixed films of pentacene and perfluoropentacene, Phys. Rev. B. 83 (2011) 245307. doi:10.1103/PhysRevB.83.245307.

[137] F. Anger, J.O. Ossó, U. Heinemeyer, K. Broch, R. Scholz, A. Gerlach, F. Schreiber, Photoluminescence spectroscopy of pure pentacene, perfluoropentacene, and mixed thin films, J. Chem. Phys. 136 (2012) 54701. doi:10.1063/1.3677839.

[138] K. Broch, C. Bürker, J. Dieterle, S. Krause, A. Gerlach, F. Schreiber, Impact of molecular tilt angle on the absorption spectra of pentacene: perfluoropentacene blends, Phys. Status Solidi-Rapid Res. Lett. 7 (2013) 1084–1088. doi:10.1002/pssr.201308085.

[139] B. Haas, K.I. Gries, T. Breuer, I. Häusler, G. Witte, K. Volz, Microstructural Characterization of Organic Heterostructures by (Transmission) Electron Microscopy, Cryst. Growth Des. 14 (2014) 3010–3014. doi:10.1021/cg5002896.

[140] L. de Broglie, XXXV. A tentative theory of light quanta, Philos. Mag. Ser. 6. 47 (1924) 446–458. doi:10.1080/14786442408634378.

[141] R. Brydson, Aberration-Corrected Analytical Transmission Electron Microscopy, 1st ed., John Wiley & Sons, Ltd, 2011. doi:10.1002/9781119978848.

[142] R. Erni, Aberration-corrected imaging in transmission electron microscopy : an introduction, ICP/Imperial College Press, London, 2010.

[143] B. Fultz, J.M. Howe, Transmission Electron Microscopy and Diffractometry of Materials, 4th ed., Springer-Verlag Berlin Heidelberg, 2013. doi:10.1007/978-3-642-29761-8.

[144] H. Rose, W. Wan, Aberration Correction in Electron Microscopy, Proc. 2005 Part. Accel. Conf. (2005) 44–48. doi:10.1109/PAC.2005.1590354.

[145] D.B. Williams, C.B. Carter, Transmission Electron Microscopy. A Textbook for Materials Science, 2nd ed., Springer US, 2009. doi:10.1007/978-0-387-76501-3.

[146] F. Krumeich, Properties of Electrons, their Interactions with Matter and Applications in Electron Microscopy, (2014). http://www.microscopy.ethz.ch/downloads/Interactions.pdf.

[147] L. Reimer, Transmission Electron Microscopy. Physics of Image Formation and Microanalysis, 4th ed., Springer Berlin Heidelberg, 1997. doi:10.1007/978-3-662-14824-2.

[148] S.A. Maier, Plasmonics: Fundamentals and Applications, 1st ed., Springer US, 2007. doi:10.1007/0-387-37825-1.

[149] E. Rutherford, LXXIX. The scattering of α and β particles by matter and the structure of the atom, Philos. Mag. 21 (1911) 669–688. doi:10.1080/14786440508637080.

[150] W.L. Bragg, The diffraction of short electromagnetic Waves by a Crystal, Proc. Camb. Phil. Soc. 17 (1914).

[151] G. Dennler, M.C. Scharber, C.J. Brabec, Polymer-Fullerene Bulk-Heterojunction Solar Cells, Adv. Mater. 21 (2009) 1323–1338. doi:10.1002/adma.200801283.

[152] The 14 Bravais lattices, (2017). http://img.tfd.com/mgh/cep/The-14-Bravais-lattices-derived-by-centering-of-the-seven-crystal.jpg (accessed May 23, 2017).

[153] G. Henderson, D. Neuville, R. Downs, Spectroscopic Methods in Mineralogy and Material Sciences, Mineralogical Society of America, 2014. doi:10.2138/am-2014-655.

[154] O. Scherzer, The Theoretical Resolution Limit of the Electron Microscope, J. Appl. Phys. 20 (1949) 20–29. doi:10.1063/1.1698233.

[155] A. Ott, Structural characterization of antimonide-based metamorphic buffer layers on (001) silicon substrate, PhD Thesis, Philipps-Universität Marburg, 2016.

[156] T. Walther, Y. Qiu, A.G. Cullis, Measuring the contrast in annular dark field STEM images as a function of camera length, J. Phys. Conf. Ser. 241 (2010) 12068. http://stacks.iop.org/1742-6596/241/i=1/a=012068.

[157] P. Hartel, H. Rose, C. Dinges, Conditions and reasons for incoherent imaging in STEM, Ultramicroscopy. 63 (1996) 93–114. doi:10.1016/0304-3991(96)00020-4.

[158] D.J. De Rosier, A. Klug, Reconstruction of Three Dimensional Structures from Electron Micrographs, Nature. 217 (1968) 130–134. doi:10.1038/217130a0.

[159] R.G. Hart, Electron microscopy of unstained biological material: the polytropic montage., Science. 159 (1968) 1464–1467.

[160] W. Hoppe, R. Langer, G. Knesch, C. Poppe, Protein crystal structure analysis with electron radiation, Naturwissenschaften. 55 (1968) 333–336.

[161] R. McIntosh, D. Nicastro, D. Mastronarde, New views of cells in 3D: an introduction to electron tomography, Trends Cell Biol. 15 (2005) 43–51. doi:10.1016/j.tcb.2004.11.009.

[162] A. Guesdon, S. Blestel, C. Kervrann, D. Chrétien, Single versus dual-axis cryo-electron tomography of microtubules assembled in vitro: Limits and perspectives, J. Struct. Biol. 181 (2013) 169–178. doi:10.1016/j.jsb.2012.11.004.

[163] J. Frank, B.F. McEwen, Alignment by Cross-Correlation, in: J. Frank (Ed.), Electron Tomogr. Three-Dimensional Imaging with Transm. Electron Microsc., Springer US, Boston, MA, 1992: pp. 205–213. doi:10.1007/978-1-4757-2163-8_9.

[164] M.C. Lawrence, Least-Squares Method of Alignment Using Markers, in: J. Frank (Ed.), Electron Tomogr. Three-Dimensional Imaging with Transm. Electron Microsc., Springer US, Boston, MA, 1992: pp. 197–204. doi:10.1007/978-1-4757-2163-8_8.

[165] J. Frank, Electron Tomography Methods for Three Dimensional Visualization of Structures in the Cell, 2nd ed., Springer-Verlag New York, 2006. doi:10.1007/978-0-387-69008-7.

[166] J. Radon, Über die Bestimmung von Funktionen durch ihre Integralwerte längs gewisser Mannigfaltigkeiten, Akad. Wiss. 69 (1917) 262–277. citeulike-article-id:7680709.

[167] A. Kak, M. Slaney, Principles of Computerized Tomographic Imaging, Society for Industrial and Applied Mathematics, 2001. doi:doi:10.1137/1.9780898719277.

[168] P. Ercius, O. Alaidi, M.J. Rames, G. Ren, Electron Tomography: Electron Tomography: A Three-Dimensional Analytic Tool for Hard and Soft Materials Research, Adv. Mater. 27 (2015) 5637. doi:10.1002/adma.201570253.

[169] N.M. Asl, A. Sadremomtaz, Analytical image reconstruction methods in emission tomography, J. Biomed. Sci. Eng. 6 (2013) 27659. doi:10.4236/jbise.2013.61013.

[170] R. Gordon, R. Bender, G.T. Herman, Algebraic Reconstruction Techniques (ART) for three-dimensional electron microscopy and X-ray photography, J. Theor. Biol. 29 (1970) 471–481. doi:10.1016/0022-5193(70)90109-8.

[171] A.H. Andersen, A.C. Kak, Simultaneous Algebraic Reconstruction Technique (SART): A superior implementation of the ART algorithm, Ultrason. Imaging. 6 (1984) 81–94. doi:10.1016/0161-7346(84)90008-7.

[172] P. Gilbert, Iterative methods for the three-dimensional reconstruction of an object from projections., J. Theor. Biol. 36 (1972) 105–117. doi:10.1016/j.jsb.2005.10.005.

[173] Avizo Fire, FEI, SAS – Visualization Sciences Group, Hillsboro, USA, (2014). https://www.fei.com/software/amira-avizo/ (accessed April 10, 2017).

[174] D. Wolf, A. Lubk, H. Lichte, Weighted simultaneous iterative reconstruction technique for single-axis tomography., Ultramicroscopy. 136 (2014) 15–25. doi:10.1016/j.ultramic.2013.07.016.

[175] C. Rompf, W. Kowalsky, Organic Molecular Beam Deposition (OMBD) for Photonic and Electronic Devices, Annu. Report, Inst. Hochfrequenztechnik, TU Braunschweig. (1995) 45–47. https://www.tu-braunschweig.de/Medien-DB/ihf/p045-047.pdf.

[176] A.K. Geim, K.S. Novoselov, The rise of graphene, Nat. Mater. 6 (2007) 183–191. doi:10.1038/nmat1849.

[177] C. Lee, X. Wei, J.W. Kysar, J. Hone, Measurement of the Elastic Properties and Intrinsic Strength of Monolayer Graphene, Science. 321 (2008) 385–388. doi:10.1126/science.1157996.

[178] A.K. Geim, Graphene: Status and Prospects, Science. 324 (2009) 1530–1534. doi:10.1126/science.1158877.

[179] K.P. Loh, Q. Bao, G. Eda, M. Chhowalla, Graphene oxide as a chemically tunable platform for optical applications, Nat Chem. 2 (2010) 1015–1024. doi:10.1038/nchem.907.

[180] J. Wu, M. Agrawal, H.A. Becerril, Z. Bao, Z. Liu, Y. Chen, P. Peumans, Organic Light-Emitting Diodes on Solution-Processed Graphene Transparent Electrodes, ACS Nano. 4 (2010) 43–48. doi:10.1021/nn900728d.

[181] A.H. Castro Neto, F. Guinea, N.M.R. Peres, K.S. Novoselov, A.K. Geim, The electronic properties of graphene, Rev. Mod. Phys. 81 (2009) 109–162. doi:10.1103/RevModPhys.81.109.

[182] Y.-M. Lin, C. Dimitrakopoulos, K.A. Jenkins, D.B. Farmer, H.-Y. Chiu, A. Grill, P. Avouris, 100-GHz Transistors from Wafer-Scale Epitaxial Graphene, Science. 327 (2010) 662. doi:10.1126/science.1184289.

[183] R.R. Nair, P. Blake, A.N. Grigorenko, K.S. Novoselov, T.J. Booth, T. Stauber, N.M.R. Peres, A.K. Geim, Fine Structure Constant Defines Visual Transparency of Graphene, Science. 320 (2008) 1308. doi:10.1126/science.1156965.

[184] J.-H. Chen, C. Jang, S. Xiao, M. Ishigami, M.S. Fuhrer, Intrinsic and extrinsic performance limits of graphene devices on SiO2, Nat Nano. 3 (2008) 206–209. doi:10.1038/nnano.2008.58.

[185] S. Bae, H. Kim, Y. Lee, X. Xu, J.-S. Park, Y. Zheng, J. Balakrishnan, T. Lei, H. Ri Kim, Y. Il Song, Y.-J. Kim, K.S. Kim, B. Ozyilmaz, J.-H. Ahn, B.H. Hong, S. Iijima, Roll-to-roll production of 30-inch graphene films for transparent electrodes, Nat Nano. 5 (2010) 574–578. doi:10.1038/nnano.2010.132.

[186] X. Wan, G. Long, L. Huang, Y. Chen, Graphene – A Promising Material for Organic Photovoltaic Cells, Adv. Mater. 23 (2011) 5342–5358. doi:10.1002/adma.201102735.

[187] L. Gomez De Arco, Y. Zhang, C.W. Schlenker, K. Ryu, M.E. Thompson, C. Zhou, Continuous, highly flexible, and transparent graphene films by chemical vapor deposition for organic photovoltaics, ACS Nano. 4 (2010) 2865–2873. doi:10.1021/nn901587x.

[188] X. Wang, L. Zhi, K. Muellen, Transparent, conductive graphene electrodes for dye-sensitized solar cells, Nano Lett. 8 (2008) 323–327. doi:10.1021/nl072838r.

[189] J. Wu, H.A. Becerril, Z. Bao, Z. Liu, Y. Chen, P. Peumans, Organic solar cells with solution-processed graphene transparent electrodes, Appl. Phys. Lett. 92 (2008) 263302. doi:10.1063/1.2924771.

[190] C. Yan, J.H. Cho, J.-H. Ahn, Graphene-based flexible and stretchable thin film transistors, Nanoscale. 4 (2012) 4870–4882. doi:10.1039/C2NR30994G.

[191] H.-K. Seo, M.-H. Park, Y.-H. Kim, S.-J. Kwon, S.-H. Jeong, T.-W. Lee, Laminated Graphene Films for Flexible Transparent Thin Film Encapsulation, ACS Appl. Mater. Interfaces. 8 (2016) 14725–14731. doi:10.1021/acsami.6b01639.

[192] S. Park, S.H. Shin, M.N. Yogeesh, A.L. Lee, S. Rahimi, D. Akinwande, Extremely High-Frequency Flexible Graphene Thin-Film Transistors, IEEE Electron Device Lett. 37 (2016) 512–515. doi:10.1109/LED.2016.2535484.

[193] R. Pawlak, M. Lebioda, J. Rymaszewski, W. Szymanski, L. Kolodziejczyk, P. Kula, A Fully Transparent Flexible Sensor for Cryogenic Temperatures Based on High Strength Metallurgical Graphene, Sensors. 17 (2017). doi:10.3390/s17010051.

[194] G. Eda, Y.-Y. Lin, S. Miller, C.-W. Chen, W.-F. Su, M. Chhowalla, Transparent and conducting electrodes for organic electronics from reduced graphene oxide, Appl. Phys. Lett. 92 (2008) 233305. doi:10.1063/1.2937846.

[195] K.S. Kim, Y. Zhao, H. Jang, S.Y. Lee, J.M. Kim, K.S. Kim, J.-H. Ahn, P. Kim, J.-Y. Choi, B.H. Hong, Large-scale pattern growth of graphene films for stretchable transparent electrodes, Nature. 457 (2009) 706–710. doi:10.1038/nature07719.

[196] Y. Wen, J. Chen, L. Zhang, X. Sun, Y. Zhao, Y. Guo, G. Yu, Y. Liu, Quantitative Analysis of the Role of the First Layer in p- and n-Type Organic Field-Effect Transistors with Graphene Electrodes, Adv. Mater. 24 (2012) 1471–1475. doi:10.1002/adma.201104055.

[197] W.H. Lee, J. Park, S.H. Sim, S.B. Jo, K.S. Kim, B.H. Hong, K. Cho, Transparent Flexible Organic Transistors Based on Monolayer Graphene Electrodes on Plastic, Adv. Mater. 23 (2011) 1752–1756. doi:10.1002/adma.201004099.

[198] S. Lee, G. Jo, S.-J. Kang, G. Wang, M. Choe, W. Park, D.-Y. Kim, Y.H. Kahng, T. Lee, Enhanced Charge Injection in Pentacene Field-Effect Transistors with Graphene Electrodes, Adv. Mater. 23 (2011) 100–105. doi:10.1002/adma.201003165.

[199] Z. Mao, Y.-C. Kim, H.-D. Lee, P. Adusumilli, D.N. Seidman, NiSi crystal structure, site preference, and partitioning behavior of palladium in NiSi(Pd)/Si(100) thin films: Experiments and calculations, Appl. Phys. Lett. 99 (2011) 13106. doi:10.1063/1.3606536.

[200] K. Xiao, W. Deng, J.K. Keum, M. Yoon, I. V Vlassiouk, K.W. Clark, A.-P. Li, I.I. Kravchenko, G. Gu, E.A. Payzant, B.G. Sumpter, S.C. Smith, J.F. Browning, D.B. Geohegan, Surface-Induced Orientation Control of CuPc Molecules for the Epitaxial Growth of Highly Ordered Organic Crystals on Graphene, J. Am. Chem. Soc. 135 (2013) 3680–3687. doi:10.1021/ja3125096.

[201] J.M. Mativetsky, H. Wang, S.S. Lee, L. Whittaker-Brooks, Y.-L. Loo, Face-on stacking and enhanced out-of-plane hole mobility in graphene-templated copper phthalocyanine, Chem. Commun. 50 (2014) 5319–5321. doi:10.1039/C3CC47516F.

[202] T. McAfee, E. Gann, T. Guan, S.C. Stuart, J. Rowe, D.B. Dougherty, H. Ade, Toward Single-Crystal Hybrid-Carbon Electronics: Impact of Graphene Substrate Defect Density on Copper Phthalocyanine Film Growth, Cryst. Growth Des. 14 (2014) 4394–4401. doi:10.1021/cg500504u.

[203] Graphenea, (2017). https://www.graphenea.com/products/suspended-monolayer-graphene-on-tem-grids (accessed April 10, 2017).

[204] J.R. Kremer, D.N. Mastronarde, J.R. McIntosh, Computer Visualization of Three-Dimensional Image Data Using IMOD, J. Struct. Biol. 116 (1996) 71–76. doi:10.1006/jsbi.1996.0013.

[205] J. Fayos, Possible 3D carbon structures as progressive intermediates in graphite to diamond phase transition, J. Solid State Chem. 148 (1999) 278–285. doi:10.1006/jssc.1999.8448.

[206] M. Kumai, A Study of Hexagonal and Cubic Ice at Low Temperatures, U.S. Army Materiel Command, Cold Regions Research & Engineering Laboratory, 1967. https://books.google.de/books?id=RulzGQAACAAJ.

[207] C.F. Macrae, P.R. Edgington, P. McCabe, E. Pidcock, G.P. Shields, R. Taylor, M. Towler, J. de Streek, Mercury : visualization and analysis of crystal structures https://www.ccdc.cam.ac.uk/Community/csd-community/freemercury, J. Appl. Crystallogr. 39 (2006) 453–457. doi:10.1107/S002188980600731X.

[208] J.W. Ponder, TINKER—Software Tools for Molecular Design, (2015) http://dasher.wustl.edu/tinker V7.1.3.

[209] S. Pratontep, M. Brinkmann, F. Nuesch, L. Zuppiroli, Nucleation and growth of ultrathin pentacene films on silicon dioxide: effect of deposition rate and substrate temperature, Synth. Met. 146 (2004) 387–391. doi:10.1016/j.synthmet.2004.08.017.

[210] S.D. Wang, X. Dong, C.S. Lee, S.T. Lee, Molecular orientation and film morphology of pentacene on native silicon oxide surface, J. Phys. Chem. B. 109 (2005) 9892–9896. doi:10.1021/jp046490p.

[211] A. Moser, J. Novak, H.-G. Flesch, T. Djuric, O. Werzer, A. Haase, R. Resel, Temperature stability of the pentacene thin-film phase, Appl. Phys. Lett. 99 (2011) 221911. doi:10.1063/1.3665188.

[212] L. von Helden, T. Breuer, G. Witte, Anisotropic thermal expansion in pentacene and perfluoropentacene: Effects of molecular packing motif and fixation at the interface, Appl. Phys. Lett. 110 (2017) 141904. doi:10.1063/1.4979650.

[213] A.A. Kelly, K.M. Knowles, Crystallography and Crystal Defects, Second edition, in: J.W.& Sons (Ed.), Crystallogr. Cryst. Defects, 2012: p. 536.

[214] Pelco silicon dioxide transparent membrane, (2017) 22–23. http://www.cp-download.de/plano11/Kapitel-1.pdf (accessed May 5, 2017).

[215] D. Guo, S. Ikeda, K. Saiki, Pentacene films grown on surface treated SiO_2 substrates, Thin Solid Films. 515 (2006) 814–817. doi:https://doi.org/10.1016/j.tsf.2005.12.208.

[216] H. Yanagisawa, T. Tamaki, M. Nakamura, K. Kudo, Structural and electrical characterization of pentacene films on SiO_2 grown by molecular beam deposition, Thin Solid Films. 464 (2004) 398–402. doi:http://dx.doi.org/10.1016/j.tsf.2004.06.065.

[217] J.T. Sadowski, G. Sazaki, S. Nishikata, A. Al-Mahboob, Y. Fujikawa, K. Nakajima, R.M. Tromp, T. Sakurai, Single-Nucleus Polycrystallization in Thin Film Epitaxial Growth, Phys. Rev. Lett. 98 (2007) 46104. doi:10.1103/PhysRevLett.98.046104.

[218] B. Haas, A. Beyer, W. Witte, T. Breuer, G. Witte, K. Volz, Application of transmission electron microscopy for microstructural characterization of perfluoropentacene thin films, J. Appl. Phys. 110 (2011) 73514. doi:10.1063/1.3646549.

[219] S. Kowarik, A. Gerlach, A. Hinderhofer, S. Milita, F. Borgatti, F. Zontone, T. Suzuki, F. Biscarini, F. Schreiber, Structure, morphology, and growth dynamics of perfluoro-pentacene thin films, Phys. Status Solidi-Rapid Res. Lett. 2 (2008) 120–122. doi:10.1002/pssr.200802052.

[220] B. Haas, Transmission Electron Microscopic Investigations of Pentacene, Perfluoropentacene and Codeposited Films on Alkali Halide Substrates, Masther Thesis, Philipps-Universität Marburg, 2011.

[221] A. Romano, J. Vanhellemont, H. Bender, J.R. Morante, A fast preparation technique for high-quality plan view and cross-section TEM specimens of semiconducting materials, Ultramicroscopy. 31 (1989) 183–192. doi:10.1016/0304-3991(89)90212-X.

[222] P.J. Goodhew, Thin film preparation for electron microscopy. Practical Methods in Electron Microscopy, Elsevier, Amsterdam, 1985.

[223] L.A. Giannuzzi, J.L. Drown, S.R. Brown, R.B. Irwin, F.A. Stevie, Applications of the FIB lift-out technique for TEM specimen preparation, Microsc. Res. Tech. 41 (1998) 285–290. doi:10.1002/(SICI)1097-0029(19980515)41:4<285::AID-JEMT1>3.0.CO;2-Q.

[224] L.A. Giannuzzi, F.A. Stevie, A review of focused ion beam milling techniques for TEM specimen preparation, Micron. 30 (1999) 197–204. doi:https://doi.org/10.1016/S0968-4328(99)00005-0.

[225] J.F. Walker, J.C. Reiner, C. Solenthaler, Focused ion beam sample preparation for TEM. In: Microscopy of Semiconducting Materials, Springer Proceedings in Physics, 1995.

[226] J.R. Fryer, F. Holland, The reduction of radiation damage in the electron microscope, Ultramicroscopy. 11 (1983) 67–70. doi:10.1016/0304-3991(83)90055-4.

[227] W. Witte, Strukturuntersuchung von Pentacen- und Perfluoropentacenfilmen mittels Transmissionselektronenmikroskopie, Bachelor Thesis, Philipps-Universität Marburg, 2010.

Curriculum Vitae

The Curriculum Vitae on pages 249-250 has been removed to protect personal data. They are therefore not included in the online publication.